



UNIVERSITAT DE
BARCELONA

Microquasar jets and their interaction with the medium: theoretical studies and observations with the MAGIC telescope

Pol Bordas Coma

ADVERTIMENT. La consulta d'aquesta tesi queda condicionada a l'acceptació de les següents condicions d'ús: La difusió d'aquesta tesi per mitjà del servei TDX (www.tdx.cat) i a través del Dipòsit Digital de la UB (diposit.ub.edu) ha estat autoritzada pels titulars dels drets de propietat intel·lectual únicament per a usos privats emmarcats en activitats d'investigació i docència. No s'autoritza la seva reproducció amb finalitats de lucre ni la seva difusió i posada a disposició des d'un lloc aliè al servei TDX ni al Dipòsit Digital de la UB. No s'autoritza la presentació del seu contingut en una finestra o marc aliè a TDX o al Dipòsit Digital de la UB (framing). Aquesta reserva de drets afecta tant al resum de presentació de la tesi com als seus continguts. En la utilització o cita de parts de la tesi és obligat indicar el nom de la persona autora.

ADVERTENCIA. La consulta de esta tesis queda condicionada a la aceptación de las siguientes condiciones de uso: La difusión de esta tesis por medio del servicio TDR (www.tdx.cat) y a través del Repositorio Digital de la UB (diposit.ub.edu) ha sido autorizada por los titulares de los derechos de propiedad intelectual únicamente para usos privados enmarcados en actividades de investigación y docencia. No se autoriza su reproducción con finalidades de lucro ni su difusión y puesta a disposición desde un sitio ajeno al servicio TDR o al Repositorio Digital de la UB. No se autoriza la presentación de su contenido en una ventana o marco ajeno a TDR o al Repositorio Digital de la UB (framing). Esta reserva de derechos afecta tanto al resumen de presentación de la tesis como a sus contenidos. En la utilización o cita de partes de la tesis es obligado indicar el nombre de la persona autora.

WARNING. On having consulted this thesis you're accepting the following use conditions: Spreading this thesis by the TDX (www.tdx.cat) service and by the UB Digital Repository (diposit.ub.edu) has been authorized by the titular of the intellectual property rights only for private uses placed in investigation and teaching activities. Reproduction with lucrative aims is not authorized nor its spreading and availability from a site foreign to the TDX service or to the UB Digital Repository. Introducing its content in a window or frame foreign to the TDX service or to the UB Digital Repository is not authorized (framing). Those rights affect to the presentation summary of the thesis as well as to its contents. In the using or citation of parts of the thesis it's obliged to indicate the name of the author.

UNIVERSITAT DE BARCELONA

DEPARTAMENT D'ASTRONOMIA I METEOROLOGIA

**Microquasar jets and their
interaction with the medium**

**Theoretical studies and observations with the
MAGIC telescope**

Memòria presentada per

Pol Bordas Coma

per optar al grau de

Doctor per la Universitat de Barcelona

Barcelona, Octubre 2009

PROGRAMA DE DOCTORAT D'ASTRONOMIA I METEOROLOGIA

BIENNI 2004–2006

Memòria presentada per **Pol Bordas Coma** per optar al grau de
Doctor per la Universitat de Barcelona

DIRECTOR DE LA TESI

Dr. Josep Maria Paredes Poy

Agraïments

Aquesta tesi ha estat realitzada gràcies a les aportacions de molta gent: els membres del Departament d'Astronomia i Meteorologia, els instituts que m'han acollit durant les estances a l'estranger, la col·laboració MAGIC, i especialment els companys que conformen el Grup de recerca on la tesi ha crescut i s'ha desenvolupat. L'impuls científic necessari, les discussions, els consells i el constant aprenentatge mantinguts amb vosaltres els darrers anys fonamenten aquest treball. El nexa entre la investigació i la resta de l'Univers té com a protagonista la Pilar, a.k.a. Nikita. Ha estat present en tot, sempre, incondicionalment... tu ets la font de tota Magia! La família i els amics i amigues han aportat la motivació i comprensió necessàries per viure aquesta etapa d'una manera esplèndida, fent grats i amens els moments més complicats.

Espero que disfruteu aquesta memòria de tesi, és ben vostra.

Contents

Resum de la tesi:

Els jets dels microquàsars i la seva interacció amb el medi. Estudis teòrics i observacions amb el telescopi MAGIC	v
---	---

1 Introduction	1
1.1 Outline of the thesis	2
2 Phenomenology of microquasars	7
2.1 Main properties	7
2.2 Quasars and microquasars	9
2.3 High mass, low mass and radio emitting X-ray binary systems	11
2.4 X-ray spectral states	13
2.5 Microquasars from radio to VHE gamma-rays	16
3 Physical processes in microquasar jets	21
3.1 Accretion disk and jet formation	22
3.2 Hadronic <i>vs</i> Leptonic jets	25
3.3 Particle acceleration	27
3.3.1 First order Fermi acceleration process	28

3.4	Radiative processes	32
3.4.1	Leptonic processes	33
3.4.2	Hadronic processes	39
3.4.3	Gamma-ray absorption processes	41
3.5	Strong shock hydrodynamic conditions	42
3.6	Self-Similar treatment of jet interactions	44
I	Interaction of microquasar jets with the medium	51
4	Jet interaction with the companion star wind and radiation field	53
4.1	Model description	54
4.1.1	Production of secondary leptons	57
4.2	Model Results	60
4.2.1	Primary gamma-ray emission	60
4.2.2	Emission from secondary leptons	61
4.3	Discussion and conclusions	63
5	Jet interaction with the interstellar medium	69
5.1	Model description	70
5.1.1	Structure of the interaction regions	71
5.1.2	The non-thermal particle populations	75
5.2	Model Results	76
5.2.1	Bow shock emission	77
5.2.2	Cocoon emission	79

5.2.3	Reconfinement region emission	79
5.3	Hydrodynamical simulations	79
5.3.1	Comparison with the analytical model	82
5.4	Discussion and conclusions	83
 II Observations of microquasars with the MAGIC telescope		91
 6 High and Very High Energy gamma-ray astrophysics		93
6.1	Space-based observatories	94
6.2	Ground-based VHE observatories	97
6.2.1	Physics of the air showers	100
6.2.2	Imaging Atmospheric Cherenkov technique	104
 7 The MAGIC telescope		109
7.1	Short overview	109
7.1.1	Mounting and drive system	110
7.1.2	Reflector and camera	111
7.1.3	Read-out, trigger and data acquisition chain	113
7.1.4	The Calibration system	114
7.2	MAGIC II	115
7.3	Data analysis procedure	116
7.3.1	Data types and observation modes	116
7.3.2	Data sample quality check	118
7.3.3	Image cleaning and parameterization	120

7.3.4	γ /hadron separation	125
7.4	Signal evaluation	126
7.4.1	Optimization of HADRONNESS and ALPHA/THETA cuts	127
7.4.2	Significance calculation	128
7.4.3	Flux sensitivity	129
7.4.4	Upper limit calculation	130
7.4.5	MAGIC Analysis and Reconstruction Software (MARS)	130
8	Observations of microquasars	135
8.1	Microquasars as Binary TeV sources	135
8.2	Observations of Cyg X-1	137
8.2.1	Source description and previous observations	137
8.2.2	Trigger conditions and data sample	138
8.2.3	Data analysis and results	140
8.3	Discussion	143
8.4	Observations of the SS 433/W50 system	148
8.4.1	Source description and previous observations	148
8.4.2	Trigger conditions and data sample	151
8.4.3	Data analysis and results	153
8.5	Discussion	157
8.5.1	Steady emission from SS 433	157
8.5.2	Interaction regions of SS 433/W50	161
9	Concluding remarks	169

Resum de la tesi:

Els jets dels microquàsars i la seva interacció amb el medi.

Estudis teòrics i observacions amb el telescopi MAGIC

0.1 - Introducció i objectius

Aquesta tesi recull un treball d'investigació centrat en la natura dels jets dels microquàsars, la seva interacció amb l'entorn i la capacitat d'emetre raigs gamma de molt alta energia. Per a aconseguir prediccions concretes ha estat necessari estudiar la física dels jets en detall: l'energia que transporten, la matèria que els constitueix, el medi que els envolta o en el qual es propaguen (camps de matèria, magnètics i de radiació), així com els processos d'acceleració que s'hi donen. El context astrofísic actual situa els microquàsars en un encreuament on diverses disciplines hi centren l'atenció. Des de l'estudi dels sistemes binaris amb una companya massiva que esdevé un objecte compacte (una estrella de neutrons o un forat negre) fins la comprensió dels orígens dels raigs còsmics que arriben a la terra des de totes les direccions. En aquests sistemes s'hi produeix l'acceleració de partícules elementals, amb masses $\sim 10^{-28}$ grams, fins a energies properes a la mil·lèsima de Joule (uns 10^4 erg en unitats Centímetre Gram Segon, CGS), i podrien explicar la natura de les noves fonts descobertes amb els telescopis Cherenkov i satèl·lits que operen en el rang GeV–TeV - un electronvolt ($1 \text{ eV} = 1.6 \times 10^{-11}$ erg és la quantitat d'energia cinètica que guanya un electró lliure quan és accelerat mitjançant una diferència de potencial electrostàtic d'un volt, un teraelectronvolt ($1 \text{ TeV} = 10^{12}$ eV i un gigaelectronvolt ($1 \text{ GeV} = 10^9$ eV. A més a més, són protagonistes de recents descobertes

no exemptes de debat científic. En particular, la natura microquàsar/púlsar dels sistemes LS 5039 i LS I 61+303, la detecció de Cyg X-1 amb el telescopi MAGIC, o el descobriment de noves fonts en el cel gamma encara no identificades, són alguns del camps per explorar. Nous experiments i observatoris en el rang GeV-TeV són necessaris per entendre l'emissió més energètica dins l'ampli espectre electromagnètic dels microquàsars. Per altra banda, la fenomenologia d'aquests sistemes és semblant en molts aspectes a la que es pot trobar en els Nuclis de Galàxies Actius (AGN). Alguns dels processos físics que s'hi donen actuen també en el marc dels microquàsars. Malgrat que existeixin diferències notables entre ambdós escenaris, alguns dels resultats obtinguts en aquest treball poden ser adaptats al context extragalàctic, afegint així rellevància als objectius de la tesi.

A continuació s'ofereix un resum en català força general dels continguts d'aquesta tesi. Es parteix en el Capítol 1 amb una introducció i motivació de la tesi. El Capítol 2 mostra una descripció global dels microquàsars, necessària per a contextualitzar la modelització dels seus jets i l'emissió a molt altes energies que s'hi pot produir. Els processos físics que s'han utilitzat es troben en el Capítol 3, que també inclou detalls de la formació i evolució dels microquàsars. S'exposa seguidament la investigació duta a terme i els resultats obtinguts. La tesi es divideix en dues parts ben diferenciades. En la primera es mostren els estudis teòrics de les interaccions amb l'estrella companya i el medi interestel·lar, mentre que la segona es centra en les observacions de raigs gamma realitzades amb el telescopi MAGIC (Major Atmospheric Gamma-ray Imaging Cherenkov telescope). La tesi tanca amb una discussió final de la interpretació dels resultats obtinguts. Cal fer notar que aquest resum inicial en català és de caràcter didàctic i no pretén entrar en detall en la física dels processos involucrats. El lector interessat trobarà tota la informació en els capítols posteriors.

0.2 - Visió general dels microquàsars

Es defineixen els microquàsars com aquells sistemes binaris de raigs X que mostren ràdio-jets relativistes. Estan formats per dues estrelles; una d'elles pot estar en la seqüència principal d'evolució o en la fase de les gegants o supergegants. L'altra pot ser una estrella de neutrons o un forat negre, nascuts en el col·lapse que sofreix una estrella quan la fusió nuclear no pot contrarestar el seu pes. Existeix un transport de la massa expulsada per l'estrella companya cap a l'objecte compacte, que cau en el potencial gravitatori d'aquest últim formant un disc d'acreció. A mesura que es precipita, el material es calenta fins a temperatures superiors a 10^6 K, emetent

intensament radiació en el rang dels raigs X. En alguns casos, a més, les parts més internes del disc poden produir emissió de partícules accelerades, és a dir, que encara no han tingut temps de termalitzar.

Una fracció de la massa transferida és expulsada en forma de dolls bipolars anomenats jets. La seva composició és incerta i els processos de llançament, difícils de reproduir en laboratoris terrestres, inclouen mecanismes hidrodinàmics i magnètics que encara no s'entenen completament. Les observacions senyalen cap a un plasma d'àtoms molt ionitzats, electrons i positrons, amb una certa densitat d'energia magnètica guanyada prop de l'objecte compacte. La radiació que emeten els jets es troba distribuïda al llarg de tot l'espectre electromagnètic, des de les ràdio-ones fins a raigs gamma d'alta energia (veure Paredes et al. 2000). Les partícules carregades que poblen els jets interaccionen amb els camps de matèria, radiació i magnètics que van trobant al seu pas. A més a més, són accelerades a mesura que el jet es desenvolupa, arribant a distàncies de fins a 10^{20} cm (≈ 100 anys llum). El medi interestel·lar circumdant actua com a calorímetre, dissipant part de l'enorme energia cinètica que els jets transporten.

El terme microquàsar fou utilitzat per a relacionar la morfologia similar en aquests sistemes amb la que mostraven els distants quàsars (veure Mirabel et al. 1992). Els quàsars són galàxies amb un forat negre super massiu central que xucla la massa del disc de la galàxia amfitriona i emet jets molt energètics (10^{45} erg $s^{-1} \approx 10^{12}$ cops la lluminositat del Sol). Les estructures que resulten de l'impacte d'aquests jets amb el medi intergalàctic poden formar closques que emeten radiació d'origen no tèrmic, indicant la presència de fronts de xoc forts. Moltes d'aquestes propietats són també presents en els microquàsars. L'acceleració de partícules en fronts de xoc, el camp magnètic i radiatiu entorn d'objectes compactes, l'emissió de raigs gamma i la seva posterior absorció actuen en els microquàsars a escales de temps d'algunes hores fins a pocs anys, en comparació amb les escales temporals cosmològiques dels quàsars. Els microquàsars ofereixen per tant una oportunitat única per investigar la física dels processos d'altres energies en sistemes que poden extreure i transformar l'energia proporcionada en forma d'acreció.

La formació de jets s'observa en un cert nombre d'objectes astrofísics a més de quàsars i microquàsars, tant galàctics com extragalàctics. Les explosions de raigs gamma i algunes estrelles massives en formació produeixen jets. Les explosions de raigs gamma són col·lapses gravitatoris que emeten enormes quantitats d'energia en pocs segons. Són fenòmens transitoris difícils d'observar perquè són imprevisibles. Les estrelles massives en formació, per altra banda, mostren jets que s'estenen a banda i banda del protoestel, i alguns d'ells podrien generar emissió d'alta energia

produïda per electrons relativistes (veure, per exemple, Araudo et al. 2007). Les causes precises que condueixen a la formació i evolució dels jets en totes les fonts on apareixen, així com les conseqüències que tenen pel medi interestel·lar/intergalàctic que les envolta, resten encara per comprendre. En el cas dels microquàsars, existeix una relació fenomenològica que connecta el ritme de transferència de massa a través del disc d'acreció amb la formació dels jets. Es defineixen dos estats anomenats “high-soft” i “low-hard” en funció de la distribució espectral d'emissió de raigs X. En l'estat “high-soft” predomina una component tèrmica, provinent d'un disc d'acreció que s'estén fins a regions properes a la superfície de l'objecte compacte. L'emissió de raigs X és per tant tova però intensa. En l'estat “low-hard” l'emissió tèrmica del disc d'acreció es redueix, i una component no tèrmica apareix a energies de l'ordre dels 100 keV. L'origen d'aquesta emissió no ha estat resolt, però podria ser generada en els jets o en una regió extensa que embolcalla les regions més internes del sistema binari anomenada corona. L'emissió en aquest estat és relativament dura però la intensitat integrada és menor que en l'estat “high-soft”.

0.2.1 - Microquàsars com a laboratoris d'altres energies

Els microquàsars són escenaris on es pot produir emissió al llarg de tot l'espectre electromagnètic. La raó d'aquesta àmplia cobertura rau en la natura dels processos no tèrmics que s'hi donen. En primer lloc, la presència de leptons accelerats i camps magnètics intensos genera radiació sincrotró que pot abastar des d'ones ràdio fins a emissió en l'infraroig, i fins i tot estendre's als raigs X. L'origen i evolució dels camps magnètics en els jets dels microquàsars continuen sent una incògnita per resoldre. En aquest treball hem parametritzat la densitat d'energia magnètica com una fracció de la densitat d'energia cinètica fluint en els jets. Quan ambdues densitats d'energia són aproximadament semblants es diu que estan en equipartició. En aquesta situació es pot demostrar (veure Longair 1992) que l'energia total requerida pel sistema (incloent les partícules emissores i el camp magnètic) és la mínima necessària per a explicar l'emissió observada.

A altes i molt altes energies, existeixen un nombre considerable d'escenaris en els quals el jet seria capaç de produir fotons en aquests rangs (per un resum detallat, el lector pot consultar el treball de Bosch-Ramon & Khangulyan 2009). En el procés de Comptonització inversa (IC) d'electrons relativistes contra fotons presents en camps de radiació externs (provinents de l'estrella companya, del disc d'acreció o de la radiació còsmica de fons) o interns (generats en el mateix jet) es pot transferir una part significativa de l'energia cinètica de l'electró vers el fotó, fent que la seva freqüència augmenti en gran mesura. A més a més, si els jets són capaços d'accelerar

protons fins a energies relativistes, els raigs gamma serien una conseqüència natural en les col·lisions d'aquestes partícules amb material present en el jet o expulsat per l'estrella companya.

L'observació de fluxos de raigs gamma produïts en els microquàsars dependrà però de les condicions d'absorció presents en les regions més internes del sistema binari. El camp de fotons d'una estrella companya massiva pot provocar que l'espessor òptic en aquestes regions arribi a valors $\tau \geq 1$, dependent de la fase orbital del sistema. Alternativament, la radiació podria provenir de regions més allunyades, als límits o inclús fora del sistema binari. A més a més, l'emissió a altes energies pot generar-se en les zones on el jet impacta amb el medi circumdant. Els forts xocs que s'hi desenvolupen poden accelerar partícules que emetin raigs gamma a partir de processos IC i Bremsstrahlung relativista.

Finalment, s'han proposat els microquàsars com possibles fonts de raigs còsmics i potser de l'emissió de neutrins. Aquest fet ha propiciat l'interès dels físics especialitzats en astropartícules en aquests sistemes. La presència d'hadrons en els jets ha estat confirmada en almenys un microquàsar, el sistema SS 433. L'enorme potència que mostren els jets, juntament amb les condicions adequades del medi on es troben, podrien explicar l'origen d'una fracció significativa dels raigs còsmics galàctics, la natura dels quals ha estat discutida des de fa més de cent anys.

0.3 - Interaccions dels jets amb el medi circumdant

0.3.1 - Interaccions hadròniques i emissió de secundaris dins el sistema binari

L'emissió de raigs gamma de molt alta energia pot ser provocada per processos hadrònics en els jets dels microquàsars. Aquesta emissió es genera quan una certa fracció dels protons continguts en els jets són accelerats fins a energies relativistes. Les interaccions amb protons provinents del vent de l'estrella companya o amb els mateixos protons no accelerats presents que poblen els jets donen lloc a la producció d'altres partícules, com els pions neutres, π^0 , i carregats, π^\pm . Els pions neutres són inestables i decauen donant lloc a l'emissió de fotons d'energies en el rang gamma. Aquests fotons són fortament absorbits si el medi on es propaguen conté una alta densitat de fotons de més baixa energia, per exemple provinents de l'estrella companya o de la radiació del mateix jet (les interaccions amb material provinent del disc d'acreció o del vent estel·lar de la companya també poden atenuar la intensitat

d'emissió). En aquest procés d'absorció es poden generar parelles electró-positró que al seu torn interaccionen amb els fotons del medi, a través de processos IC, en el qual els fotons prenen part de l'energia de les partícules. Aquest fotons energitzats tornen a ser absorbits interaccionant amb altres fotons de més baixa energia. Es produeix així un fenomen recurrent anomenat cascada electromagnètica. El resultat final dóna lloc a una redistribució de l'energia inicial a energies més baixes, i en major o menor mesura ha de ser present en totes les fonts amb capacitat d'emetre fotons gamma de molt alta energia. La Fig. 1 mostra l'espectre inicial dels fotons gamma per decaïment de π^0 així com l'espectre resultant de les cascades produïdes dins el sistema binari.

Els pions carregats, per altra banda, decauen ràpidament donant lloc a la producció d'electrons i positrons, que venen anomenats “secundaris”, i són per tant una conseqüència natural dins els models d'emissió hadrònics. Una part substancial de l'energia inicial dels protons relativistes pot anar a parar a aquests secundaris. Els secundaris interaccionen amb els camps magnètics i de radiació del medi que els envolta, donant lloc a una emissió que pot estendre's des de longituds d'ona ràdio fins a raigs gamma. Les propietats d'aquesta emissió vindran donades per la distribució inicial de secundaris injectats i per la seva evolució mentre es propaguen al llarg del jet, així com per les diferents condicions del medi a mesura que la distància a l'objecte compacte i la brillant estrella companya creix. La detecció dels rastres d'aquesta emissió pot proveir important informació dels processos físics i les propietats del medi que es donen a les parts internes i en els immediats veïnats dels microquàsars.

El nostre objectiu ha estat modelitzar l'emissió dels leptons secundaris d'una manera autoconsistent (és a dir, determinant-ne la injecció, calculant-ne les pèrdues per radiació i expansió adiabàtica, i estimant-ne l'emissió final) per tal de poder trobar indicis determinants en l'espectre final que apuntessin cap a un origen hadrònic del material que forma els jets.

Amb aquesta motivació hem implementat un model numèric partint d'un escenari simplificat d'un microquàsar compost per un forat negre de 10 masses solars en òrbita circular entorn d'una estrella massiva. El pou de potencial de l'objecte compacte genera la formació del disc d'acreció alimentat per la massa expulsada en el fort vent de l'estrella companya. Una fracció de la massa i energia del disc d'acreció és reconduïda cap a la formació de dos jets orientats en la direcció de l'eix de rotació del disc. Sense entrar en els detalls dels mecanismes que donen lloc a la seva formació, hem suposat per simplicitat dos jets continus (per exemple generats durant els estat “low-hard” dels microquàsars), de geometria cònica i amb veloci-

tats d'ejecció mitjanament relativistes (a $v_{\text{jet}} \sim 0.6c$, sent c la velocitat de la llum). Una part desconeguda de l'energia global del jets és destinada a accelerar protons. Aquesta fracció ha estat mantinguda com un paràmetre lliure dins el nostre model, per poder estudiar-ne després la seva dependència amb les característiques finals de l'emissió calculada.

Les interaccions hadròniques dels protons relativistes continguts en els jets i els ions provinents del vent de l'estrella companya tenen lloc bàsicament en el si del sistema binari. Més enllà, el vent estarà molt diluït, el ritme de les interaccions decaurà ràpidament i la producció de fotons i secundaris serà menyspreable. Per tal d'estudiar aquestes interaccions dins el volum delimitat pel jet, ha de suposar-se un cert factor de penetració del vent estel·lar dins el jet, que prenem també com un paràmetre lliure dins el model. Els camps magnètics en la regió d'interès poden arribar a canalitzar una quantitat significativa de l'energia total del jet. Per a efectuar els càlculs radiatius hem pres una fracció constant de la densitat d'energia magnètica injectada a la base del jet i hem considerat una evolució del camp magnètic al llarg de l'eix de coordenades z orientat en la direcció del jet segons un patró $\propto z^{-1}$ ($z = 0$ correspon a la posició de l'objecte compacte).

Havent establert l'energia cinètica, la densitat de protons fitó i el camp magnètic presents en els jets, s'estableix una distribució espectral dels protons relativistes per a poder procedir amb la modelització del sistema. Aquesta distribució es caracteritza mitjançant una llei de potència en el sistema de referència del jet, en la qual el nombre de partícules per unitat d'energia és $N(E) \propto E^{-p}$, sent p l'índex espectral de la distribució. L'energia màxima de la distribució és d'uns 100 TeV i ve determinada pel giroradi que els protons poden arribar a mantenir sense superar les fronteres delimitades pel radi del jet a cada posició z .

Amb aquestes parametritzacions és possible obtenir estimacions de la producció de radiació gamma primària i partícules secundàries en el jet. Els fluxos totals de fotons de molt alta energia dependran de l'angle d'orientació del jet respecte a l'observador, que pot fer variar la lluminositat apreciablement. Respecte els secundaris, un cop injectats a diferents alçades al llarg del jet sofriran pèrdues energètiques per procés sincrotró dependents del camp magnètic i per IC dependents, a primer ordre d'aproximació, del camp de fotons emès per l'estrella companya. Així mateix, els secundaris perdran energia degut a l'expansió adiabàtica contra el medi, pèrdues que poden arribar a dominar quan els efectes de sincrotró i IC disminueixin en les regions més allunyades del jet. Un tractament autoconsistent ha de tenir present, a més, que noves partícules són injectades al llarg del jet, de manera que la distribució final a cada z ve donada per una superposició de poblacions de diferents edats que se

sumen des de la zona inicial d'injecció fins al punt actual on s'avalua la distribució final dels secundaris.

Tenint presents tots aquests factors i emprant les expressions necessàries per a determinar els processos d'emissió rellevants, hom pot obtenir finalment la distribució espectral d'energia (SED) de la radiació provinent dels leptons secundaris (veure Fig. 2). Les característiques d'aquesta emissió no dependran en aquest cas de l'angle d'observació atès que els electrons i positrons es distribueixen isotròpament en el sistema de referència del jet. Per altra banda, la quantitat d'energia inicialment canalitzada cap a protons relativistes juga un paper rellevant en l'emissió final dels secundaris, ja que en modifica bé el nombre total de partícules que són injectades, bé el valor del camp magnètic a què aquestes són posteriorment sotmeses.

Hem calculat l'emissió produïda per aquests secundaris a través de processos sincrotró i IC (en l'aproximació de Thompson atès que els efectes Klein-Nishina, malgrat existir, es veuen emmascarats per l'emissió gamma hadrònica primària i no afecten les pèrdues). La radiació global d'aquests secundaris ha resultat ser una fracció comparativament important de la produïda pel decaïment directe de pions neutres. L'espectre final en ràdio és relativament dur, i dona lloc a fluxos de l'ordre dels mJy ($1 \text{ Jy} = 10^{-23} \text{ erg s}^{-1} \text{ Hz}^{-1} \text{ cm}^{-2}$) si la font es localitza a una distància d'uns quants kpc. Això representaria aproximadament un 10% dels fluxos trobats en sistemes de característiques similars i en l'estat "low-hard". L'emissió ràdio dels secundaris donaria lloc per altra banda a la morfologia col·limada pròpia d'un jet (provinent dels secundaris generats dins del jet) circumdada per un halo ràdio-emetent (provinent de l'absorció de fotons gamma dins el sistema binari). Per tant, els nostres resultats indiquen que una component leptònica primària és necessària per a explicar els nivells elevats de radiació observada en alguns d'aquests sistemes a baixes energies. Malgrat tot, un procés de reacceleració dels secundaris efectiu a llargues distàncies, podria fer augmentar els nivells d'emissió finals. En aquest cas els processos hadrònics podrien explicar per si sols l'emissió global a aquestes longituds d'ona. En la banda dels raigs X tous, l'emissió per processos sincrotró és als nivells de detecció dels satèl·lits actualment en funcionament. Malgrat tot, l'emissió provinent del disc podria emmascarar la contribució dels secundaris en certa mesura. Per a raigs X durs, en canvi, els nivells d'emissió són inferiors als detectats en fonts amb característiques semblants. En cas que la radiació sigui produïda en l'interior dels jets, una component leptònica primària sembla ser requerida.

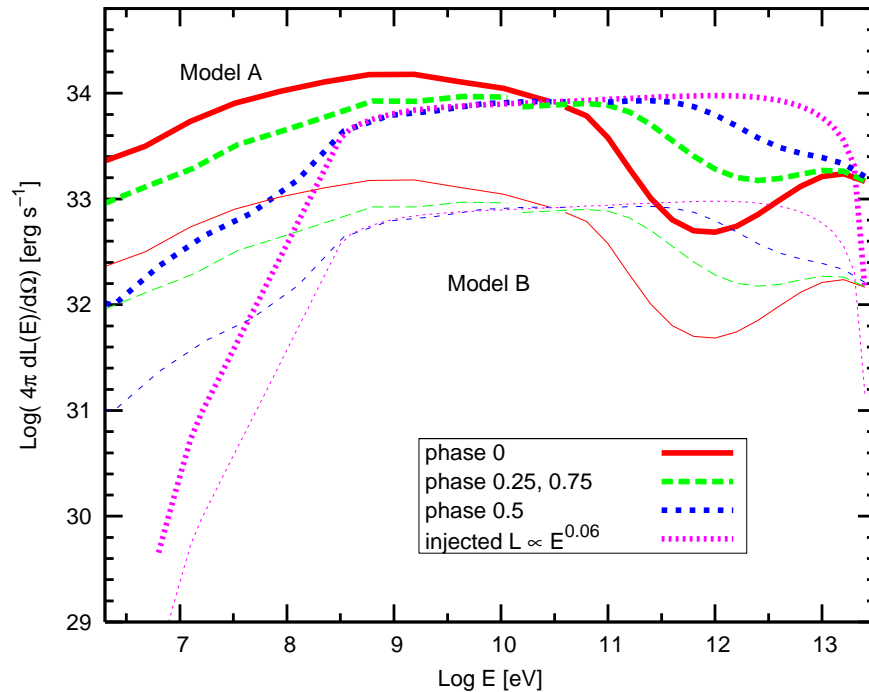


Figura 1: Distribució espectral de l'energia de la cascada electromagnètica produïda a diferents fases orbitals (la fase 0 es defineix com aquella en la qual el forat negre es troba darrera l'estrella companya). La producció de rajos gamma degut al decaïment dels π^0 està indicada per a dos models diferents d'injecció. El Model A correspon a un poder cinètic del jet equivalent a una fracció 0.005 de la lluminositat d'Eddington del sistema, mentre que el Model B correspon a una fracció deu cops més petita, 0.0005. L'espectre inicial dels fotons gamma abans de sofrir les cascades està representat per les línies puntejades de color magenta per ambdós models.

0.3.2 - Interaccions amb el medi interestel·lar

D'una forma similar a com ocorre en els AGNs, quàsars o radiogalàxies, els jets dels microquàsars transporten el moment i l'energia que contenen fins a regions llunyanes, on es diposita en el medi interestel·lar. Aquest procés pot generar xocs forts a les parts finals dels jets, regions on es poden accelerar partícules eficientment i on hom hi espera trobar rastres d'emissió no tèrmica donades certes condicions del medi circumdant. Els ràdio-lòbuls i els "hot spots" formats en aquest procés són trets comuns en l'estudi dels objectes extragalàctics, mentre que en el cas dels microquàsars evidències de les interaccions dels seus jets amb el medi són més aviat escasses (en part degut a què el nombre de fonts conegudes no és tan elevat). Malgrat tot, existeixen casos rellevants on aquestes interaccions han estat efectivament observades, com per exemple en els microquàsars SS 433, Cyg X-1 o Cir X-1, mentre que en altres fonts la presència d'emissió no tèrmica als fronts de xoc ha estat suggerida malgrat el consens no sigui global (per exemple en els microquàsars GRS

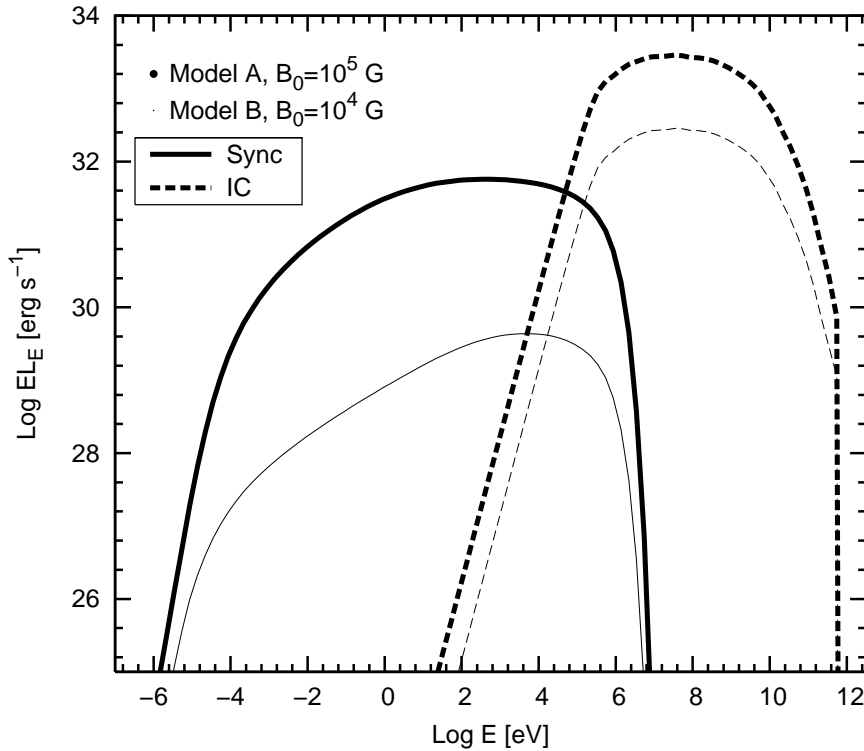


Figura 2: Emissió sincrotró i IC generada pels leptons secundaris dins el jet per als dos valors de la potència total injectada al jet, $6 \times 10^{37} \text{ erg s}^{-1}$ i $6 \times 10^{36} \text{ erg s}^{-1}$, corresponents al Model A i Model B, respectivament. El camp magnètic considerat correspon a una certa fracció del poder cinètic del jet. L'emissió sincrotró es veu modificada tant per la quantitat de partícules relativistes presents en la zona d'emissió com pel valor del camp magnètic, mentre que la contribució IC és independent d'aquest últim factor i la diferència en les lluminositats obtingudes en els dos models és menor.

1915 +105 i Cyg X-3). Per a un resum més extens, el lector pot acudir al treball de Bordas et al. (2009).

La modelització teòrica en aquest camp és força limitada, ja sigui respecte la hidrodinàmica de les interaccions dels jets amb el medi interestel·lar, o pel que respecta a les condicions que donen lloc a la radiació no tèrmica provinent d'aquests xocs (veure, però, Heinz & Sunyaev 2002, Perucho & Bosch-Ramon 2008 i referències en aquests treballs). Una part important de la investigació duta a terme en aquest treball de tesi ha anat precisament dirigit a l'estudi teòric d'aquestes interaccions. Aprofundir en la formació i evolució d'aquests processos ha donat lloc a la caracterització d'aquells casos en els quals es pot esperar emissió detectable a diferents longituds d'ona, així com altres casos on les interaccions són massa febles per poder ser observades. Hem intentat dur a terme un estudi de caràcter general. Els nostres resultats poden ser aplicats a fonts de característiques relativament variades, així com a diferents condicions del medi que les envolten. En concret, el nostre model

pot ser aplicat a microquàsars d'alta i baixa massa, donant lloc a resultats diferents. Aquests dos tipus de fonts solen ser d'edats molt diverses, mostren poders cinètics dels seus jets que poden variar fins a dos o tres ordres de magnitud, i estan situats en regions separades dins la nostra Galàxia. Tot i així, ambdós poden desenvolupar les estructures d'interacció, ja que l'energia dipositada al medi, $E = t_{\text{MQ}} \times L_{\text{cin}}$ (on t_{MQ} és l'edat de la font i L_{cin} és l'energia per unitat de temps fluïnt en els jets), és similar en sistemes relativament dèbils i vells i en sistemes potents i joves.

El nostre objectiu ha estat realitzar un model analític que caracteritzés les tres regions on la interacció del jet amb el seu entorn pot donar lloc a emissió no tèrmica provinent de partícules accelerades en fronts de xoc forts. Hem partit d'un model aplicat a quàsars i radiogalàxies basat en el creixement autosimilar de les estructures d'interacció. Assumint que els jets dels microquàsars neixen prop de l'objecte compacte, el material ejectat comença a desaccelerar-se quan ha acumulat davant seu una quantitat de massa similar a la que està transportant. Dos xocs es formen en els extrems dels jets: un xoc cap endavant, propagant-se en el medi interestel·lar, i un xoc cap enrera, propagant-se en el mateix material que constitueix el jet. El xoc extern acumula massa progressivament, formant així una closca el·líptica amb el material post-xoc del medi. El material del jet, per altra banda, forma un embolcall en travessar el xoc intern, que envolta el jet protegint-lo de possibles perturbacions externes. A més a més, un tercer xoc es forma dins el jet en el punt precís on la pressió d'aquest s'igualava amb la de l'embolcall, produint un efecte de col·limació que transforma la geometria cònica d'expansió inicial del jet a una de radi constant, de geometria cilíndrica. En el nostre escenari, els tres xocs són de caràcter fort. Això implica que les condicions a una banda i altra del jet poden ser molt diferents en quant a temperatura, densitat i pressió. Hem aplicat les equacions de Rankine-Hugoniot per a cada front de xoc, i hem tingut en compte l'evolució temporal de les estructures formades. Per a cada regió, la geometria i les propietats de l'emissor han estat determinades en funció de l'edat de la font. Això inclou el camp magnètic transportat en el jet i present també en les zones d'interacció i el camp de radiació provinent de l'estrella veïna, el més important en el nostre escenari. Per al primer, hem suposat que la densitat d'energia magnètica és una certa fracció de la densitat d'energia transportada en els jets i dipositada al medi, mentre que per al segon s'ha considerat la distància de cada zona respecte a la posició de l'estrella companya.

Per a caracteritzar la distribució energètica de leptons accelerats en cada front de xoc, hem usat una llei de potència del tipus $N_e = K \times E^{-p}$, sent K una constant derivada de la quantitat d'energia cinètica en els jets que és utilitzada per a l'acceleració de les partícules. A més a més, hem derivat les energies màximes de les partícules considerant pèrdues d'energia i per expansió adiabàtica allà on aquesta

és rellevant, confrontant-ho amb els guanys en el context del procés d'acceleració de Fermi de primer ordre. Així mateix, hem tingut en compte l'envelliment energètic de les partícules injectades al llarg de la vida de la font (en els quals, de retruc, les condicions físiques dels acceleradors són diferents). La distribució final resultant obtinguda a un cert instant de temps ha tingut en compte, per tant, la història de la font fins aquell moment. Posteriorment, ha estat calculada per cadascuna de les zones d'interacció la radiació generada per processos sincrotró, Bremsstrahlung relativista i IC per a diferents valors dels paràmetres que defineixen la font i el medi: el poder cinètic del jet, l'edat de la font i la densitat de partícules del medi que l'envolta.

Per altra banda, hem dut a terme simulacions numèriques detallades de l'evolució dels jets en les interaccions amb el medi. Aquestes simulacions, realitzades al centre de computació del Max Planck Institut a Bonn, han usat valors similars als introduïts en el model analític. D'aquesta manera hem tingut la possibilitat de verificar variables físiques com la pressió, la velocitat i la densitat de partícules en les diferents zones estudiades, així com la seva geometria, en funció del temps d'evolució de la font. Les assumpcions establertes en el model analític han resultat ser remarcablement semblants als resultats de les simulacions amb una sola excepció: les simulacions mostren la generació de múltiples xocs de col·limació al llarg del jet mentre aquest es va desenvolupant. El nostre model en considera només un, subestimant així la capacitat d'acceleració que pot tenir lloc en aquesta regió.

Els resultats del nostre treball mostren que l'emissió sincrotró és el canal a través del qual s'obtenen lluminositats més elevades en totes les regions, arribant fins a valors $\sim 10^{33}$ erg s⁻¹ en els casos de fonts més potents, més velles i immerses en medis relativament més densos. A altes i molt altes energies, el mecanisme dominant és el de IC en les zones de col·limació i xoc invers, proporcionant lluminositats de l'ordre dels $\sim 10^{32}$ erg s⁻¹, mentre que el Bremsstrahlung relativista domina en la regió post-xoc del medi. Les Fig. 3 i Fig. 4 mostren les SEDs per alguns dels casos estudiats. Per altra banda, s'han establert diferències notables en la geometria de les zones emissores degut a la seva extensió i a la distància respecte de l'estrella companya. Així mateix, la densitat del medi juga un paper important en aquest sentit, atès que els xocs es produeixen més a prop del sistema binari com més dens és el medi. En quant al poder cinètic dels jets, els resultats radiatius obtinguts en depenen d'una forma quasi lineal, permetent així establir-ne la magnitud un cop establerts els valors de la resta de variables mitjançant mètodes alternatius.

Els fluxos obtinguts a diferents longituds d'ona, assumint una distància font-observador d'uns 3 kpc, han estat comparats amb les facilitats astronòmiques pre-

sents que operen a diferents rangs energètics. En ràdio, densitats de flux entorn els 100 mJy a 5 GHz podrien ser fàcilment detectats per instruments amb resolucions angulars de 1 mJy beam^{-1} , considerant una extensió de la font al cel d'uns quants minuts d'arc. En raigs X, els emissors presenten grandàries molt més reduïdes atès que existeixen importants pèrdues energètiques de les partícules. Malgrat tot, els fluxos podrien ser observables des de satèl·lits com *XMM-Newton* i *Chandra* a escales d'uns pocs segons d'arc. Respecte de l'emissió de radiació gamma, els fluxos resultants són inferiors a les capacitats dels actuals telescopis Cherenkov treballant a aquestes energies. Malgrat tot, és important subratllar que els nivells d'emissió depenen fortament dels paràmetres usats en el model analític, en concret de la fracció d'energia destinada a l'acceleració leptònica i el poder cinètic del jet. En el cas que la font presenti valors més elevats d'aquestes variables, l'emissió podria arribar a ser mesurable.

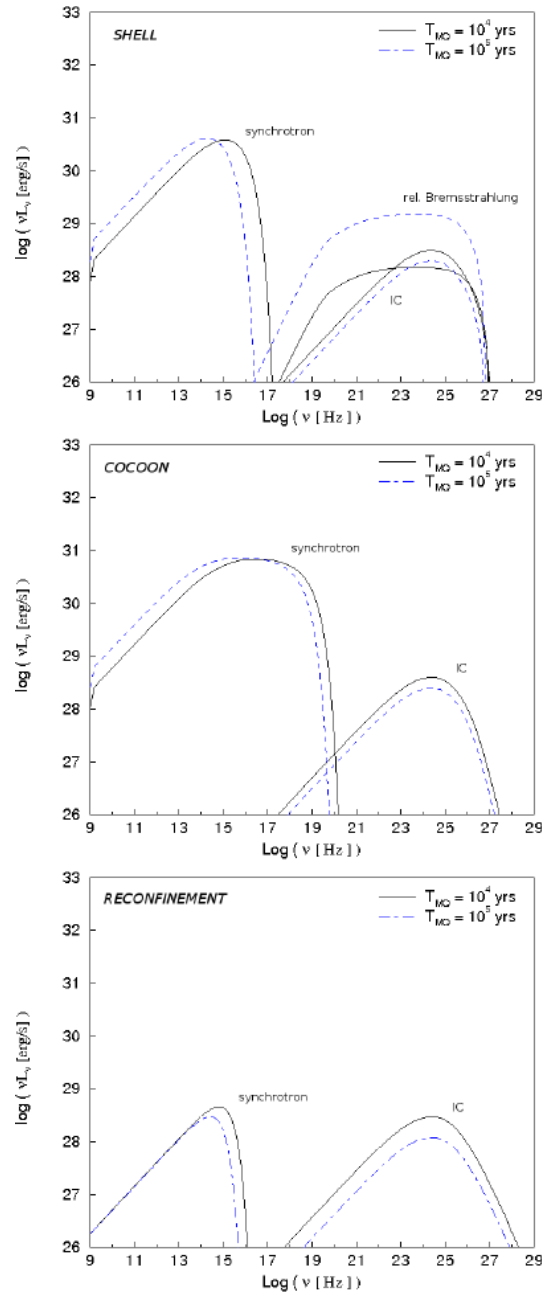


Figura 3: Distributions espectrals d'energia provinents de les diferents zones d'interacció considerades. Els valors dels paràmetres que defineixen el poder cinètic del jet ($L_{\text{cin}} = 10^{36} \text{ erg s}^{-1}$) i la densitat del medi ($n_{\text{ISM}} = 0.1 \text{ cm}^{-3}$) són aquells que produeixen una emissió global més dèbil en els casos estudiats. Dues edats diferents per a la font venen representades, així com les contribucions dels diferents processos radiatius rellevants en cada regió.

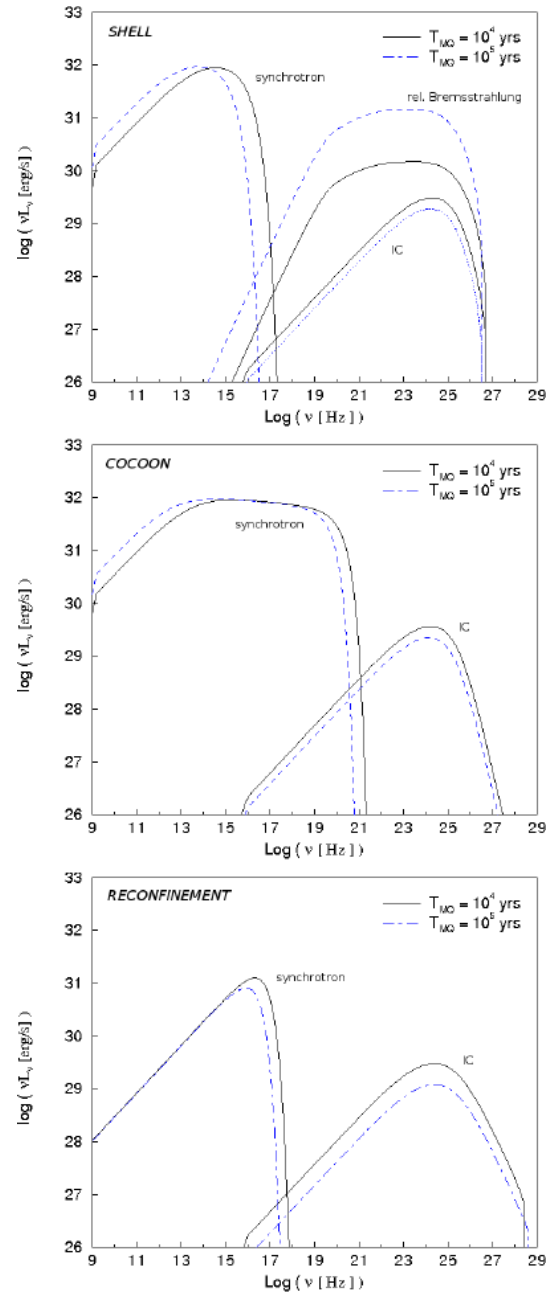


Figura 4: Mateixa SED que la mostrada en la Fig. 3 però per als valors dels paràmetres tractats que fan les fonts més il·luminoses, $L_{\text{cin}} = 10^{37} \text{ erg s}^{-1}$ i $n_{\text{ISM}} = 1 \text{ cm}^{-3}$.

0.4 - El telescopi MAGIC i el procés d'anàlisi de dades

El telescopi MAGIC és un telescopi que ha estat dissenyat per a l'observació de raigs gamma de molt alta energia, en el rang 50 GeV–10 TeV, mitjançant la tècnica d'obtenció d'Imatges Atmosfèriques Cherenkov (IACT). MAGIC està situat a l'Observatori Astrofísic El Roque de los Muchachos a La Palma, a les illes Canàries (28 deg, 45'N; 17 deg, 54' W) a 2200 metres sobre el nivell del mar. La ubicació fou escollida per les seves bones condicions atmosfèriques presents durant la major part de l'any. El projecte compta amb més de 20 institucions provinents de 8 països arreu d'Europa i els Estats Units. En conjunt, hi treballen uns 150 científics i uns 100 tècnics. MAGIC fou concebut a principis dels anys 90, la seva construcció començà l'any 2001 i la inauguració oficial es va fer a l'octubre de l'any 2003. Un segon telescopi MAGIC ha estat construït a 85 metres del primer. La seva inauguració, prevista pel 19 de setembre de 2008, ha estat finalment celebrada durant el mes d'abril de 2009. Durant l'escriptura d'aquesta tesi el segon telescopi es troba en fase de proves abans no comenci les operacions normalment.

Les principals característiques que fan de MAGIC un instrument únic dins els IACTs operatius actualment són un reflector de 17 metres de diàmetre, una estructura lleugera construïda amb fibra de carboni, un sistema de control actiu dels miralls del reflector, una càmera constituïda per 577 fotomultiplicadors ultrasensibles amb un camp de visió d'uns 3.5 deg, un sistema de trigger completament reprogramable i un transport òptico-analògic del senyal rebut a la càmera fins a la seva digitalització, que es realitza a través d'un sistema capaç d'enregistrar les dades a una freqüència superior als 2 GHz. L'objectiu fou el d'obtenir un telescopi que oferís la oportunitat de rebaixar l'energia lliardar d'observació fins als 30 GeV, i que fos capaç així mateix d'apuntar a fenòmens transitoris celests en el menor temps possible.

MAGIC es serveix de la tècnica Cherenkov per a realitzar les observacions de fonts de molt alta energia. Aquesta tècnica permet la detecció indirecta de raigs gamma un cop entren dins l'atmosfera terrestre. La física present en la generació de pluges atmosfèriques extenses (EAS) és complexa. A continuació en donarem una descripció global sense entrar en profunditat en els processos que les caracteritzen. El lector pot acudir als treballs de Longair (1992) i Gaisser (1990) per a un tractament més detallat.

0.4.1 - La radiació Cherenkov

Les EAS desenvolupen cascades de partícules carregades i radiació electromagnètica produïda per la interacció d'un raig còsmic o un fotó gamma d'alta energia amb els ions i molècules presents en l'atmosfera. En aquestes interaccions es generen partícules/fotons secundaris que al seu torn interaccionen amb altres ions i molècules atmosfèrics. Aquest procés iteratiu distribueix l'energia de la partícula primària incident entre els subproductes generats a cada pas. La cascada s'atura quan l'energia d'una determinada partícula secundària és inferior a un cert valor llindar, sota el qual la producció de noves partícules ja no és possible. La major part del flux de raigs còsmics que arriben a la terra i que són capaços d'iniciar EAS està constituïda per partícules carregades, ions i electrons. Una petita porció és en canvi en forma de raigs gamma i neutrins, que són neutres per definició, i per tant no es veuen sotmesos a l'acció deflectant dels camps magnètics presents en el medi interestel·lar/intergalàctic. La distribució dels raigs còsmics incidents en la nostra atmosfera és per tant majoritàriament isòtropa amb l'excepció del flux de raigs gamma i neutrins, que apunten directament cap a les fonts que els generen.

Quan una partícula carregada viatja a través d'un medi a una velocitat $v = \beta \cdot c$ superior a la de la llum en aquell medi (és a dir, $v > c/n$, on n és l'índex de refracció del medi) emet llum Cherenkov. La radiació Cherenkov és el resultat de la reorientació dels dipols elèctrics induïts per la partícula carregada en el seu pas a través de les molècules constituents del medi. Quan la velocitat és petita, les càrregues entorn la posició de la partícula incident es distribueixen simètricament i es cancel·len, i no es produeix radiació. Si la velocitat és prou alta, en canvi, una polarització neta es manté breument en el medi al llarg de la trajectòria de la partícula incident i es generen curts impulsos de llum que es propaguen esfèricament. Com que la partícula viatja més ràpid que els fronts de l'ona electromagnètica, es crea una "ona de xoc" darrera seu a mesura que travessa el medi degut a processos d'interferència constructiva de la llum. El front de xoc es propaga en un cert angle respecte de la direcció de la partícula, que depèn només de β i n , i forma així un con de llum que és projectat vers la superfície terrestre. La radiació Cherenkov global d'una EAS consisteix en l'acumulació de llum emesa per les partícules generades en la pluja mentre aquesta es propaga dins l'atmosfera. La superposició de l'emissió a cada alçada genera una cercle de llum quasi homogènia (la variació de n amb l'alçada produeix un lleuger augment entorn al seu perímetre) que és possible d'observar amb instruments prou sensibles.

La radiació Cherenkov provinent de EAS generades per electrons/positrons i fotons és diferent de la induïda per protons o ions. En el primer cas, les interaccions

produeixen únicament parelles d'electrons-positrons i fotons, i venen anomenades pluges electromagnètiques. En les pluges hadròniques, en canvi, les interaccions donen inicialment pions neutres i carregats i kaons. Els pions neutres decauen ràpidament a fotons, que inicien al seu torn sub-pluges electromagnètiques, mentre que els pions carregats i els kaons decauen a muons molt energètics que en la seva majoria arriben a terra sense pèrdues apreciables (una petita part decau també a electrons/positrons i neutrins). El resultat final és que les cascades iniciades per electrons/positrons i fotons són més col·limades que les iniciades per hadrons, i es comencen a produir en punts més elevats de l'atmosfera degut a què les interaccions involucrades tenen longituds típiques més curtes.

0.4.2 - La detecció indirecta de raigs gamma de molt alta energia

Els IACTs constitueixen els instruments terrestres més eficaços avui dia per a detectar raigs gamma. De manera semblant als telescopis que operen a altres longituds d'ona, estan constituïts a grans trets de tres elements bàsics: un sistema motor que permet seguir una font al cel, una superfície col·lectora que focalitza la radiació vers una càmera i un sistema receptor que converteix la llum rebuda en una imatge enregistrable del camp de visió observat. En el cas dels IACTs, l'objectiu és detectar raigs gamma mitjançant l'observació de l'emissió Cherenkov indirecta produïda en les EAS. La imatge formada a la càmera, constituïda per fotomultiplicadors ultrasensibles, és una projecció geomètrica de les EAS. La informació continguda en aquestes pluges ha de ser correctament processada per a poder obtenir, en última instància, l'energia i la direcció de la partícula que les ha generat. La quantitat total de llum continguda en una imatge és el principal indicador de l'energia incident de la partícula. La orientació i extensió de la imatge a la càmera són indicadors de la natura (hadrònica o electromagnètica) i de la direcció de la partícula original.

El procés d'obtenció de dades comença en els fotomultiplicadors, amb una conversió de la pluja Cherenkov captada a fotoelectrons. El senyal generat a la càmera es transmet fins al centre d'enregistrament mitjançant tubs de fibra òptica. Els receptors recuperen el senyal i apliquen un primer filtre selectiu que té present l'amplitud de cada esdeveniment, el seu desenvolupament temporal i la distribució que la pluja ha presentat en un cert nombre (modulable segons es requereixi) de píxels a la càmera. Simultàniament al processament del senyal de les EAS, s'obtenen calibracions de la resposta dels fotomultiplicadors per a cada esdeveniment mitjançant una font artificial de llum làser situada al centre del mirall reflector del telescopi, i que són enregistrats constantment durant la presa de dades. Així mateix, són

enregistrats també esdeveniments que contenen informació del soroll provinent de l'electrònica del telescopi. Els esdeveniments que han passat la selecció així com els esdeveniments de calibratge i les mesures del soroll són finalment enregistrats en discs durs localitzats a la sala d'electrònica, i solen arribar a significar uns 150 GB de dades per nit d'observació. Les dades són posteriorment enviades al Centre de Processament de la Informació (PIC), on es posen a disposició per a poder ser analitzades.

0.4.3 - El procés d'anàlisi

El major repte dels telescopis IACTs és la discriminació entre el senyal de raigs gamma provinent de la font estudiada i el soroll de fons produït bé per les pluges iniciades per hadrons, bé per la llum residual que el cel pot mostrar degut a la presència de la lluna, estrelles en el camp de visió, reflex de la llum solar en la pols interplanetària, llum zodiacal, i inclús la pol·lució lumínica generada en ciutats properes al lloc d'observació. Hem de tenir present que per cada fotó de molt alta energia provinent d'una font lluent com la Nebulosa del Cranc, hom obté de l'ordre de 10^4 esdeveniments corresponents a soroll de fons. Per tal d'efectuar aquesta discriminació i extreure tota la informació de les imatges obtingudes, s'utilitza el Software d'Anàlisi i Reconstrucció de MAGIC (MARS). Aquest paquet programat en C++ fa ús del sistema ROOT, un entorn de programació àmpliament utilitzat en experiments de física de partícules i desenvolupat al CERN.

El procés d'anàlisi comença accedint al PIC on poden obtindre's els tres tipus de dades enregistrades: les dades de la font observada, les calibracions i aquelles corresponents al soroll intrínsec del telescopi. El primer pas en la reducció és una selecció de les seqüències a analitzar en funció del ritme d'esdeveniments per unitat de temps que presenten i els informes aportats per estacions meteorològiques especialitzades indicant quines condicions atmosfèriques eren presents a La Palma durant les observacions. A més, es tenen presents els informes que nit a nit els observadors elaboren i on s'hi detallen les possibles incidències tècniques que poguessin haver ocorregut durant la presa de dades. Posteriorment es realitza una neteja de la imatge en la qual es determinen quins píxels han de ser considerats a l'hora d'estudiar el senyal i quins, en canvi, mostren només fluctuacions degudes al soroll de fons del cel.

En aquest punt es procedeix a la parametrització de les EAS, mitjançant els anomenats Hillas Parameters (Hillas 1985) basats en el primer, segon i tercer moments de la distribució bidimensional de l'el·lipse formada pel senyal de cada imatge

estudiada. Els moments es calculen respecte un sistema de referència amb l'origen en el centre de gravetat de la imatge, l'eix X segons l'eix major de la el·lipse i l'eix Y en la direcció de l'eix menor. El conjunt de paràmetres de Hillas estudiats es poden classificar en dos grans grups: aquells que descriuen la forma de la pluja i que són per tant independents de qualsevol punt de referència a la càmera, i aquells que en canvi depenen d'algun punt a la càmera (que representa, per exemple, la posició esperada de la font).

Dins el primer grup, els paràmetres més importants són: SIZE, el nombre total de fotoelectrons continguts en la imatge; LENGTH i WIDTH, corresponents a la meitat de la longitud total de l'eix major i menor de l'el·lipse i que dóna idea del desenvolupament longitudinal i transversal de la pluja, respectivament; CONC, la fracció de fotoelectrons continguts en els dos píxels més il·luminats i que dóna informació de la posició del centre de la pluja; M3LONG, el tercer moment de la imatge al llarg de l'eix longitudinal de la pluja, que dóna una idea de la posició del “cap” i la “cua” del desenvolupament de la el·lipse, i LEAKAGE, la fracció del senyal total continguda en els píxels situats en la perifèria de la càmera, que indica si la imatge de la pluja ha quedat escapçada. Finalment, el paràmetre THETA representa el radi angular dins el qual es considera que el senyal ha estat generat, i és utilitzat en els casos en què la font és relativament estesa o la seva posició no és coneguda amb precisió.

Dins el segon grup de paràmetres, ALPHA determina l'angle entre l'eix major de la imatge i el vector que uneix el centre de gravetat de la imatge i la posició estimada de la font a la càmera; DIST representa la distància entre el centre de gravetat de la imatge i un cert punt de referència a la càmera, normalment el centre, i que dóna informació respecte al paràmetre d'impacte de la pluja observada. Finalment, el paràmetre TIME RMS té en compte l'evolució temporal de la imatge de la pluja a la càmera. Atès que TIME RMS calcula el gradient temporal del desenvolupament de la pluja respecte les dues direccions en què aquesta es pot estendre, depèn de la posició assumida de la font a la càmera.

L'estudi d'aquests paràmetres és utilitzat per a diferenciar entre les pluges electromagnètiques i aquelles generades per hadrons o per soroll de fons. En concret, per a la separació d'esdeveniments tipus gamma d'aquells tipus hadrònic, hom es basa en la forma i posició de les pluges observades. Per aquest propòsit, és necessari disposar d'un conjunt de referència d'esdeveniments tipus gamma “purs” per a poder comparar amb les imatges obtingudes. Els IACTs treballen amb simulacions numèriques Monte Carlo que intenten reproduir el senyal que s'obtidria d'una font d'una certa intensitat i distribució espectral. Aquestes simulacions han de tenir presents tots

els passos fins a què la imatge és registrada, i això inclou el desenvolupament de la pluja en l'atmosfera, les característiques del telescopi en el moment d'observació, i la pròpia cadena d'enregistrament de les dades. Les simulacions d'esdeveniments gamma “purs” juntament amb una mostra de dades purament hadròniques són utilitzades per optimitzar els criteris de selecció en un mètode de classificació anomenat Random Forest, que posteriorment s'apliquen al conjunt global de les dades a analitzar. Els criteris utilitzats per a la discriminació de les dades estan basats en els resultats que mostren quan són aplicats a una font intensa i ben coneguda, que actua com a “candela estàndard”, i que és usualment la Nebulosa del Cranc.

Per a cada esdeveniment, s'aïlla finalment un paràmetre anomenat HADRONNESS, el valor del qual està comprès en el rang $[0,1]$ i que mesura la probabilitat que un determinat esdeveniment sigui d'origen hadrònic. Per $\text{HADRONNESS} = 0$, l'esdeveniment és purament electromagnètic, mentre que $\text{HADRONNESS}=1$ equivaldria a un esdeveniment hadrònic pur. Aquest darrer paràmetre, juntament amb ALPHA, són els discriminadors més potents durant l'anàlisi. El primer basa el seu poder diferenciador en la morfologia de la pluja, mentre que el tall exclusiu dels esdeveniments que mostren un ALPHA baix (per sota de 8 graus, per exemple) elimina totes les pluges que es generen amb direcció aleatòria degut a la isotropia de la distribució de raigs còsmics arribant a la terra.

La reconstrucció de l'energia del fotó gamma i la seva direcció són obtingudes mitjançant els paràmetres de cada pluja. La avaluació de la rellevància estadística d'un resultat final positiu en l'observació d'una font de raigs gamma és finalment estudiada. Ha d'especificar-se un cert interval de confiança que doni la probabilitat que els resultats obtinguts no siguin merament una fluctuació espúria del soroll de fons. Els descobriments d'una font són usualment acceptats quan el senyal obtingut presenta una probabilitat per sobre d'un cert valor llindar, usualment 5 desviacions estadístiques, equivalents a un interval de confiança del 99.993% que el fenomen correspongui efectivament a una font de raigs gamma.

All llarg d'aquest complex procés d'anàlisi de les dades els mètodes i criteris utilitzats no estan exempts d'una certa subjectivitat de l'analista. És per aquesta raó que la col·laboració MAGIC exigeix un contra-anàlisi per a cada resultat positiu (ó límit superior en el cas de no haver obtingut cap senyal de la font observada) que sigui completament independent, i que estigui en acord amb els resultats obtinguts en el primer anàlisi.

0.5 - Observacions de microquàsars amb el telescopi MAGIC

La incorporació del grup d'Altes Energies del departament d'Astronomia i Meteorologia a la col·laboració MAGIC va venir estretament lligada a l'inici d'observacions dels microquàsars amb aquest telescopi. En el període comprès entre els anys 2005–2008 han estat observats els sistemes LSI +61 303, Cyg X-1, Cyg X-3, GRS 1915 i SS 433. El treball que hem dut a terme en el marc del Grup d'Astrofísica Galàctica dins la col·laboració MAGIC s'ha basat en la modelització multilongitud d'ona i la predicció de la seva emissió a molt altes energies. A més, hem contribuït en la preparació de les campanyes d'observació, les estances al Roque de los Muchachos en alguns casos i la interpretació científica dels resultats obtinguts de l'anàlisi de les dades.

LSI +61 303 és una binaria de raigs X composta per una estrella del tipus Be i un objecte compacte de natura encara desconeguda, amb un període orbital de ~ 26.5 dies, que mostra emissió periòdica a través de tot l'espectre electromagnètic, des de ràdio fins a raigs X i gamma. El telescopi MAGIC l'ha observat al llarg dels cicles I, II, i III durant un total de 166 hores en diferents punts de la seva òrbita. S'ha detectat emissió puntual a fases orbitals al voltant de 0.65 (Albert et al. 2006) i en la fase 0.8-0.9. A través de campanyes multilongitud d'ona s'ha establert una possible correlació entre l'emissió de raigs X i raigs gamma i una anticorrelació entre emissió ràdio i gamma.

Els microquàsars Cyg X-3 i GRS 1915+105 varen ser observats per la primera generació de telescopis Cherenkov a finals dels anys 80. Es varen publicar evidències de la seva emissió de raigs gamma, però la significança del senyal no va superar en cap cas les 4 desviacions estadístiques (veure Bonnet-Bidaud & Chardin 1988). El desenvolupament de les tècniques de detecció que han donat lloc a la instrumentació actual han estat en part motivades per a poder esbrinar si aquestes dues fonts són capaces d'emetre radiació de molt alta energia. MAGIC ha observat ambdues fonts durant els cicles II, III i IV, per un total de més de 45 h cadascuna. L'anàlisi del conjunt complet d'observacions i el realitzat nit a nit per tal de trobar variabilitat en la seva emissió no han donat cap indicatiu de senyal. Els resultats han estat publicats recentment (Saito et al. 2009), i un treball focalitzat en les conseqüències que es poden extreure dels límits superiors de l'emissió d'ambdós microquàsars és en preparació.

Les observacions de les fonts Cyg X-1 i SS 433 en els cicles III i IV han estat

analitzades i es mostren en el capítol 8 al final de la tesi. A continuació s'ofereix un resum d'aquest anàlisi així com de la interpretació física resultant. Els models presentats anteriorment en aquest resum, i en detall en els capítols 4 i 5, han estat aplicats en la mesura que les condicions dels sistemes ho han permès.

0.4.5 - Observacions de Cyg X-1

Cyg X-1 és un microquàsar d'alta massa constituït per un forat negre d'unes 21 masses solars orbitant cada 5.6 dies un estrella supergegant del tipus O9.7 de 40 masses solars. MAGIC ha observat aquesta font durant els cicles II, III i IV. Només en el primer d'ells s'ha detectat un índex d'emissió a molt altes energies durant una de les 26 nits, corresponent al 24 de Setembre de 2006. Aquesta detecció ha coincidit amb un màxim històric de l'emissió X provinent d'aquesta font observat amb el satèl·lit RXTE, així com amb un augment de l'emissió de raigs gamma tous observats amb INTEGRAL durant les mateixes dates. A més, Cyg X-1 es trobava en el màxim de la seva modulació supra-orbital de ~ 326 dies observada en raigs X.

Una característica que destaca de manera notable en l'adequació dels models teòrics existents en el moment en què es va donar la detecció és el fet que el sistema es trobava en la fase 0.91, en el qual l'objecte compacte es troba pràcticament darrere de l'estrella companya. Això implica que l'absorció dels fotons de molt alta energia és la màxima possible, donant pes a una localització de l'emissor a distàncies majors o iguals a l'escala del sistema binari (altrament la intensitat del camp radiatiu de la companya atenuaria l'emissió en un factor $\sim 10^3$).

L'espectre de la radiació a molt altes energies observat amb MAGIC s'ajusta a una llei de potència amb índex espectral de -3.2, i el flux correspon a un 30% del que presenta la Nebulosa del Cranc. Malgrat tot, la significança de la detecció és de 4.1 desviacions estadístiques, que no és suficient per a poder descartar (al nivell habitual en el context dels experiments IACTs) la possibilitat que fos produïda per una fluctuació del soroll de fons. Noves observacions s'han dut a terme en els cicles III i IV per tal de confirmar l'emissió a molt altes energies de Cyg X-1. S'ha fet ús d'una estratègia basada en el coneixement de l'estat de la font en raigs X mitjançant el monitoreig permanent dut a terme amb els instruments RXTE i Swift, assegurant que la font es trobés en l'estat "low-hard" en què els jets són permanents.

Durant el cicle III l'estratègia utilitzada ha donat lloc a tres nits d'observació durant el mes de Juliol de 2007 i quatre més durant Octubre i Novembre del mateix any, acumulant-se així un total de 14.5 hores de dades. L'anàlisi ha estat efectuat a partir dels fitxers ja calibrats i emmagatzemats al PIC. S'han seleccionat les

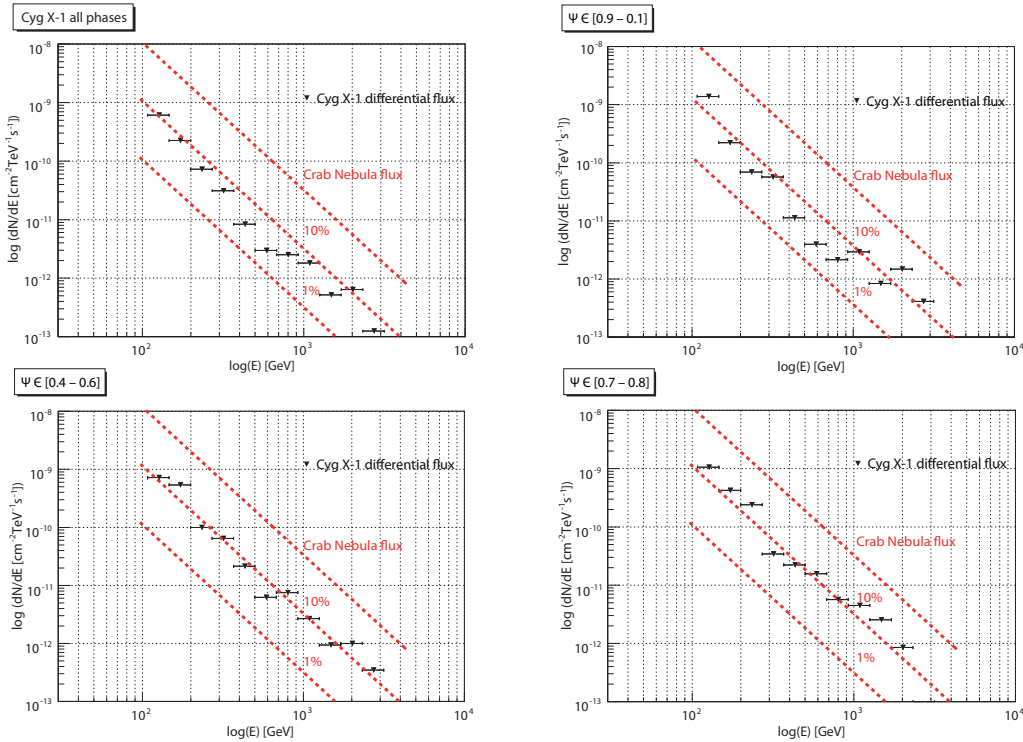


Figura 5: Límits superiors diferencials del flux de raigs gamma del microquasar Cyg X-1 corresponents a les observacions del cicle III durant l'any 2007. Es mostren els resultats per al conjunt complet de dades així com tres rangs en la fase orbital del sistema separatament, $[0.9 - 0.1]$, $[0.4 - 0.6]$ i $[0.7 - 0.8]$. Les línies puntejades vermelles mostren el flux de la Nebulosa del Cranc i les seves fraccions d'un 1% i un 10%.

seqüències que no presentaven problemes tècnics durant l'adquisició i obtingudes en bones condicions atmosfèriques (evitant, en concret, aquelles dades afectades per la presència de pols provinent del Sàhara que fan disminuir notablement el nivell del senyal obtingut). S'ha fet ús de simulacions Monte Carlo de raigs gamma. Així mateix, s'han emprat dades de la Nebulosa del Cranc per a l'optimització de l'anàlisi, corresponents a les observacions efectuades durant l'octubre de 2007. Tant les observacions de Cyg X-1 com les de la Nebulosa del Cranc foren preses en l'anomenat "mode wobble", en què les fonts se situen 0.4° allunyades del centre de la càmera. D'aquesta manera s'obté simultàniament (en la regió simètrica respecte de la posició de la font) dades del soroll de fons que després s'haurà de sostraure durant el procés d'anàlisi. Els paràmetres més rellevants trobats durant aquest anàlisi (és a dir, els filtres en algunes de les propietats dels esdeveniments que optimitzen la sensibilitat de les observacions de la Nebulosa del Cranc) han estat $\text{SIZE} \leq 200$ phe, $\text{HADRONNESS} \leq 0.07$ i $\text{ALPHA} \leq 8^\circ$.

Els resultats de l'anàlisi no ha proveït cap senyal d'intensitat superior a les fluctuacions del soroll de fons. S'han analitzat les observacions a diferents rangs

energètics, i s’han separat les dades tant per cadascuna de les nits d’observació com agrupades en diferents rangs de fases orbitals del sistema. S’ha volgut identificar d’aquesta manera possibles rastres de variabilitat. Aquests anàlisis no han trobat tampoc indicis d’emissió. S’ha procedit a calcular els límits superiors al flux de raigs gamma de Cyg X-1. Els quatre panells de la Fig. 5 mostren els límits superiors diferencials de l’emissió de la font per a diferents fases orbitals. El flux provinent de la Nebulosa del Cranc observat pel telescopi MAGIC durant l’any 2007 (Albert et al. 2007) també es mostra per comparació. La integració de la intensitat emesa entre els 300 GeV i els 5 TeV ha donat lloc a un límit superior d’uns 10^{-12} fotons $\text{cm}^{-2} \text{s}^{-1}$, que corresponen a un $\sim 2\%$ del flux de la Nebulosa del Cranc a un interval de confiança del 95%.

Hem explorat la producció de raigs gamma en el microquasar Cyg X-1 mitjançant el model hadrònic presentat en el capítol 4, atès que els valors dels paràmetres emprats allí són similars als que defineixen aquesta font. Els nivells d’emissió han estat estimats a diferents fases orbitals. Això permet fer una comparació directa amb els resultats de l’anàlisi de les observacions. Els resultats més restrictius venen donats pels límits superiors durant la fase orbital [0.4 - 0.6], ja que l’atenuació del senyal degut al camp de fotons de l’estrella companya és mínim en aquest rang. En particular, una lluminositat $L_\gamma \lesssim 1.7 \times 10^{33} \text{ erg s}^{-1}$ a $E = 0.6 \text{ TeV}$ constreny la potència injectada en el jet en forma de protons relativistes, $L_p \lesssim 5.48 \times 10^{35} \text{ erg s}^{-1}$. Això implica que menys d’una una fracció $q_{rel} = 4.56 \times 10^{-4}$ vegades la lluminositat d’Eddington del sistema va a parar a aquestes partícules, ja que un valor superior violaria els límits obtinguts amb MAGIC.

Hem utilitzat el valor de q_{rel} derivat per a estimar així mateix la radiació no tèrmica produïda pels leptons secundaris. Cyg X-1 mostra uns fluxos a radio-freqüències d’uns 12–15 mJy (Fender et al. 2000) durant l’estat “low-hard”. Els fluxos obtinguts amb el nostre model mostren són propers a $1.2 \times 10^{-3} \text{ erg cm}^2 \text{ s}^{-1} \text{ Hz}^{-1} = 1.2 \text{ mJy}$, i per tant a un nivell clarament inferior. És necessari concloure, per tant, que una component leptònica primària ha de ser considerada. Alternativament, una possible reacceleració de les partícules al llarg del jet podria arribar a ajustar el flux ràdio típic observat a Cyg X-1 en l’estat “low-hard”. Aquesta possibilitat no ha estat explorada en el model, malgrat tot, i roman com a material per a un treball d’investigació futur.

En el rang dels raigs X durs, la font mostra una lluminositat d’uns $5 \times 10^{36} \text{ erg s}^{-1}$ en el rang (10–150) keV (Malzac et al. 2008). Malgrat que encara no se sap si l’origen d’aquesta emissió és tèrmic o no tèrmic. L’emissió en aquest rang d’energies obtingut en l’aplicació del model a Cyg X-1 és $\sim 10^{32} \text{ erg s}^{-1}$. Aquest valor no pot

explicar els nivells observats, i per tant una component leptònica primària, tèrmica o no tèrmica, sembla ser requerida.

Finalment, l'expansió de les estructures formades en la interacció dels jets de Cyg X-1 i el medi que l'envolta es troba en un règim radiatiu. Això significa que una fracció important de l'energia cinètica del sistema va a parar a radiació (d'origen tèrmic). En aquest escenari, el model d'interaccions presentat en el capítol 5 proveiria tan sols una estima rude de la geometria i les propietats físiques de les regions d'interacció. A més a més, la eficiència per accelerar partícules en els fronts de xoc en el règim radiatiu són reduïdes. L'emissió ràdio no tèrmica resultant seria àmpliament suprimida o sota els nivells actualment detectables, tal i com reflecteix el fet que no hagi estat detectada fins ara. També l'emissió a més altes energies es veuria afectada. En particular els fluxos esperats en el rang gamma estarien molt per sota de les possibilitats tècniques dels IACTs com MAGIC.

0.4.5 - Observacions de SS 433/W50

SS 433 va ser el primer objecte compacte estel·lar en el qual es varen descobrir jets relativistes (Spencer 1979). Des que fou identificat fa més de 30 anys, nombrosos estudis han estat centrats en aquest sistema degut les seves propietats úniques. Es troba a una distància d'uns 5.5 kpc, i està compost per un forat negre de 9 masses solars orbitant entorn d'una supergegant de tipus espectral A3-7 en una òrbita quasi circular de radi $\sim 5 \times 10^{12}$ cm i període ~ 13 dies. Els jets d'aquest sistema són els únics en els quals s'ha pogut determinar directament la presència d'ions. Núvols de plasma amb contingut bariònic s'han observat a distàncies de fins 10^{17} cm, sense mostres apreciables de desacceleració. A més a més, el ritme d'acreció de matèria de l'estrella companya vers el forat negre és excepcionalment alt. Aquesta alta eficiència d'acreció podria ser responsable del fet que l'energia cinètica dels jets sigui tan elevada com 10^{39} erg s^{-1} .

SS 433 es troba immers en el romanent d'una explosió de supernova. La nebulosa formada en aquesta explosió, W50, mostra una forma estesa en les direccions en les quals es desenvolupa el jet. L'acció progressiva de la potència del jet sobre el dens medi circumdant ha produït diferents zones d'interacció, que mostren a més evidències de radiació no tèrmica. S'ha deduït la presència d'electrons que són accelerats en els fronts de xoc i emeten fortament en el rang X. Aquesta emissió implica la possibilitat de trobar també radiació de raigs gamma generats per les mateixes partícules a través d'IC i emissió Bremsstrahlung relativista, sempre que es trobin amb un camp de fotons o partícules fitó prou densos, respectivament.

El sistema de telescopis de raigs gamma HEGRA va observar SS 433 en diverses campanyes que inclouen un sondeig de l'emissió del pla galàctic, observacions en “mode wobble” i apuntats centrats en la font. Un total de 100 hores varen ser obtingudes per al sistema central i les zones d'interacció situades a l'est del sistema binari (Aharonian et al. 2005). Cap indicatiu de senyal fou obtingut, i límits superiors al flux integral per energies superiors a $E = 800$ GeV varen ser establerts al nivell d'un $\sim 3\%$ del flux produït per la Nebulosa del Cranc. Per altra banda, els telescopis Cherenkov CANGAROO II també van apuntar cap a SS 433/W50 durant els anys 2002–2003 per un temps total d'observació d'unes 85 hores. Desafortunadament, no se n'ha resolt cap detecció significativa, i no han estat publicats els límits superiors corresponents.

La estratègia seguida per a realitzar les observacions amb el telescopi MAGIC s'ha basat en la variació de les condicions d'absorció presents en el sí del sistema binari. El disc d'acreció i els jets de SS 433 precessionen amb un període de 162 dies. Les zones més internes del sistema queden cobertes periòdicament pel disc i pel fort vent de partícules associat a aquest últim degut a l'elevat ritme d'acreció. Per altra banda, l'alta inclinació del sistema (d'uns $\sim 78^\circ$ de mitja) provoca un eclipsi de les regions internes properes a la base del jet produït pel trànsit cíclic de l'estrella companya creuant la línia de la visual (per un estudi detallat de les condicions d'absorció presents a SS 433, veure el treball de Reynoso et al. 2008). Les observacions han tingut en compte aquests factors, i s'han realitzat durant 9 nits al llarg del mes d'agost de 2008 per un total acumulat d'unes 15 hores.

Al Roque de los Muchachos SS 433 es trobava en aquelles dates visible sota un angle zenital comprès en el rang $[24^\circ\text{--}30^\circ]$. Les observacions es van realitzar en el “mode wobble”, proporcionant no només regions de cel fosc necessàries per a la determinació del soroll de fons durant l'anàlisi, sinó també dades de les zones d'interacció jet/medi situades a l'est de la font. Aquestes zones, anomenades “e1” i “e2”, quedaren centrades a la càmera només durant la meitat del temps total d'observació degut al posicionament del telescopi en “mode wobble”. El seu anàlisi ha procedit de forma diferent que el corresponent a les zones centrals, ja que s'han hagut de cercar observacions de regions de cel fosc per estimar el soroll de fons. S'han utilitzat dades d'una font galàctica, PSR J0358, observada a inclinacions semblants a les de SS 433 i assegurant que no existissin indicis de senyal en el camp de visió (Oscar Blanch, comunicació privada).

El procés d'anàlisi ha requerit a més a més observacions de la Nebulosa del Cranc per a optimitzar la configuració dels patrons de selecció dels esdeveniments registrats així com simulacions Monte Carlo necessàries per a la discriminació senyal/soroll de

fons. Com que les observacions del sistema central i de les zones d'interacció “e1” i “e2” són en “mode wobble” i centrats a la càmera respectivament, diferents campions de dades de la Nebulosa del Cranc i simulacions Monte Carlo han estat usades per cadascun dels anàlisis.

S'ha seguit el procés estàndard d'anàlisi de dades mitjançant el paquet de programes MARS. S'ha fet un control de qualitat de cadascuna de les seqüències de dades per assegurar una constància en les condicions d'observació (variacions de les condicions meteorològiques, esdeveniments espuris il·luminant la càmera durant la presa de dades, etc.). S'ha procedit amb la obtenció dels paràmetres de Hillas i s'ha usat el mètode iteratiu de Random Forest a partir de les simulacions Monte Carlo per a determinar amb quina probabilitat cada esdeveniment registrat corresponia a una pluja originada per un fotó gamma i no a una generada per un raig còsmic. S'han trobat els valors dels paràmetres de Hillas amb més poder discriminador, ALPHA (per a les regions internes), THETA (per a les zones d'interacció) i HADRONNESS, que feien màxima la sensitivitat en l'anàlisi de les dades de la Nebulosa del Cranc. Els valors obtinguts han estat $\text{ALPHA} \leq 9^\circ$, $\text{THETA} \leq 0.16^\circ$, $\text{HADRONNESS} \leq 0.04$ (per l'anàlisi del sistema central) i $\text{HADRONNESS} \leq 0.07$ (per a l'anàlisi de les interaccions). El valor de THETA escollit respon a l'extensió aproximada de les zones d'interacció “e1” i “e2” observades en raigs X (veure, per exemple, Safi-Harb & Petre 1999).

L'anàlisi no ha mostrat indicis de senyal a nivells significatius per a les dades corresponents al sistema central ni tampoc per a les zones d'interacció. S'han realitzat anàlisis a diferents rangs energètics sense resultats positius. S'han establert per tant límits superiors a l'emissió de raigs gamma de la font. Els valors del fluxos integrals per energies $E \geq 150$ GeV provinents del sistema central i de les zones d'interacció han estat restringits respectivament a un valor inferior a un 0.9 % i a un 5.5 % del flux integral de la Nebulosa del Cranc a aquestes energies. S'han calculat els límits superiors al flux diferencial per ambdós anàlisis. Els resultats es mostren en les Figs. 6 i 7.

Els resultats de l'anàlisi de les observacions de SS 433/W50 amb el telescopi MAGIC han estat utilitzats per restringir els processos físics que podrien donar lloc a emissió de raigs gamma. Per a les regions centrals dels sistema, s'han explorat dos escenaris diferents, basats en models senzills d'emissió leptònics i hadrònics. S'ha assumit que una certa fracció q_e i q_p de l'energia cinètica total dels jets és destinada a l'acceleració d'electrons (ó positrons) i protons, respectivament. Aquest paràmetre s'ha deixat lliure dins el model. S'han computat els fluxos de raigs gamma generats a partir de dues alçades diferents en el jet $z_{min} = 10^{13}$ cm i $z_{min} = 10^{14}$ cm, atès que en

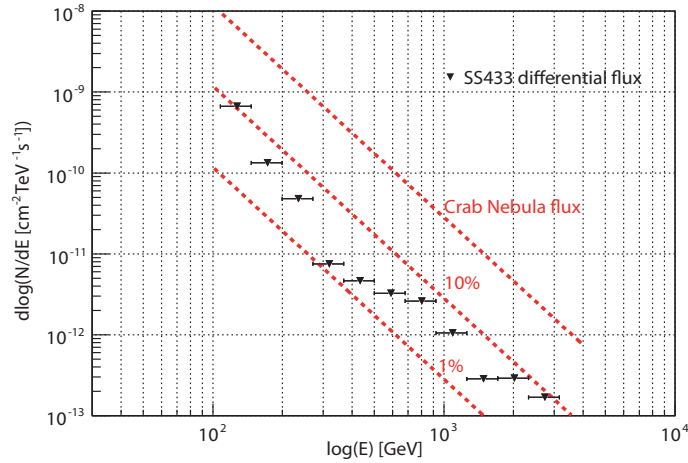


Figura 6: Límits superiors al flux diferencial de raigs gamma corresponents a l'anàlisi de les regions centrals de SS 433. Les línies puntejades de color vermell indiquen el flux de la Nebulosa del Cranc i les respectives fraccions d'un 1% i un 10% per comparació.

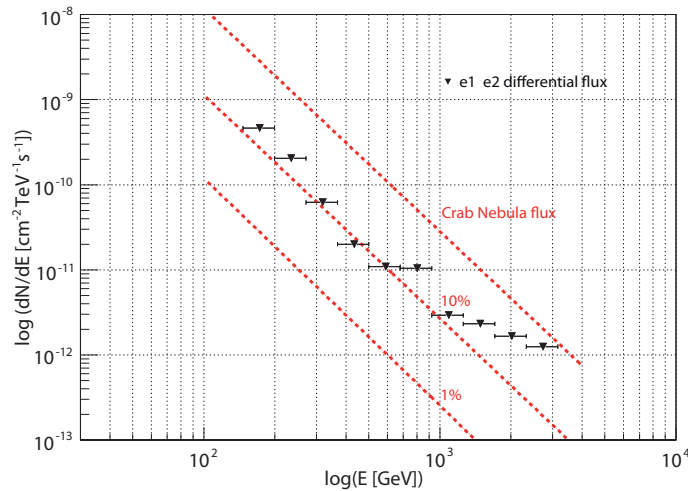


Figura 7: Límits superiors al flux diferencial corresponent a l'anàlisi de les zones d'interacció "e1" + "e2".

les regions $z \in [10^9 - 10^{13}]$ l'emissió pot ser fortament atenuada per la proximitat de l'estrella companya i del disc d'acreció i el vent de partícules associat (veure Reynoso et al. 2008). En l'escenari leptònic, s'ha modelitzat la distribució de partícules accelerades mitjançant una llei de potència, $N(E) \propto E^{-p}$, amb un índex espectral $p = 2$ característic del processos d'acceleració com el de Fermi de primer ordre.

S’han assumit valors raonables d’acord amb estudis anteriors de la font respecte els paràmetres que la defineixen (potència del jet $L_{\text{cin}} = 10^{39} \text{ erg}^{-1}$, distància del sistema $d = 5.5 \text{ kpc}$, inclinació de 78°) i s’ha calculat l’emissió IC prenent com a fotons fitó els proporcionats per l’estrella companya. Atès que estem interessats en l’emissió produïda per les partícules més energètiques, s’ha considerat una regió d’emissió igual a la d’acceleració. Els resultats finals han estat expressats en termes del flux integral per energies superiors a 150 GeV per tal de poder comparar amb les observacions realitzades amb el telescopi MAGIC. Això ha permès establir un límit superior a la fracció d’energia cinètica continguda en la distribució de leptons accelerats, $q_e \lesssim 10^{-4} - 10^{-5}$ prenent $z_{\text{min}} = 10^{14} - 10^{13} \text{ cm}$, respectivament.

Cal remarcar que les nostres estimes són optimistes, ja que no han considerat que les pèrdues energètiques de les partícules poden venir dominades per emissió sincrotró. Per evitar aquestes pèrdues, s’ha fixat el valor del camp magnètic en la zona d’acceleració/emissió a un valor suficientment baix. Per altra banda, el nostre model no té en compte les pèrdues per expansió adiabàtica. Per tal de tenir-les presents en cas que fossin dominants, els valors estimats per q_e haurien de ser escalats un factor $\sim t_{\text{IC}}/t_{\text{ad}}$, on t_{IC} i t_{ad} són els temps escala associats a les pèrdues per IC i expansió adiabàtica, respectivament.

S’ha aplicat en darrer lloc el model d’interaccions presentat en detall en el capítol 5 comparant-lo amb els resultats de l’anàlisi de les regions “e1” i “e2”. El creixement autosimilar de les estructures d’interacció no es veu alterat malgrat l’elevada potència dels jets de SS 433. La geometria i les propietats físiques d’aquestes estructures han estat establertes, i s’ha pres una edat de la font $t_{\text{MQ}} = 10^5$ anys i una densitat del medi $n_{\text{ISM}} = 1 \text{ cm}^{-3}$. La Fig. 8 mostra la SED resultant de la suma de l’emissió provinent del medi post-xoc, de la closca constituïda pel material del jet després de travessar el xoc de reflexió que es propaga vers el sistema binari al llarg del jet, i de la zona de col·limació del jet quan la seva pressió iguala a la de la closca, a distàncies $\sim 10^{18} \text{ cm}$. El flux total integrat a energies $E \geq 150 \text{ GeV}$ és de l’ordre de $1.6 \times 10^{-13} \text{ fotons cm}^{-2} \text{ s}^{-1}$, que és un factor $\sim 1/3$ inferior al límit superior establert en les observacions a aquestes energies. L’emissió a energies més baixes, en el rang X i ràdio, ha estat comparada amb els valors publicats en estudis pertinents de la font. Els resultats del model i els valors mitjans previstos són raonablement semblants, donant més solidesa als fluxos predits en el rang gamma.

L’enorme energia cinètica per unitat de temps fluïnt en els jets de SS 433 i la presència de material bariònic observada a distàncies de fins 10^{17} cm del sistema central proporcionen un marc adequat per estudiar l’emissió produïda per interaccions protó-protó en les regions d’interacció amb el medi. Malgrat deixar aquest estudi

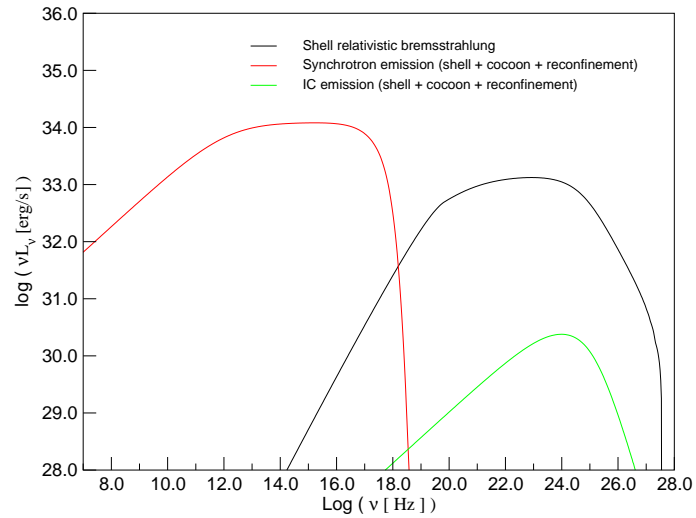


Figura 8: *SED de l'emissió provinent de les zones "e1" i "e2" considerant la radiació produïda en el medi post-xoc, en la closca que embolcalla el jet i en el xoc de col·limació dins el jet. L'emissió per Bremsstrahlung relativista és important només en el medi post-xoc, ja que les densitats de partícules en la closca i en el jet són molt baixes. Veure el text per a més informació dels paràmetres emprats.*

per a un treball futur, volem subratllar que les estimes obtingudes en els treballs de Bosch-Ramon et al. (2005) i Heinz & Sunyaev (2002) mostren que aquest mecanisme pot generar fluxos d'emissió TeV i característiques espectrals que podrien ajudar a la comprensió dels processos físics presents en aquesta font.

Bibliografía

- Aharonian, F. A., Akhperjanian, A. G., Aye, K.-M., et al. 2005b, A&A, 442, 1
- Albert, J., Aliu, E., Anderhub, H., et al. 2006, Science, 312, 1771
- Albert, J., Aliu, E., Anderhub, H., et al. 2007, ApJ, 665, L51
- Araudo, A. T., Romero, G. E., Bosch-Ramon, V., & Paredes, J. M. 2007, 476, 1289
- Bordas, P., Bosch-Ramon, V., Paredes, J. M. & Perucho, M. 2009, A&A, 497, 325
- Bosch-Ramon, V., Aharonian, F. A., & Paredes, J. M. 2005, A&A, 432, 609
- Bosch-Ramon, V. & Khangulyan, D. 2009, 18, 347
- Bonnet-Bidaud J.M.,& Chardin G. 1988, Phys. Reports, 170, 325
- Fender, R. P., Pooley, G. G., & Durouchoux, P. 2000, MNRAS, 312, 853.
- Gaisser, T. K. in Cosmic rays and particle physics, Cambridge and New York, Cambridge University Press
- Heinz, S. & Sunyaev, R. 2002, A&A, 390, 751
- Hillas, A. M. 1985, proceedings of the 19th ICRC, 3, 445.
- Longair, M. S. 1992, in *High energy astrophysics. Vol.1: Particles, photons and their detection*, Cambridge, UK: Cambridge University Press.
- Malzac, J., Lubiński, P., Zdziarski, A. A., et al. 2008, A&A, 492, 527
- Mirabel, F., Rodríguez, L. F., Cordier, et al. 1992, Nature, 358, 215
- Paredes, J.M., Martí, J., Ribó, M., & Massi, M. 2000 Science 288, 2340
- Perucho, M. & Bosch-Ramon, V. 2008, A&A, 482, 917
- Reynoso, M. M., Romero, G. E., & Christiansen, H. R. 2008, MNRAS, 387, 4, 1745
- Saito, T. Y., Zanin, R., Bordas, P. et al. 2009, Proceedings of the 31st ICRC
- Safi-Harb, S., & Petre, R. 1999, ApJ, 512, 784

Spencer, R. E. 1979, *Nature*, 282, 483

Chapter 1

Introduction

The discovery of microquasars have historically proceeded in a quite unusual way as compared to the common astrophysical findings leading to new types of sources. Microquasars, binary systems that populate the disk and the halo of our own Galaxy, were conceptually defined a few years after the discovery of quasars. In the early 1960 these "quasi-stellar radio sources", supermassive black-holes showing relativistic jets located hundreds of Mpc away from us, were detected through their radio and optical emission. The first observed quasar was 3C273, the 273th object in the third Cambridge catalog, located in the Virgo constellation at a redshift of 0.158 (Schmidt 1963). 15 years later the binary system SS 433, the 433th object in the Stephenson & Sanduleak Catalog of bright H α sources, was the first source where radio jets resembling those of quasars but with longitudes of about only some light-years and the presence of a stellar-mass compact object and a companion in the role of mass-donor were identified (Spencer 1979).

The reason for such a gap between the discovery of these two classes of objects is linked, of course, to the technical conditions which are needed to effectively detect them. For a black hole accreting at the Eddington limit, the typical black body temperature of the last stable orbit in the accretion disk scales as $T \propto M_{\text{bh}}^{-1/4}$ (Rees 1984). For a massive black-hole in a quasar this implies that the emission peaks at the optical/UV band. The emission from the same process but taking a solar-mass black hole instead of a milion solar-mass one, is shifted towards the X-ray band. It means therefore that microquasars had to wait until X-ray astronomy was fully developed in order to be discovered.

In the early 90's, the term microquasar was adopted for those X-ray binary systems displaying relativistic jets (Mirabel et al. 1992). The similitudes with quasars

were not only restricted to the presence of a compact object and accretion/ejection processes. After the discovery of 1E1740.7-2942 and GRS 1758-258, the morphological analogies comprised the extended emission produced in the interaction of jets with their surroundings. Since then, microquasars have been extensively studied, and the search for new candidates have led to the ~ 17 systems actually known. They are exceptional laboratories where high and very high energy processes occur. The nature of these process is however not yet fully understood. The study of the connection between the disk and the jet formation permits to understand the relation between the processes of accretion and the ejection of powerful outflows in scales of \sim days. Non-thermal emission is observed from a few Schwartzchild radius from the compact object up to scales of hundreds of pc. The study of the radiative mechanisms allows the characterization of the intense matter, radiation and magnetic fields. Efficient acceleration of particles is required in different regions to explain the observations. The underlying physics of microquasars is very rich and embraces both astrophysics and particle physics research fields, on the edges of general relativity theory and quantum mechanics.

The broadband emission produced in microquasars permits to study all these physical processes in a wide range of energies (from radio to very high energies, more than 20 orders of magnitude). Although initially discovered through their radio and strong X-ray emission, microquasars have proved to be also bright sources of gamma-rays. They were proposed as counterparts of the unidentified sources discovered with the EGRET instrument onboard the Compton Gamma-Ray Observatory (Paredes et al. 2000), and VHE have been recently observed from three microquasar candidates (Aharonian et al. 2005; Albert et al. 2006 ; Albert et al. 2007). Gamma-ray astronomy is indeed one of the most fast-evolving disciplines in astrophysics - and in physics in general. The recent developement of new Cherenkov observatories and satellite-borne instruments is providing the scientific community with a new window were the extreme Universe shows up. Microquasars are some of the most suitable laboratories where high and very high energy processes can be effectively studied.

1.1 Outline of the thesis

The present thesis focuses on the investigation of some of the high energy processes occurring in microquasars. The matter content and the power transported in the jets of microquasars are studied, the effects that they have on the surrounding medium are quantified, and their expected capability to emit at high end very high

energies is constrained. Since these are quite broad objectives, we have treated them separately. The thesis is therefore divided in two distinct parts, preceded by a short overview of the microquasar phenomenology and a characterization of the physical mechanisms that will be needed further on (Chapters 1 to 3). Although we note that other processes may occur in microquasars, our description is however limited to those directly related to the problems faced in some specific scenarios.

In Part I (Chapters 4 and 5) we explore the interactions that microquasar jets have with their environments. In Chapter 4 the interactions of microquasar jets with the wind and radiation fields of the companion star are explored. We investigate the radiative consequences of the presence of relativistic hadrons in the jets. We study the primary hadronic emission in the gamma-ray domain, and we then focus on the secondary particles generated in proton-proton interactions. We analyse how the detection of the emission of these secondaries could point to the presence of hadrons in the jet. We consider a high-mass system with a constant energy injection rate in a circular orbit, but our results can be extended to more realistic scenarios. After inspection of the obtained results, we conclude that the non-thermal radiation output from secondaries alone cannot account for the radio and X-ray flux levels observed in microquasars. The existence of a primary lepton population seems therefore to be required.

In Chapter 5 we examine the impact of microquasar jets with the interstellar medium (ISM). Extended emitting structures are thought to be formed when the jets are effectively decelerated by the surrounding gas. The situation is analogous to that found in AGNs, where radio-lobes and hot spots are frequently observed at the jet termination regions. The jet composition is difficult to constrain in these studies. Both primary hadronic and e^+e^- plasmas can provoke similar effects in their surroundings. Our model can provide an estimate of the total power carried in the jets when the source age and the medium properties are known. More importantly, these studies are independent from other approaches in which the jet kinetic power is derived directly from its radiative output (in radio, assuming minimum energy arguments and rough equipartition of the magnetic field; at higher energies, by using the observed flux and assuming a certain constant fraction of jet power converted to non-thermal power). They provide therefore constraints to be applied in all cases where jet/ISM interactions occur. It must be noted in this sense that an increasing number of microquasars do indeed show evidences of such interactions.

In Part II (Chapters 6 to 8) we present the results of the search of VHE gamma-ray emission from microquasars. We make use of the exceptional capabilities of the MAGIC telescope for this purpose. The Cherenkov Imaging technique has become

the most successful method to detect gamma-ray emission from ~ 100 GeV up to 10 TeV. Four well-known microquasars have been observed by MAGIC, namely Cyg X-1, Cyg X-3, GRS 1915+105 and SS 433. No evidence of steady signal have been found, whereas an evidence of detection of a flare was found only from Cyg X-1 in September 2006. Particular source conditions have been used to trigger the observations. They were based on the presence of the source in the low-hard state in which radio jets are thought to be present, and in state transitions, when strong radio/X-ray flares can be produced. The MAGIC upper limits are compared to recent theoretical models predicting gamma-rays from the observed sources. We study in detail several physical mechanisms in the light of the collected results in both hadronic and leptonic scenarios.

Conclusions derived from the attained results are included separately in each Part, and we close this thesis with some concluding remarks of the main outcomes obtained, which are presented in Chapter 9.

Bibliography

- Aharonian, F. A., Akhperjanian, A. G., Aye, K.-M., et al. 2005, *Science*, 309, 746
- Albert, J., Aliu, E., Anderhub, H., et al. 2006, *Science*, 312, 1771
- Albert, J., Aliu, E., Anderhub, H., et al. 2007, *ApJ*, 665, L51
- Mirabel, I. F., Rodriguez, L. F., Cordier, B., et al. 1992, *Nature*, 358, 215
- Paredes, J. M., Martí, J., Ribó, M., & Massi, M. 2000, *Science*, 288, 2340
- Rees, M. J. 1984, *ARA&A*, 22, 471
- Schmidt, M. 1963, *Nature*, 197, 1040
- Spencer, R. E. 1979, *Nature*, 282, 483

Chapter 2

Phenomenology of microquasars

2.1 Main properties

In the next chapters we will refer to different processes occurring in the microquasar scenario, so it is desirable to begin with the properties that define these systems. A general description will follow, and we refer to prior works for detailed treatments on the multiple aspects that determine these sources. (Mirabel & Rodríguez 1994, Paredes et al. 2000, Ribó 2002, Kaufman Bernadó 2004, Bosch-Ramon 2006). A sketch of a microquasar scenario is displayed in Fig. 2.1

In short, one can define as microquasars all those X-ray binary systems which display relativistic radio jets. Despite its clean definition, there may be some situations in which a given source could still be missed from being properly identified as a microquasar. The binary nature, for instance, must be clearly assigned through spectroscopic observations of orbital Doppler shifted absorption lines or by the generation of periodic emission, although it does not prevent from identifying what could be e.g. binary systems where radio emission is produced through the collision of the star winds. More importantly, the jet nature of the radio emission has to be undoubtedly established. Nevertheless, other scenarios could show radio signatures that can be morphologically similar (see, e.g., Dubus 2006, Bosch-Ramon et al. 2008a)

As X-ray Binary systems, microquasars are constituted by two stars orbiting one around each other. One of them is a compact object, either a Neutron Star (NS) or a stellar-mass Black Hole (BH). The other is a normal, non-degenerate star, which can be found in its Main Sequence phase or in later stages of its evolution.

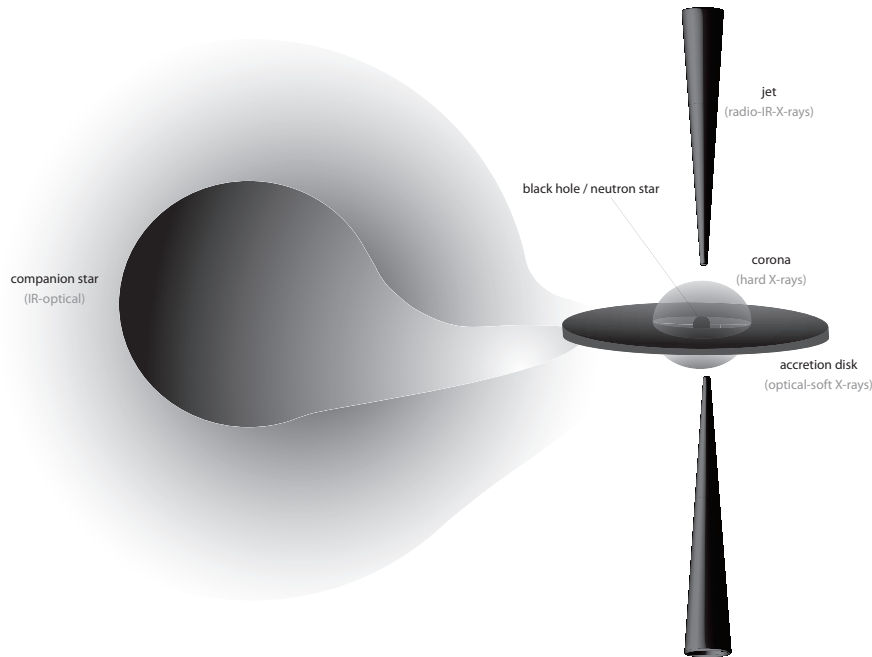


Figure 2.1: *Sketch of the microquasar scenario. The different components that constitute the system are indicated, together with the emission that is produced in each region.*

Matter expelled from the companion is transferred to the compact object due to the strong gravitational attraction. The material delivered through the expansion of the expanded most external layers of the star fills the Roche lobe, overflowing it and falling into the compact object potential well. Alternatively, the companion can directly feed the compact object through strong stellar winds.

Once the stellar material approaches the NS/BH vicinity, it is distributed over a plane perpendicular to the direction of its average angular momentum vector and forms an accretion disk. Along the way towards the compact object, viscous dissipation forces transform the potential energy and angular momentum of the infalling flow into heat and radiation output. More importantly, under specific physical circumstances, a fraction of the hot and highly ionised material present in the inner regions of the accretion disk could be ejected, allowing in this way the formation of jets (jet formation will be discussed in Sect. 3.1)

The fate of the remaining material of the disk which is spiraling towards the center of the gravitational potential well will depend on the nature of the compact object. For a NS with a strong magnetic field, the accretion disk will be disrupted well before reaching the surface of the compact object; the flow will follow the mag-

netic field lines, which will drive the material towards the magnetic poles producing strong X-ray radiation. It is interesting to note that in case the magnetic field is misaligned with respect to the NS rotation axis, this scenario would correspond to a particular class of X-ray binaries, the accreting X-ray pulsars. Their detection depends on whether the beamed magnetic pole emission crosses the observer line of sight or not. In the case that the NS have a weaker magnetic field, the infalling material will eventually impact on the surface of the compact object. The flow energy that survived the disk dissipation process is now entirely deposited onto the hard NS surface, and will produce again high levels of X-ray emission.

When the compact object is a BH, the matter crossing the horizon of events will keep falling and no surface will permit it to liberate the remaining energy. The fraction of the total accreted matter/energy which is finally directed towards the center of the singularity is uncertain, and uncertain is also the amount of angular momentum swallowed by the BH. The radiation produced in the accretion disk is however more intense than that around a NS. The last stable orbit around the BH is closer to the compact object. The material has more time to radiate part of the transported energy and near the compact object the temperature gets higher and thermal black body emission is efficiently produced.

The main description of microquasars is not yet closed. In fact, microquasars extend their effects milion times further away than the binary system typical length-scales. The large amounts of kinetic energy ejected in the formation of jets is deposited into the surrounding ISM. A kind of cycle is therefore accomplished, in which the gravitational collapse of dense ISM regions leads to the binary system formation, which evolves and gives back a fraction of its kinetic energy to the medium.

2.2 Quasars and microquasars

The adoption of the term microquasar appeared because of the apparent similarities with the quasars or, more generally, with active galactic nuclei (AGN). As mentioned before, it is generally accepted that the accretion of material towards the compact object is the source of the immense power output coming out from these systems. This power can exceed in some cases the Eddington luminosity for a one solar mass object ($\sim 10^{38}$ erg s⁻¹). Moreover, accretion is energetically more efficient than the nuclear fusion sustaining normal (non-degenerate) stars. Since in AGNs the power source is also believed to rely on accretion onto a BH (in this case of millions to thousand of milion solar masses), analogies in the physical processes in both AGNs

and microquasars could be also present beyond the similar morphologies. The understanding of the processes occurring in microquasars would then be important not only to explain the behaviour of some particular "local" systems, but also to better interpret the behaviour of the powerhouses of our Universe, the AGNs. Nevertheless, the term microquasar began to be broadly used after the discovery of the Great Annihilator, 1E1740.7 - 2942, located at the center of our Galaxy (Mirabel et al. 1992; see also Rodriguez et al. 1992). The original motivation came from the effects that this system had on the surrounding medium, namely the presence of large-scale radio emitting lobes - as those often observed in distant quasars. The study of the consequences of the interaction of the microquasar jets with its medium is a central part of this thesis, and will be presented in detail in Chapter 5.

Within the most important parallelisms that the two kind of objects display there is the jet formation process. The same magnetohydrodynamical mechanisms could be behind the jet launching process in both kind of systems. The extraction of the jet kinetic energy from the accretion disk and/or the compact object rotational energy has been proposed in both scenarios. AGNs offer however a better opportunity to reveal the most inner regions at the jet base. The jet formation region has been directly imaged in some AGNs like M87 up to ~ 100 Schwartzchild radius, $R_{\text{sch}} = 2GM_{\text{BH}}/c^2$ (Junor et al. 1999). Comparing M87 to X-ray binaries in our own Galaxy, the ratio of distances is so much smaller than the ratio of BH masses, that such imaging is not possible. For example, a structure of size 100 Schwarzschild radii around a $10 M_{\odot}$ BH at a distance of 5 kpc would have an angular size of a few times 10^{-9} arcsec.

Furthermore, a universal scaling between the jet radio luminosity and both the mass and accretion rate onto the compact object have been suggested (Merloni et al. 2003; see also K rding et al. 2006). Intimately related to this issue, radio emission from AGNs is correlated to X-ray spectral properties of the source, as it is observationally found in the XRB scenario, as well as to the geometry of the inner accretion flow. Radio-loud AGNs typically have harder X-ray spectra than radio-quiet AGNs (Elvis et al. 1994, Zdziarski et al. 1995). Further on, analogies between Seyfert I galaxies and the high-soft state (see below) and between low-luminosity FR-I sources (Fanaroff & Riley 1974) and the low-hard state have been drawn (see Pounds et al. 1995, Meier et al. 2001, Falcke et al. 2003).

There are, however, important differences arising between both types of objects. Radio emission was detected from quasars due to Doppler boosting of the flux densities of their approaching jets. These systems appear therefore as bright radio sources when their jets point roughly towards our line of sight, a condition which is

not necessary in the case of microquasars. Being nearby sources, extreme Doppler boosting is not required, and most of times both the approaching and receding jets are detected. In addition, the nature of the mass donor plays a central role in the interpretation of the variability observed in the galactic systems. This situation is radically different in quasars, fed by the host galaxy, whose emission from radio to VHE energies does not show any sign of periodic pattern due to accretion rate variability. Moreover, jets in these sources are steady, permanent features, whereas in microquasars jet emission can be completely suppressed in some source states. The conditions under which high energy emission can be produced could be very different in both scenarios. While IC off the disk and companion star photon fields can play a major role in microquasars, non-thermal X to γ ray emission is often related in a quasar scenario to synchrotron or IC scattering off the diffuse radiation of the broad-line region (BLR) or the Cosmic Microwave Background (CMB) photon field.

2.3 High mass, low mass and radio emitting X-ray binary systems

X-ray binaries are usually classified in two groups depending on the mass of the companion or donor star. The 299 systems actually known in our Galaxy and in the Large and Small Magellanic Clouds are hence divided in High Mass (112) and Low Mass (187) X-ray binary systems, labeled HMXBs and LMXBs respectively¹ (see Liu et al. 2006 and Liu et al. 2007 for updated catalogs of High Mass and Low Mass systems, respectively).

This classification is of major importance regarding the study of microquasars, since it already points to different system properties such as the companion's photon field, the matter distribution inside the binary system, and the source age and localization in the Galaxy (and hence the surrounding medium). These properties will turn out to be decisive in the interpretation of the physical processes occurring in these systems and the mechanisms through which we will be able to understand them.

¹One should have in mind that some of the cataloged systems are still to be confirmed and in a few more their nature is only derived when interpreting the X-ray behaviour.

- High Mass X-ray Binary systems (HMXB)

An early type star constitutes the companion in HMXBs, being of O or B spectral type. In our Galaxy, they are predominantly distributed along the galactic plane, since they are young Population I systems hosted in the spiral arms. Some of the HMXBs can be further subdivided into systems containing a Be star (Be class), implying the existence of emission lines, or those bearing a supergiant O or B star (SG class); the rest of sources does not fit neither in one nor in the other group since there is not a clear identification so far.

Some notable differences arise between the Be/SG classes. In the Be case the emission lines are produced in a strong equatorial decretion disk from a B star of luminosity class III to V, whose mass range between 8 and 20 M_{\odot} . Accretion towards the compact object is accomplished through the mass transfer of the decretion disk, rather than filling their Roche lobe. During periastron passage, which can be produced each 10-250 days, short X-ray bursts can be observed - likely related to a variation in the accretion rate in an excentric orbit. Most of these systems seem to contain an X-ray pulsar, harbouring a NS with strong magnetic fields which prevent the formation of steady jets. Typically long life-times define these systems, reaching values of about 10^7 years.

In the SG class, the O-B supergiant stars show an extremely high luminosity in the I to III class. These companions are heavy stars, with masses beyond 15 M_{\odot} , and the systems show a short orbital period of about ~ 5 days. Mass transfer to the compact object is realised through stellar winds or Roche lobe overflow in this case, and the observed X-ray emission is persistent, probably because systems tend to be circularized and the conditions do not vary too much along the orbit. The age of this subclass ranges between $10^5 - 10^6$ years.

- Low Mass X-ray Binary systems (LMXB)

LMXBs contain an evolved companion star of type later than B. Their mass is $\lesssim 2 M_{\odot}$, and show very short orbital periods in the range $0.01 \lesssim \tau_{\text{orb}} \lesssim 15$ days. The mass transfer is accomplished through Roche lobe overflow. Despite the fact that their orbits display a low eccentricity, most of the LMXBs are transient sources. This suggests the presence of variations in the accretion rate due to instabilities in the accretion disk or to variable ejection episodes from the companion star. LMXBs are old systems, with ages around $10^8 - 10^9$ years. On the other hand, a considerable fraction of LMXBs show X-ray bursts due to thermonuclear flashes on the surface of the NS. The LMXBs known so far are primarily located in the galactic bulge and in globular clusters at relatively high galactic latitudes, since they are old stellar systems of Population II.

It must be noted that the influence that HMXBs and LMXBs have on their surrounding medium can be comparatively similar. As it will be shown in detail in Chapter 5, the kinetic luminosity transported in the jets of this two types of X-ray binaries uses to differ by a factor of 10 – 100, being LMXBs less powerful. The longer time these last sources have been providing their energy and momentum to the medium, however, equals the total amount of energy cumulatively delivered to the surrounding ISM. Radio lobes and acceleration at the jet termination regions may be common in both types of binaries.

Radio emitting X-ray binaries

Among the 299 XRBs, about 65 of them are radio-loud (see Liu et al. 2006, Liu et al. 2007) and catalogued as radio emitting X-ray binaries (REXBs). The division between HMXBs and LMXBs is probably not important for the study of the radio emission from these systems. The only relevant aspect seems to be their capability to produce jets that emit through synchrotron mechanism. Nevertheless, in all systems this emission has to be undoubtedly resolved as coming from a relativistic collimated outflow. Only in such a case a given source can be included in the microquasar class.

The fraction of established microquasars would radically increase if we could know that there are even more XRBs in the Galaxy. Grimm et al. (2002) derived a luminosity function of the known XRBs by using public *RXTE* data. When extrapolating the results from known systems to lower luminosities, they derive a total number of ~ 700 XRBs brighter than 10^{34} erg s $^{-1}$. In fact, some authors sustain that jets are a quite common feature of X-ray binary systems, suggesting that up to 70% of XRBs might produce them (see Fender 2004) but we are not capable of detecting them due to their faint emission. It seems expectable then that new microquasar candidates will appear when new instruments with more sensitivity and resolution at X-ray and radio bands will be available.

2.4 X-ray spectral states

The global X-ray spectra of black-hole XRBs can be usefully considered as the summation of two main components. The first one refers to the thermal contribution produced in the accretion disk, modeled as a multi-color blackbody - essentially the disk solution first proposed by Shakura & Sunyaev (1973) and Novikov & Thorne (1973). A Shakura-Sunyaev disk displays a gradient radial profile of temperatures,

$T_{\text{disk}} \propto r_{\text{disk}}^{-1/4}$, each annulus emitting X-rays roughly at an energy given by $2.7K_{\text{B}}T$, $K_{\text{B}} = 8.6 \times 10^{-5} \text{eV}$ being the Stefan-Boltzmann constant. The second component accounts for a power-law spectral distributed radiation, sometimes ending in a exponential cut-off. The nature of the physical processes responsible for this power-law contribution is still unclear. A hot flow composed by a geometrically thick and optically thin plasma (often called the corona) could be present in the innermost regions of the accretion disk. This plasma could up-scatter soft thermal X-rays up to hard X-rays, rendering the power-law tail without the necessity of invoking additional particle populations.

The relative weights of the fluxes of the two components give a phenomenological definition of two main X-ray spectral states, although other less-prominent states exist between them. These two main states are the so-called Low-Hard (LH) and High-Soft (HS) states. When the disk component dominates and the (thermal) spectrum peaks at some few keV the source is in the HS state. The overall luminosity is high and the emission at hard X-ray energies is low - this is, the spectra is soft since the spectral index is high. It has to be noted, however, that in this state a weak power law tail is also observed, but it is not energetically important. Differently, when the spectrum peaks at hard X-rays at about ~ 100 keV, and the power-law drives the overall emission we are found in the LH state. The integrated luminosity is now lower (below 10% of the Eddington luminosity) but it extends to higher energies - i.e., the spectrum is hard compared to the HS state. This is the state in which accreting BH spend most of the time, and the power-law emission observed is usually interpreted as the result of thermal Comptonization by a population of hot ($k_{\text{B}}T \sim 70$ keV) electron population with an optical depth close to 1 (Thorne & Price 1975; Sunyaev & Truemper 1979).

In addition to the LH and HS states, there exist the so-called Intermediate, Very High and Quiescent states. The first one is seen during transitions between the LH and HS states, the global spectrum properties being now half way between them. Occasionally, some systems show a very high luminosity, and the non-thermal power-law and blackbody component become comparable in flux. They are referred then to be in the Very High state (the power-law component does not show evidences of a cut-off up to hundreds of keV). Finally, the Quiescent state originally defined the transient black-hole XRBs showing a flux level orders of magnitude below that of the other states. The spectrum in this state is not of thermal origin, as in the LH state, although slightly softer (McClintock et al. 1995).

Historically, it was supposed that the states described above were roughly a one-dimensional function of the mass accretion rate, which in turn could be tracked by

means of the soft X-ray flux from the accretion disk. From the Quiescent state through the LH state, the Intermediate state up to the HS state, and eventually reaching the high luminosities of the Very High state. This picture became however less clear after realizing that the X-ray spectral and timing properties could be the same despite very different accretion rates. Detailed observations of XTE J1550 - 564 demonstrated that at least two observable parameters are needed to describe the appearance of the source and to account for the occurrence of the different states. Phenomenologically, the two parameters describing this two-dimensional behavior are the count rate and the spectral hardness. Physically, the two underlying parameters might be for instance the mass accretion rate (roughly increasing with count rate) and the size of a comptonizing medium (increasing with spectral hardness). We will not enter in greater detail in the spectral classification. The reader is referred to the work of Homan et al. (2001) and Nowak (1995) for an extensive study on this subject (see also the review of Remillard & McClintock 2006).

Steady jets are present during the LH state, as it is derived from observational campaigns on some well established XRBs (Fender et al. 2003). Persistent flat non-thermal radio synchrotron emission, originated in collimated jets, has been resolved down to milli-arcsecond scales in this state. The physical process behind the relation between jet formation and accretion rate - X-ray spectral state is however still limited to a phenomenological level. The steady jet seems to be suppressed during the transition from the LH to the HS states, i.e., during the Intermediate state. In the course of this transition, the accretion rate increases and the X-ray emission peak shifts towards higher energies (higher temperatures), probably related to the material orbiting at radii closer to the compact object. In the meanwhile, the Comptonizing medium radiates still at a significant level. At a certain point, a release of "extra" energy is produced and channeled through the jet in the form of blobs or magnetohydrodynamic shock waves. The nature of the instability responsible for this energy discharge is unknown, but after this abrupt ejection it is clearly seen how the jet emission disappears. Once entered into the HS state, the soft thermal enhanced disk emission as well as a soft power-law tail remain.

This strongly non-linear behaviour permits, however, the realisation of extreme conditions in which acceleration of particles could occur under the presence of dense particle, radiation and magnetic fields. The extreme conditions during transition phases could be adequate for the production of non-thermal radiation at high energies. In fact, evidences of emission up to VHE gamma-rays have been detected in the microquasar Cygnus X-1 quasi-simultaneously to an X-ray flare (Albert et al. 2007), although the search for steady VHE production during the LH state in this source did not yield any positive result so far (we will come back on this issue later

in Chapter 8).

2.5 Microquasars from radio to VHE gamma-rays

The study of microquasars has to involve necessarily the information coming from a broadband range of frequencies in the electromagnetic spectrum. Different emission components at low and high energies can be observed in these systems, each of them providing interesting constraints on the physical mechanisms operating inside the binary system, along the jet and further away, in the interaction with the surrounding medium.

As a first order approach one should separately consider thermal and non-thermal radiation production since the physical mechanisms behind them are quite different. Radiation beyond X-rays can not be attributed to thermal processes since it would correspond to an extremely high temperature plasma in thermal equilibrium. Acceleration of particles is required to generate such high and very high energy emission, where processes are given in time-scales much shorter than the thermalisation one. Moreover, the particle distribution itself clearly shows a power-law morphology far different from a typical thermal Maxwellian distribution and pretty close instead to what would be expected in many acceleration scenarios (see Sect. 3.3).

Blackbody emission at UV and optical wavelengths comes primarily from the companion star in HMXBs. Emission at these frequencies is also detected from the companion's wind and from the coldest, most external parts of the accretion disk. In the case of LMXBs, the optical continuum is dominated by the emission from the accretion disk, which is the result of reprocessing of a fraction of the X-rays into optical photons in the disk. The contribution from the companion is generally small (van Paradijs & McClintock 1995) in these systems.

Multi-color blackbody X-ray emission is produced in the accretion disk. Depending on its extension up to the inner radius close to the compact object, the temperature can grow up to 10^8 K, radiating intensely at the X-ray band. The extraordinary luminosity released in the accretion process is the reason why XRBs were first discovered as powerful X-ray sources, while correlation at other wavelengths followed to unveil its binary nature. X-rays of non-thermal origin are produced in the comptonization of soft disk X-rays in the corona up to $\lesssim 100$ keV. Furthermore, soft gamma-ray emission at MeV energies has also been observed in some cases, although its origin is still not fully understood.

Microquasar's jet radiation extends from low-energy radio emission possibly up to VHE gamma-rays. The reason for these wide coverage relies on the multiple non-thermal processes operating there. First of all, the presence of accelerated leptons and a magnetic field leads to synchrotron radiation that generates the emission from radio to IR and can extend up to X-rays in some cases (see, for instance, Markof et al. 2001). The origin and precise evolution of the magnetic field are not known. The magnetic field to the total energy density ratio is usually parametrized, since this has not been derived so far from solid theoretical grounds. Similar considerations refer to the non-thermal particle population generating the emission. The mechanism(s) responsible for the acceleration of particles is not well known - although effective candidates do exist (see Sect. 3.3)

At the high and very high energies, several jet scenarios can be considered (for a recent review see Bosch-Ramon & Khangulyan 2009). Inverse Compton scattering off external (companion star, disk, CMB) or internal (jet synchrotron-generated) photons by relativistic leptons could provide the necessary conditions for its production. Furthermore, if the jet is able to accelerate protons to relativistic energies, gamma-rays would be a natural signature of the collisions between these particles and the target ions from the companion's wind in HMXBs or against the thermal pool of protons within the jet itself both in HMXBs and LMXBs. The observation of VHE fluxes from microquasars will strongly depend, however, on the absorption conditions present at the inner regions of the binary system. The stellar photon field in high mass systems can be severe enough to easily rise the optical depths up to values about $\tau \sim 10$ depending on the orbital phase of the system (see, for instance, Bednarek 1997; Bottcher & Dermer 2005; Reynoso et al. 2008). Alternatively, emission could be generated outside the binary system length-scales, although the conditions there regarding the target photons are poorer (see, e.g., Bosch-Ramon et al. 2008b). At about 10^{13} cm the photon density will be a factor ~ 100 lower, although acceleration should still be active at these regions. Moreover, moderate gamma-ray emission could be also generated at the interaction of microquasar jets with the ISM under conditions that may be given in some sources. We will discuss gamma-ray emission from well-established microquasars in Chapter 8.

Finally, microquasars could be sites of cosmic ray electrons and protons production, and astroparticle physicists are becoming increasingly interested in them as a possible galactic neutrino sources. The presence of protons in their jets, as already confirmed in the case of SS 433 where hot ions have been directly observed (Margon 1984; Kotani et al. 1998; Marshall et al. 2002), could entail photo-meson and proton-proton interactions (see Distefano et al. 2002; Heinz & Sunyaev 2002; Reynoso et al. 2008). The great power of microquasar jets together with a suit-

able ambient photon/ion target densities could be responsible for a non-negligible fraction of the galactic cosmic rays whose origin is still questioned - more than 100 years after their discovery.

Bibliography

- Albert, J., Aliu, E., Anderhub, H., et al., 2007, ApJ, 665, L51
- Bednarek, W. 1997, A&A, 322, 523
- Bosch-Ramon, V. 2006, Ph.D. Thesis, Universitat de Barcelona
- Bosch-Ramon, V., Khangulyan, D., & Aharonian, F. A. 2008a, A&A, 482, 397
- Bosch-Ramon, V., Khangulyan, D., & Aharonian, F. A. 2008b, A&A, 489, L21
- Bosch-Ramon, V., & Khangulyan, D. 2009, IJMPD, 18, 347.
- Böttcher M., & Dermer C. D. 2005, ApJ, 634, L81
- Distefano, C., Guetta, D., Waxman, E., & Levinson, A. 2002, ApJ, 575, 378
- Dubus, G. 2006, A&A, 456, 801
- Elvis, M., Wilkes, B. J., McDowell, J. C., et al. 1994 ApJ, 95, 1
- Falcke, H., Körding, E., & Markoff, S. 2004, A&A, 414, 895
- Fanaroff, B. L., & Riley, J. M. 1974, MNRAS, 167, 31P
- Fender, R.P. 2004, in *Compact Stellar X-ray Sources*, eds. W.H.G. Lewin & M. van der Klis
- Fender, R. P., Gallo, E., & Jonker, P. G. 2003, MNRAS, 343, L99
- Grimm, H.-J., Gilfanov, M., & Sunyaev, R. 2002, A&A, 391, 923
- Heinz S., & Sunyaev R., 2002, A&A, 390, 751
- Homan, J., Wijnands, R., van der Klis, M., et al. 2001, ApJS, 132, 377
- Junor, W., Biretta, J. A., & Livio, M. 1999, Nature, 401, 891
- Körding, E., Falcke, H., & Corbel, S. 2006, A&A, 456, 439
- Kaufman Bernadó, M. M. 2004, Ph.D Thesis, Universidad de Buenos Aires
- Kotani, T., Kawai, N., Matsuoka, M., & Brinkmann, W. 1998, in *The Hot Universe*,

- IAU Symp., 188, 358
- Liu, Q. Z., van Paradijs, J., & van den Heuvel, E. P. J. 2006, A&A, 455, 1165
- Liu, Q. Z., van Paradijs, J., & van den Heuvel, E. P. J. 2007, A&A, 469, 807
- Margon B., 1984, ARA&A, 22, 507
- Markoff, S., Falcke, H., & Fender, R. 2001, A&A, 372, L25
- Marshall, H. L., Canizares, C. R., & Schulz, N. S. 2002, ApJ, 564, 941
- McClintock, J. E., Horne, K., & Remillard, R. A. 1995, ApJ, 442, 358
- Meier, D. L., Koide, S., & Uchida, Y. 2001, Science, 291, 84
- Merloni, A., Heinz, S., & di Matteo, T. 2003, MNRAS, 345, 1057
- Mirabel, F., Rodríguez, L. F., Cordier, P., et al. 1992, Nature, 358, 215
- Mirabel, F., & Rodríguez, L. F. 1994, Nature, 371, 46
- Novikov, I.D., & Thorne, K.S. 1973, in *Black Holes - Les Astres Occlus*, eds. C. De Witt & B. De Witt, Gordon & Breach, New York
- Nowak, M. A. 1995, PASP, 107, 1207
- Paredes, J.M., Martí, J., Ribó, M., & Massi, M. 2000, Science, 288, 2340
- Pounds, K. A., Done, C., & Osborne, J. P. 1995, MNRAS, 277, L5
- Remillard, R. A., & McClintock, J. E. 2006, ARA&A, 44, 49
- Reynoso, M. M., Christiansen H. R., & Romero G. E. 2008, APh, 28, 565
- Ribó, M. 2002, Ph.D. Thesis, Universitat de Barcelona
- Rodríguez, L. F., Mirabel, I. F., & Martí, J. 1992, ApJ, 401, L15
- Shakura, N.I., & Sunyaev, R.A. 1973, A&A, 24, 337
- Sunyaev, R. A., & Truemper, J. 1979, Nature, 279, 506
- Thorne, K. S., & Price, R. H. 1975, ApJ, 195, L101
- van Paradijs, J., & McClintock, J. E. 1995, in *Optical and ultraviolet observations of X-ray binaries*, ed. W. H. G. Lewin, J. van Paradijs, & E. P. J. van den Heuvel, Cambridge University Press, Cambridge
- Zdziarski, A. A., Johnson, W. N., Done, C., Smith, D., & McNaron-Brown, K. 1995, ApJ, 438, L63

Chapter 3

Physical processes in microquasar jets

We have explored the physical processes in a relativistic jet when computing its non-thermal emission. The jet is launched by means of a magnetohydrodynamical mechanism, although it is not clearly defined yet how this mechanism operates. There exists a magnetic field somehow entangled with the outflowing jet material. The jet power is treated phenomenologically, carrying a fraction of the total accretion kinetic power of the system. Particle acceleration takes place at certain regions along the jet or in a continuous and extended zone. Fermi acceleration is considered as the main process leading to the production of such acceleration, first order Fermi mechanism being at work in the shock fronts along the jet. These shocks are strong, and the spectral distributions for the non-thermal accelerated particles can be derived. These relativistic populations (whose composition can be hadronic, leptonic, or a composition of both) interact with matter, radiation and magnetic fields to produce radiation at different energy bands. Some of the physical assumptions just exposed could seem rather arbitrary without some further explanations. They will be covered in some detail below, but the reader should keep in mind that the results obtained in Parts I and II of this thesis do not intend to be conclusive regarding the complexity of these processes - but rather to constrain them by checking their consistency with other observational and theoretical results.

3.1 Accretion disk and jet formation

Phenomenology of jet formation in XRBs

Flat-to-slightly inverted radio spectra (i.e. $\alpha = 0.0 - 0.3$, where the flux density is $f_\nu \propto \nu^\alpha$) are often observed in XRBs. Although synchrotron emission is expected from a compact jet, (Blandford & Königl 1979; Hjellming & Johnston 1988) such radio spectra are also seen, for example, from HII regions and planetary nebulae, the radio emission being thermal in these cases. Additional evidence is required therefore to prove that this radio emission has a synchrotron origin. Evidences of this may come from the very high brightness temperatures implied by the fluxes of radio emission. For a flux at the level of ~ 50 mJy at \sim GHz radio frequencies for a source located at 10 kpc, the emitting region will be about $\geq 10^{13}$ cm, much larger than the orbital separation of the binary. Such large extension is more likely to come from an outflow (Fender 2002). Furthermore, polarization signatures could also point to synchrotron emission, whereas different polarisation features could also help to constrain the jet composition (see, e.g., Wardle & Homan 2001). Additionally, hints of mildly relativistic jets have been suggested from the X-ray/optical correlation observed in some microquasars (Malzac et al. 2004).

The formation and evolution of jets in XRBs is often related to a phenomenological association between their radio and hard X-ray emission. As mentioned before, this relationship is likely associated with a physically motivated connection between accretion flows and jet production. Radio emission is well correlated with hard X-rays and anticorrelated with soft X-rays. This is valid for both NS and BH systems, although there exist some differences between them. The best fitting power law index for the radio/X-ray luminosity relation in NS is $L_{\text{Radio}} \propto L_{\text{X-ray}}^{1.4}$, twice as steep as the relation for BH, $L_{\text{Radio}} \propto L_{\text{X-ray}}^{0.7}$ (Migliari & Fender 2006). It has been interpreted as evidence that BH systems advect energy across their event horizons, whereas NS systems release this energy in their boundary layers. Furthermore, at higher luminosities NS are detectable radio emitters in their equivalents of the HS state. Their radio fluxes are however well below those in the HS, so jet production is, in some sense, suppressed in NS as it is in BHs. We will simply consider here that the energy for the jet formation is extracted from the accretion process onto a compact object and, perhaps, from its rotational energy.

Magnetohydrodynamic processes in the formation of jets

The currently favoured mechanism for launching, accelerating and collimating bipolar outflows has a magnetohydrodynamic origin. A strong electromagnetic field, coupled with differential rotation in the inner regions of the binary system, serves to convert rotational kinetic energy into kinetic energy of the outflow. A magnetic pressure gradient (and maybe also the action of thermal and/or radiation pressure) is thought to lift the material out of the gravitational potential well, while the pinch effect collimates the outflow into a jet. In these conditions, the wind accelerates as it expands vertically away from the rotator. The jet is rather broad at the base, and it slowly focuses as it is accelerated, becoming a well collimated conical-to-cylindrical jet.

Matter from the companion star forms an accretion disk due to the conservation of the angular momentum that this matter transports. Energy is dissipated in the disk and the angular momentum is transported outwards, allowing the matter to approach the compact object. The density and temperature of the disk increase while accumulating closer to the compact object. The magnetic field in the inner regions, through magneto-centrifugal forces, can drive some disk matter away from the disk plane.

The fraction of matter that is finally directed towards the jet is unknown, but it could be a significant fraction of that present in the accretion disk. The accretion luminosity as a function of the distance r to the compact object can be expressed as

$$L_{\text{accr}} \approx \frac{GM_{\text{co}}\dot{m}}{r} = \frac{1}{2}\dot{m}V^2 \quad (3.1)$$

where G is the gravitational constant, V is the free fall speed of the infalling matter ($V = \sqrt{2GM_{\text{co}}/R_{\text{co}}}$), M_{co} is the compact object mass and R_{co} its radius. In the Bondi-Hoyle accretion scenario (Bondi 1952) there exists a maximum theoretical value for the accretion rate when considering spherical accretion onto a compact object. This limit comes from the balance of radiation pressure and gravity, and is usually referred as the Eddington limit:

$$\dot{m}_{\text{Edd}} = \frac{4\pi m_{\text{p}}cR_{\text{co}}}{\sigma_{\text{T}}} \quad (3.2)$$

where m_{p} is the proton mass and σ_{T} is the Compton cross section. The maximum

accretion luminosity will correspond to:

$$L_{\text{accr,Edd}} = \frac{4\pi GM_{\text{co}}m_{\text{p}}c}{\sigma_{\text{T}}} \quad (3.3)$$

Although accretion through a disk geometry could enhance the accretion rate as compared to the spherical case, this is nevertheless a good first-order approximation (we note that in the inner parts of the disk the flow is suspected to be disturbed and could become geometrically thicker).

A given fraction k of the matter accretion rate will go to the formation of the jet and counter-jet, and the rest will be advected by the compact object: $\dot{m}_{\text{accr}} = 2 \times \dot{m}_{\text{jet}} + \dot{m}_{\text{adv}}$. Assuming that the ejection process takes place at a certain distance r_{ej} from the compact object, the kinetic jet energy will be given by the sum of two contributions: the kinetic energy necessary to drive the jet out of the potential well, and that carried by the jet in the infinity. The jet total kinetic luminosity $L_{\text{k,jet}}$ can be expressed as a function of the jet bulk Lorentz factor $\Gamma_{\text{jet}} = [1 - (v_{\text{jet}}/c)^2]^{-1/2}$ in the infinity as:

$$L_{\text{k,jet}} = \frac{GM_{\text{co}}\dot{m}_{\text{jet}}}{r_{\text{ej}}} + (\Gamma_{\text{jet}} - 1)(\dot{m}_{\text{jet}}c^2) \quad (3.4)$$

The kinetic jet power is partially extracted from the accretion power, but other sources of energy can be behind the process of launching and accelerating it. The orbital motion of the infalling matter and the disk coronal magnetic field can provide the ingredients for this launching mechanisms and can operate in both NS and BH systems. In addition, rotational energy from the compact object can be extracted. BHs with similar mass and accretion rate can differ in their observed radio power by several orders of magnitude. Hence, the extraction of rotational energy could provide a third parameter that breaks the mass/accretion rate degeneracy and potentially can explain why some sources are radio loud whereas others are radio quiet (see, e.g., Meier 2001). Jet production mechanisms under different scenarios was first suggested in Blandford (1976) and Lovelace (1976), and has been applied to rotating black holes (BZ-mechanism, Blandford & Znajek (1977) and magnetized accretion disks (BP-mechanism, Blandford & Payne 1982).

Whatever it is the source of energy to launch the jet, one can assume as a first-order approach that a certain fraction of the maximum accretion kinetic energy, that is, $\sim L_{\text{accr,Edd}}$, is efficiently converted to jet kinetic energy. Equating this fraction to expression 3.4, the jet bulk Lorentz factor can be determined.

The phenomenological treatment derived above can be used in the modelization of both permanent jets as well as in transient ejections. The dynamical time scale for a BH can be estimated as $r_{\text{Sch}}/v_{\text{jet}}$. For stellar-mass BHs, this time is much shorter than the typical duration of jet ejection events. As a first order approximation, one could therefore consider these ejections as a continuous and steady formation process (Gliozzi et al. 1999).

3.2 Hadronic *vs* Leptonic jets

One of the most basic and still unsolved questions about the nature of jets is that of their composition. Are jets made from protons and electrons, or electron-positron pairs, or from a mixture of all of them? And still, which is the role of the magnetic field - and hence the energy outflowing in the form of a Poynting flux - and how does it determine the dynamics of the jet compared with matter?

Theoretical, observational as well as numerical simulation approaches have faced this question in different ways. The consensus is, nevertheless, far from being reached. The possibility to establish a unique framework capable to explain the properties of jets seems a rather difficult task. Population studies have been performed in order to extract averaged information on the consequences that different jet compositions should provide observationally (Ghisellini et al. 1992; Celotti & Fabian 1993). Alternatively, concrete source-by-source studies can become useful since in some cases the parameters defining the physical conditions where jets are embedded in are well known - and here the XRBs can play a vital role; see, for instance, Heinz (2006). Assuming that the same processes should operate at least in similar sources, some constraints can be derived on the origin of the particles transported in jets.

The questions about jet composition is nonetheless closely related to that of the formation of the jet itself. As pointed out in the last section, jets could be launched through a variety of mechanisms. Electromagnetically dominated outflows, such as those generated by the extraction of spin energy from the compact object, should become pair-dominated with low barionic content - a small amount could come from “pollution” from the accretion disk material (Blandford & Znajek 1977). Jets which are generated instead through hydromagnetic winds from the accretion disk will be made of baryonic plasma (Lovelace et al. 1999). Both mechanisms could be however at work simultaneously; a *two-flow* scenario have been considered, where the jet is composed of a beamed relativistic pair plasma surrounded by a mildly relativistic,

wind/disk accelerated electron-proton plasma (Sol et al. 1989). Another composite scenario is suggested in Sikora & Madejski (2000): initially proton-electron jets are later on pair-loaded through photon absorption processes at the base of the jet. X-rays produced in the accretion disk or corona are compton scattered to produce soft gamma-rays. These high energy photons are absorbed by coronal X-rays (the original ones, at about 100 keV) to produce pairs, which in turn will develop an electromagnetic cascade lasting until the forming jet becomes transparent to the coronal radiation.

Despite the complexity of the jet matter/energy content studies, there exist further physical insights which can be used to give some light into the problem. Importantly, they come from independent analysis, and therefore their conclusions can be fully applied to strength the parameter range found through other approaches. First of all, the interaction of jets with their environments is a useful tool to constrain the jet (averaged) power, provided the age of the source and the medium characteristics are known. The formation of radio-lobes and cocoons is directly related to the amount of injected energy, as will be seen in next Chapters. This approach does not directly measure the jet composition itself, but the energy content in the unknown $e^{+/-}$ -p plasma and the magnetic energy density.

Additionally, there exists the study of jet polarisation features. In particular, circular polarisation holds the promise of a unique insight into the conditions in the emitting plasma. It may be produced in a synchrotron process or via conversion of linear to circular polarization. The strength of this measurements is that they could permit a direct measurement of the composition of the radiating plasma (see, e. g., Wardle & Homan 1998; Kennett & Melrose 1998). Circular polarisation has been detected from at least three XRBs: SS 433 (Fender et al. 2000), GRS 1915+105 (Fender et al. 2002) and GRO J1655-40 (Macquart et al. 2002). However, the state of observations together with current polarisation models can not put yet strong quantitative constraints on the composition of the jets in these sources; new observations and more conclusive analysis methods are probably going to be developed in next future, and polarisation can become a key piece when trying to unveil the jet composition puzzle.

In this thesis we have assumed a jet that is cold-matter dominated by protons, whereas the non-thermal accelerated particles (both leptons and/or protons) represent only a relatively small fraction of the jet power - see, for instance, Bosch-Ramon et al. (2006). Our investigation has been based on the radiative constraints obtained in both hadronic and leptonic scenarios. We have focused on the magnetic field value and the number of electrons/positrons required to sustain the non-thermal emission

produced through different radiation processes. We have investigated the generation of secondary leptons in a hadronic scenario. We have also accounted for the leptonic contribution at higher energies for some well-known microquasars and compared it to the upper limits derived from dedicated observations with the MAGIC telescope. In one of these sources, the microquasar SS 433, both hadronic and leptonic models have been studied, since it remains the only source from which evidences of hadronic content has been directly detected (Kotani et al. 1998; Marshall et al. 2002).

3.3 Particle acceleration

Particle acceleration phenomenon is nowadays a matter of intense study, since it is involved in nearly all astrophysical scenarios where non-thermal emission plays a decisive role. Furthermore, it can provide by itself not only a precise insight into the microphysics of such systems, but also into the extreme environment conditions where the acceleration processes are taking place. There exists a number of concrete acceleration frameworks where particles emerge in a power-law distribution of the type $N(\gamma) = K_0 \times \gamma^{-p}$, ranging from a given Lorentz factor γ_{\min} up to γ_{\max} where the distribution is cut off. Such distributions are entirely consistent with the well-studied radiation mechanisms like synchrotron and Inverse Compton emission processes and the fluxes detected from jet sources. The details of each factor included in their expression are, however, framework-dependent, and can affect largely the interpretation of a given case in study.

There is a tight relation between the launching mechanisms and the energy carriers in the jet and the acceleration processes operating in there. In the following paragraphs, we will argue about the Fermi acceleration processes. This is the mechanism that we applied to compute the non-thermal distributions in different physical scenarios. Nonetheless, other acceleration mechanisms exist beyond the Fermi processes. Particle acceleration in shear flows can occur as a consequence of energetic particles encountering different local flow velocities as they are elastically scattered off small-scale magnetic field inhomogeneities that are contained in the moving background flow (Jopikii & Morfill 1990; Rieger & Duffy 2006). The "converter" mechanism, instead, operates via continuous conversion of accelerated particles from charged into neutral state and back. It is efficient for acceleration of both protons and electrons/positrons. Its acceleration time is somewhat larger at low energies, but could be able to compete with First order Fermi acceleration at higher energies (see, e.g., Derishev et al. 2003). Although these processes can be relevant in a specific scenario we did not use them in detail in our computations.

3.3.1 First order Fermi acceleration process

First order Fermi acceleration, also called diffusive shock acceleration, represents one of the most effective mechanisms and provides the required acceleration in microquasar jets. The energy gain $\delta E/E$ is first order in $\beta = v/c$ (v is the flow velocity and c the speed of light). Although it was originally applied to supernova shocks, it is generally applicable to strong shocks in other astrophysical contexts, and to microquasars in particular. Our discussion will be brief and omit a number of subtleties, outlining only those aspects which may become useful in next Chapters. For a detailed treatment, the reader is referred to the works of Blandford & Ostriker (1978), Berezhko & Krymskii (1988) and the extensive reviews by Drury (1983) and Jones & Ellison (1991), among a vast number of works devoted to it and its applications.

We assume a strong (non-relativistic) shock wave that propagates along the jet. The origin of this shock can come, for example, from different velocity ejected blobs, or the interaction of the jet material with the medium. Let the shock front separate the region where the material is still unaware of the shock, the upstream region, and the region already affected by the passage of the shock, the downstream region. The shock velocity propagation, as seen from the upstream region, will be denoted as V_S . The velocity of the shocked material in the same reference frame will be V_P . Moving to the shock reference frame, gas flows from upstream into the shock with a given speed $u_1 = V_S$ and density ρ_1 and flows out of the shock to the downstream region with a speed $u_2 = V_S - V_P$ and density ρ_2 . For a strong non-relativistic shock, the one we are interested in, the compression ratio is given by $R = \rho_1/\rho_2 = u_1/u_2 = (\gamma_{\text{ad}} + 1)/(\gamma_{\text{ad}} - 1)$, where γ_{ad} is the ratio of specific heats or adiabatic index of the medium. For an ionised medium, the gas will be monoatomic and hence $\gamma_{\text{ad}} = 5/3$, so a strong shock will have $R = 4$. Further details on the shock conditions are given in Sect. 5.4.

To derive the energy gain of a given particle crossing the shock, scattering centers are assumed to exist tied to the plasma on either side of the shock. Taking V_S to be non-relativistic, one can assume that the accelerated particles are isotropic in both upstream and downstream frames. The rate at which downstream particles cross the shock front to the upstream region and that of upstream to downstream crossings determines the energy gain rate. The amount of energy gained per particle can be expressed as (Protheroe 1999):

$$\frac{\delta E}{E} \simeq \frac{4}{3} \beta \simeq \frac{4}{3} \frac{V_P}{c} \simeq \frac{4}{3} \frac{R-1}{R} \frac{V_S}{c} \quad (3.5)$$

The energy spectrum obtained in first order Fermi acceleration is derived from the probability of a particle crossing the shock in a number of occasions, hence summing up the given amount δE each time. The flux of particles which are lost downstream is $\phi_{\text{loss}} = n_{\text{part}} V_S / R$, whereas that of particles going from upstream to downstream is $\phi_{\text{cross}} = n_{\text{part}} v_{\text{part}} / 4$. Here, v_{part} is the velocity with which particles are travelling against the shock front as seen from the upstream region (note that from the shock front reference frame, it would be $V_S + v_{\text{part}} \cos(\phi)$, where ϕ is the angle of the velocity to the normal to the shock surface). The probability of crossing the shock once and then escaping from the shock, being lost downstream, is the ratio of these two fluxes:

$$\mathcal{P}_{\text{escape}} = \frac{\phi_{\text{loss}}}{\phi_{\text{cross}}} \approx \frac{4V_S}{Rv_{\text{part}}} \quad (3.6)$$

The probability of returning to the shock after crossing from upstream to downstream is then $\mathcal{P}_{\text{return}} = 1 - \mathcal{P}_{\text{escape}}$, so the probability of returning to the shock a given number m of times will be given by $\mathcal{P}_{\text{cross} \geq m} = [1 - \mathcal{P}_{\text{escape}}]^m$, and the energy after m shock crossings will be

$$E = E_0 \left(1 + \frac{\delta E}{E} \right)^m. \quad (3.7)$$

Here E_0 is the initial particle energy; from the expressions above, the number of particles N with an energy greater than E must be $N(\geq E) \propto [1 - \mathcal{P}_{\text{escape}}]^m$ where now $m = \ln(E/E_0)/\ln(1 + \delta E/E)$. After some algebra, one can find out that the particle acceleration integral spectrum follows a power law:

$$N(\geq E) \propto E^{-(p-1)} \quad (3.8)$$

where $p \approx (R + 2)/(R - 1)$. The differential spectrum is hence

$$\frac{dN}{dE} \propto E^{-p} \quad (3.9)$$

For a strong shock with $R = 4$, one arrives at the well-known differential spectrum $\propto E^{-2}$.

Maximum energies that accelerated particles can reach will depend on the bal-

ance between the energy gain attained in the acceleration mechanism and losses in a particular environment due to, e.g, radiative and expansion losses. The rate at which particles gain energy in the first order Fermi process depends on the time the particles take to perform an entire cycle from the upstream region, crossing the shock to the downstream region and re-crossing back to the upstream region. This cycle time can be expressed as (see Protheroe 1999):

$$t_{\text{cycle}}(E) \approx \frac{4}{c} \left(\frac{k_1(E)}{u_1} + \frac{k_2(E)}{u_2} \right) \quad (3.10)$$

where $k_{1,2}(E)$ are the diffusion coefficients at each side of the shock. From this expression, the acceleration rate, defined as $r_{\text{accel}} \equiv \frac{1}{E} \frac{dE}{dt} \Big|_{\text{accel}}$, can be expressed as

$$r_{\text{accel}}(E) \approx \frac{(R-1)u_1}{3R} \left(\frac{k_1(E)}{u_1} + \frac{k_2(E)}{u_2} \right)^{-1} \quad (3.11)$$

The acceleration timescale, t_{accel} can be finally computed ($t_{\text{accel}} = 1/r_{\text{accel}}(E)$) for the given shock conditions when a prescription for the diffusion coefficient is provided. The extreme cases are quasi-parallel and quasi-perpendicular shock surface normal vectors with respect to the magnetic field direction. For quasi-parallel shocks and assuming $k_1 = k_2 = \eta k_{\text{Bohm}} = \eta (1/3) r_g c$, where $r_g = (\gamma m c^2)/(q_e B)$ is the particle gyroradius, q_e the electron charge and $\eta \geq 1$, the acceleration time is:

$$t_{\text{accel},\parallel} \approx \frac{20}{3} \frac{\eta E c}{q_e B_1 u_1^2} \quad (3.12)$$

For oblique shocks, instead, one can consider $k = k_{\parallel} \cos^2(\theta) + k_{\perp} \sin^2(\theta)$, being θ the inclination angle of the shock surface to the magnetic field direction. Using that $k_{\perp} \approx k_{\parallel}/(1 + \eta^2)$ for $\eta \lesssim 10$ (Jokipii 1987), the acceleration time for the extreme case where the shock is perpendicular ($\theta = \pi/2$) reads:

$$t_{\text{accel},\perp} \approx \frac{8}{3} \frac{E c}{\eta q_e B_1 u_1^2} \quad (3.13)$$

Although perpendicular shocks provide a much lower t_{accel} than parallel shocks, its efficiency is somewhat diminished if the particles to be accelerated have low initial velocities (Ellison et al. 1995).

Some remarks must be provided with respect to the applicability of the previous treatment to a microquasar scenario. First of all, we have considered a non-relativistic framework to derive the spectral shapes of particle distributions and the acceleration time-scales. Relativistic shocks, with $V_S \gtrsim 0.1c$ may take place in microquasars. Relativistic gases have adiabatic indices of $\gamma_{\text{ad}} = 4/3$, and hence are more compressible than their non-relativistic counterparts: they can generate compression ratios as large as $R = 7$. Power-law distributions are generated in relativistic shocks, although the expressions given above are no longer valid to derive its parameters, primarily because of isotropy assumption is not accomplished in that case. Relativistic shock fronts move sufficiently fast that even ultrarelativistic particles have difficulties in catching them. Hence escape from the shock is greater and particle isotropy is impossible to achieve. The effect is that the spectral index p of the particle distribution decreases with increasing the shock speed (see the work of Kirk & Schneider 1987 and Baring 1997 for a detailed study of relativistic shocks).

Furthermore, to undergo efficient acceleration through first-order Fermi processes, particles have to be already pre-accelerated in order to have enough energy to diffuse through the shock. The diffusion length of particles must be greater than the shock width, which for a magnetized plasma can be taken as a first order approach similar to the gyroradius of the particles that form the shock itself (Bosch-Ramon 2006). Roughly speaking, particles with energies lower than the shock particle energy will not be able to be efficiently accelerated, thus putting a constraint on the minimum Lorentz factor of accelerated particles. To solve this so called “injection problem” some proposed theoretical mechanisms could be at work (see, e.g., Rieger et al. 2007; Dieckmann et al. 2004). The problem is nevertheless very complex, and it is usually investigated through numerical simulations. We did not treat this “injection problem” in detail, and we have instead assumed that an unspecified mechanism provides the means by which particles have already the necessary minimum energy to undergo efficient acceleration.

Second-order Fermi acceleration

Some microquasars show non-thermal extended emission along the jet up to pc (and even higher) distances. The absence of observable knotty structures and the fact that they display the same spectra along large distances suggest that first order Fermi acceleration is not the only mechanism at work at least in some cases. Stochastic acceleration like second order Fermi acceleration is a viable mechanism in that situations.

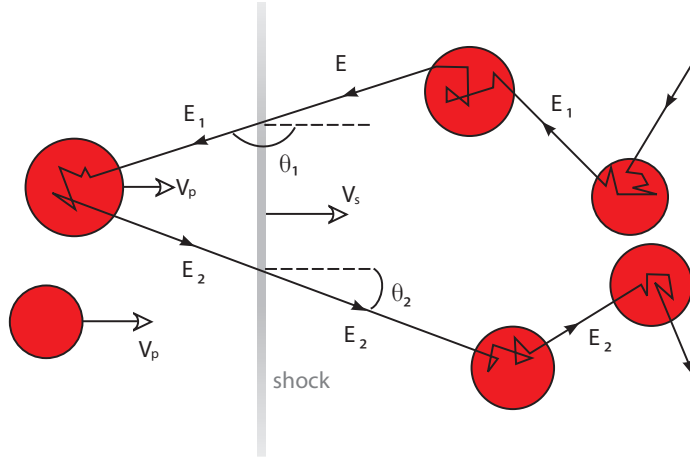


Figure 3.1: Sketch of the multiple scatterings transferring a given amount of energy to the particle that crosses the shock front during the Fermi acceleration process.

Assuming that the magnetic scattering centers show a non-negligible random velocity in the plasma, and without the necessity of a strong shock, energetic particles will experience both head-on and overtaking collisions. The rate of head-on collisions is higher than the overtaking ones, but to a lesser extent than in shock acceleration, $\propto (\vec{v} - \vec{u})/v$ (\vec{v} and \vec{u} are the particle and the inhomogeneities velocities, respectively). The average energy gain per collision is now second order in β , $\delta E/E \propto \beta^2 = (u/c)^2$. A power-law distribution is also expected but somewhat harder than in the first order case, $p < 2$. Since these are freshly accelerated particles, radiative or escape losses can make p to decrease, and $N \propto \gamma^{-p}$ to be steeper. This diffusive mechanism could therefore provide continuous acceleration along a slice of the jet. Maximum energies reachable will depend on the acceleration time-scale, that is lower by a factor $\sim u_s/V_A$ as compared to first order Fermi process; here $V_A = B/\sqrt{4\pi\rho}$ is the Alfvén velocity and ρ is the total mass density of the charged plasma.

3.4 Radiative processes

Proper understanding of astrophysics requires to know the processes which produce a given amount of radiation per unit time per unit area from a given direction (and also at a given degree of polarization). The mechanisms leading to such emission have to be accurately understood, and tested. In this section we will provide some expressions that are valid for a broad range of sources and conditions. Most non-thermal emitters, from radio to VHE gamma-rays, share them. The given conditions regarding the photon, matter and magnetic fields, as well as the particle

energy distribution, will decide in which range the radiation should be produced. Below, we will center on synchrotron, IC, relativistic Bremsstrahlung, p-p interactions and decay processes, as well as on photon absorption, since they offer the clues to understand the most energetic emission from microquasars can release. When specified, further assumptions or simplifications used later in Part I and II will be provided, although the specific values will be determined in each case of study.

3.4.1 Leptonic processes

Synchrotron emission

Synchrotron radiation in astrophysical applications may account for the non-thermal emission from radio up to hard X-ray - soft gamma-rays. It is a great undertaking to work out properly all the properties of this emission mechanism, and we will instead focus on the final expressions for those quantities directly related to the computations carried out in this thesis. The reader is referred to the books of Rybicki & Lightman (1979) and Pacholczyk (1970) for a complete treatment.

Consider an electron of velocity $v = \beta c$ and energy $E = \gamma m_e c^2$, where $\gamma = [1 - (\beta)^2]^{-1/2}$ is its Lorentz factor. The electron spirals around a magnetic field line defined by $\vec{\mathbf{B}}$, the electron velocity making a pitch angle φ with respect to the magnetic field direction. Lorentz forces will make it to gyrate at a gyrofrequency $\omega = eB/\gamma m_e c$ in a plane perpendicular to the magnetic field direction. This is the frequency of the variation of the the electromagnetic fields in the electron's rest frame. It would correspond to the helicoidal motion in a reference frame where the electron is instantaneously at rest or moving with a non-relativistic velocity.

Synchrotron emission is concentrated around a given characteristic frequency $\nu_{cr}(\gamma, B) = 4.22 \times 10^6 \gamma^2 B \sin(\varphi)$ (Pacholczyk 1970). Considering the acceleration of the electron in its helicoidal motion, the energy loss rate of an electron for the synchrotron process can be expressed as:

$$\left. \frac{dE}{dt} \right|_{\text{sync}} = -\frac{2}{3} r_0^2 \beta c \gamma^2 B^2 \sin^2 \varphi \quad (3.14)$$

where $r_0 = q_e^2/m_e c^2 = 2.82 \times 10^{-13}$ cm is the classical electron radius. The above expression can be put forward in the extreme relativistic case ($v \sim c$) for an isotropic distribution of velocities (that is, averaging over $\sin^2 \varphi$) as

$$\frac{dE}{dt} = -\frac{4}{3}\sigma_T c \gamma^2 u_B \quad (3.15)$$

where $\sigma_T = 8\pi r_0^2/3 = 6.65 \times 10^{-25}$ cm is the Thompson cross section and $u_B = B^2/8\pi$ is the magnetic field energy density.

The next step is to find out the spectral distribution of synchrotron radiation for a single electron. We closely follow the procedure of Pacholczyk (1970), which provide in detail the exact derivation, and merely quote the final results. The power per unit frequency per electron, already integrated over the electron solid angle element, is found to be:

$$p_\nu = \frac{\sqrt{3} q_e^3}{mc^2} B \sin \varphi F(x) \quad (3.16)$$

where $x = \nu/\nu_{cr}$, and $F(x)$ can be expressed as the integral of the Bessel functions of order 5/3:

$$F(x) = x \int_x^\infty K_{5/3}(z) dz \quad (3.17)$$

$F(x)$ has its maximum at $\nu \approx 0.29 \nu_{cr}$, and its asymptotic behaviour at low and high frequencies is $F(x) \propto x^{1/3}$ and $F(x) \propto x^{1/2} e^{-x}$, respectively. Note the strong suppression of emission at frequencies above $\sim \nu_{cr}$.

We will deal with non-thermal electron distributions that follow a power-law form of the type $N(E) = K E^{-p}$. The total emissivity will be hence given by the integration over the energy distribution:

$$j_\nu = \frac{\sqrt{3}}{4\pi} \frac{q_e^3}{mc^2} B \sin \varphi \int_{E_{min}}^{E_{max}} N(\gamma) F(x) d\gamma \quad (3.18)$$

The emissivity will have a dependency on the emitted frequency and magnetic field of the form $j_\nu \propto B^{(p+1)/2} \nu^{-\alpha}$, where $\alpha = (p-1)/2$.

To the synchrotron emission process corresponds a synchrotron self-absorption process that, taking a a randomly oriented magnetic field, is (Pacholczyk 1970):

$$k_\nu = -\frac{\sqrt{3}}{8\pi} \frac{q_e^3}{m} \frac{1}{\nu^2} B \sin \varphi \int_0^\infty E^2 \frac{d}{dE} \left(\frac{N(E)}{E^2} \right) F(x) dE \quad (3.19)$$

Now, considering the intensity of the total synchrotron emission of a given distribution of electrons from a certain slab with thickness s , the radiation transfer equation states

$$\frac{dI_\nu(s)}{ds} = j_\nu - k_\nu I_\nu(s). \quad (3.20)$$

The solution, using that $k_\nu ds = d\tau_\nu$ ($\tau_\nu = \int d\tau_\nu$ is the optical depth at a given frequency ν) is given by:

$$I_\nu(\tau_\nu) = \frac{j_\nu}{k_\nu} (1 - e^{-\tau_\nu}) \quad (3.21)$$

For an optically thin source, $\tau_\nu < 1$, the intensity will be $I_\nu \propto \nu^{-(p-1)/2}$ (i.e. the same behaviour as the emissivity) whereas for the optically thick case, $\tau_\nu > 1$, it will behave as $I_\nu \propto \nu^{5/2}$, typical of auto-absorbed sources.

Inverse Compton emission

When a given population of electrons is embedded in a photon field, there exist electrodynamic interactions between electrons and photons where energy is transferred from one particle to the other one. Direct Compton scattering occurs when the photon delivers a given amount of energy to the electron. On the contrary, when the electron has a higher momentum with respect to the photon (in the laboratory reference frame), it transfers part of its energy when scattering off the photon, and the process is called Inverse Compton - IC from now on.

In a general case, one should consider a given electron distribution with a differential number density given by $dn_e = n_e(\gamma, i_{\Omega_e}) d\gamma d\Omega_e$, that is, the number of electrons per unit volume per unit Lorentz factor moving along a direction defined by the unit vector i_{Ω_e} and the element of solid angle $d\Omega_e$. Besides, this electron population is surrounded by a photon field, which differential number density is $n_{ph}(\epsilon_0, i_{\Omega_{ph,0}}) d\epsilon_0 d\Omega_{ph,0}$. The goal is to obtain the distribution in outgoing energy ϵ_1 and solid angle $\Omega_{ph,1}$ of the scattered photons.

The solution for this problem in the completely general case is very complicated. However, a number of simplifications result in certain limiting cases that, in fact, correspond to conditions found in the scenarios we will be considering along this thesis. Firstly, we shall only consider the interactions of relativistic electrons ($\gamma \gg 1$). Secondly, two different regimes will be defined as a function of the energy of the incident photon ($\epsilon_0 mc^2$) with respect to the energy of the electron ($E = \gamma m_e c^2$). For $\epsilon_0 \gamma \ll 1$ we will be in the Thompson regime where the Compton cross section is roughly independent of the energy of the incoming photon. The opposite case, for $\epsilon_0 \gamma \gg 1$, corresponds to the extreme Klein-Nishina limit in which the Compton cross section is somewhat more complicated, since it depends on ϵ_0 , ϵ_1 and the electron energy, E . The main difference between the two scenarios consists in a reduction of the cross section in the Klein-Nishina regime with respect to the Thompson regime, a signature which is important when investigating the high and very-high energy regime.

A useful expression for the differential Compton cross section which is valid for both the Thompson and Klein-Nishina with the angular dependence already averaged can be found in Blumenthal & Gould (1970),

$$\frac{d\sigma_{IC}(\epsilon_0, \epsilon_1, \gamma)}{d\epsilon_1} = \frac{3\sigma_T}{4\epsilon_0\gamma^2} \left[2q \ln q + q + 1 - 2q^2 + \frac{(4\epsilon_0\gamma q)^2}{2(1 + 4\epsilon_0\gamma q)}(1 - q) \right]; \quad (3.22)$$

where

$$q = \epsilon_1 / [4\epsilon_0\gamma^2(1 - \epsilon_1/\gamma)] \quad (3.23)$$

This expression can be approximated for cases deep in the Thompson and KN as $\sigma_{IC} \approx c\sigma_T(1 - 2\epsilon_0\gamma)$ and $\sigma_{IC} \approx [(3c\sigma_T)/(8\epsilon_0\gamma)]\ln(4\epsilon_0\gamma)$, respectively (see Coppi & Blandford 1990).

Once the differential cross section is obtained, one can compute the emissivity of IC process of a given distribution of photons scattered by an electron distribution for arbitrary ϵ_0 and γ . When isotropic electron distributions are considered, one obtains:

$$j_{\epsilon_1} = mc^2 \int_{\gamma_{min}}^{\gamma_{max}} \int_{1/4\gamma^2 \leq q \leq 1} \epsilon_0 n_{ph}(\epsilon_0, i_{\Omega_{ph,0}}) n_e(\gamma, i_{\Omega_e}) \frac{d\sigma_{IC}(\epsilon_0, \epsilon_1, \gamma)}{d\epsilon_1} d\gamma d\epsilon_0 \quad (3.24)$$

where the double integral over the electron energy and the initial photon energy has to satisfy $1/4\gamma^2 \leq q \leq 1$.

The energy loses of an electron due to IC processes can be separately derived for the two regimes:

$$\frac{dE}{dt} \Big|_{\text{IC}} = \begin{cases} -\frac{4}{3} \sigma_T m c^3 \epsilon_0 n_{ph} \gamma^2 & \text{Thompson regime} \\ -\frac{3}{8} \sigma_T m c^3 \frac{n_{ph}}{\epsilon_0} \left[\ln \left(\frac{4\epsilon_0 E}{m_e c^2} \right) - 11/6 \right] & \text{Klein-Nishina regime} \end{cases}$$

One can see the similitude of the energy loses in the Thompson regime with that of the energy loses due to synchrotron emission (see Equation 3.14). As nicely pointed out in Blumenthal & Gould (1970), it is due to the fact that synchrotron process can be understood as electrons scattering off virtual magnetic photons of energy $h\omega$, so when a given virtual photon distribution is considered, with energy density given by $u_B = B^2/8\pi$, both expressions are equivalent.

Relativistic Bremsstrahlung

Radiation due to the acceleration of a charge in the Coulomb field of another charge produces Bremsstrahlung or free-free emission. For the purposes of this thesis, we are mainly interested in the electron-ion Bremsstrahlung where electrons are the primary radiators. Given that the ion is comparatively more massive, it is permissible to treat the electron as moving in a fixed Coulomb field of the ion. We will focus in relativistic Bremsstrahlung process, since we will consider non-thermal distribution of relativistic electrons accelerated in strong shocks produced in different regions along the jets of microquasars.

A comprehensive derivation of the relativistic Bremsstrahlung cross-section can be found in Bethe & Heitler (1934) (see also Blumenthal & Gould 1970). Here we simply quote the final expressions (see also Lang 1999). For a relativistic electron with energy E colliding against nuclei of charge Zq_e , the cross-section will depend on the degree of nuclei screening. In the two most extrem cases we have:

$$\frac{d\sigma(E_\gamma, \epsilon_1)}{d\epsilon_1} = \frac{4\alpha Z^2 q_e^4}{\epsilon_1 (mc^2)^3} \left[1 + \left(1 - \frac{E_\gamma}{E} \right)^2 - \frac{2}{3} \left(1 - \frac{E_\gamma}{E} \right) \right] \times$$

$$\times \begin{cases} \ln \left[\frac{2E(E-E_\gamma)}{m_e c^2} \right] - \frac{1}{2} & \text{bare nuclei} \\ \ln \left(\frac{191}{Z^{1/3}} \right) + \frac{1}{9} \left(1 - \frac{E_\gamma}{E} \right) & \text{screened nuclei} \end{cases}$$

where $\alpha \approx 1/137$ is the fine structure constant.

The energy loss rate by Bremsstrahlung for ultrarelativistic electrons can be expressed as (Longair 1992):

$$\left. \frac{dE}{dt} \right|_{\text{Brem}} = -4 \times 10^6 n_{\text{H}} Z^2 r_e^2 \alpha c \mathcal{G} E \quad (3.25)$$

where n_{H} is the number density of target hydrogen atoms and \mathcal{G} is the Gaunt factor which can take two different expressions depending on the nucleous screening level:

$$\mathcal{G} = \begin{cases} \ln(E/m_e c^2) + 0.36 & \text{bare nuclei} \\ \ln(183 Z^{-1/3}) + \frac{1}{18} & \text{screened nuclei} \end{cases}$$

The lifetime of electrons will correspond to $t_{\text{Brem}} = E/(dE/dt)$. It is interesting to note that this lifetime depends very weakly on the energy of the electron (through the factor $\ln E$). This implies that for a given power-law distribution of electrons, Bremsstrahlung processes will not change much the original electron spectrum (differently as it occurs, for instance, when synchrotron or IC losses dominate, changing the electron distribution from $N_e \propto E^{-p}$ to $N_e \propto E^{-p-1}$)

3.4.2 Hadronic processes

Gamma-rays from p-p interactions

The production of high and very high energy gamma-rays through hadronic interactions can provide direct information on the particle composition and the physical conditions actually present in the source under study. It has been suggested that gamma-rays from several astrophysical scenarios like AGNs, supernovae, GRBs and microquasar jets could be produced through this channel. In the following, we provide a brief resume on the processes which may be of interest when applied to microquasars.

Relativistic protons produce high and very high energy gamma-rays in inelastic collisions with target hadrons, provided for instance by the companion's wind or thermal protons in the jet. At high energies, this process leads to the production of neutral and charged pions with comparable probabilities. The spectral form of π -mesons is generally determined by a few leading particles which carry a significant fraction of the nucleon energy.

The conversion of the kinetic energy transported by the relativistic protons to gamma-ray emission is mainly provided by the decay of neutral π -mesons. For this process to occur, the kinetic proton energy has to be greater than a certain threshold value, $E_p \geq E_{\text{th}} = 2m_\pi c^2(1 + m_{\pi^0}/m_p) \approx 280$ MeV, being $m_{\pi^0} = 134.97$ MeV. After produced, neutral pions decay into two gamma-ray photons, in a timescale equal to that of π^0 lifetime, $\tau_{\pi^0} = 8.4 \times 10^{-17}$ s.

The decay of charged pions leads to the production of neutrinos with spectra similar to that of gamma-rays produced through π^0 decay. However, the decay timescale of charged mesons is larger than that of π^0 , $\tau_{\pi^\pm} = 2.6 \times 10^{-8}$ s. In such a “long” time, charged mesons could interact with nucleons or photons present in their surroundings, so their energy will degrade resulting in a significantly smaller fluxes of neutrinos compared to gamma-rays (see Kelner et al. 2006). The neutrino production in microquasars can become a clue since their detection would provide a unique signature of hadronic processes occurring in these sources (see, e.g., Levinson & Waxman 2001; Heinz & Sunyaev 2002).

The emissivity of gamma-rays for a broad energy distribution of protons require precise integrations over differential cross-sections obtained experimentally at particle accelerators. Nevertheless, a formalism approximation can be obtained with good accuracy over a broad gamma-ray energy range. The gamma-ray emissivity

$j_\gamma(E_\gamma)$ is defined through that of secondary pions $j_\pi(E_\pi)$ as

$$j_\gamma(E_\gamma) = \int_{E_{min}}^{\infty} \frac{j_\pi(E_\pi)}{\sqrt{E_\pi^2 - m_\pi^2 c^4}} \quad (3.26)$$

where $E_{min} = E_\gamma + m_\pi^2 c^4 / 4E_\gamma$. The pion emissivity $j_\pi(E_\pi)$ can be expressed, using the δ -function approximation for the cross-section, as:

$$\begin{aligned} j_\pi(E_\pi) &= cn_H \int \delta(E_\pi - k_\pi E_{kin}) \sigma(E_p) n_p(E_p) dE_p \\ &= \frac{cn_H}{k_\pi} \sigma_{pp} \left(m_p c^2 + \frac{E_\pi}{k_\pi} \right) n_p \left(m_p c^2 + \frac{E_\pi}{k_\pi} \right) \end{aligned} \quad (3.27)$$

where $n_p(E_p)$ is the energy distribution of relativistic protons and n_H that of the target nuclei, k_π is the mean fraction of the kinetic energy carried by protons ($E_{kin} = E_p - m_p c^2$) which for the energies of interest, in the GeV-TeV domain is $k_\pi \sim 0.17$, and $\sigma_{pp}(E_p)$ is the total cross section of inelastic p-p collisions (Kelner et al. 2006):

$$\sigma_{pp}(E_p) = (34.3 + 1.88L + 0.25L^2) \times \left[1 - \frac{122 \text{ GeV}}{E_p^4} \right]^2 \times 10^{-27} \text{ cm}^2 \quad (3.28)$$

being $L \equiv \ln(E_p/1\text{TeV})$.

With the expression for the total cross-section already obtained, the energy losses of relativistic protons colliding with the target ions of density n_H can be expressed as:

$$\frac{dE_p}{dt} = n_H \sigma_{pp} f c E_p \quad (3.29)$$

where $f \approx 0.5$ stands for the inelasticity coefficient and accounts for the fact that the relativistic proton loses on average about half of its energy per interaction. It is interesting to note that the characteristic cooling time of relativistic protons in these interactions, given by $t_{pp} = E_p / (dE_p/dt)$, is weakly dependent on the proton energy.

3.4.3 Gamma-ray absorption processes

Since a notable part of this thesis is devoted to the study of the high and very high energy radiation produced in microquasars, it seems reasonable to account also for the processes which could absorb the gamma-ray emission in these sources. The most relevant absorption mechanism in our context is that of photon-photon pair production, where the target photon fields can be produced in the companion star and in the accretion disk (and also in its envelope and in the corona).

The absorption of a gamma-ray of energy E interacting with photons of energy ϵ_0 must satisfy the energy constraints,

$$E\epsilon_0 \geq \frac{2m_e c^2}{(1 - e_\gamma e_\star)} \quad (3.30)$$

where e_γ and e_\star are unit vectors directed along the propagation of the gamma-ray and the target photon, respectively. The minimum threshold is then given for head-on collisions, and the opacity seen by gamma-rays of a given energy will strongly depend on its emission location with respect to the source of the photon field:

$$d\tau_{\gamma\gamma} = (1 - e_\gamma e_\star) n_{ph} \sigma_{\gamma\gamma} d\epsilon_0 dl. \quad (3.31)$$

Here n_{ph} is the density of the target photon field per unit energy per unit solid angle, dl is the differential path of the gamma-ray through the photon field and $\sigma_{\gamma\gamma}$ is the cross section for $\gamma\gamma \rightarrow e^+e^-$, given by (Gould & Schreder 1967):

$$\sigma_{\gamma\gamma}(E, \epsilon_0) = \frac{\pi r_0^2}{2} (1 - \xi^2) \times \left[2\xi(\xi^2 - 2) + (3 - \xi^4) \ln \left(\frac{1 + \xi}{1 - \xi} \right) \right] \quad (3.32)$$

being r_0 the classical electron radius and

$$\xi = \left[1 - \frac{2(m_e c^2)^2}{E\epsilon_0(1 - e_\gamma e_\star)} \right]^{1/2} \quad (3.33)$$

The total opacity for gamma-rays of energy E travelling along a path l due to the interaction with a target photon field n_{ph} will be therefore given by:

$$\tau(E) = \int_0^l \int_{\epsilon_0 \geq \frac{2m_e c^2}{E(1-\epsilon_\gamma \epsilon_\star)}} \sigma_{\gamma\gamma}(E, \epsilon_0) n_{\text{ph}} d\epsilon_0 dl \quad (3.34)$$

The flux from the emission region under study will be correspondingly absorbed by a factor $e^{-\tau(E)}$. This restricts the observation of gamma-rays from regions where the photon field is rarefied enough, $\tau \lesssim 1$

3.5 Strong shock hydrodynamic conditions

We consider here the shock conditions that govern the behaviour of the physical variables at each side of the shock front. We will concentrate on a strong shock, with a Mach number \mathcal{M} much greater than 1 and will derive the Rankine-Hugoniot conditions across the shock discontinuity: at the shock front boundary, matter, momentum, and energy fluxes are conserved (with velocities given in the rest frame of the shock). In general, the conservation equations which relate those variables are given by:

$$\rho_1 V_1 = \rho_2 V_2 \quad (3.35)$$

$$P_1 + \rho_1 V_1^2 = P_2 + \rho_2 V_2^2 \quad (3.36)$$

$$\rho_1 V_1 w_1 + \frac{1}{2} \rho_1 V_1^3 = \rho_2 V_2 w_2 + \frac{1}{2} \rho_2 V_2^3 \quad (3.37)$$

where w is the enthalpy ($w = E + PV$, being E the gas internal energy). For a perfect gas with an adiabatic index γ_{ad} given by the ratio of specific pressure to specific volume, $\gamma_{\text{ad}} = C_P/C_V = w/E$, $E = P/(\gamma - 1)\rho$ and then $w = \gamma P/(\gamma - 1)\rho$ so we can rewrite equation 3.37 as

$$\frac{\gamma}{\gamma - 1} V_1 P_1 + \frac{1}{2} \rho_1 V_1^3 = \frac{\gamma}{\gamma - 1} V_2 P_2 + \frac{1}{2} \rho_2 V_2^3 \quad (3.38)$$

Arranging terms and substituting equation 3.35, one finds

$$\frac{\rho_1 V_1^2}{\rho_2} = \frac{2\gamma(P_1\rho_2 - P_2\rho_1)}{(\gamma - 1)(\rho_1^2 - \rho_2^2)} \quad (3.39)$$

Similarly, from a rearrangement of 3.36 and substituting in 3.35, we get

$$\frac{\rho_1 V_1^2}{\rho_2} = \frac{P_2 - P_1}{\rho_2 - \rho_1} \quad (3.40)$$

an combining these two results,

$$2\gamma(P_1\rho_2 - P_2\rho_1) = (1 - \gamma)(P_2 - P_1)(\rho_1 + \rho_2) \quad (3.41)$$

which leads, for a strong shock ($P_2 \gg P_1$), to

$$\frac{\rho_2}{\rho_1} = \frac{(\gamma - 1)P_1 + (\gamma + 1)P_2}{(\gamma + 1)P_1 + (\gamma - 1)P_2} \approx \frac{\gamma + 1}{\gamma - 1} \quad (3.42)$$

The pressure ratio can be expressed for any shock with an associated Mach number $\mathcal{M} = v/v_s$ where v_s the velocity of sound in the plasma, $v_s = (\gamma P/\rho)^{1/2}$, as

$$\frac{P_2}{P_1} = 1 - \gamma\mathcal{M}^2\left(\frac{\rho_1}{\rho_2} - 1\right) \quad (3.43)$$

for a strong and supersonic shock ($\mathcal{M} \gg 1$) the pressure ratio at both sides of the shock surface is

$$\frac{P_1}{P_2} \approx \frac{2\gamma\mathcal{M}^2}{\gamma + 1} \quad (3.44)$$

Strong shocks could be produced in a microquasar scenario in different regions along the jet axis. The powerfull and collimated outflow will interact with previously ejected material travelling at lower velocities. Furthermore, when the mass of the accumulated ISM material in front of the jet roughly equals that of the jet, a transfer of momentum will make the outflow to decelerate and strong shocks to be formed both forward into the ISM and inwards into the ejected material. Particle acceleration is thought to be at work at the shock surface (Sect. 3.3), and non-thermal high energy emission can be produced assuming that magnetic or photon fields dense

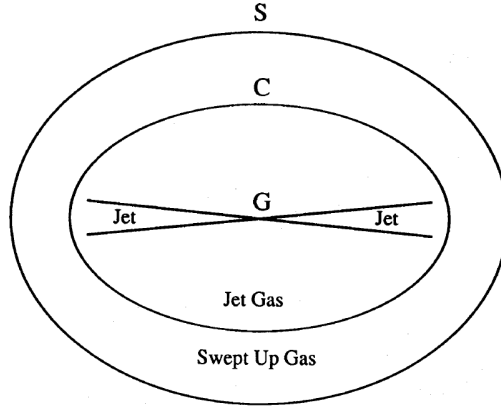


Figure 3.2: A sketch of the surface S bounding the medium shocked material and the discontinuity surface C separating it from the jet material.

enough are present in the region. We will make use of the shock conditions in next chapters when required to account for the hydrodynamic variables. The magnetic field value will be taken as a given fraction of the energy density at each side of the shock. In Chapter 5 we will also show numerical simulations of jet strong shocks developing in the surrounding medium.

3.6 Self-Similar treatment of jet interactions

Jets present in microquasars, radio-loud galaxies and AGNs generally propagate for distances which are large when compared to the scale on which they are generated. The structures formed in the interaction of large-scale jets with the medium show similar patterns despite the different conditions found in each source (for instance the jet power, the medium density or the source age). It seems then natural to look for similarity solutions to describe these large-scale structures and their evolution.

Without entering in the details of the jet formation process (see Sect. 3.1), we assume two symmetric conical and supersonic jets emerging from the central engine with a given jet power Q_{jet} , mass flux \dot{M}_{jet} and opening angle Ψ_{jet} . The ambient gas mass density is chosen to have a spherically symmetric distribution centered on the source as a first-order approximation. It is parameterized as a power-law, $\rho_{\text{medium}}(R) = \rho_0 R^{-\alpha}$, where ρ_0 is a constant, R is the distance from the source and α is the index which determines the density radial decay. From these parameters, one can form a characteristic length:

$$l_0 = \left(\frac{\rho_0 Q_{\text{jet}}^{1/2}}{\dot{M}_{\text{jet}}^{3/2}} \right)^{\frac{1}{\alpha-2}} \quad (3.45)$$

For the particular case in which $\alpha = 0$, the external mass density is uniform (this will be the case studied in Chapter 5), and l_0 becomes

$$l_0 = \frac{\dot{M}_{\text{jet}}^{3/4}}{Q_{\text{jet}}^{1/4} \rho_0^{1/2}}. \quad (3.46)$$

Assuming some typical values for the variables involved in this expression (in our case, $Q_{\text{jet}} \sim 10^{37} \text{ erg s}^{-1}$, $\dot{M}_{\text{jet}} = Q_{\text{jet}}/c^2$, $\rho_0 \sim m_p \text{ cm}^{-3}$), one finds $l_0 \sim 5 \times 10^{14} \text{ cm}$. This length-scale is much smaller than the large-scale jet distances found in some sources, which can reach values of $l_{\text{jet}} \sim 10^{20} \text{ cm}$.

Once the jet has become much larger than l_0 , the swept up ambient material dominates the mass involved in the motion, and the flow of this gas ought not to depend on the jet mass flux \dot{M}_{jet} . The situation is sketched in Fig. 3.2 where the surface S is the shock bounding the shocked material and C is the discontinuity surface separating the shocked medium material to the gas from the jet. The shape of the surfaces S and C can be generically expressed as

$$S(r, z, t, Q_{\text{jet}}, \dot{M}_{\text{jet}}, \Psi, \gamma_{\text{ad}}) = 0$$

$$C(r, z, t, Q_{\text{jet}}, \dot{M}_{\text{jet}}, \Psi, \gamma_{\text{ad}}) = 0$$

where r and z are cylindrical coordinates with z being directed along the jet axis. Once the jet becomes larger than l_0 dimensional arguments imply their shapes to follow $S(\xi, \eta, \rho_0, \Psi, \gamma_{\text{ad}}) = 0$ and $C(\xi, \eta, \rho_0, \Psi, \gamma_{\text{ad}}) = 0$, where the similarity variables are defined as

$$\xi = r \left(\frac{\rho_0}{Q_{\text{jet}} t^3} \right)^{1/5} \quad (3.47)$$

and

$$\eta = z \left(\frac{\rho_0}{Q_{\text{jet}} t^3} \right)^{1/5} \quad (3.48)$$

The shocked material region will vary on time as $t^{3/5}$, and this dependence will be the same in both r and z directions. In this way, the self-similar parameter \mathcal{R} used later in Chapter 5, which denotes the length-to-wide ratio of the interaction structures, will be constant regardless the precise value of the source age, medium density and jet power.

Bibliography

- Baring, M. G. 1997, in *Very High Energy Phenomena in the Universe*, ed. Y. Giraud-Heraud & J. Tran Thanh Vanastro. Paris: Editions Frontieres
- Berezhko, E. G., & Krymskii, G. F. 1988, *Soviet Phys. Usp.*, 31, 27
- Bethe, H. A. & Heitler, W. 1934, *Proc. Roy. Soc. London*, 146, 83
- Blandford 1976, *MNRAS*, 176, 465
- Blandford, R. D., & Znajek, R. L. 1977, *MNRAS*, 179, 433
- Blandford, R. D., & Königl, A. 1979, *ApJ*, 232, 34
- Blandford, R. D., & Ostriker, J. P. 1978, *ApJ*, 221, L29
- Blandford, R. D., & Payne 1982, *MNRAS*, 199, 883
- Blumenthal & Gould 1970, *Rev. Mod. Ph.*, 42, 237
- Bondi, H. 1952, *MNRAS*, 112, 195
- Bosch-Ramon, V., Romero, G. E., & Paredes, J. M. 2006, *A&A*, 447, 263
- Bosch-Ramon, V. 2006, Ph.D. Thesis, Universitat de Barcelona
- Celotti A, & Fabian AC. 1993, *MNRAS*, 264, 228
- Coppi, P. S., & Blandford, R. D. 1990, *MNRAS*, 245, 453
- Derishev E. V., Aharonian F. A., Kocharovskiy V. V., & Kocharovskiy, V. V., 2003, *Phys Rev D*, 68, 043003
- Dieckmann, M.E., Eliasson, B., & Shukla, P.K. 2004, *ApJ*, 617, 1361
- Drury, L. O. 1983, *Reports of Progress in Physics*, 46, 973
- Ellison, D. C., Baring, M. G., & Jones, F. C. 1995, *ApJ*, 453, 873
- Fender, R., Rayner, D., Norris, R., Sault, R. J., & Pooley, G. 2000, *ApJ*, 530, L29
- Fender, R. P., Rayner, D., McCormick, D. G., et al. 2002, *MNRAS*, 336, 39

- Fender, R. 2002, in *Relativistic outflows in Astrophysics*, ed. A.W. Guthmann, M. Georganopoulos, A. Marcowith, & K. Manolakou, Lecture Notes in Physics, 589, 101
- Ghisellini, G., Celotti, A., George, I. M., & Fabian, A. C. 1992, MNRAS, 258, 776
- Gliozzi, M., Bodo, G., & Ghisellini, G. 1999, MNRAS, 303, 37
- Gould, R. J., & Schröder, G. P. 1967, Phys. Rev., 155, 1408
- Heinz S., & Sunyaev R., 2002, A&A, 390, 751
- Heinz, S. 2006, ApJ, 636, 316
- Hjellming, R. M., & Johnston, K. J. 1988, ApJ, 328, 600
- Jones, F. C., & Ellison, D. C. 1991, Space Sci. Rev., 58, 259
- Jokipii J. R. 1987, ApJ, 313, 842
- Jokipii, J. R., & Morfill, G.E. 1990, ApJ, 356, 255
- Kelner, S. R., Aharonian, F. A., & Bugayov, V. V., 2006, Phys. Rev. D, 74, 034018
- Kennett, M., & Melrose, D. 1998, Publ. Astron. Soc. Austr., 15, 211
- Kirk, J. G., & Schneider, P. 1987, ApJ, 315, 425
- Kotani, T., Kawai, N., Matsuoka, M., & Brinkmann, W. 1998, in *The Hot Universe*, IAU Symp., 188, 358
- Lang, K. R. 1999, in *Astrophysical formulae*, New York : Springer
- Levinson, A., & Waxman E. 2001, Phys. Rev. Lett., 87, 171101
- Longair, M. S. 1992, in *High energy astrophysics. Vol.1: Particles, photons and their detection*, Cambridge, UK: Cambridge University Press
- Lovelace, R. V. E 1976, Nature, 262, 649
- Lovelace, R. V. E., Romanova, M. M., & Bisnovatyi-Kogan, G. S. 1999, ApJ, 514, 368
- Macquart, J.-P., Wu, K., Sault, R. J., & Hannikainen, D. C. 2002, A&A, 396, 615
- Malzac, J., Merloni, A., & Fabian, A. C. 2004, MNRAS, 351, 253
- Marshall, H. L., Canizares, C. R., & Schulz, N. S. 2002, ApJ, 564, 941
- Migliari, S., & Fender, R. P. 2006, MNRAS, 366, 79
- Meier, D. L. 2001, ApJ, 548, L9
- Pacholczyk, A., G. 1970, in *Radio astrophysics. Nonthermal processes in galactic and extragalactic sources*, San Francisco: Freeman

- Protheroe, R. J. 1999, in *Topics in Cosmic-Ray Astrophysics; Horizons in World Physics*, Ed: Michael A. DuVernois. Nova Science Publishers, Inc., Commack, New York
- Rieger F. M., & Duffy P., 2006, ApJ, 652, 1044
- Rieger F., Bosch-Ramon V., & Duffy P., 2007, Ap&SS, 309, 119
- Rybicki, G. B. & Lightman, A. P. 1979, in *Radiative processes in astrophysics*, New York, Wiley-Interscience
- Sikora, M., & Madejski, G. 2002, ApJ, 534, 109
- Sol, H., Pelletier, G., & Asseo, E. 1989, MNRAS, 237, 411
- Wardle, J. F. C., Homan, D. C., Ojha, R., & Roberts, D. H. 1998, Nature, 395, 457
- Wardle J. F. C., & Homan D. C. 2001, in *Particles and fields in Radio Galaxies*, ASP, 250, 152, R.A. Laing and K.M. Blundell

Part I

Interaction of microquasar jets with the medium

Chapter 4

Jet interaction with the companion star wind and radiation field

We consider a microquasar scenario where a given fraction of the protons populating the jets are accelerated to relativistic energies. We concentrate on the radiative consequences from the interactions of these protons against target ions from the companion's wind, which give place to the generation of neutral π^0 and charged pions π^\pm . Neutral pions are unstable and decay producing gamma-ray photons, while charged pions will lead to the generation of muons and muonic neutrinos. These muons will in turn decay to produce electrons/positrons and a new release of electronic and muonic neutrinos. We do not consider the primary leptonic population that could be accelerated in the jets, for which the reader is referred to other works (see, e.g., Georganopoulos et al. 2002, Bosch-Ramon et al. 2006a, Paredes et al. 2006, Dermer & Böttcher 2006, Gupta et al. 2006).

Observational evidences of the acceleration of relativistic hadrons in microquasar jets would come for instance from the detection of neutrinos produced in p-p interactions (see, for instance, Aharonian et al. 2006). Further clues can be searched in the high-energy cut-off of the photon spectrum, which in general occur in hadronic scenarios at higher energies than in leptonic models since proton energy losses are lower than those affecting electrons/positrons (see, for instance, Orellana & Romero 2007). In our study of the baryonic content of microquasar jets through their interaction with the companion's wind, we have centered our attention on the radiation signatures imprinted by the secondary leptons that come across in p-p interactions.

Relativistic leptons are injected along the jet by the π^\pm decay while taking a substantial fraction of the initial energy of relativistic protons. These secondaries are expected to be confined in the jet by the magnetic field and exposed to adiabatic and radiative energy losses of the same kind as in primary leptonic models. In addition, the strong absorption of very high-energy gamma-rays produced in the decay of π^0 due to the companion's photon field could inject e^\pm pairs in the photosphere of the system. These fresh electrons will interact again with stellar photon fields through IC if the ambient magnetic field is low enough, giving place to emission of gamma-rays of energies slightly below those of the original photons produced in π^0 -decays.

In the next section we outline the microquasar hadronic model. We then compute the secondary populations injected in the jet through hadronic interactions against the companion's wind for the assumed parameters. In Sect. 4.2 we briefly resume the primary gamma-ray emission produced through π^0 -decay as well as the cascade reprocessing effects. We then focus on the contribution of the secondary leptons in the jets to recover some features which could distinguish this emission from that of primary leptonic models.

4.1 Model description

We consider a high-mass microquasar composed by a BH and a bright companion star, orbiting one around each other. An accretion disk is formed around the compact object, which is fed by the companion's spherical wind. We have assumed a circular orbit for the system, and the mass accretion rate is therefore taken constant along the orbit. Some of the accreted matter and energy is redirected into the outflowing jets, relating in this way the total power of the jets with the total accretion energy budget (see Sect. 3.1). For simplicity, the jets are considered perpendicular to the orbital plane. These jets move away from the injection point at distance z_0 above and below the orbital plane and expand laterally as a cone with a jet semi-opening angle $\psi \sim 5^\circ$. They propagate with a mildly relativistic velocity characterized by a bulk Lorentz factor $\Gamma = 1.5$. Figure 4.1 shows a sketch of the scenario.

We further assume that the jet is continuous, as observed in the stable configuration of a microquasar in a LH X-ray state (see Sect. 2.4; see also Fender et al. 2004). We do not enter in details about the jet launching mechanism, but magnetohydrodynamical processes are thought to be behind the initial ejection and

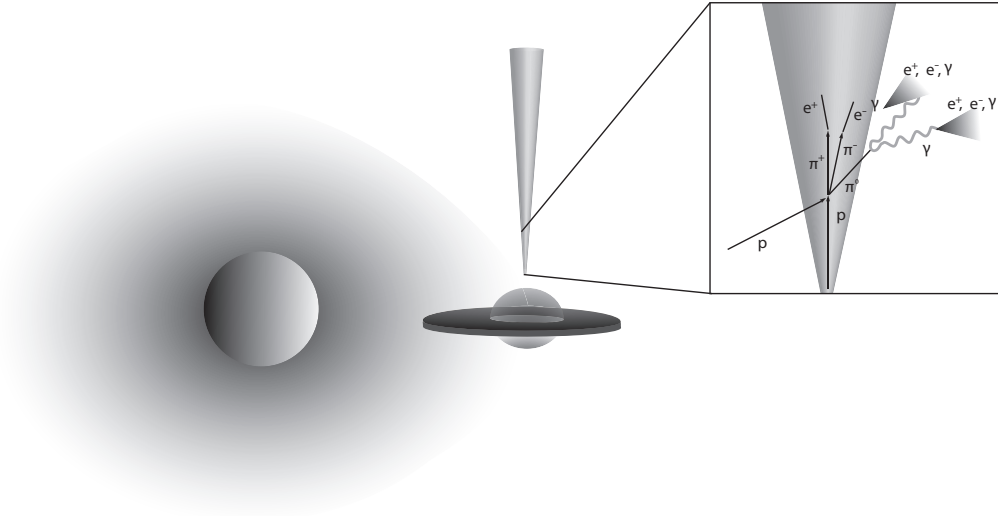


Figure 4.1: *Sketch (not to scale) of the interactions produced between the companion star wind ions and the jet relativistic protons. Secondary leptons are generated after π^\pm -decay. In addition, gamma-rays produced through π^0 -decay can escape the jet volume (here only one jet is displayed) and generate a cascade process when they impact against the photon field that fills the binary system.*

acceleration of jets. The kinetic power of relativistic protons in each jet, Q_p^{rel} , is taken as a constant fraction (q_{rel}) of the Eddington luminosity of the compact object ($L_{\text{Edd}} = 4\pi GM_{\text{BH}}m_p c / \sigma_T$, where M_{BH} is the black hole mass and σ_T is the Thompson cross-section). In this phenomenological approach, q_{rel} is a free parameter to adjust, and may be constrained by observations or upper limits to the source fluxes at a given energy band. Here we have considered two values for q_{rel} , labeled as Model A for $q_{\text{rel}} = 0.005$, i.e. $Q_p^{\text{rel}} = 0.005 \times L_{\text{Edd}} = 6 \times 10^{36} \text{ erg s}^{-1}$, and Model B for $q_{\text{rel}} = 0.0005$, i.e. $Q_p^{\text{rel}} = 0.0005 \times L_{\text{Edd}} = 6 \times 10^{35} \text{ erg s}^{-1}$. As we will see later, similar jet power are obtained through the inspection of their impact on the medium. In fact, jet power in the range between $10^{35} \text{ erg s}^{-1}$ and $10^{37} \text{ erg s}^{-1}$ are often inferred in a microquasar scenario, e.g. in Cyg X-1 (Gallo et al. 2005) and Cyg X-3 (Marti et al. 2005).

The parameter values adopted in the model are listed in Table 8.5. They correspond to those inferred for a high-mass microquasar like Cyg X-1, formed by an O9.7 Iab super-giant and a compact object of $10 M_\odot$. The inclination of the orbital plane is taken to be $i = 30^\circ$. Although the orbit is circular, its orientation induces periodic changes in the optical depth for photons produced close to the compact object. In order to obtain the gamma-ray absorption effects dependent on the orbital phase, we take $\phi = 0$ at the superior conjunction of the compact object, when the compact object is behind the primary (see Szotek & Zdziarski 2006; Bednarek & Giovannelli 2007).

Table 4.1: *Parameter values used in the model. The primes indicate quantities measured in the jet co-moving frame. The values are chosen to be similar to those for a system like Cyg X-1.*

<i>Parameter</i>	<i>Symbol</i>	<i>Value</i>
Eccentricity	e	0
Orbital semi-major axis [R_*]	a	3
Orbital inclination [$^\circ$]	i	30
Stellar mass [M_\odot]	M_*	30
Stellar mass loss rate [$M_\odot \text{ yr}^{-1}$]	\dot{M}_*	3×10^{-6}
Terminal velocity of the wind [cm s^{-1}]	v_∞	2×10^8
Compact object mass [M_\odot]	M_{BH}	10
Jet base radius [R_{Sch}^\dagger]	R_0	5
Jet initial point [R_{Sch}]	z_0	50
Jet semi-opening angle	ψ	5°
Proton power-law index	α	2
Proton minimum Lorentz factor	γ_p^{min}	2
Proton maximum Lorentz factor	γ_p^{max}	10^5
Bulk Lorentz factor	Γ	1.5
Stellar radius [R_\odot]	R_*	15
Stellar bolometric luminosity [erg s^{-1}]	L_*	6×10^{38}
Stellar surface temperature [K]	T_*	3×10^4
Wind-jet penetration factor	f_p	0.3

$^\dagger R_{\text{Sch}} = 2GM_{\text{BH}}/c^2$

A randomly oriented magnetic field is assumed to be contained in the jet, likely related to its magnetohydrodynamical origin. Due to adiabatic expansion of the jet, the magnetic field follows $B_{\text{jet}} = B_0(z_0/z)$, where $z_0 = 50 R_{\text{Sch}}$. At the base of the jet we constrain the value of the magnetic field by assuming a given fraction of its equipartition value, that is, $B_{0,eq} \sim \sqrt{8\pi u_p^{\text{rel}}}$, with the energy density of relativistic protons $u_p^{\text{rel}} = Q_p^{\text{rel}}/(\pi R_0^2 c)$. Here, R_0 is the radius of the jet at z_0 . An equipartition fraction of 10 % of the energy density of the relativistic protons is used to compute the jet secondary synchrotron emission.

4.1.1 Production of secondary leptons

Secondary leptons are generated in p-p interactions of hot protons in the jet with the companion star wind, which is expelled isotropically from the star, producing charged and neutral pions through the reaction channel $p + p \rightarrow p + p + \xi_{\pi^0} \pi^0 + \xi_{\pi^\pm} (\pi^+ + \pi^-)$, where $\xi_{\pi^\pm} \sim 2(E_p/\text{GeV})^{1/4}$ is the charged pion multiplicity. When charged and neutral pions are created, the first will decay to muons and subsequently to electrons and positrons, while the second decays into two gamma-ray photons,

$$\pi^+ \rightarrow \nu_\mu + \mu^+ \rightarrow \nu_\mu + e^+ + \nu_e + \bar{\nu}_\mu \quad (4.1)$$

$$\pi^- \rightarrow \bar{\nu}_\mu + \mu^- \rightarrow \bar{\nu}_\mu + e^- + \bar{\nu}_e + \nu_\mu \quad (4.2)$$

$$\pi^0 \rightarrow 2\gamma \quad (4.3)$$

We assume that the target wind ions are capable to penetrate the jet volume laterally. A penetration factor of 0.3 is used to account for the mixing between the jet and the wind material in a phenomenological way (see Romero et al. 2003; Romero et al. 2005). We take the radial dependence of the wind particle velocity as $v(r) = v_\infty(1 - R_*/r)$ (Lamers & Cassinelli 1999), where $v_\infty \approx 2 \times 10^8 \text{ cm s}^{-1}$ is the wind terminal velocity. The particle density is obtained from the continuity equation. Taking the jet along the z axis it yields:

$$n_{\text{H}}(z) = \frac{\dot{M}_\star}{4\pi m_p v_\infty (z^2 + a^2)} \left(1 - \frac{R_\star}{\sqrt{z^2 + a^2}}\right)^{-1}. \quad (4.4)$$

The region where pions are effectively produced has a size of about that of the binary system, since farther away the wind dilutes and the number of interactions

decreases rapidly.

The spectrum of relativistic protons is assumed to be a power law in the jet reference frame, $N_p(E_p) = K_0 E^{-p}$, where K_0 is a normalization constant related to the total energy injected in relativistic protons in the jet. The spectral index is $p = 2$, resulting from e.g. shock diffusive acceleration processes. The proton flux flowing in the jet will be given by $J_p(E_p) = (c/4\pi)N_p(E_p)$. Due to the conical geometry assumed for the jet and the conservation of the number of protons that traverse the jet cross section at any height z , this flux can be related to that at the injection point, $J_p(E_p, z) = J_{p,z_0}(z_0/z)^2 = (c/4\pi)K_0^{-p}(z_0/z)^2 E^{-p}$.

The maximum value for the proton energy, E_p^{\max} , is obtained by balancing the acceleration rate with the rate of energy loss by synchrotron, p-p and p- γ interactions and the energy constraints imposed by the equality between the maximum particle gyroradius and the size of the accelerator, the latter taken as 0.1 times the jet radius at each height, $R_{\text{jet}}(z) = z \tan \psi$. This last constraint is the most restrictive under the assumed parameter set of values, and leads to $E_p^{\max} = 0.1eB_0R_0 \sim 100$ TeV. We note that E_p^{\max} is constant along the jet since $B(z) \propto R_{\text{jet}}^{-1}(z)$. This value is used to impose an exponential cut-off on the above proton-flux. This maximum energy may decrease at distances where the jet decelerates, but this will occur far away from the regions we are interested with.

The expressions given by Kelner et al. (2006) are used to compute the leptonic energy distribution of e^\pm injected along the jet by π^\pm -decay. The resulting injection rate (leptons per energy, volume, and time units) can be expressed in terms of the variable $x = E_{e^\pm}/E_p$ as

$$q_e(E_e, z) = c n_H(z) \int_0^1 \sigma_{\text{inel}}(E_e/x) J_p(E_e/x, z) F_e(x, E_e/x) \frac{dx}{x}. \quad (4.5)$$

Here, $F_e(x, E_e/x)$ is the spectrum of electrons from the $\pi \rightarrow \mu \nu_\mu$ decay, and it is described by

$$F_e(x, E_p) = C_1(E_p) \frac{[1 + C_3(E_p)(\ln x)^2]^3}{x + 0.3x^{[1-C_2(E_p)]}} [-\ln(x)]^5, \quad (4.6)$$

where

$$C_1(E_p) = \frac{1}{69.5 + 2.65 L + 0.3 L^2}, \quad (4.7)$$

$$C_2(E_p) = \frac{1}{(0.201 + 0.062 L + 0.00042 L^2)^{1/4}}, \quad (4.8)$$

$$C_3(E_p) = \frac{0.279 + 0.141 L + 0.0172 L^2}{0.3 + (2.3 + L)^2}. \quad (4.9)$$

Here $L = \ln(E_p/1 \text{ TeV})$ and the inelastic cross-section of p-p interaction is $\sigma_{\text{inel}}(E_p) = (34.3 + 1.88 L + 0.25 L^2) \text{ mb}$ (Kelner et al. 2006).

For the considered proton flux, we obtain $q_e(E_e, z_0) \sim 3 \times 10^{27} (E_e/\text{eV})^{-1.92}$ leptons $\text{erg}^{-1} \text{ s}^{-1} \text{ cm}^{-3}$, at the base of the jet, in the observer's reference frame for Model B and an order of magnitude higher for Model A. Once produced, we assume that the linear momentum of the leptons loses any possible angular dependence, erased by the random nature of the magnetic field, and treat the population as isotropic in the jet reference frame.

The evolution of the particle energy distribution is studied by dividing the jet into slices of suitable size in order to consider the physical conditions as homogeneous within each of them. The leptons injected along the jet suffer from radiative cooling due to synchrotron and IC processes (see Sect. 3.4). The companion star's photon field energy density used to calculate IC losses is $u_{\text{star}} = L_*/(4\pi d^2(z)c)$ where $d(z)$ is the distance from the star and in our case $L_* = 6 \times 10^{38} \text{ erg s}^{-1}$. We have accounted also for adiabatic expansion losses:

$$\left. \frac{dE_{e\pm}}{dt} \right|_{\text{exp}} = -\frac{2}{3} \frac{V_{\text{exp}}}{R(z)} E_{e\pm}. \quad (4.10)$$

where $V_{\text{exp}} = dR_{\text{jet}}(z)/dt$ is the lateral expansion velocity of the jet. Fresh electrons and positrons that have been injected at a certain point into the jet suffer the different energy losses modifying in this way their spectral distribution. Moreover, different evolution stages sum at each height. The injection of fresh particles occurs all along the jet and a mix of multiple evolved populations arises. To compute it in a consistent way, we have considered the continuity equation

$$N_e(E_e, z) dE_e = N_{0,e}(E_{0,e}, z_0) dE_{0,e} \quad (4.11)$$

where $N_{0,e}(E_{0,e}, z_0) = K_{0,e}E_{0,e}^{-P}$ is the initial energy spectrum for the injected particle density. Solving the equations for the evolution of the particle energy along the jet axis (see, e.g., Bordas et al. 2007), one can find the spectral distribution at each slice, compute the differential luminosity at each height and finally integrate to find the total luminosity.

4.2 Model Results

In our framework both high-energy emission from primary hadrons and lower-energy radiation from secondary particles is expected. Below we shortly describe the emission resulting from the cascade reprocessing of gamma-rays produced in π^0 -decays interacting with the companion's photon field. The details of these computations can be found in Orellana et al. (2007). Regarding secondary emission, we focus on the jet confined emission. A detailed treatment for the non-thermal radiation from secondaries outside the jet can be found in Bosch-Ramon et al. (2008)

4.2.1 Primary gamma-ray emission

The γ -ray spectra produced in cascades traversing the anisotropic stellar radiation field have been computed (see Orellana et al. 2007). The companion field has been treated as a black-body spectrum, characterized by $T_{\text{eff}} \sim 30000$ K and $R_{\star} = 15R_{\odot} \sim 10^{12}$ cm. The contribution from other radiative fields, like that of the accretion disk, are less important in the present context. The cascade begins when energetic e^{\pm} pairs are materialized by photon-photon interactions. These leptons, in turn, boost the stellar photons to high-energies via IC scattering. The γ -ray absorption and production mechanisms can proceed very fast, resulting in the development of an electromagnetic cascade (see Bednarek 1997; Aharonian et al. 2006). As a result, the energy of the original photons is distributed between a certain number of secondary particles and photons with lower energy.

A detailed description of the Monte Carlo code used for the cascade process is given in Orellana et al. (2006) (see also Orellana et al. 2007). For simplicity, any effects of the presence of a magnetic field are disregarded in these simulations. However, we note that the cooling rates by synchrotron and IC processes are equal at a small value of the magnetic field, namely $B \sim 0.1 - 1$ G for electron energies ~ 1 TeV, deep in the KN regime. The value of B is crucial for the development of the cascade, and such values of the magnetic field are found for instance in the

colliding wind regions of WR+OB systems (Benaglia & Romero 2003). Effects of the magnetic field influencing the pure IC cascade by changing the lepton direction of propagation have been treated in detail by Bednarek (1997). We nevertheless assume that, at the lepton energies to which most of the cascade develops, particles radiate before isotropizing after their creation.

The farthest distance from the source up to which the cascades develop is ~ 10 times the orbital separation. In our calculations, photons that pass beyond that distance are stored to form the outgoing spectra. At distances greater than the orbital separation, the cascade efficiency is reduced by the dilution of the stellar radiation field. The spectra are obtained by sorting photons into energy bins of width $\Delta(\log E) = 0.5$. The emerging spectra are shown in Fig. 4.2. The injected primary power is clearly re-distributed to lower energies. At energies higher than ~ 10 GeV, the spectra do not follow a simple power-law, but present a more complex structure, much softer than the injected spectrum. At energies below ~ 100 MeV, the cascade effect is essential for raising the luminosity, and the phase dependence is stronger than at higher energies. The results point to a time dependence anti-correlated for \sim GeV signal compared with that at \sim TeV.

4.2.2 Emission from secondary leptons

The secondary synchrotron emission is calculated in the presence of the magnetic field, which is determined by its value at the base of the jet B_0 . We compute the emission for $B_0 = 10^5$ G (Model A) and $B_0 = 10^4$ G (Model B). We assume the same lepton maximum energy in both models, since for simplicity E_p^{\max} is fixed to 100 TeV in either case. For synchrotron emission, we used the expressions given in Sect. 3.4, using the electron distribution evolution in equation 4.11. The specific differential luminosity at a certain height z in the jet can be expressed as

$$\frac{dL_\nu(z)}{dz} = 2\pi R_{\text{jet}}(z) \frac{\varepsilon_\nu}{k_\nu} (1 - e^{-l_j k_\nu}) \quad (4.12)$$

where l_j is the typical size of the synchrotron emitting plasma region. Now, integrating over the entire jet length we find the spectral energy distribution,

$$\nu L_{\text{sync}} = \nu \int_{z_0}^{z_{\text{max}}} \delta^2 \frac{dL_\nu(z)}{dz} dz \quad (4.13)$$

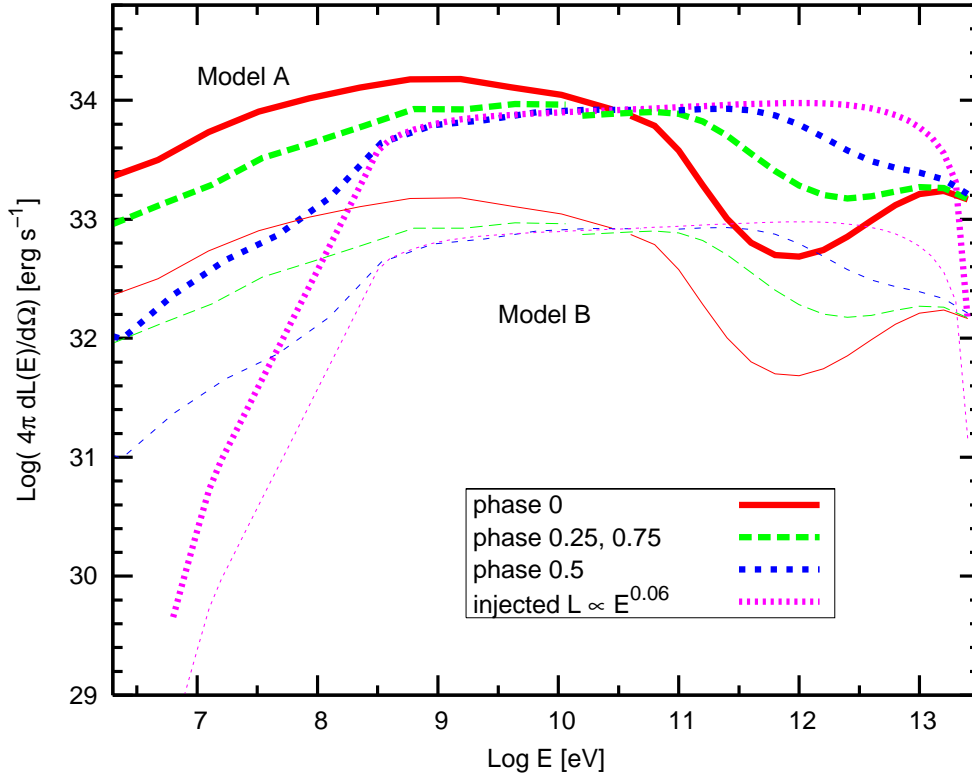


Figure 4.2: Spectral energy distribution (SED) of the electromagnetic cascade at different orbital phases ($\phi = 0$ when the BH is behind the companion). The production of gamma-rays from the π^0 -decay is indicated. Model A is represented by thick lines, while thin lines are used for Model B.

where $\delta = [\Gamma(1 - \beta \cos \theta_{obs})]^{-1}$ is the Doppler boosting factor.

Regarding IC emission, we assumed that it takes place for any lepton energy in the Thomson regime and under an isotropic photon field. Actually, the Thomson approximation is not valid for particles with energies above ~ 10 - 100 GeV, i.e. at the highest energies of the secondary leptons produced in this scenario. Above these energies, the IC interactions occur in the KN regime. This fact does not affect the radiated synchrotron spectrum significantly, since it is mainly produced in the inner regions of the jet, close to the compact object, where the synchrotron process is the main cooling mechanism; i.e. the particle spectrum is not noticeably affected by KN cooling there. The KN effect would otherwise affect the highest energies of the IC spectrum, but this energy range is dominated in our scenario by the contribution from the neutral pion decay.

In Figure 4.3, we show the synchrotron and IC spectra for Model A and Model B. The set of explored parameters illustrate the impact of the IC/synchrotron energy loss balance in the secondary broadband spectrum. It is seen that the synchrotron

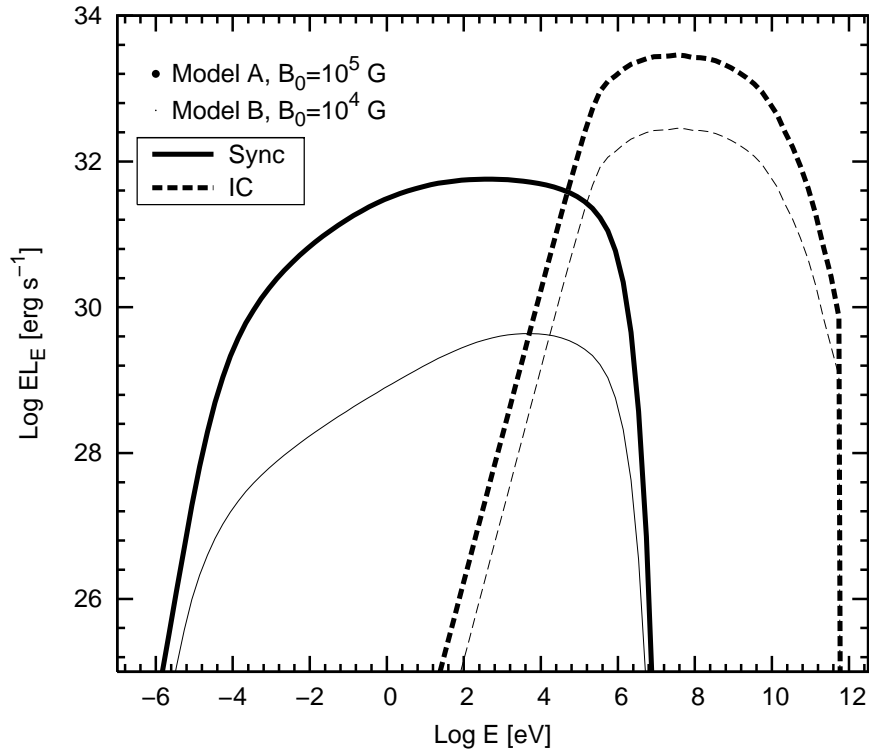


Figure 4.3: *Synchrotron and IC emission from the secondary leptons produced inside the jet by the charged pions decay. The results for both Model A and B are displayed, corresponding to a jet power of $6 \times 10^{37} \text{ erg s}^{-1}$ and $6 \times 10^{36} \text{ erg s}^{-1}$, respectively. The magnetic field is taken as a given fraction of the jet power. The amount of synchrotron radiation depends both on the magnetic field and the total number of relativistic leptons, whereas the IC contribution depends only on this last term, since the target photon field has the same value in both Model A and Model B.*

luminosity is at most $\sim 10^{32} \text{ erg s}^{-1}$, and well below the IC emission for both values of the adopted magnetic field.

4.3 Discussion and conclusions

The primary hadronic emission is found to be strongly affected by the pure IC cascade development in the photosphere of the primary star. We note that the synchrotron dominance of the leptonic energy losses can prevent the pure IC cascade from developing. In our treatment, we restrict ourselves to a low magnetic field in the region where the cascade occurs. In the case of a strong magnetic field, cooling via synchrotron radiation of the leptons injected by $\gamma - \gamma$ absorption will suppress the cascade development (see, e.g., Khangulyan et al. 2008).

Despite the fact that Doppler boosting should make the jet radiation to dominate,

photons absorbed in different directions from that of the observer can present lower energy emission re-directed toward the observer since their direction of motion could indeed be randomized. Under moderate magnetic fields ($B \sim 10$ G), significant amount of synchrotron radiation up to keV energies will be produced by leptons created by photon-photon absorption in the stellar photon field (see Bosch-Ramon et al. 2008).

The cascade reprocessing can lead to significant emission $\sim 10^{33}$ erg s⁻¹ at energies well below those originally injected (with primary energy $E_\gamma > 1$ GeV, due to the pion-creation threshold). The total radiation produced inside and outside the jet by charged pion and cascade secondaries is similar to that produced at gamma rays by the neutral pion decay.

Detectability under the parameters assumed here can be discussed at different bands. At radio frequencies, the obtained spectra are significantly hard, yielding a flux of a few mJy at distances of a few kpc. Although small, these fluxes would be already a substantial fraction of the fluxes found in microquasars in the LH state, i.e. ~ 15 mJy (for Cygnus X-1, see, e.g., Pooley et al. 1999). The radio emission produced by secondaries would appear morphologically as a jet-like source surrounded by a radio halo, because of the highly beamed relativistic leptons generated by charged pion decays, on the one hand, and those generated by pair creation in the stellar photon field on the other (see Bosch-Ramon et al. 2008). The faint radio emission produced by the secondaries in a hadronic model seems to indicate that a primary leptonic component would be needed to explain the observed radio fluxes. The need for this primary component could be avoided, however, if secondaries could be reaccelerated once they have lost their energy (for instance through first and/or second order Fermi processes, see Sect. 3.3). Thus, it cannot be ruled out that the radio emission is in fact produced by secondaries, in which case a primary electron population might not be necessary. The study of this is beyond the scope of this work, but could be interesting to explore in the future.

At soft X-rays, synchrotron emission from secondaries could be detectable by the current X-ray instruments, although microquasars in the LH state also present significant X-ray emission produced in the accretion disk and the corona, which could mask this non thermal contribution to some extent. At hard X-rays, it is still not clear which is the physical origin of the radiation observed in some objects (see, e.g. Markoff et al. 2005; Maccarone 2005; Bosch-Ramon et al. 2006b). In any case, the luminosities at hard X-rays obtained here by summing different contributions would not suffice for explaining those observed in some microquasars during the LH state.

The radiation in the MeV range seems to be non negligible, reaching $\sim 10^{33}$ erg s⁻¹, although it still appears too low to be detected on a reasonable time span for the present instruments. At high and very high-energy gamma rays, *Fermi* and ground-based Cherenkov telescopes have sensitivities good enough to detect the source, which would present a moderately soft spectrum due to electromagnetic cascading.

Even from the simple model considered here, we have been able to discuss the emission produced by the presence of relativistic hadrons in microquasar jets at different energy bands. Many factors should lead to more complex results. For instance, realistic modeling of the variability would include a variable accretion rate (e.g. induced through the variable nature of the outflows of the donor star, or simply through an eccentric orbit) and possible changes through the misalignment between the jet and the orbital axis (i.e. a precessing jet, see Kaufman Bernadó et al. 2002). In such scenario, the angular dependence in the cross section of the IC mechanism would produce variable spectra and fluxes at different energy bands for different orbital phases (see, e.g., Khangulyan et al. 2008).

Bibliography

- Aharonian, F. A., Anchordoqui, L., Khangulyan, D., & Montaruli, T. 2006, *J. Phys. Conf. Ser.*, 39, 408
- Bednarek, W. 1997, *A&A*, 322, 523
- Bednarek, W. & Giovannelli, F. 2007, *A&A*, 464, 437
- Benaglia, P., & Romero, G. E., 2003, *A&A*, 399, 1121
- Bordas, P., Paredes, J., Bosch-Ramon, V., & Orellana, M., 2007, *Ap&SS*, 309, 339
- Bosch-Ramon, V., Romero, G.E., & Paredes, J. M. 2006a, *A&A*, 447, 263
- Bosch-Ramon, V., Romero, G. E., Paredes, J. M., et al. 2006b, *A&A*, 457,1011
- Bosch-Ramon, V., Khangulyan D., & Aharonian, F. 2008, *A&A*, 482, 397
- Dermer, C. D., & Böttcher, M. 2006, *ApJ*, 643, 1081
- Fender, R. P., Belloni, T.M., & Gallo, E., 2004, *MNRAS*, 355, 1105
- Gallo, E., Fender, R., Kaiser, C., et al. 2005, *Nature*, 436, 819
- Georganopoulos, M., Aharonian, F. A., & Kirk, J. G. 2002, *A&A*, 388, L25
- Gupta, S., Böttcher, M., & Dermer, C. D. 2006, *ApJ*, 644, 409
- Khangulyan, D., Aharonian, F. & Bosch-Ramon, V., 2008, *MNRAS*, 383, 467
- Kaufman Bernadó, M. M., Romero, G. E., & Mirabel, I. F., 2002, *A&A*, 385, L10
- Kelner, S. R., Aharonian, F. A., Bugayov V. V., 2006, *Phys. Rev. D*, 74, 034018
- Lamers, H. J. G. L. M. & Cassinelli, J. P., 1999, in *Introduction to Stellar Winds*, Cambridge University Press, Cambridge
- Maccarone, T. J. 2005, *MNRAS*, 364, 971
- Markoff, S., Nowak, M. A., & Wilms, J., 2005, *ApJ*, 635, 1203
- Martí, J., Pérez-Ramírez, D., Garrido, J. L., et al. 2005, *A&A*, 439, 279

- Orellana, M., Bordas, P., Bosch-Ramon, V., et al. 2007, *A&A*, 476, 9
- Orellana, M., & Romero, G. E., 2007, *Ap&SS*, 309, 333
- Orellana, M., Romero, G. E., & Pellizza, L. J., 2006, *BAAA*, 49, 330
- Paredes, J. M., Bosch-Ramon, V., & Romero, G. E. 2006, *A&A*, 451, 259
- Pooley, G. G., Fender, R. P., & Brocksopp, C., 1999, *MNRAS*, 302, L1
- Romero, G. E., Torres, D. F., Kaufman-Bernadó, & M., Mirabel, I. F. 2003, *A&A*, 410, L1
- Romero, G. E., Christiansen, H. R., & Orellana, M., 2005, *ApJ*, 632, 1093
- Szostek, A., & Zdziarski, A. A., 2007, *MNRAS*, 375, 793

Chapter 5

Jet interaction with the interstellar medium

In analogy with radio-loud quasars and AGNs, which show jets impacting on the intracluster medium, one may expect to find radiative signatures due to strong shocks in the termination regions of microquasar jets as well. Hot spots and double-lobe morphologies are common features of the powerful extragalactic FR-II sources (Fanaroff & Riley 1974), in which a variety of large-scale non-thermal structures are revealed at radio wavelengths. In the case of microquasars, convincing evidences of jet interaction with the interstellar medium (ISM) are not numerous, partially due to the relatively small number of known sources. Nevertheless, hints or evidences of such interactions have been observed, at different wavelengths, in SS 433 (Zealey et al. 1980), 1E 1740.7–2942 (Mirabel et al. 1992), XTE J1550–564 (Corbel & Fender 2002), Cygnus X-3 (Heindl et al. 2003), Cygnus X-1 (Martí et al. 1996; Gallo et al. 2005), GRS 1915+105 (Kaiser et al. 2004), H1743–322 (Corbel et al. 2005), and Circinus X-1 (Tudose et al. 2006). Nevertheless, only some theoretical work has been done regarding the hydrodynamics of the interaction and the resulting non-thermal emission (e.g. Aharonian & Atoyan 1998; Velázquez & Raga 2000; Heinz & Sunyaev 2002; Bosch-Ramon et al. 2005; Perucho & Bosch-Ramon 2008).

Microquasar ejections can transport large amounts of kinetic energy and momentum very far from the binary system. The age of the source times the jet kinetic power, $\tau_{\text{MQ}} \times Q_{\text{jet}}$, can be as high as $3 \times 10^4 \text{ yr} \times (10^{37} - 10^{39}) \text{ erg s}^{-1} \sim 10^{49} - 10^{51} \text{ erg}$ (see. e.g., Cygnus X-1, Gallo et al. 2005; SS 433, Zealey et al. 1980). Even for low radiative efficiencies converting this energy into non-thermal emission, microquasar jet termination regions could produce significant fluxes if they were at distances of few kpc from us. It could well be that microquasars were associated, via interaction

with their surrounding medium, to some of the extended non-thermal radio sources detected in the Galaxy which origin is still unknown (see, e.g., Paredes et al. 2007).

One of the central parts of this thesis is intended to study whether a typical microquasar fulfills the conditions to be detectable when interacting with the surrounding ISM. We have adopted for this purpose some reasonable assumptions for the microquasar power and age, and the density of the ISM, as well as for the non-thermal energy and magnetic field equipartition fraction in the interaction regions. We study the case of a high-mass system to see the role of a massive and hot companion. In the case of a low-mass system, the radiation field of the companion star and therefore the IC contribution would be much lower. The energy input into the surrounding medium in the case of a low-mass system could be, nevertheless, similar to the case of a high-mass system. This is because though low-mass systems use to show a lower value of the (averaged) kinetic jet power, since they are older systems the product $\tau_{\text{MQ}} \times Q_{\text{jet}}$ could be therefore similar for both types of systems.

We present in the next Section an analytical interaction model to characterize the different regions formed in the shocks of the jet/medium interaction; for each region, the main properties of the non-thermal emitters are studied, and the physical conditions and geometry are established. We have used the formulae provided in Chapter 3 for the shock conditions found in the different interaction regions, as well as the particle acceleration and radiation mechanisms described there. The non-thermal particle populations have been computed self-consistently. In Sect. 5.2 we calculate the total emission produced through synchrotron, relativistic Bremsstrahlung, and IC processes for the different sets of parameters used in the model. In Sect. 5.3 we have also carried out hydrodynamical simulations to study in more detail the jet evolution when interacting with the ambient medium. These simulations allow us also to test and enforce the validity of the assumptions of the analytical model. Finally, in Sect. 5.4 we discuss the obtained results, giving detectability predictions at different energy bands.

5.1 Model description

We have used a model adapted from those applied to extragalactic sources in order to investigate the interactions of microquasar jets with their environment. Falle (1991) and Kaiser & Alexander (1997) have developed an analytical model where self-similarity is used to characterize the evolution of the jet/medium interaction structures in radio galaxies (see Sect. 3.6). We have closely followed their treatment,

adapting it for the correct application to the microquasar context.

We consider twin conical jets emerging from the central source in opposite directions. The ejecta begin to decelerate when the mass of the swept up external gas becomes similar to the mass carried by the jet. Two shocks are formed at the jet tip: a forward shock (also called the bow shock) propagating into the ISM and a reverse shock directed inwards into the jet material. Matter crossing the reverse shock inflates the cocoon, which protects the jet from disruption due to turbulent gas entrainment. Moreover, a reconfinement shock is also formed in the jet at the point where its pressure equals that of the cocoon.

In our scenario, all the shocks are assumed to be strong. The density and pressure of the shocked material are calculated using the Rankine-Hugoniot conditions for a strong shock at each front. We note that since the conditions in the shocked regions evolve with time, all related physical variables will also change with time. Therefore, the non-thermal particle population will be calculated considering the time dependence of the radiative and adiabatic losses. Given that all the considered shocks are weakly relativistic, we adopt an adiabatic index $\gamma_{\text{ad}} = 5/3$. We assume the presence of a randomly oriented magnetic field B in the downstream regions, derived taking the magnetic energy density to be $\sim 10\%$ (magnetic equipartition fraction $\eta = 0.1$) of the thermal energy density. In each shock region, the fraction of kinetic luminosity assumed to be transferred to non-thermal particles is taken to be 1% ($\chi = 0.01$).

5.1.1 Structure of the interaction regions

We focus our studies in three separated emitting zones. The first one, the shell region, corresponds to the ISM material swept up by the bow shock. The second one, the cocoon region, corresponds to the material of the jet crossing the reverse shock. The third zone accounts for the shocked jet material after crossing the conical reconfinement shock. A sketch of the model is shown in Fig. 5.1.

Bow shock

We are interested in the case when the bow shock can accelerate particles, and we concentrate on its adiabatic phase (Sedov 1959), which implies that the inertia of the medium must be large enough to take a significant fraction of the energy and momentum from the jet. Although in the extragalactic context it is thought that the

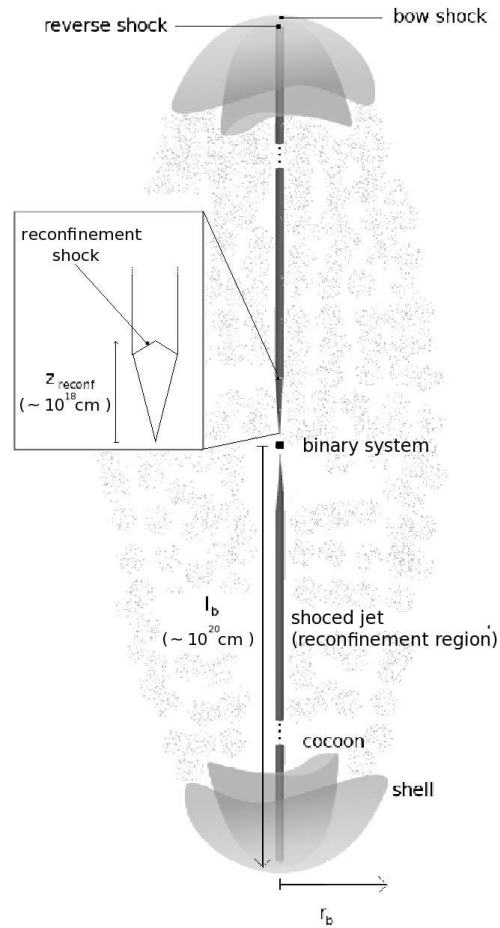


Figure 5.1: Scheme of the model (not to scale) representing the three different zones. The central binary system is located at the center. Two jets emerge from it and extend outwards until they are effectively decelerated at a distance $\sim 10^{20}$ cm. Jet material that crosses the reverse shock inflates the cocoon, which expands exerting work on the shocked ISM. A contact discontinuity separates the cocoon and the shocked ISM, the latter being further limited by the bow shock.

non-thermal radio emission comes solely from the shocked jet material in the cocoon, we have explored the possibility to have also a contribution from the shocked ISM material. After the interaction structures have reached a characteristic length-scale l_0 (see Sect. 3.6) the equations for the length and velocity of the bow shock at a given source age t_{MQ} are (see Falle 1991; Kaiser & Alexander 1997):

$$l_{\text{b}} = c_1 \left(\frac{Q_{\text{jet}}}{\rho_{\text{ISM}}} \right)^{1/5} t_{\text{MQ}}^{3/5}, \quad (5.1)$$

and

$$v_{\text{b}} = \frac{d}{dt}(l_{\text{b}}) = \frac{3l_{\text{b}}}{5t_{\text{MQ}}}. \quad (5.2)$$

respectively. Here Q_{jet} is the jet power, ρ_{ISM} is the ISM mass density and $c_1 \approx 1$ is a dimensionless constant that depends on the adiabatic index of the jet material and the geometry of the bow shock.

To determine the radius of the bow shock, r_{b} , we assume a self-similar relationship between its length and width given by $R \equiv l_{\text{b}}/r_{\text{b}}$, which can change from source to source in the range $R \in [2 - 3]$ (see for instance Leahy et al. 1989, Kaiser et al. 2004, Perucho & Marti 2007). Here we use a fiducial value of $R = 3$ (similar to the value from our simulations; see Sect. 5.3). We assume a plane shock and do not enter in the details concerning the precise geometry of the bow shock. Nevertheless, we need the accelerator size in order to compute the maximum energies that particles can reach, as well as an estimation of the emitter size to provide the surface brightness of the source. In the case of the bow shock, both the accelerator and the emitter size are taken to be $\sim r_{\text{b}}$. The pressure, assumed equal to that of the cocoon, and the mass density have been taken homogeneous in the whole shell. Since the bow shock velocity evolves with time, the mass density and the pressure change as well (the pressure in the shell has been calculated as $P_{\text{b}} = (3/4) \rho_{\text{ISM}} v_{\text{b}}^2$). Therefore, the magnetic energy density varies also with time. Finally, the radiation field energy density depends on l_{b} , $u_{\star} \approx L_{\star}/4 \pi l_{\text{b}}^2 c$ (where L_{\star} is the companion luminosity).

Cocoon

The cocoon is filled with jet material that crosses the reverse shock. A contact discontinuity separates the cocoon and the shell region materials (surface C in Sect. 3.6). We do not consider the mixing of the gas of both zones that could occur due to Kelvin-Helmholtz and/or Rayleigh-Taylor instabilities. The cocoon pressure

is taken to be the same as that in the other side of the contact discontinuity at any time, $P_c = P_b$. Given the strong compression of the ISM gas in the shell zone, the length and the width of the cocoon are taken to be also $\sim l_b$ and $\sim r_b$, respectively. For the accelerator size, the reverse shock, we adopt the constant jet width after the reconfinement point (see below). The pressure and mass density of the material can be taken as homogeneous for the whole cocoon to first order approximation. The homogeneity assumption comes from the fact that the cocoon material is expected to be subsonic. The evolution of both pressure and mass density will depend on the time evolution of the reverse shock velocity, like the magnetic and radiation fields, in the same way as in the case of the ISM shocked region.

Reconfinement region

The conical jet initially emerging from the central engine has an opening angle $\Psi \simeq r/z \sim 0.1$ rad, where z is the distance to the injection point and r is the jet radius. Given the pressure exerted by the surrounding cocoon, the jet radius becomes approximately constant at z_{conf} , the distance where the lateral jet pressure becomes similar to the cocoon one. Following Kaiser & Alexander (1997), we obtain the following radius for the reconfined jet:

$$r_{\text{conf}} \sim \Psi \sqrt{\frac{2Q_{\text{jet}}v_{\text{jet}}}{(\gamma_{\text{ad}} + 1)(\Gamma_{\text{jet}} - 1) \pi c^2 P_c}}, \quad (5.3)$$

where $\gamma_{\text{ad}} = 5/3$ is the adiabatic index of the cocoon material and v_{jet} is the jet velocity. For a recent semi-analytical treatment of reconfinement shocks, see Nalewajko & Sikora (2009). Downstream the shock, the material still moves almost at the jet velocity. The normal component of the velocity of the reconfinement shock, i.e., the one that suffers a discontinuity, is much smaller than v_{jet} . The jet keeps most of its thrust and remains supersonic until it is braked at the reverse shock. From the reconfinement point the jet roughly keeps a constant radius. We neglect further recollimation shocks that may occur (see Sect. 5.3).

The size of the accelerator is taken as the width of the jet at the recollimation shock, r_{conf} . Once accelerated, relativistic particles are approximately advected at the jet velocity, and propagate up to the reverse shock. The length of the emitter, assumed to be one-dimensional, is therefore taken to be $\sim l_b$ since $z_{\text{conf}} \sim r_{\text{conf}}/\Psi \ll l_b$. The magnetic field in the reconfinement region is derived as in the other interaction zones. The radiation density, however, gradually decays from z_{conf} to l_b as the in-

verse square of the distance to the companion star. The density and the pressure are considered to remain roughly constant after the reconfinement point since the jet radius is constant beyond z_{conf} .

5.1.2 The non-thermal particle populations

Diffusive shock acceleration for non-relativistic velocities predicts a power-law index of $P \sim 2$ for the injected particle spectrum in strong shocks (see Sect. 3.3; see also Drury 1983). We take this value for the non-thermal particle spectra injected at the reconfinement, reverse and bow shock fronts, i.e. $N(E) = K E^{-2}$. As noted above, the normalization constant K is taken such that $\sim 1\%$ of the kinetic power flowing in the jets is converted into non-thermal energy in the postshock region right after each shock. We remark that the radiation luminosities scale linearly with this non-thermal fraction.

The maximum energies of the relativistic particles, E_{max} , are calculated at any source age equating the energy gain to the different cooling processes. In case radiative cooling is not effective, the maximum energy is constrained by the Hillas limit (Hillas 1984), i.e. the particle gyroradius, r_g , equals the accelerator size. We have used the Bohm diffusion coefficient ($D = r_g c/3$) and the different values for the magnetic field in each shocked region to calculate the rate at which particles gain energy (see Sect. 3.3 and references therein).

Focusing hereafter on electrons, the particle energy distribution is computed taking the expressions of Sect. 3.4 for synchrotron, relativistic Bremsstrahlung and IC processes. Adiabatic losses along the lifetime of the source are also considered. As pointed out in Blundell & Rawlings (2000) in their study on extragalactic double radio sources, the spectral aging of the non-thermal populations depends on the evolution of the physical conditions in each region, in particular the expansion velocities and magnetic fields for each interaction zone. At each time, the conditions for the radiative and adiabatic losses change. The non-thermal particle distribution at a given source age t_{MQ} has to be therefore computed summing up the differently evolved contributions of the particles injected previously at the shock fronts all along the source lifetime until reaching t_{MQ} .

For the synchrotron losses, we use the magnetic field considered above for each interaction region. Relativistic Bremsstrahlung is calculated accounting for the densities in the downstream regions. To compute IC losses, we consider the dominant radiation field from the companion, an OB star with luminosity $L_{\star} = 10^{39}$ erg s $^{-1}$.

Table 5.1: *List of the parameters that remain with a constant value in the analytic model.*

<i>Parameter</i>	<i>Symbol</i>	<i>Value</i>
Jet Lorentz factor	Γ_{jet}	1.25
Jet half opening angle	Ψ	0.1 rad
Luminosity companion star	L_{\star}	$10^{39} \text{ erg s}^{-1}$
Self-Similar parameter	R	3
Magnetic equipartition fraction	η	0.1
Non-thermal luminosity fraction	χ	0.01

Adiabatic losses, $\dot{E}(t) = -[v(t)/r(t)] E$, are computed from the size of the emitters $r(t)$ and the expansion velocity $v(t)$. At the downstream region, after the reconfinement shock, there is no expansion since the jet radius keeps roughly constant. In the case of the shell region, the expansion velocity is v_b , and for the cocoon, it is $\sim 3/4 v_b$ (see Sect. 5.4; Landau & Lifshitz 1987).

As noted above, the electron population properties, the adiabatic coefficient, and the magnetic and radiation fields are taken homogeneous as a first order approximation in the bow shock and cocoon regions. A study of the detailed spatial structure of the magnetic field, pressure and mass density at each interaction region is beyond the scope of our work. For the electrons injected at the reconfinement shock, we compute their evolution assuming a one-dimensional emitter, the jet, with the stellar radiation density decaying as $\propto 1/z^2$.

The list of the parameters that remain constant in our analytic model are presented in Table 5.1. Given E_{max} and the evolved electron distribution in each emitting region, and accounting for the mentioned radiation mechanisms, we have computed the SEDs for each zone. This is presented in the next section.

5.2 Model Results

We have studied how the computed SEDs are affected by varying the source age, t_{MQ} , the jet kinetic power, Q_{jet} , and the ISM particle density, n_{ISM} . In Fig. 5.2 and Fig. 5.3 we show the SEDs for the shell (top), cocoon (middle) and jet reconfinement (bottom) regions. The contribution of only one jet interacting with the ISM is accounted. The whole set of parameter values, required for the different cases to

obtain the particle evolution and subsequent emission, are presented in Table 8.7.

Synchrotron emission from the three interaction zones is the channel through which the highest radiation output is obtained, with bolometric luminosities that can be as high as $\sim 10^{33}$ erg s $^{-1}$ for powerful sources (see Figs. 5.2 and 5.3). At high and very high energies, IC emission is the dominant process in the cocoon and reconfinement regions, reaching luminosities up to $\sim 10^{30}$ erg s $^{-1}$, while for the shell zone relativistic Bremsstrahlung dominates at this energy range, with luminosities up to $\sim 10^{32}$ erg s $^{-1}$. Notable differences are found in the reported SEDs when varying the source age t_{MQ} from 10^4 to 10^5 yr. For older sources, the interaction zones are located at larger distances from the companion star, its radiation energy density u_* decreases and the IC contribution gets slightly lower, although particle aging leads to higher emission at lower energies in the shell and cocoon regions. Relativistic Bremsstrahlung in the shell zone is strongly affected by the source age, due to a particle accumulation effect, giving luminosities a factor of ~ 10 larger for old sources. Regarding the ambient medium density, higher values of n_{ISM} make the jet to be braked at shorter distances from the central engine. The interaction regions are then under a higher radiation energy density from the companion star, and the IC emission is accordingly enhanced. The relativistic Bremsstrahlung emission in the shell zone is also higher for denser mediums, since the luminosity is proportional to the target ion field density, $n_t = 4n_{\text{ISM}}$. Finally, we note that in our model all the non-thermal luminosities are proportional to Q_{jet} .

5.2.1 Bow shock emission

Under the acceleration conditions in this region, the maximum energies E_{max} of electrons for the different cases range 2–10 TeV, being always limited by synchrotron losses. The electron energy distribution has an energy break, E_b , at which the radiative cooling timescale and the age of the source are the same. E_b changes its value depending on the physical conditions: older sources render smaller E_b , since particles have cooled via synchrotron for a longer time; higher densities yield lower E_b , due to smaller l_b and therefore larger B and synchrotron cooling. Larger jet powers enhances B as well, reducing again E_b (this discussion about E_b is valid also for the other interaction regions). The energy break is manifested in the synchrotron spectrum at frequencies in the range $\sim 10^{14} - 10^{16}$ Hz. Given the long synchrotron cooling timescales $\tau_{\text{sync}} \sim 10^{14} B_{-4}^{-2} E_b^{-1}_{\text{GeV}}$ s (where $B_{-4} = B/10^{-4}$ G) compared with the age of the source $\sim 10^{12}$ s, only the highest energy band of the particle spectrum has reached the steady state. The synchrotron luminosities reach values up to $\sim 10^{33}$ erg s $^{-1}$ (see Figs. 5.2 and 5.3). The Relativistic Bremsstrahlung has

Table 5.2: *Parameter values adopted to compute the SEDs for the three emitting zones. The target density, n_t , is only shown when non-negligible. We show the parameter values at t_{MQ} , but we remark that they smoothly vary with time. The computation of the non-thermal particle distribution have taken this into account. See text for details.*

<i>Parameter</i>	Fig. 5.2 (left)		Fig. 5.2 (right)		Fig. 5.3 (left)		Fig. 5.3 (right)	
Jet kinetic power Q_{jet} (erg s ⁻¹)	10 ³⁶				10 ³⁷			
ISM density n_{ISM} (cm ⁻³)	0.1		1		0.1		1	
Source age t_{MQ} (yr)	10 ⁴	10 ⁵						
<i>SHELL</i>								
Magnetic field B (G)	2.9×10^{-5}	1.1×10^{-5}	5.8×10^{-5}	2.3×10^{-5}	4.6×10^{-5}	1.8×10^{-5}	9.2×10^{-5}	3.6×10^{-5}
Shock velocity v_b (cm s ⁻¹)	4.3×10^7	1.7×10^7	2.7×10^7	1.0×10^7	6.9×10^7	2.7×10^7	4.3×10^7	1.7×10^7
Emitter size r (cm)	2.3×10^{19}	9.1×10^{19}	1.4×10^{19}	5.7×10^{19}	3.62×10^{19}	1.44×10^{20}	2.3×10^{19}	9.1×10^{19}
Rad. energy dens. u_* (erg cm ⁻³)	5.0×10^{-12}	3.2×10^{-11}	1.2×10^{-13}	8.0×10^{-13}	2.0×10^{-12}	1.3×10^{-12}	5.0×10^{-13}	3.2×10^{-13}
Maximum energy E_{max} (TeV)	8.1	5.1	3.6	2.3	10.2	6.4	4.5	2.8
Target density n_t (cm ⁻³)	0.4	0.4	4.0	4.0	0.4	0.4	4.0	4.0
<i>COCOON</i>								
Magnetic field B (G)	3.8×10^{-5}	1.5×10^{-5}	7.5×10^{-5}	3.0×10^{-5}	5.9×10^{-5}	2.4×10^{-5}	1.2×10^{-4}	4.7×10^{-5}
Shock velocity v_s (cm s ⁻¹)	1.8×10^{10}							
Emitter size r (cm)	6.5×10^{18}	2.5×10^{18}	4.0×10^{19}	1.6×10^{19}	1.0×10^{19}	4.0×10^{18}	6.5×10^{19}	2.5×10^{19}
Rad. energy dens. u_* (erg cm ⁻³)	7.0×10^{-12}	1.7×10^{-11}	4.4×10^{-13}	1.1×10^{-12}	2.8×10^{-12}	1.7×10^{-12}	7.0×10^{-13}	4.4×10^{-13}
Maximum energy E_{max} (TeV)	275.5	275.5	275.5	275.5	871.2	871.2	871.23	871.2
<i>RECONFINEMENT</i>								
Magnetic field B (G)	2.6×10^{-5}	1.0×10^{-5}	5.2×10^{-5}	2.1×10^{-5}	4.2×10^{-5}	1.6×10^{-5}	8.3×10^{-5}	3.3×10^{-5}
Shock velocity v_{conf} (cm s ⁻¹)	1.8×10^9							
Emitter size r (cm)	1.9×10^{19}	7.6×10^{19}	1.2×10^{19}	4.8×10^{19}	3.0×10^{19}	1.2×10^{20}	1.9×10^{19}	7.6×10^{19}
Rad. energy dens. u_* (erg cm ⁻³)	2.5×10^{-8}	4.0×10^{-9}	1.0×10^{-7}	1.6×10^{-8}	6.4×10^{-9}	1.0×10^{-9}	2.5×10^{-8}	4.0×10^{-9}
Maximum energy E_{max} (TeV)	3.2	3.2	3.2	3.2	10.1	10.1	10.1	10.1

a strong dependence on the density, follows the energy distribution of electrons, and can reach luminosities $\sim 10^{32}$ erg s $^{-1}$ in the 1 MeV–10 GeV range. The IC luminosities are well below the synchrotron ones in all the studied cases .

5.2.2 Cocoon emission

Electrons in the cocoon can reach energies of about $E_{\max} \sim 100$ TeV, being limited by escape losses. Synchrotron emission, again the dominant radiative channel, extends up to hard X-rays, with luminosities reaching up to $\sim 10^{33}$ erg s $^{-1}$ (see Fig. 5.3) depending on the different parameter values. As in the shell region, the IC luminosities are well below the synchrotron ones. Otherwise, due to the low particle densities, relativistic Bremsstrahlung is negligible in this zone.

5.2.3 Reconfinement region emission

The size of the accelerator (Hillas 1984) put a limit of ~ 10 TeV on the maximum energies that electrons can acquire at the reconfinement shock. An increase in both the synchrotron and the IC emissivities is found for denser mediums, in which case P_c is larger yielding smaller z_{conf} , which determines the magnetic and radiation field energy densities. The synchrotron luminosity is similar to the IC one for weak jets, whereas it is well above it for powerful jets, where luminosities $\sim 10^{32}$ erg s $^{-1}$ are obtained (see Fig. 5.3). This is due to the stronger dependence of the synchrotron emission with the jet power. The stellar radiation field enhances the IC contribution when the set of parameters makes z_{conf} shorter. As in the cocoon region, the relativistic Bremsstrahlung contribution is negligible.

5.3 Hydrodynamical simulations

Numerical simulations have been performed in order to check the physical values adopted in the analytical model. We used a two-dimensional finite-difference code based on a high-resolution shock-capturing scheme, which solves the equations of relativistic hydrodynamics written in conservation form. This code is an upgrade of the code described in Martí et al. (1997) (see also Perucho et al. 2005). The simulation has been carried out in two dual-core processors in the Max-Planck-Institut für Radioastronomie.

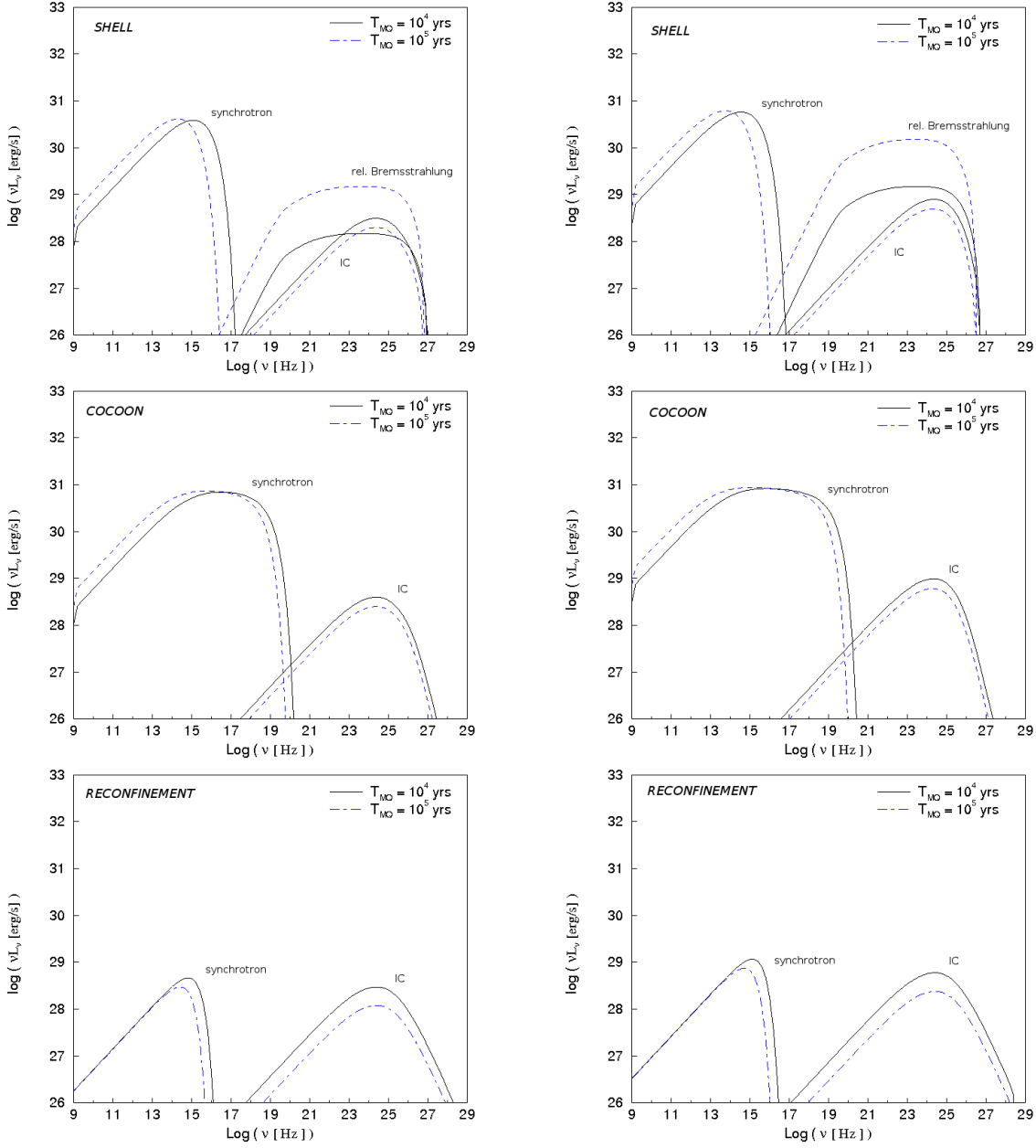


Figure 5.2: Obtained SEDs for the shell (top), cocoon (middle) and jet reconfinement (bottom) regions taking the values for the external gas particle density $n_{\text{ISM}} = 0.1 \text{ cm}^{-3}$ (left panel) and $n_{\text{ISM}} = 1 \text{ cm}^{-3}$ (right panel). The jet power is $Q_{\text{jet}} = 10^{36} \text{ erg s}^{-1}$ and two different values for the source age are represented, $t_{\text{MQ}} = 10^4 \text{ yr}$ (solid line) and 10^5 yr (dashed line). See Table 8.7 for details on the parameter values for each region.

The numerical grid of the simulation is formed by 320 cells in the radial direction and 2400 cells in the axial direction in a uniform region, with physical dimensions of $40 \times 600 r_j$. An expanded grid with 320 cells in the transversal direction brings the

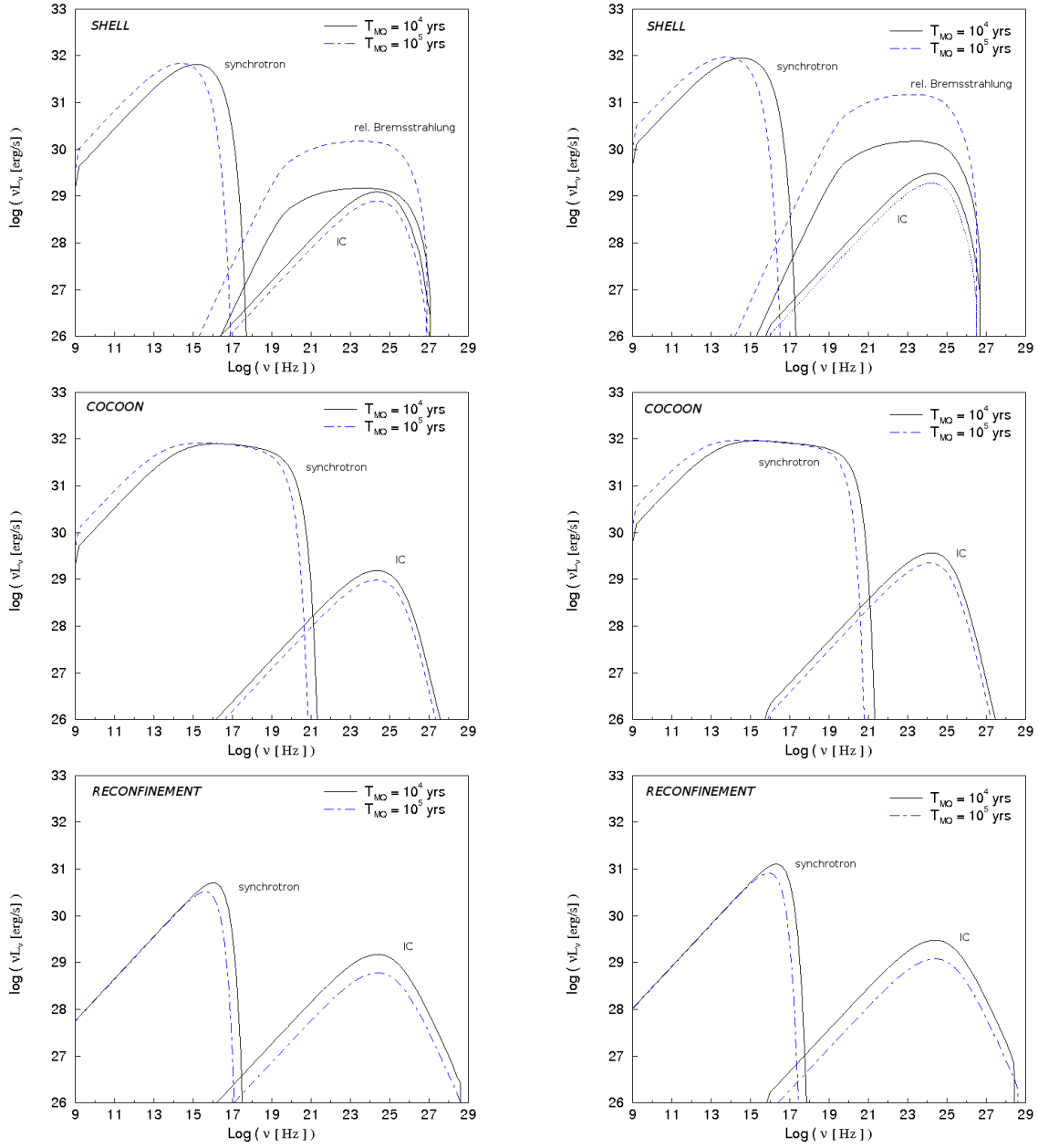


Figure 5.3: Same as in Fig. 5.2 but taking $Q_{\text{jet}} = 10^{37} \text{ erg s}^{-1}$. See the physical parameter values in Table 2.

boundary from $40 r_j$ to $500 r_j$, where r_j is the jet radius, whereas an extended grid in the axial direction, consisting of 440 extra cells, spans the grid axially from $600 r_j$ to $900 r_j$. The enlargement of the grid is necessary to ensure that the boundary conditions are sufficiently far from the region of interest, and to avoid numerical reflection of waves in the boundaries affecting our results. The conditions at the

boundaries are reflection on the jet axis and in the side where the jet is injected, simulating the presence of the counter-jet cocoon, with the exception of the injection point, where inflow conditions are used. Finally, outflow conditions in the outer axial and radial boundaries are used.

The jet is injected in the grid at a distance of 10^{18} cm from the compact object, and its initial radius is taken to be $r_0 = 10^{17}$ cm. The time unit of the code is thus equivalent to $\approx 3 \times 10^6$ s, which is derived using the radius of the jet at injection and the speed of light (r_j/c). Both the jet and the ambient medium are considered to be formed by a non-relativistic gas with adiabatic exponent $\Gamma = 5/3$. The number density in the ambient medium is $n_{\text{ISM}} = 0.3 \text{ cm}^{-3}$. The velocity of the jet at injection is $0.6c$, its number density $n_j = 1.4 \times 10^{-5} \text{ cm}^{-3}$, and temperature $T \sim 10^{11}$ K (which corresponds to a sound speed $\sim 0.1 v_{\text{jet}}$). These parameter values result in a jet power $Q_{\text{jet}} = 3 \times 10^{36} \text{ erg s}^{-1}$.

Several reconfinement shocks are obtained in the simulations, as can be seen in the pressure profile along the jet axis in Fig. 5.4. The evolution of the self-similar parameter R reaches a value between 2.5 and 2.7 at the end of the simulations, as can be seen in Fig. 5.5. The upper (lower) panels in Fig. 5.6 show the evolution of the pressure and the mass density with simulation time for the shell (cocoon) region, whereas Figs. 5.7 and 5.8 show the velocity, Mach number, mass density and pressure maps obtained in the numerical simulations.

5.3.1 Comparison with the analytical model

The values of Q_{jet} , t_{MQ} and n_{ISM} used in the hydrodynamical simulations are similar to those assumed in the analytical model for both the cocoon and shell pressure. The pressure evolution with time has been computed for the shell and cocoon regions. From an initial value of $\sim 2 \times 10^{-9} \text{ erg cm}^{-3}$, the cocoon pressure smoothly reaches $\sim 8 \times 10^{-11} \text{ erg cm}^{-3}$ at $t = 7 \times 10^{11}$ s. The shell behaves similarly, as expected, with a final pressure of $\sim 8 \times 10^{-11} \text{ erg cm}^{-3}$. These values are in reasonable agreement with those found in the analytical model, ranging between $(2 - 7) \times 10^{-10} \text{ erg cm}^{-3}$. Concerning the mass densities, ρ_{ISM} stabilizes at $\sim 2 \times 10^{-25} \text{ g cm}^{-3}$ and $\rho_{\text{co}} \sim 4 \times 10^{-29} \text{ g cm}^{-3}$ for the shell and the cocoon regions, respectively. These values are again very similar to those found in the analytical treatment. On the other hand, the self-similar ratio used in the analytical model is $R = 3$, which is in accordance with the results of the numerical simulations (2.5–2.7). Finally, we note that in our model only a strong shock at the reconfinement point is assumed, and no additional shocks are considered along the jet. Otherwise, the hydrodynamical simulations

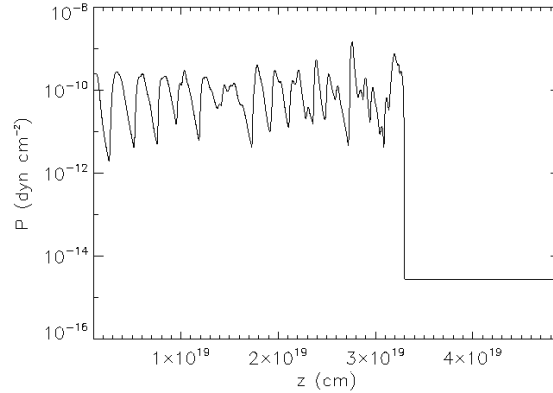


Figure 5.4: *Pressure along the jet axis as a function of distance from its injection point, at $\sim 10^{18}$ cm, as found in the hydrodynamical simulations. Several reconfinement shocks are present, due to the pressure balance with the surrounding cocoon: each time the jet pressure falls below that of the cocoon, a shock is formed. This keeps the jet radius roughly constant until it reaches the reverse shock.*

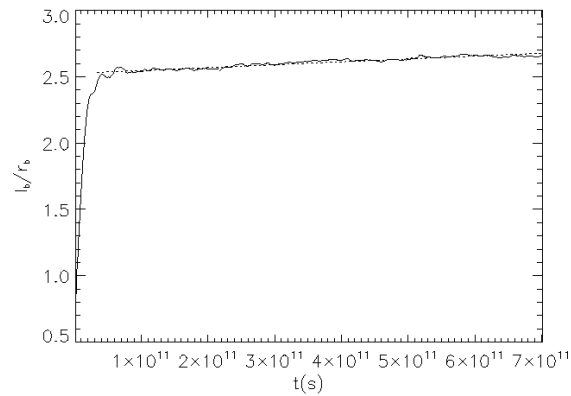


Figure 5.5: *Evolution of the self-similar parameter $R = l_b/r_b$ as a function of time. After the pronounced initial increase, R remains between 2.5 and 2.7 for most of the simulated time.*

show the existence of several conical shocks that develop in the jet when its pressure falls to that of the surrounding cocoon (see Fig. 5.4). Therefore, the non-thermal emission presented in Figs. 5.2 and 5.3 for the reconfinement region, with only one strong shock and an acceleration efficiency of $\chi = 0.01$, should be taken as a rough approximation of the real situation.

5.4 Discussion and conclusions

We have explored whether non-thermal emission can be expected from the bow shock, the cocoon and the reconfinement regions in the interaction of microquasar

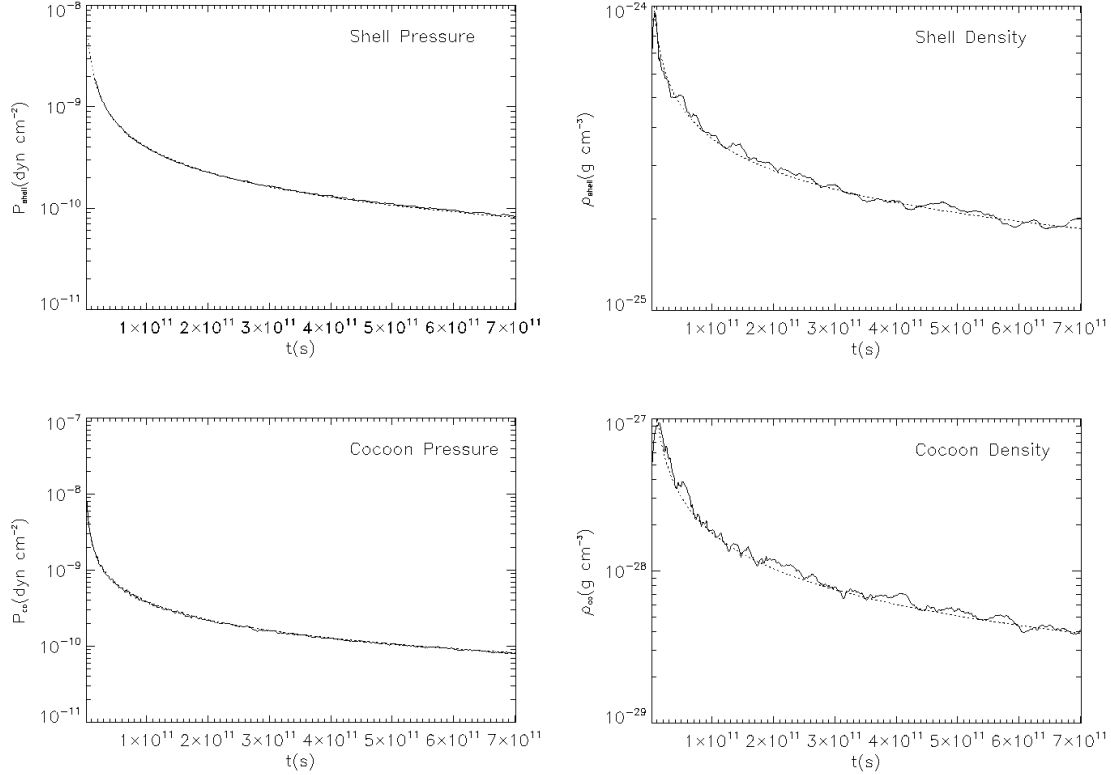


Figure 5.6: Pressure (left) and mass density (right) evolution in the shell (top) and cocoon (bottom) regions as a function of time. A fitting of the results is also shown for both variables (dotted line). This fit serves to estimate the simulation values at longer times. This extrapolation is strictly valid only if an homogeneous external medium and a constant injection energy rate are assumed.

jets with their environment. In the extragalactic framework, non-thermal radiation is assumed to come only from the cocoon as extended radio emission, as well as locally in the hot spots at the jet tips. Although the shocked ambient material plays an important role in the growing of FR II galaxies (Blandford et al. 1974; Scheuer 1974), no radio emission is usually assumed to be produced there (see, however, Rudnick et al. 1988). In our model, the bow shock velocity is still large enough to accelerate particles, so we compute the expected non-thermal emission also from this region. Our results show that its contribution can be comparable to that of the cocoon and higher than that coming from the reconfinement region. The geometry of the interaction structures, however, makes difficult to disentangle the emission at low energies from the cocoon and the bow shock region since they could appear co-spatial in the plane of the sky. A clear relativistic Bremsstrahlung component in the SED would favour a shell origin of the emission.

The highest radiation output within the studied set of parameters corresponds to the case: $Q_{\text{jet}} = 10^{37} \text{ erg s}^{-1}$, $t_{\text{MQ}} = 10^5 \text{ yr}$ and $n_{\text{ISM}} = 1 \text{ cm}^{-3}$. In case the emitting

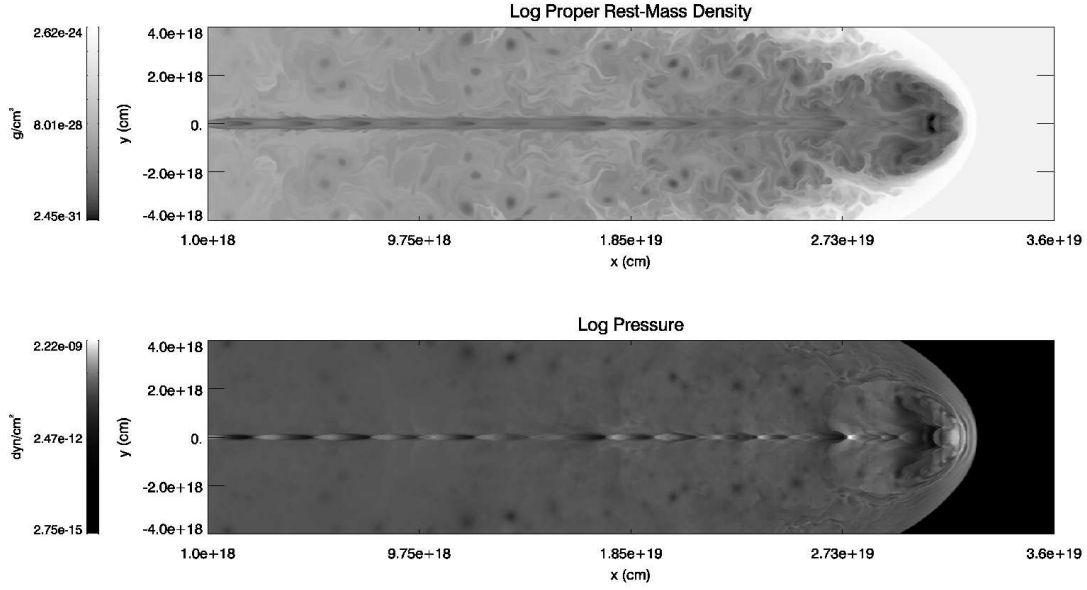


Figure 5.7: Mass density (top) and pressure (bottom) maps resulting from hydrodynamical simulations. The simulations were performed using $Q_{\text{jet}} = 3 \times 10^{36} \text{ erg s}^{-1}$, $t_{\text{MQ}} = 3 \times 10^4 \text{ yr}$ and $n_{\text{ISM}} = 0.3 \text{ cm}^{-3}$.

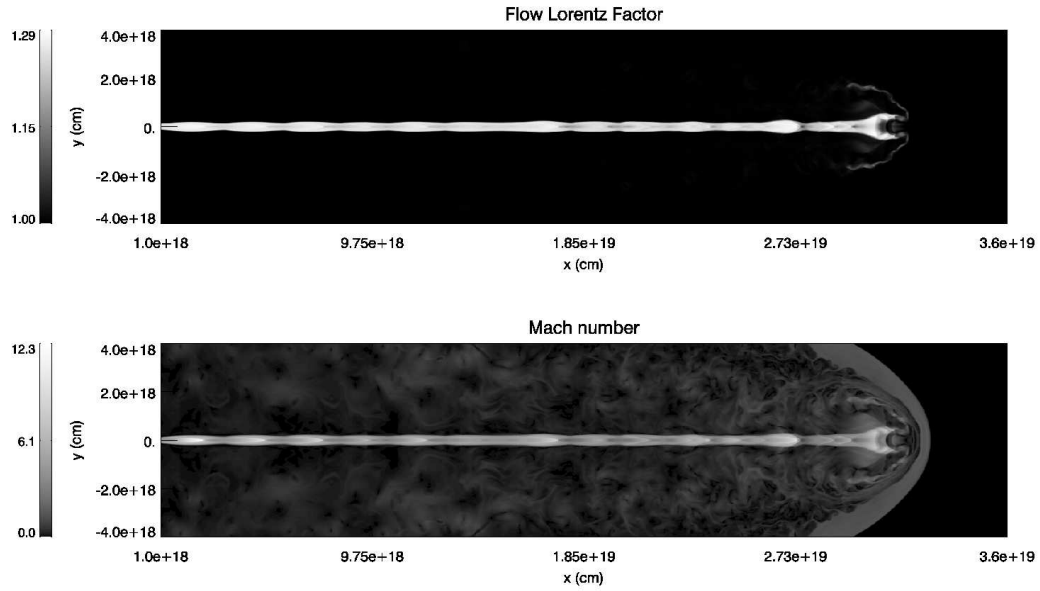


Figure 5.8: Lorentz factor (top) and Mach number (bottom) maps resulting from hydrodynamical simulations. The adopted parameters are the same as those of Fig. 5.7.

source were located at 3 kpc, this would imply a flux density of $\sim 150 \text{ mJy}$ at 5 GHz. The emitting size would be of a few arcminutes, since the electron cooling timescale

is longer than the source lifetime and they can fill the whole cocoon/shell structures. Considering this angular extension and taking a radio telescope beam size of $10''$, radio emission at a level of ~ 1 mJy beam $^{-1}$ could be expected. At the X-ray band, we find a bolometric flux in the range 1–10 keV of $F_{1-10\text{keV}} \sim 2 \times 10^{-13}$ erg s $^{-1}$ cm $^{-2}$. The electrons emitting at X-rays by synchrotron have short time-scales, and the emitter size cannot be significantly larger than the accelerator itself. Although the X-rays produced in the shell through relativistic Bremsstrahlung are expected to be quite diluted, the X-rays from the cocoon would come from a relatively small region close to the reverse shock, and could be detectable by *XMM-Newton* and *Chandra* at scales of few arcseconds. In the gamma-ray domain, the flux between 100 MeV and 100 GeV is $F_{100\text{ MeV} < E < 100\text{ GeV}} \sim 10^{-14}$ erg s $^{-1}$ cm $^{-2}$, while the integrated flux above 100 GeV is $F_{E > 100\text{ GeV}} \sim 10^{-15}$ erg s $^{-1}$ cm $^{-2}$. These values are too low to be detectable by current satellite and Cherenkov telescopes operating in the gamma-ray domain. However, taking into account the rough linearity between Q_{jet} , n_{ISM} , t_{MQ} , χ and d^{-2} with the gamma-ray fluxes obtained, sources with higher values of these quantities than the ones used here may render the microquasar jet termination regions detectable at these energies. For the weakest jets, i.e, lowest ISM densities and youngest sources adopted in our model ($Q_{\text{jet}} = 10^{36}$ erg s $^{-1}$, $t_{\text{MQ}} = 10^4$ yr and $n_{\text{ISM}} = 0.1$ cm $^{-3}$), the fluxes are strongly suppressed. In the radio band, the specific flux is $F_{5\text{ GHz}} \sim 0.1$ mJy beam $^{-1}$; the integrated flux at X-rays in this case is $F_{1-10\text{ keV}} \sim 10^{-14}$ erg s $^{-1}$ cm $^{-2}$, and at gamma-rays $F_{100\text{ MeV} < E < 100\text{ GeV}} \sim 2 \times 10^{-17}$ erg s $^{-1}$ cm $^{-2}$ and $F_{E > 100\text{ GeV}} \sim 2 \times 10^{-16}$ erg s $^{-1}$ cm $^{-2}$. We remark that the fluxes showed above strongly depend on the non-thermal luminosity fraction χ . In the present model we use a quite conservative value of $\chi = 0.01$. In the case of a source able to accelerate particles at a higher efficiency at the interaction shock fronts, then the expected non-thermal fluxes would be enhanced by a factor $(\chi/0.01)$.

The non-thermal emission from the shock regions in microquasars presents characteristic features that can be distinguished from emission coming from the central binary system. First of all, the interaction structures are localized at distances up to $\sim 10^{20}$ cm. The lifetime of electrons radiating at high and very high energies is relatively short, and thus the emission region should be localized near the accelerator (but far away from the central system). Regarding radio emission, synchrotron cooling times are expected to be larger than the source lifetime, $t_{\text{MQ}} = 10^4 - 10^5$ yr. The cocoon and bow shock emitting regions would be expected to form a kind of radio nebula around the central system and the flux densities at the level showed above would then come from a quite extended source.

The detection of non-thermal emission from the interaction zones would be a

proof that efficient acceleration of particles up to relativistic energies is taking place far away from the central binary system. The averaged kinetic power carried away in the jets could be better constrained, eventually showing that it can be much higher than that inferred directly from observations of the inner jet emission alone (Gallo et al. 2005; Heinz 2006)

Despite we focus on the non-thermal emission from the microquasar jet termination regions, thermal Bremsstrahlung emission should be expected from the shell. Although the shocks considered here are still adiabatic, a non-negligible fraction of the jet kinetic luminosity of up to a few % may be radiated via thermal Bremsstrahlung. For bow-shock velocities of few times 10^7 cm s^{-1} the thermal emission would peak at UV-soft X-rays. Observations of the thermal radiation in radio and optical from the interaction structures have been used to extract information of the shell physical conditions (e.g. Cygnus X-1, Gallo et al. 2005; Russell et al. 2007).

Given the conditions in the strong shocks we are considering, relativistic protons may reach energies of about 100 TeV; for shell densities $\sim 1 \text{ cm}^{-3}$, the accelerated protons have lifetimes of about 10^{15} s . To reach the gamma-ray fluxes detectable for the present generation of satellite borne, with sensitivities $\sim 10^{-12} \text{ erg cm}^{-2} \text{ s}^{-1}$ for energies $\gtrsim 1 \text{ GeV}$, and ground based gamma-ray instruments, with sensitivities $\sim 10^{-13} \text{ erg cm}^{-2} \text{ s}^{-1}$ for energies $\gtrsim 100 \text{ GeV}$, the energy in non-thermal protons stored in the shell should be as high as $\sim 10^{48} \text{ erg}$ at few kpc distances. For a source age of $t_{\text{MQ}} = 10^5 \text{ yr}$, the required injected power in relativistic protons should be about $\sim 3 \times 10^{35} \text{ erg s}^{-1}$, thus implying that moderate levels of hadronic emission from microquasar jet termination regions may be eventually detected from powerful jets, i.e. $Q_{\text{jet}} \gtrsim 10^{37} \text{ erg s}^{-1}$.

The evolution of the pressure, mass density, the velocities and the Mach number predicted by the analytical model are in good agreement with those found in the hydrodynamical simulations for the shell and the cocoon regions. Otherwise, these simulations show that several conical shocks may be present within the jet as a consequence of pressure adjustments with the surrounding cocoon, instead of the one strong shock adopted in the analytical treatment. Finally, the length and width of the structures in the model and those found through the numerical simulations are also similar, with a constant ratio $R \sim 3$ in both cases, implying that the physical assumptions used in the analytical treatment are valid to first order.

The reason why some microquasars show non-thermal emission from the jet/ISM interaction regions, whereas in other cases such emission remains undetected, is still unclear. In the context of our model, we can study the effects of varying the set

of parameters defining the source and their environment, and predict some cases in which the interaction structures may or may not be detectable. First of all, the energy input injected to the medium should be high enough, and there exist strong differences in the jet kinetic power from source to source. In addition, it could be also the case that the density of the surrounding medium is so low that the shell and the cocoon get very large and their radiation too diluted to be detectable (see, for instance, Heinz 2002). Moreover, in some cases microquasar jets could get disrupted at some source age, as it is found in FR I galaxies. If this happened within times much shorter than the microquasar lifetime, the probability to detect a cocoon/shell structure in the microquasar surroundings would be smaller (although the detection of some other kind of structures is not discarded). On the other hand, some sources may be too far, or the non-thermal fraction too small, to detect significant emission from the interaction regions.

Bibliography

- Aharonian, F. A. & Atoyan, A. M. 1998, *NewAR*, 42, 579
- Blandford, R. D., & Rees, M. J. 1974, *MNRAS*, 169, 395
- Blundell, K. M. & Rawlings, S. 2000, *AJ*, 119, 1111
- Bosch-Ramon, V., Aharonian, F. A., & Paredes, J. M. 2005, *A&A*, 432, 609
- Corbel, S., Kaaret, P., Fender, R. P., et al. 2005, *ApJ*, 632, 504
- Corbel, S., & Fender, R. P. 2002, *ApJ*, 573, L35
- Drury, L. 1983, *SSRv*, 36, 57
- Falle, S. A. E. G. 1991, *MNRAS*, 250, 851
- Fanaroff, B. L., & Riley, J. M. 1974, *MNRAS*, 167P, 31F
- Gallo, E., Fender, R. P., Kaiser, C., et al. 2005, *Nature*, 436, 819
- Heindl, W. A., Tomsick, J. A., Wijnands, R., & Smith, D. M. 2003, *ApJ*, 588, L97
- Heinz, S. & Sunyaev, R. 2002, *A&A*, 390, 751
- Heinz, S. 2006, *ApJ*, 636, 316
- Hillas, A. M. 1984, *ARA&A*, 22, 425
- Kaiser, C. R., & Alexander, P. 1997, *MNRAS*, 286, 215
- Kaiser, C. R., Gunn, K. F., Brocksopp, C., & Sokoloski, J. L. 2004, *ApJ*, 612, 332
- Landau, L. D., & Lifshitz, E. M. 1987, in *Fluid Mechanics*, 2nd English Edition, Oxford: Pergamon
- Leahy, J. P., Muxlow, T. W. B., & Stephens, P. W. 1989, *MNRAS*, 239, 401
- Martí, J., Rodriguez, L. F., Mirabel, I. F., & Paredes, J. M. 1996, *A&A*, 306, 449
- Martí, J. M., Müller, E., Font, et al. 1997, *ApJ*, 479, 151
- Mirabel, F., Rodriguez, L. F., Cordier, B., et al. 1992, *Nature*, 358, 215

- Paredes, J. M., Martí, J., Ishwara Chandra, C. H., & Bosch-Ramon, V. 2007, ApJ, 654, L135
- Perucho, M., Martí, J. M., & Hanasz, M. 2005, A&A, 443, 863
- Perucho, M. & Martí, J. M. 2007, MNRAS 382, 526
- Perucho, M. & Bosch-Ramon, V. 2008, A&A, 482, 917
- Rudnick, L., 1988, ApJ, 325, 189
- Russell, D. M., Fender, R. P., Gallo, E., & Kaiser, C. R. 2007, MNRAS, 376, 1341
- Scheuer, P. A. G. 1974, MNRAS, 166, 513
- Sedov, L. I. 1959, in *Similarity and Dimensional Methods in Mechanics*, New York: Academic Press
- Nalewajko, K., & Sikora, M. 2009, MNRAS, 392, 1205
- Tudose, V., Fender, R. P., & Kaiser, C. R., et al. 2006, MNRAS, 372, 417
- Velázquez, P. F. & Raga, A. C. 2000, A&A, 362, 780
- Zealey, W. J., Dopita, M. A., & Malin, D. F. 1980, MNRAS, 192, 731

Part II

Observations of microquasars with the MAGIC telescope

Chapter 6

High and Very High Energy gamma-ray astrophysics

In this Thesis we have investigated the gamma-ray emission that can be produced in a microquasar scenario. Although these systems are observed to emit in the whole electromagnetic spectrum, the gamma-ray band is the best suited framework where the non-thermal processes can be explored, since it provides a picture characterized by the most extreme conditions are found. Besides gamma-rays, neutrinos are also expected to be produced in hadronic gamma-ray production channels. Both gamma-rays and neutrinos freely propagate in space, without deflecting in the interstellar and intergalactic magnetic fields, and thus can trace the original source position. Neutrino and gamma-ray astronomy are slowly converging in what refers to the achieved sensitivity and angular resolution. However, the extremely small cross-sections of neutrinos interaction and hence the extremely large collection areas required by neutrino detectors, make of gamma-ray astronomy the only viable technique nowadays to study the highest energy phenomena produced in a selected astrophysical source.

The gamma-ray energy domain spans the energy range $E \gtrsim m_e c^2 \simeq 0.5 \times 10^6$ eV up to $E \sim 10^{20}$ eV. The lower bound characterises the region of nuclear γ -ray lines and the electron-positron annihilation line. The upper bound roughly represents the highest energy that have been observed in cosmic rays, and hence the maximum acceleration that particles can reach in cosmic accelerators. This broad energy range is covered rather inhomogeneously with different detection methods and flux sensitivities of space- and ground-based instruments.

Observational gamma-ray astronomy is often divided into several areas, depend-

ing on the explored range in energy: Low (LE, below 30 MeV), High (HE, 30 MeV - 30 GeV), Very High (VHE, 30 GeV - 30 TeV), Ultra High (UHE, 30 TeV - 30 PeV) and Extremely High (EHE, above 30 PeV) energies. Observations in the LE and HE bands are performed by satellite or balloon-borne detectors, whereas the VHE domain is studied using ground-based facilities. No gamma-ray sources have been detected so far in the UHE and EHE ranges. It must be noted, however, that the free path of γ -rays is strongly energy-dependent due to photon-photon absorption. For gamma-rays of less than a few GeV, the mean free path exceeds the Hubble size of the Universe, whilst that for 1 PeV photons is only of about 8.5 kpc, limiting their observation the galactic environment. The TeV range, on the other hand, has a visibility depth of approximately 100 Mpc, although VHE sources at higher redshifts have been discovered (see, e.g., Albert et al. 2008a)

Before entering in the details of the search of gamma-ray emission from microquasars with the MAGIC telescope, we present in next sections a brief resume of gamma-ray detection techniques and the available instrumentation. Chapter 7 is devoted to the description of the MAGIC telescope performance and the Cherenkov data analysis procedure. In Chapter 8 we provide the results of the MAGIC observations of GRS 1915+105, Cyg X-3, Cyg X-1 and the system SS 433/W50.

6.1 Space-based observatories

The Earth's atmosphere is opaque to gamma-rays. The atmosphere is 1030 g cm^{-2} thick at the sea level, which corresponds to 28 radiation lengths; this implies that the probability that an incident photon reaches the ground level without interacting electromagnetically is $\sim 3 \times 10^{-10}$. Even at high altitude observation sites the probability that a photon will survive is negligibly small. The observation of primary cosmic gamma-rays has therefore to be done from balloons or satellites.

The first detection of HE gamma-rays was obtained with the Orbiting Solar Observatory, OSO-3, which detected photons of energies above 70 MeV originated in the Galactic plane (Kraushaar et al. 1972). In the early 1970's, the higher spatial resolution performance of the SAS-2 satellite confirmed the HE emission from the Crab Nebula and revealed the production of gamma-rays from another source, Vela-X (Thompson et al. 1977). A few years later, the COS-B satellite discovered for the first time a significant number of sources which could not be identified at other wavelengths (Bignami & Hermsen 1983).

The successor of COS-B was the Compton Gamma-ray Observatory (CGRO),

which was equipped with a powerful set of gamma-ray instruments covering the energy range between some tens of MeV up to few GeV. In particular, the Energetic Gamma-ray Telescope (EGRET) on board CGRO produced a gamma-ray catalog with 271 sources detected with high significance, of which around 170 of them are still unidentified. One of the unexpected results from EGRET was the detection of gamma-ray emission from a large number of blazars, the majority of which exhibited highly variable emission. In addition, EGRET permitted for the first time the identification of gamma-rays coincident with a microquasar candidate, namely LS 5039, an association proposed by Paredes et al. (2000). A recent comprehensive review by Thompson (2008) summarizes the observational results and describes some of the pioneering science from EGRET during its nine-year mission.

The COMPTEL experiment was also on board CGRO. It observed in the 0.75-30 MeV energy range, and reported ~ 30 new sources (some of them X-ray binaries as Cyg X-1; see McConell et al. 1994)

The INTEGRAL satellite was launched in 2002, and operates in the range 20 keV - 8 MeV. Its FoV is about 16° , it has a detector area of 500 cm^2 and an angular resolution of 2 arcmin. The *Swift* satellite, a mission intended for the detection of gamma-ray bursts (GRBs) was launched in 2004. It is a multi-wavelength observatory (including gamma, X-ray, UV and optical bands) which, thanks to its fast reaction time of about 50 seconds, has been capable to observe more than 100 GRBs and their subsequent X-ray afterglows.

The Astro-rivelatore Gamma a Immagini LEggero (AGILE) satellite has been launched in 2007. It is provided with three instruments, which cover the energy range from tens of keV to 50 GeV, being the first space facility which can simultaneously observe in the X-ray and Gamma-ray band. Its point source sensitivity is comparable to that of EGRET for on-axis sources, and substantially better for off-axis sources. Its much larger FoV as compared to EGRET offers however a big improvement in the background subtraction during the data reduction process. A significant disadvantage of AGILE is, however, its very thin calorimeter, only 1.5 radiation lengths, which limits its spectral capability. The reader is referred to Tavani et al. (2008) for a more detailed description of the AGILE instrument.

Finally, the Fermi satellite is successfully operating since June 2008. Fermi has already begun to survey the gamma-ray sky with a much more improved sensitivity than EGRET and will detect and catalog about an order of magnitude more sources. The Fermi mission includes two instruments: the Large Area Telescope (LAT) and the GRB Monitor (GBM). LAT is a pair-conversion telescope capable to measure the direction and energy of the incoming gamma-ray photons in the energy range of

30 MeV to 100 GeV. The LAT sensitivity is improved with respect to EGRET by a factor ≥ 20 , placing a 5σ point source sensitivity at a level of $3 \times 10^{-9} \text{ cm}^{-2} \text{ s}^{-1}$, for a steady source after a 1-year all-sky survey and assuming a high-latitude source with a spectral index of 2.1 and inclusion of all photons above 100 MeV. The field of view is twice larger than that of EGRET, and it offers a better angular and energy resolutions, of about 15% over its full spectral range. In addition, off-axis observations are significantly improved with the LAT instrument. The GBM instrument, on the other hand, is designed for the study of GRBs by detecting hard X-ray and gamma-ray photons with full-sky coverage.

Fermi normally operates in an all-sky survey mode, although it is also capable of making pointed observations. Furthermore, it can autonomously repoint at any time, by up to 70° in less than 5 min, toward GRB targets detected by the GBM. Nevertheless, even when operating in pointed mode, LAT's 2.4 sr field of view can observe numerous sources simultaneously.

Initial results from Fermi are already exciting. A comparison of the first Fermi sky-maps with those corresponding to four years of EGRET observations strongly indicates the great potential afforded by Fermi. A strong evidence of Fermi's capabilities is the first list of bright Fermi-LAT sources, with 205 sources with at least 10σ significance (Abdo et al. 2009). Furthermore, all Fermi-LAT photon data will be released to the public during the delivering of this thesis, in August 2009, one year after the beginning of science operations. The interested reader is referred to the NASA Fermi Science Support Center web site <http://fermi.gsfc.nasa.gov/ssc/> for details on how to access the data and the software tools needed in order to analyzeTable it.

6.2 Ground-based VHE observatories

Photon fluxes at HE and VHE gamma-rays are typically low as compared to emission at lower energies. For instance, the strongest gamma-ray source in the sky, Vela-X, with a flux above 100 MeV of $\sim 10^{-5}$ ph cm² s⁻¹ and with a differential flux $\propto E^{-1.89}$ would represent one photon/hour collected from a 1000 cm² satellite detector at GeV energies. VHE astronomy must use therefore much larger collection areas, not allowed to be included in satellite payloads. This can be accomplished, however, with ground-based VHE facilities.

The bulk of observational results at TeV energies have come from telescopes using the atmospheric Cherenkov technique (ACT), with the notable exception of the results reported by the Milagro experiment. Though the concept of this new generation of telescopes was already proposed a long time ago (Jelley & Porter 1963, Weekes & Turver 1977), it was not until the development of the so-called Imaging Atmospheric Cherenkov Technique (IACT) that the first indication of significant emission from the Crab Nebula by the Whipple observatory was apparent (Weekes et al. 1989). However, given the difficulties that characterized the early results at gamma-ray energies, it is not surprising that this early detection was treated with some skepticism.

The energy threshold of the Whipple, HEGRA and CAT IACTs operating in the 1990s was in the range of several hundreds GeV to TeV energies. The new generation IACTs are equipped with larger dishes which bring the energy threshold below 100 GeV. In table 6.1 the current major ACT facilities are listed, together with their main technical characteristics. The substantial progress recently accomplished during last years has been led by the H.E.S.S, MAGIC and VERITAS Collaborations. The reader is referred to the recent reviews by De Angelis et al. (2007), Weekes (2008) and Aharonian et al. (2008) for details on the recent development of the IACT technique.

IACTs offer a wide spectral energy range which covers from about ~ 25 GeV up to ~ 100 TeV. As the size of the telescopes has increased and the sophistication of the triggering improved, the energy threshold has dropped from the ~ 5 TeV of the earliest experiments down to the ~ 25 GeV recently achieved by the MAGIC telescopes (Aliu et al. 2008). However, though most IACT observatories strive to achieve the lowest possible energy threshold, in practice the technique is still most sensitive at energies around 200 GeV, and this is where most of the new sources have been discovered. On the other hand, the flux range where TeV sources have been discovered span from 0.01 to 15 times (for instance in flaring AGNs) that of

Table 6.1: *List of the major ACT existing facilities and their main characteristics*

Observatory	Elevation (km)	# Telescopes	Mirror Area (m ²)	FoV (°)	first light	Threshold (GeV)	Sensitivity [‡] (% Crab)
Whipple	2.3	1	75	2.2	1985	400	10
TACTIC	1.3	1	10	2.8	2001	1500	70
PACT	1.1	24	107	3	2001	750	11
H.E.S.S	1.8	4	428	5	2003	100	0.7
MAGIC	2.2	2	236	3.5	2005	30	1.6
CANGAROO III	0.1	3(4) [†]	172 (230)	4	2006	400	10
VERITAS	1.3	4	424	3.5	2007	100	1
HAGAR	4.3	7	31	3	2008	60	9

[†] only three of the original four telescopes are now in operation

[‡] in 50 h ob observation time to get a 5σ detection

the Crab Nebula. The detection of the weakest sources are strongly affected by systematics, which put a limit on the necessary longer integration times to reveal their signal.

The usual standard for acceptance a new source detection is that the signal should be at the 5σ level, corresponding to a probability of $\sim 5 \times 10^{-7}$ that the signal is produced by a background fluctuation. This is a fairly conservative criteria and is probably justified when the systematics are not fully understood.

IACTs have energy resolutions of about 15%-30%; at low energies spectral measurements are limited by threshold effects, whereas at the highest energies it is limited by statistics. On the other hand, angular resolution can reach values down to a few arcmin scale. In general, extended sources are more difficult to detect by IACT telescopes, though recent results of observations of the Galactic plane have revealed that many galactic sources are often extended (Aharonian et al. 2006a). Time variability studies with IACTs can offer important clues to the physics behind TeV sources. Observations of extragalactic sources like PKS 2155-302 (Aharonian et al. 2007), and Mrk 501 (Albert et al. 2008b) have shown extremely variable emission at the highest energies, with duration of only some minutes. In galactic observations, time variability has demonstrated to be a powerful tool to establish the properties of binary systems (Aharonian et al. 2006b, Albert et al. 2006), which have been detected in some cases only during flaring events (Albert et al. 2007).

The present IACTs have produced a picture of the VHE sky which was not foreseen 20 years ago, when only the Crab Nebula was known to be a TeV emitter and

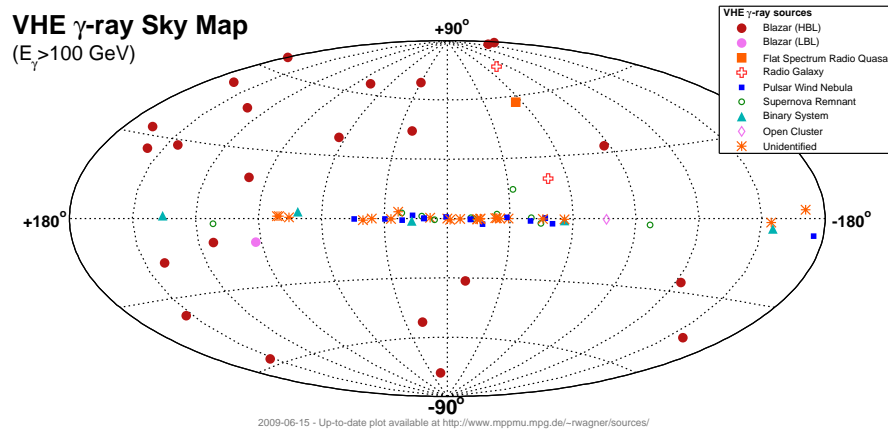


Figure 6.1: Skymap of the TeV sources detected by the current IACTs. An updated TeV skymap can be found at Robert Wagner's webpage: <http://www.mpp.mpg.de/~rwagner/sources/>

it was supposed that the TeV sky would be dominated by a small number of sources. Fig. 6.1 shows the 71 VHE sources detected so far (68 of which thanks to the IACT technique); both galactic and extragalactic objects are displayed. The Cherenkov technique have unveiled a new window where distinct sources are observed, mostly in the galactic plane (Aharonian et al. 2006a). An early assumption was that the VHE sky would be a weak extension of the rich 100 MeV sky revealed by SAS-2, COS-B and EGRET. On the contrary, the existence of many unidentified galactic sources highlights the fact that they could have their main energy output in the TeV domain. In addition, most of them show a hard spectrum, being detected at ≥ 150 GeV, which points to the high efficiency of galactic accelerators.

Future facilities: CTA

The Cherenkov Telescope Array (CTA) is a proposed open ground-based observatory based on the Imaging Cherenkov Technique. About 34 Institutes in Europe and the USA contribute to this project. CTA is being designed to be the next generation of Cherenkov Telescopes. CTA will be about a factor of ten more sensitive than current experiments, reaching the mCrab threshold (see Fig. 6.2). It will allow in-depth studies of known classes of gamma-ray emitters and also detect new source classes that are below the sensitivity of current instruments. The full energy range will cover from 10 GeV up to 100 TeV, with an angular resolution a factor of 5 times better than current telescopes thanks to the many instruments forming the array. Time resolution should permit the study of transient phenomena down to time-scales lower than minutes.

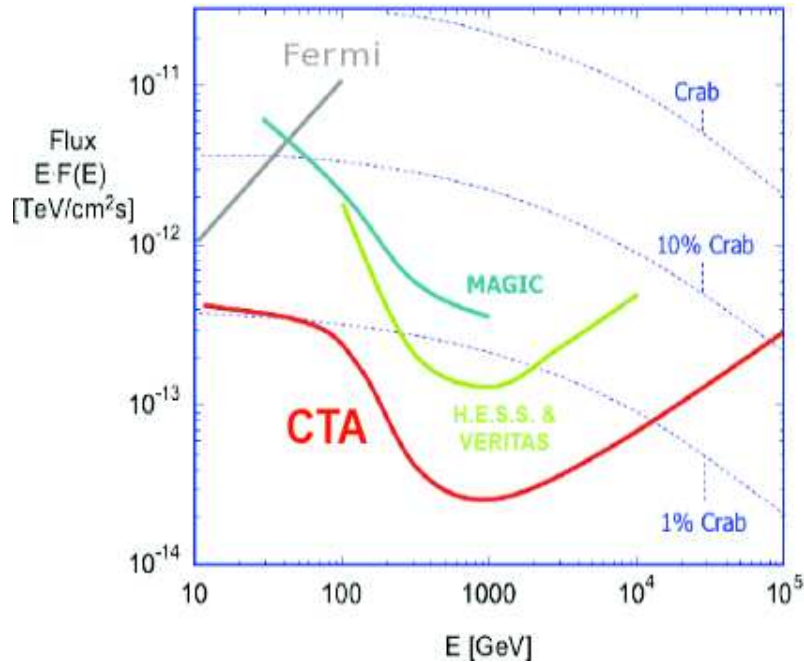


Figure 6.2: Approximate sensitivity curves for the IACTs MAGIC, H.E.S.S. and VERITAS together with the expected sensitivity of CTA. Note that CTA is actually in its design phase, so this curve has to be taken as a rough estimation.

The exact design of CTA is still under study. First Monte Carlo studies of whether the aimed sensitivity and angular resolution can be achieved have been performed. In this regard, the Physics Package of CTA is responsible for providing the physics case which will drive the final design of the array. We have participated actively with observational proposals intended to establish accurately the technical requirements for positive detection. In particular, extended emission from the interaction of microquasar jets with the environment (see Chapter 4) are within the potential sources that CTA will be able to fruitfully explore.

6.2.1 Physics of the air showers

Gamma-ray photons and cosmic rays (CRs), mainly composed of atomic nuclei ($\sim 98\%$) and electrons ($\sim 2\%$), are the highest energy messengers that reach the Earth atmosphere. CRs are usually deflected by galactic and intergalactic magnetic fields, and their distribution at the top of the atmosphere appears isotropically distributed. Gamma-rays, neutrinos and CRs with energies $E \gtrsim 10^{18}$ eV, instead, can be used to trace back the position of a given astrophysical source. The interaction of a high-energy CR or a gamma-ray photon with ions and molecules of the atmosphere generates secondary particles. These secondaries interact in turn with atmospheric

targets and produce a new generation of secondary particles. The number of particles grows rapidly while the incident particle/photon energy is redistributed over secondary products. This process continues up to the point in which secondary energy falls below the threshold for further particle production. Eventually ionization and Compton scattering losses dominate, and the extended air shower (EAS) dies out.

Electromagnetic and hadronic EAS

Important differences arise in the EAS development depending on whether it has hadronic (protons, ions) or electromagnetic (electrons/positrons, gamma-rays) nature. Gamma-rays and electrons develop an EAS which mainly produce secondary photons, electrons and positrons. When a primary gamma-ray interacts with the Coulomb field of an atmospheric nucleus, an electron-positron pair is produced. This e^\pm -pair will suffer Bremsstrahlung losses in the Coulomb field of other atmospheric nuclei. If the energy of the produced photon is higher than $2 \times m_e c^2 = 1.022$ MeV, new e^\pm -pairs will be produced, which will further undergo Bremsstrahlung losses. As a result of this process an avalanche of photons, electrons and positrons is created. When the primary CR is an electron, the same cascade development occurs, but this time beginning with the Bremsstrahlung emission process. Electron-induced EASs are an unavoidable background for ground-based gamma-ray detectors. Other processes like $\gamma + \text{nucleus} \rightarrow \text{hadrons}$ do occur in electromagnetic EAS. Their cross-sections are however much smaller than those of e^\pm -pair production and Bremsstrahlung processes.

Both gamma-ray and electron generated EAS roughly follow the direction of the primary CR. A sketch of an electromagnetic EAS is shown on the left side of Fig. 6.3. The shower transverse broadening comes from the multiple scattering processes and the deflection of the charged particles by the Earth magnetic field. On the other hand, the shower maximum is reached when the mean energy of electrons/positrons falls below a critical energy $E_c \sim 83$ MeV, when ionization losses dominate over Bremsstrahlung. Simultaneously, the mean shower photon energy has decreased and the cross-section for e^\pm production becomes similar to that of Compton scattering and photoelectric absorption. The precise expressions for the electromagnetic EAS development both in the transverse and longitudinal directions can be found in Greisen (1956) and Greisen (1960) (see also Gaisser 1990).

An EAS generated through the interaction of hadronic CR with an atmospheric nucleus mainly produces pions, but also kaons and ions lighter than the incident

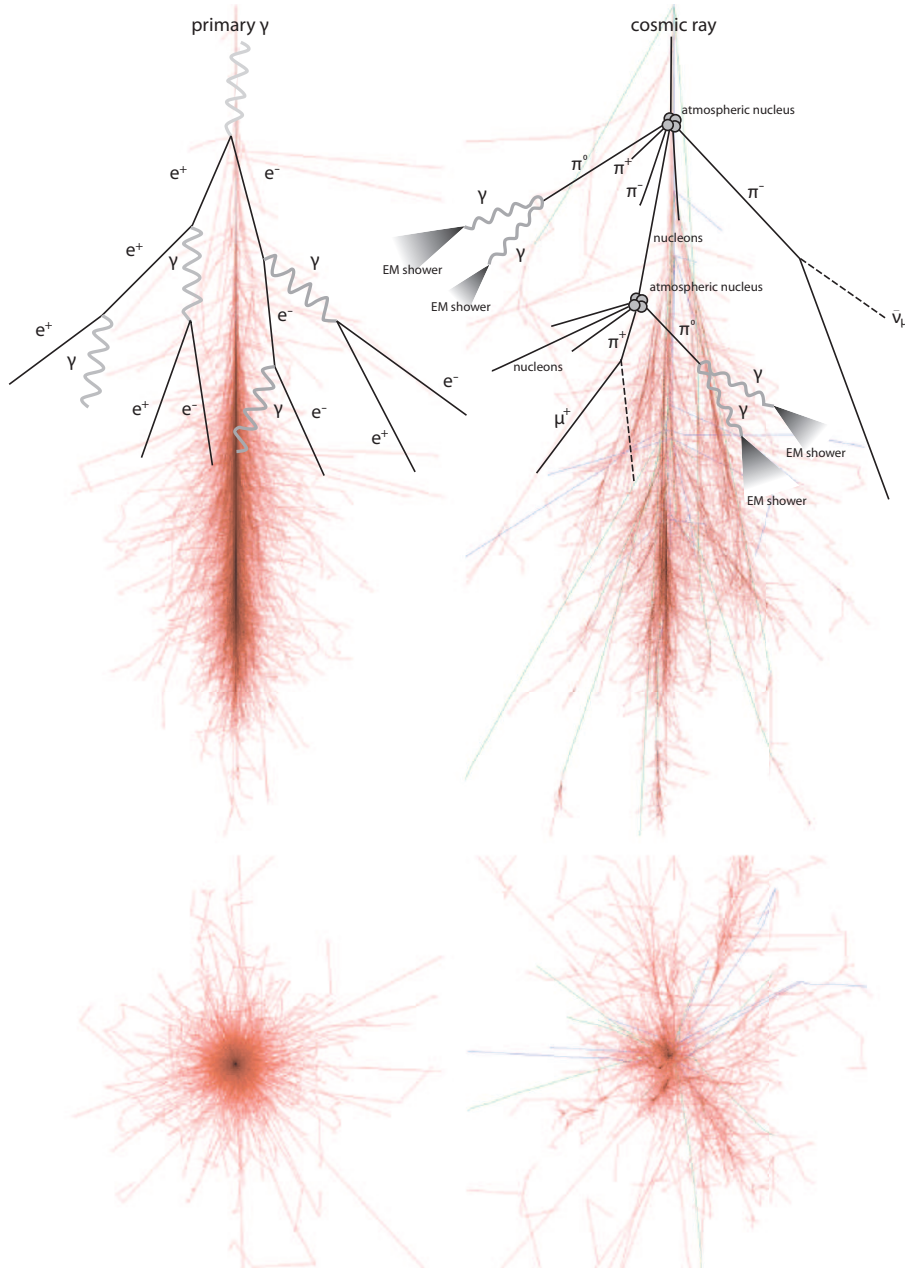


Figure 6.3: Schematic description of the electromagnetic (left) and hadronic (right) induced EAS.

CR. About 2/3 of the produced pions are charged whilst the remaining 1/3 are neutral pions which rapidly decay into two gamma-ray photons. These photons will initiate electromagnetic showers, so $\sim 1/3$ of the primary hadronic CR will be used for the development of an electromagnetic EAS. On the other hand, charged pions and kaons will decay into muons and neutrinos, feeding the muonic component of the shower. Muons have a relatively large lifetime (about 2×10^{-6} s) until secondary $e^{+/-}$ and neutrino decay process occurs. However, their high Lorentz factors allow

most of them to reach the ground before decaying. A sketch of an hadronic EAS is shown in right side of Fig. 6.3. As can be appreciated, hadronic showers are broader than electromagnetic ones. Hadronic interactions provoke the relatively wide lateral spread. In addition, hadronic interaction lengths in the atmosphere are almost twice the radiation length of bremsstrahlung emission and e^\pm -pair production interaction lengths. This implies that the starting point and the shower maximum of an hadron-induced EAS occurs deeper in the atmosphere as compared with EAS generated by a gamma-ray photon with the same energy.

Cherenkov radiation

Charged particles travelling at a speed higher than that of light in a given medium ($v > c/n$, n is the refractive index of the medium), produce a reorientation of the electric dipoles of the medium molecules giving place to Cherenkov radiation. Charges around the incident particle cancel out for low values of v , whereas a net polarization briefly remains along the particle path at higher v . Electromagnetic impulses are emitted when the medium molecules rapidly turn back to their ground state. A sketch of the Cherenkov radiation production process is shown in Fig. 6.4. As the incident charged particle crosses the medium, a wavefront is created behind it. The wavefront surface vector is composed by the coherent summation of the light emitted from different points along the particle trajectory, and sustains an angle θ_{Ch} with respect to the particle path. Its maximum value corresponds to ultra-relativistic velocities of the incident particle and is given by $\cos \theta_{\text{Ch}}^{\text{max}} = 1/n$. The threshold energy for Cherenkov light production is $E_{\text{Ch}}^{\text{thr}} = m_0 c^2 / \sqrt{1 - (1/n)^2}$. The refractive index n changes with the atmospheric altitude. For an isothermal atmosphere which density decreases exponentially with the height h from the ground, $n(h) = 1 + n_0 \cdot e^{(-h/h_0)}$, where $n_0 = 2.9 \times 10^{-4}$ and $h_0 = 7.1$ km. The Cherenkov energy threshold $E_{\text{Ch}}^{\text{thr}}$ will therefore vary along the shower path, being higher in the upper layers of the atmosphere and decreasing as the EAS develops towards the ground. Cherenkov radiation from electrons will be emitted even beyond the EAS maximum (provided $E_{\text{Ch}}^{\text{thr}}$ is lower than E_c). Muons can also contribute to the total Cherenkov light production and can be used as powerful tools in ground-based detectors for calibration purposes.

The variation of θ_{Ch} with h produces a characteristic enhancement of the Cherenkov light density at the borders of the shower-projected perimeter, with a radius of about 100 to 130 m from the center of the Cherenkov light pool. Transverse dispersion of the emitting particles due to multiple scatterings makes this ring structure to spread out to some extent. For hadronic showers, the dispersion is even more important,

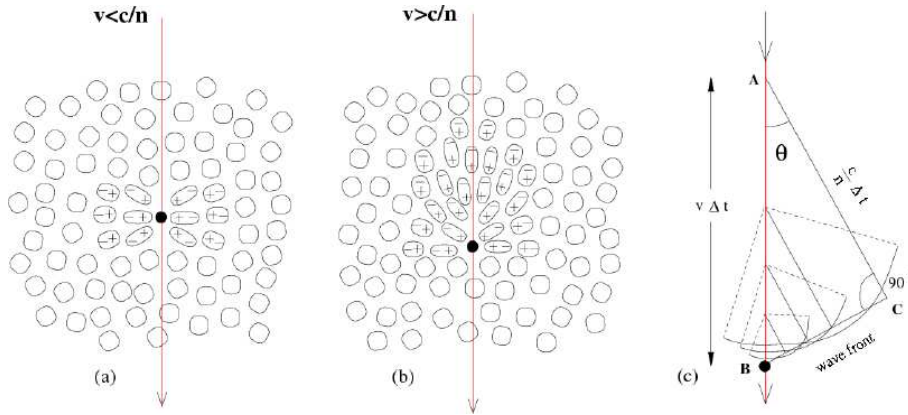


Figure 6.4: The neutral medium (panel a) suffers a short charge polarisation when a charged particle crosses it (panel b). The Cherenkov light is produced and the light fronts are generated along the particle path. The lateral distribution at the detector level is shown in panel c. Figure adapted from Paneque (2004).

and secondary e^\pm scatter further away from the shower axis.

The EAS Cherenkov radiation original spectrum peaks at UV wavelengths and decreases at the optical band (see Wao et al. 2006; see also Wagner 2007). However, several interactions of Cherenkov photons strongly affect the above spectrum as observed at the ground level, where it peaks at about 330 nm. Such attenuation factors include Rayleigh-scattering off air molecules, dominant in good atmospheric conditions and affecting the UV/blue part of the spectrum, Mie-scattering off aerosols and dust, and ozone, H_2O and CO_2 absorption, which effects on the spectrum attenuation will have a zenith dependence due to the molecules density gradient along the atmosphere.

6.2.2 Imaging Atmospheric Cherenkov technique

An IACT consists of a mechanical structure for tracking an astrophysical object, a collection area to gather the Cherenkov radiation and focus it to a camera located at the focal plane, and a receiver system to convert the collected light in a recordable image of the telescope FoV. The short time responses of light detectors are characteristic of IACTs, since both gamma-ray EAS and hadronic (background) EAS develop at \sim ns time-scales.

The image formed in the camera is a geometrical projection of the EAS. As a consequence of the angle dependence of the Cherenkov radiation, light coming from the upper part of the shower is focused onto a region close to the camera center,

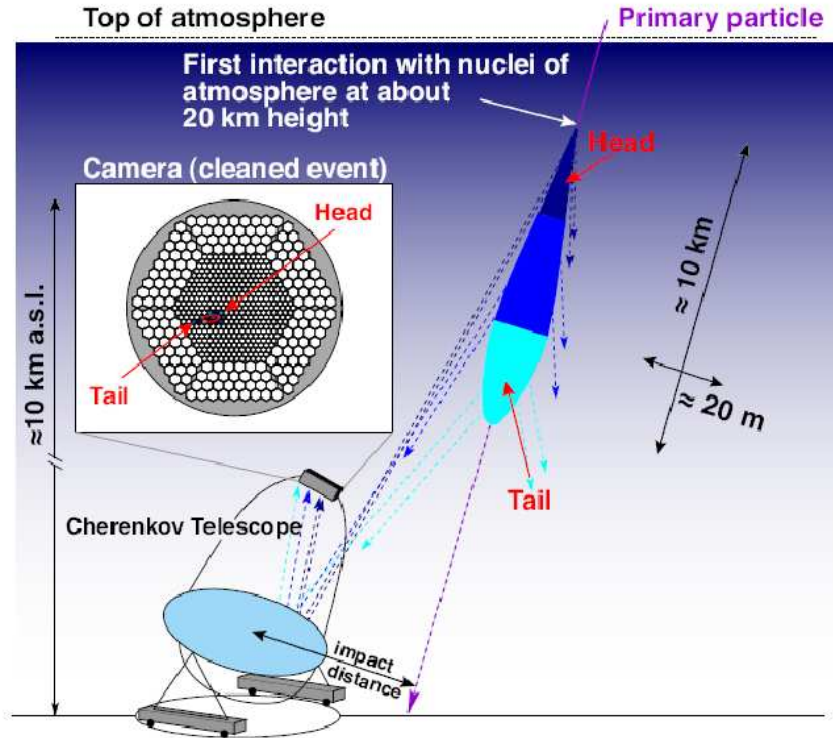


Figure 6.5: Sketch of the geometrical distribution of the cherenkov photons produced in an EAS and collected by an IACT telescope, focused to the camera and recorded for further analysis. Figure adapted from Mazin (2007).

whereas light emitted from the last stages of the shower is mapped further away (see Fig. 6.5). The shower development information is used to infer the characteristics of the particle that originated the EAS (see Sect. 7.3). Since the ratio between Cherenkov and ionization energy losses is roughly constant, the total Cherenkov light contained in the image is a good estimator of the primary particle energy. The orientation and shape of the recorded image are indicators of the direction of the primary.

High IACT sensitivity is accomplished thanks to the light spread of EASs and consequently the huge collection areas attainable, of about 10^5 m^2 . This enhances probability to detect a gamma-ray signal. The minimum detectable gamma-ray flux in a given number of observation hours is a function of the instrument sensitivity, which has a time dependence of the form $S(t) \propto \sqrt{t}$. We will enter into the details of signal analysis in Chapter 7.

On the other hand, the dilution over the Cherenkov light pool requires large mirrors and high sensitivity photodetectors. The photon density diminishes as the

energy of the primary particle gets lower. The reconstruction of the image parameters needs a minimum number of detected Cherenkov photons, so gamma-ray showers below a certain energy threshold E_{thr} can not be used for the signal reconstruction. $E_{thr} \propto \sqrt{\frac{\phi \Omega t}{A \epsilon}}$ (Longair 1994) is inversely proportional to the telescope mirror surface A and the light detection efficiency ϵ , which measures the efficiency conversion from Cherenkov photons to photoelectrons. It depends also on the background night sky radiation ϕ , on the solid angle subtended by the telescope Ω and on the total integration time t . In order to compare the E_{thr} of different IACTs, it is used to evaluate the peak of the trigger rate distribution for a specified object, such as the Crab Nebula for the northern observatories.

Bibliography

- Abdo, A. A., Ackermann, M., Ajello, M., et al. 2009, ApJS, 183, 46
- Aharonian, F. A., Akhperjanian, A. G., Bazer-Bachi, A. R., et al. 2007, ApJ, 664, L71
- Aharonian, F. A., Akhperjanian, A. G., Bazer-Bachi, A. R., et al. 2006a, ApJ, 636, 777
- Aharonian, F., Akhperjanian, A. G., Bazer-Bachi, A. R., 2006b, A&A, 460, 743
- Aharonian, F., Buckley, J., Kifune, T., & Sinnis, G. 2008, Reports on Progress in Physics, 71, 096901
- Albert, J., Aliu, E., Anderhub, H., et al. 2006, Science, 312, 1771
- Albert, J., Aliu, E., Anderhub, H., et al. 2007, ApJ, 665, L51
- Albert, J., Aliu, E., Anderhub, H., et al. 2008a, Science, 320, 1752.
- Albert, J., Aliu, E., Anderhub, H., et al. 2008b, Phys. Lett. B, 668, 253
- Aliu, E., Anderhub, H., Antonelli, L. A., et al. 2008, Science, 322, 1221
- De Angelis, A., Mansutti, O., & Persic, M., 2008, Rivista Il Nuovo Cimento, 31, 187
- Greisen, K. 1956, Prog. Cosmic Ray Physics, 3, 1
- Greisen, K. 1960, Annual Review of Nuclear Science, 10, 63
- Gaisser, T. K. in *Cosmic rays and particle physics*, Cambridge and New York, Cambridge University Press
- Jelley, J. V., & Porter, N. A. 1963, MNRAS, 4, 275
- Kraushaar, W. M., Clark, G. W., Garmire, G. P., et al. 1972, ApJ, 177, 341
- Longair, M. S. 1994, in *High energy astrophysics. Volume 2. Stars, the Galaxy and the interstellar medium*, Cambridge University Press, Cambridge
- Mazin, D. 2007, Ph.D Thesis, Technische Universität, München

- McConnell, M. L., Forrest, D., Ryan, J., et al. 1994, *ApJ*, 424, 933
- Paneque, D., Gebauer, H. J., Lorenz, E., & Mirzoyan, R. 2004, *NIMPA*, 518, 619
- Paredes, J. M., Martí, J., Ribó, M., & Massi, M. 2000, *Science*, 288, 2340
- Tavani, M. Barbiellini, G., Argan, A., et al 2008, *Nucl. Instrum. Methods Phys. Res. A*, 588, 52
- Thompson, D. J., Fichtel, C. E., Kniffen, D. A., & Ogelman, H. B. 1977, *ApJ*, 214, L17
- Thompson, D. J. 2008, *Rep. Prog. Phys.*, 71, 116901
- Wao, W. -M. 2006, *Journal of Physics G*, 33, 1232
- Wagner, R. M. 2007, Ph.D Thesis, Max Planck Institut für Physik, Werner Heisenberg Institut, München
- Weekes T. C., & Turver K. E., 1977, *Recent Advances in Gamma-Ray Astronomy*, 124, 279
- Weekes, T. C., Cawley, M. F., Fegan, D. J., et al. 1989, *ApJ*, 342, 379
- Weekes, T. C. 2008, *Proceedings of the 4th International Meeting on High Energy Gamma-Ray Astronomy*. AIP Conference Proceedings, 1085, 3

Chapter 7

The MAGIC telescope

7.1 Short overview

The MAGIC Telescope (Major Atmospheric Gamma Imaging Cherenkov Telescope) is located at Observatorio del Roque de los Muchachos, in the Canary island of La Palma, at latitude 28.8° North and longitude 17.9° West, and at 2200 m above sea level. The site is known for its good observation conditions, and previous gamma-ray experiments like the HEGRA CT1 (Mirzoyan et al. 1994), the HEGRA CT system of five telescopes (Daum et al. 1997), and the HEGRA array (Aharonian et al. 2002) operated at El Roque, and it also hosts several optical telescopes and solar observatories, including the 10.4 m diameter Gran Telescopio CANARIAS. The MAGIC Collaboration actually involves an international teamwork of physicists and technicians from 20 institutions from several european countries and also the United States. More than 200 are people involved in the project. MAGIC is being equiped with a second 17 m telescope. Below we will outline the MAGIC I main characteristics, and a brief description of MAGIC II is presented in Sect. 7.2.

MAGIC first Cherenkov images were recorded in March 2003, and the telescope became fully operative after one year of commissioning phase, which had lasted until autumn 2004. The telescope was thought as a novel experiment. Several new technologies are present in its design and system operations. Fig 7.1 shows a picture of the MAGIC I telescope. It has a huge reflector dish of 17 m diameter, the largest of the IACTs operating nowadays. The telescope frame is made of light weight carbon fiber tubes. The camera is composed by 577 PMTs with a 3.5° field of view (FoV). The signals registered in the camera are transported through optical fibers to an electronic room, where fast digitizers record them after a trigger logic selection.



Figure 7.1: *The MAGIC I telescope*

The technical details of the MAGIC hardware were firstly published in the late 90's (Barrio et al. 1998). Numerous technical improvements have been applied since then. The reader is referred to Goebel et al. (2008), Albert et al. (2008a), Aliu et al. (2009) and references therein for a complete description. In next sections we will briefly outline the main telescope characteristics to put in context the scientific output that the experiment is delivering.

7.1.1 Mounting and drive system

One of the goals of the MAGIC Telescope is the capability to reposition to any direction in the sky in a short time. This is intended to catch the prompt emission of Gamma-Ray Bursts (GRB) after an alert from an X-ray or gamma-ray satellite. To achieve this, the total weight of the moving parts of the telescope is required to be as low as possible, especially for the mirror frame. The choice was to support the mirror dish with a structure made of low-weight carbon fiber-epoxy tubes joined by aluminum knots. The weight of the combined frame and mirror dish is less than 20 tons, and the final weight of the telescope is about 64 tons.

The telescope tracking system is alt-azimuthal. Shaft encoders are responsible to maintain the angular position of the telescope both in azimuth and declination, providing an accuracy of $\sim 0.02^\circ$. The optical axis is calibrated using a CCD camera

located at the center of the mirror dish. This camera takes pictures of the stars in the FoV that are used to produce a telescope bending model. The positioning of the telescope is also ensured through the Starguider system (see below), which makes use of an independent CCD camera also located in the reflector frame. MAGIC cannot be operated in the so called *reverse* mode and cannot move over zenith. This causes just a small delay in the minimum repositioning time of the whole structure, currently of about 40 s.

7.1.2 Reflector and camera

The reflector has a parabolic shape with a focal length f equal to the dish diameter D , $f = D = 17$ m. This geometry ensures the near-simultaneity for the arrival times of light coming from all the mirrors. This permits a very short integration time window to collect the Cherenkov flashes, and reduces the effects of the Night Sky Background (NSB) light. As a counter effect, coma aberration affects the off-axis observations. It can deviate a given point observation up to 7% of the distance from the camera center as would be measured without aberration, and also the gradual stretching of the images in the radial direction has to be taken into account.

The reflector is composed by 956 squared mirror elements of 0.245 m² surface. Their shape is also parabolic, but their radii vary in order to match the global reflector geometry. The mirrors are build up with 5 mm thick AlMgSi alloy plates. The reflectivity of the mirrors ranges between 80% and 90%, although it has to be monitored to ensure that aging of the mirrors does not degrade the amount of light effectively collected.

Individual mirrors are grouped and mounted in an 1 m × 1 m support panels which further improve the dish focusing. This is accomplished through an Active Mirror Control (AMC) system (see Garczarczyk 2007). Two actuators and a red laser pointer are mounted in each mirror panel. A special camera records the position of the laser spots enclosing the MAGIC camera. Each mirror panel can be steered independently until the laser spot turns to its nominal position, which is indicated with respect to the position of some LEDs installed on the camera lids. The corresponding mirror panel positions are stored for each zenith angle in Look Up Tables (LUTs). They are used for quasi-instantaneous repositioning of the mirrors during data taking.

The Starguider system (Dorner et al. 2008), on the other hand, further improves the telescope pointing. It uses the catalog position of the stars in the FoV of a CCD

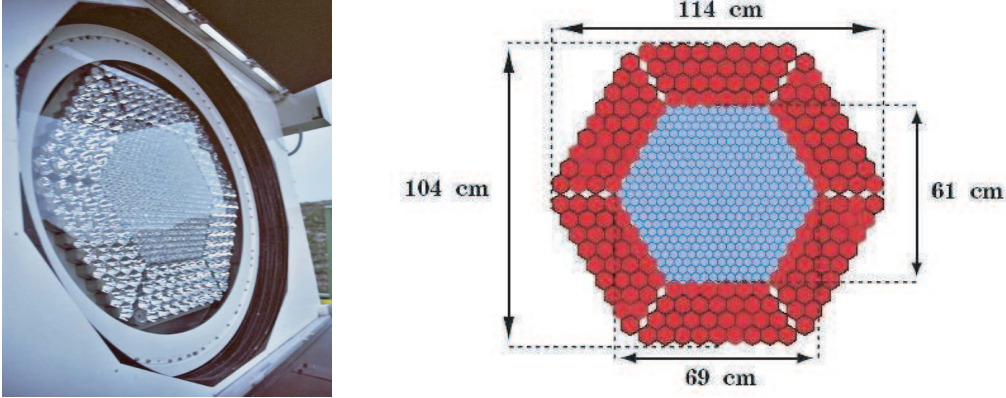


Figure 7.2: The MAGIC I camera is composed by the inner PMTs forming the triggering region and arranged in an hexagonal geometry, and the outer PMTs, with a wider FoV, that cover the external region of the camera and used for the estimation of the LEAKAGE parameter of the Cherenkov showers (see Sect. 7.3).

that points towards the MAGIC camera to correct for the misspointing during the offline data analysis. The Starguider system provides additionally information about the weather conditions during data taking, since the presence of clouds provokes the recognition of a smaller number of stars than clear night observations.

The MAGIC I camera (see Fig. 7.2) is composed by 577 PMTs that register the Cherenkov flashes and send the information via optical fibers to the counting house where they are recorded. Camera light losses are minimized by using hexagonal light catchers, known as Winston cones. The PMTs are designed to maximize their sensitivity to UV Cherenkov photons. The inner camera 397 PMTs have a FoV of about 0.1° each and form an hexagonal arrangement covering a total of about 2° . These inner pixel region is surrounded by 180 outer PMTs of 0.2° each. The whole MAGIC I camera PMTs cover a FoV of about 3.5° . The camera region containing the PMTs is protected by a UV transmitting plexiglass. A detailed description of the MAGIC I camera can be found in Gaug et al. (2006).

The PMTs convert the Cherenkov light into an AC signal through ultra-fast preamplifiers. Fast current driver amplifiers coupled to vertical cavity surface emitting laser diodes (VCSELs) convert back the pre-amplified PMT signal to light. The recorded signal can be as short as 2 ns duration, substantially avoiding the NSB contribution. The analog optical signal travels in optical fibers 162 m long up to the counting house without almost no signal attenuation. Fig. 7.3 shows the scheme of the signal collection diagram and the further data readout chain, which is explained below.

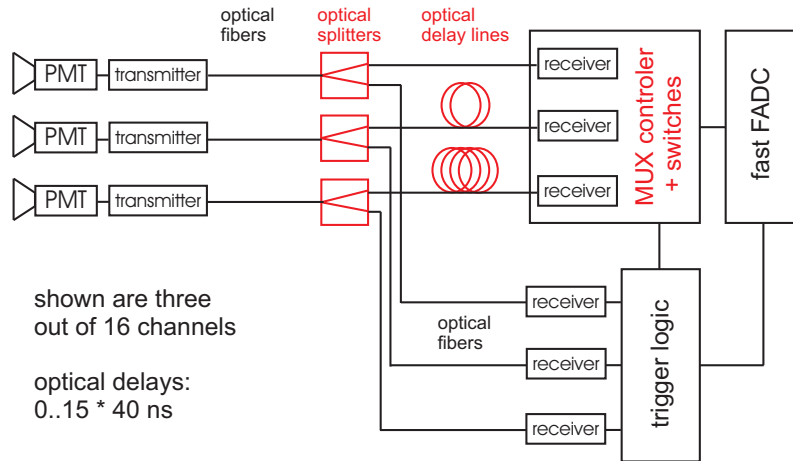


Figure 7.3: Readout chain of the whole MAGIC data acquisition system (figure adapted from Goebel et al. 2008).

7.1.3 Read-out, trigger and data acquisition chain

The optical signals reach the receivers located in the counting house and converted back to electrical impulses by fast GaAs diodes. The signal is separated in two parts. One part goes to the trigger branch, and the other one goes to the digitalization system (see Fig. 7.3). The trigger scheme is divided in two different levels. The first level trigger, Level-0, produces a ~ 6 ns long digital signal if the incoming receivers signal amplitude is higher than a given value. This value can be adjusted independently for each pixel. For instance, it can be higher for those pixels containing the light from a star in the FoV or those pixels collecting a higher flux from the NSB. This adjustable Individual Pixel Rate (IPR) is typically in the range of 100 MHz to 500 MHz, and works only for the inner camera PMTs. About 90% of the gamma-ray showers from a point source are contained in this Level-0 trigger region. Light flashes contained in the outer part of the camera which likely do not have a gamma-ray origin will not be triggered, providing a background rejection already at this stage.

Next trigger level, Level-1, is based on an event coincidence logic. The signals from Level-0 trigger are grouped in 19 cells containing 36 pixels each. A signal is triggered by Level-1 only if at least on of the 19 cells fulfills a next neighbor (NN) pixel criteria in a close compact configuration. Since images of electromagnetic showers are compact, this strategy helps to reject part of the background signal contribution. During normal data taking, a 4 NN logic is used, leading to a ~ 250 Hz - 300 Hz trigger rate.

When an event passes the trigger stage, it is recorded by the Data Acquisition

system (DAQ). A 8-bit Flash analog-to-digital converter (FADC) system digitizes the signal at a 2×10^9 Samples per second (2GS/s) rate (Goebel et al. 2008) by using a novel fiber-optic multiplexing technique. Such a high sampling rate provides information of the timing development of the showers, which is used to distinguish between hadronic and electromagnetic Cherenkov events. The dynamical operating range is enhanced by dividing the signal coming from the receiver into a High-gain and Low-gain channels. When the High-gain channel shows a larger signal amplitude than a given value, the Low-gain channel is digitized with a 55 ns delay. The total signal in such a case is composed by the summation of both channel contributions.

The MAGIC trigger rate is kept between 20 Hz and 250 Hz, corresponding to an energy threshold of ~ 60 GeV. Although the lowering of the Level-0 level would lower the energy threshold, the NSB fluctuations, the PMT afterpulses¹ and the DAQ limitations would make the trigger rate too unstable.

7.1.4 The Calibration system

The acquisition chain described above up to the FADC signal processing has to be calibrated, both in number of photoelectrons (phe) generated by the Cherenkov showers and the time units of their development. This is accomplished through the MAGIC calibration system (see Gaug 2006). Pulses of light at different wavelengths (370 nm, 460 nm and 520 nm), intensities and pulsation frequencies are generated in a calibration pulser box. The calibration proceeds then in two steps. A relative calibration equalizes the response of different channels when subjected to the same input signal, whereas an absolute calibration is then the responsible to convert the recorded signal from FADC counts to physical quantities related to the photon fluxes arriving to the camera. The absolute calibration makes use of a PIN diode and blind pixels mounted in the MAGIC camera. The PIN diode is used to monitor the light pulses emitted by the calibration box. The mean number of photons that arrive at the camera plane are estimated from the signal collected in the PIN diode, its quantum efficiency, the light spectrum of the different wavelength LEDs and the geometry of the system. A blind pixel is an attenuated pixel able to resolve a single phe. This permits the estimation of the mean number of phe produced in the photocathode from the pulses sent by the calibration box. Finally, a complementary method to calibrate the signal is the Excess Noise Factor, or F-Factor method (Mirzoyan 1997). This method is based on the linear relation between the

¹Afterpulses are generated in the PMTs as a consequence an ion detached from the dynode impacting on the photocathode. This generates many electrons which provoke a huge signal. The afterpulse signal is randomly generated, and its mean rate is about 0.3% of the pixel rate.

excess noise produced by the PMTs and the initial number of phe. The F-factor of a given device is defined as $F = (\text{Signal/Noise})_{\text{in}} / (\text{Signal/Noise})_{\text{out}}$. By knowing the F -Factor of the PMTs and using the analysis of the output signal of each pixel, the average number of phe arriving at each PMT can be derived.

7.2 MAGIC II

The MAGIC Collaboration has been upgraded with the construction of a second 17 m diameter telescope. The new telescope is found at El Roque de los Muchachos at about 80 meters away from the original one (see Fig. 7.4). The commissioning phase is taking place during the redaction of this Thesis. MAGIC II is expected to be fully operational during Autumn 2009. Although we did not make use of this new facility, we outline here some of the major characteristics and improvements it will bring in the detection of VHE gamma-ray sources.

The frame of the second telescope is very similar to that of MAGIC I, and is made of light-weight reinforced carbon fiber tubes. The drive system and the AMC are slightly improved, whereas the reflector uses larger mirror elements, with surface of 1 m^2 with a reflectivity of about 80%-85%. Substantial improvements are present in the camera layout. MAGIC II camera is composed by 1039 pixels of 25.4 mm diameter each. They cover a FoV similar to that of MAGIC I, $\sim 3.5^\circ$. In MAGIC II there are no bigger pixels on the outer part of the camera, so a larger number of pixels is required to cover the whole FoV. The trigger region covers a radius of about 1.25° . A novel modular design arranges pixels in groups of seven, which makes easier the control and maintenance of the camera. The readout system is also improved. The optical signal from the camera is transmitted via optical fibers to a digitalization system based on a low power analog sampler, the so-called Domino Ring Sampler. The analog signals are stored in a ring buffer. Once a trigger is received, a region in the ring buffer is read out at a frequency of 40 MHz and sent to a computer which stores the events in a disk.

The new telescope can be operated both independently or in stereoscopic mode with the old one. This last option can improve the MAGIC capabilities in several ways. First of all, the reconstruction of the image parameters (see next Section) will be easier. The source position will be obtained from the intersection of the major axes of the two independent images of the shower. In addition, the height of the shower maximum will be determined easily with the stereoscopic observation. Also the background suppression efficiency will be enhanced, since rejection of non



Figure 7.4: *MAGIC telescopes at El Roque de Los Muchachos in the canary island of La Palma, Spain. The MAGIC I telescope is on the left, the MAGIC II telescope on the right. The small building at the left corner of the picture is the counting house where the operation of both telescopes is realized.*

gamma-ray events can be checked twice when quasi-simultaneity of the registered signal is established. The angular resolution is also refined, leading to an estimated improvement of about 20 %. Furthermore, energy resolution at about 15% will be possible (with MAGIC I alone it was about 25 %). According to the latest Monte Carlo simulations, the overall improvement in sensitivity of the stereo system will be about a factor 2-3 with respect to single telescope observations.

7.3 Data analysis procedure

We describe in this Section the steps followed in this Thesis for the analysis of the MAGIC telescope data. After a brief outline of the different types of data and background events to be handled during the analysis, we will focus on the quality check selection of runs and single events required for a good performance of the analysis chain, and will refer to the signal extraction, image parameterization and γ /hadron separation processes necessary for the final signal evaluation.

7.3.1 Data types and observation modes

The acquisition chain ends up with the DAQ storage of large amounts of raw data files containing the information of the signal readout of every camera pixel. Each raw data file is called a run, and is identified by a unique number assigned to it. There are three main types of runs recorded during MAGIC data taking :

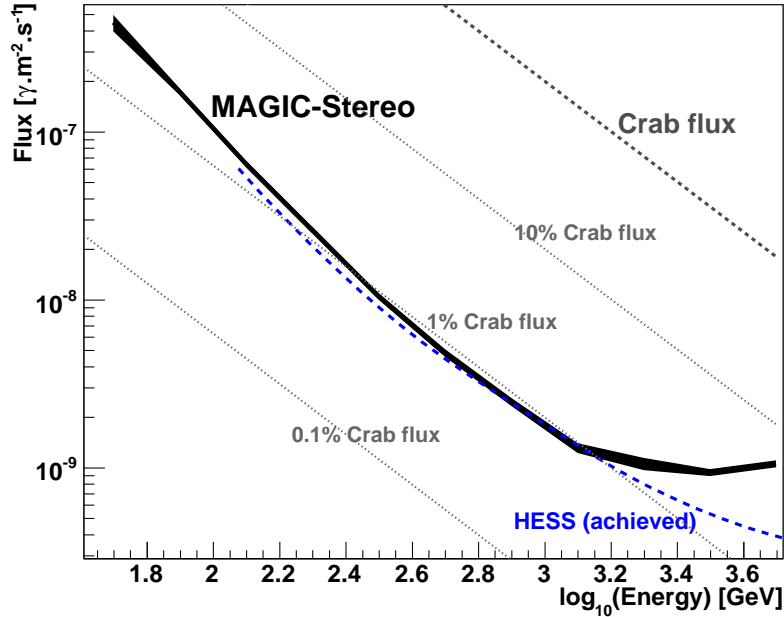


Figure 7.5: *Estimated sensitivity of the MAGIC telescopes in stereoscopic mode. The Crab Nebula flux and its 0.1 % and 1% levels as well as the performance achieved by the HESS array of telescopes are also displayed for comparison. Figure adapted from Colin et al. (2009).*

Data runs First of all, data runs are those corresponding to the events recorded when tracking a given astrophysical source. Only events satisfying a specified trigger criteria are stored (see Sect. 7.1.3). Secondly, a sample of Monte Carlo simulated gamma-ray showers is needed. The analysis chain relies on these simulations to know the detector response to gamma-ray showers. The agreement between new Monte Carlo simulations accounting for hardware changes is continuously checked (Majumdar et al. 2005). The Monte Carlo gamma showers are used to optimize the cuts for background rejection and to estimate the effective collection area after all cuts. This is done by using the CORSIKA 6.019 package (Heck et al. 1998), which simulates the development of the gamma-ray air shower in the atmosphere. In a second step, the absorption of the Cherenkov light in the atmosphere (accounting for Rayleigh and Mie scattering, see Sect. 6.2) is also simulated, as well as the telescope reflector characteristics. In addition, the camera response, the trigger and the acquisition system is also taken into account in the Monte Carlo models. Finally, apart from data from the astrophysical source of interest and Monte Carlo simulations, also Crab Nebula data is used during the analysis. The Crab Nebula was the first detected source in the VHE gamma-ray domain (Weekes et al. 1989). Since then, it has been extensively studied in the whole spectrum. Recently, MAGIC reported the Crab pulsed emission at VHE, which was never seen before (Aliu et al. 2008). Both the Nebula and the pulsar emission hide physical processes to be understood, but this does not prevent to use it as a standard calibration source to

test the telescope performance of ground-based gamma-ray observatories.

Calibration runs contain 50000 dedicated UV calibration events recorded right before the initialization of the observation of each of the scheduled source every night. Furthermore, if a source is tracked for more than \sim one hour or if data taking weather conditions change substantially, extra calibration runs are recorded. In addition, interleaved calibration events are also taken between different data runs during normal data-taking.

Pedestal runs provide information on the Night Sky Background (NSB) and other sources of noise that can produce an offset in the recorded data. When taking pedestal events, the read out is triggered randomly with 500Hz to measure the unwanted offset, which is later subtracted from the signal. At least one run with 1000 pedestal events is taken together with a group of calibration runs before each data run, whereas interleaved pedestal runs are also recorded during data taking.

The MAGIC telescope operates in two different observation modes, the so-called ON-OFF mode and the so-called *Wobble* mode. In the ON-OFF mode the source is located at the center of the camera. The background is determined from a dedicated OFF measurement, for which a region of the sky with similar star field and NSB conditions is required. To avoid spending too much time for OFF observations, the same OFF data are used for different sources. One just has to make sure that the data quality and telescope performance is the same for both ON and OFF data. In the *Wobble* mode, instead, OFF data are not necessary, as the source is observed 0.4° away from the camera center and the background can be determined from symmetric regions also offset by 0.4° from the camera center not including any bright source (see Fig. 7.6). The simultaneous acquisition of OFF data in *Wobble* mode avoids this requirement. In the analysis of the microquasars described in Chapter 8, only *Wobble* data is used. The analysis of the eastern interaction regions of SS433/W50, however, makes use of *Wobble* data as ON observations, whereas PSR J0358 ON observations are used as OFF data, since no gamma-ray signal is found in dedicated previous analysis of this source. Crab Nebula observations and Monte Carlo simulations for the optimization and energy estimation of the signal in ON or *Wobble* mode are required to analyze each type of data.

7.3.2 Data sample quality check

The first step in the reduction process is the selection of the data sample that will be further analyzed. A data quality check is performed to ensure the good conditions

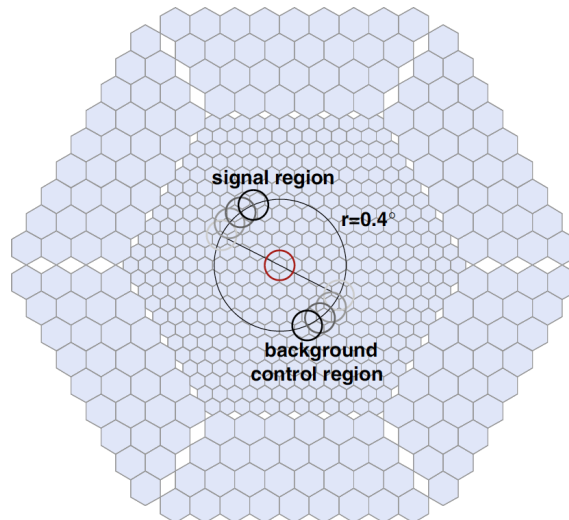


Figure 7.6: *Different observation modes of the MAGIC telescope. In ON (OFF) observations, the source (background) is localized in the center of the camera, here represented with a red circle, whereas in Wobble mode the source and the background control region, the antisource, are located 0.4° away from it. Further background regions can be obtained along the 0.4° radius black circle (up to 5 regions can be used). Furthermore, systematic errors like camera inhomogeneities can be partially avoided since the source position in the camera moves during data-taking and data from different camera regions are recorded.*

of the sample runs for the whole data-set obtained under different telescope and atmospheric conditions. A number of factors has to be considered in this selection processes.

- The trigger event rate, monitored during normal data taking, has to be checked for each run and compared between observations during different nights. If the trigger rate is too low, bad atmospheric conditions could be present at La Palma during observations. Alternatively, some telescope misbehavior could be present during data taking, and could appear as a strange behavior of the trigger rate. In the analysis of the microquasars Cyg X-1 and SS 433 presented in Chapter 8 we discarded all those runs showing a trigger rate below 20 % of the mean level for each observation night.
- An online runbook is provided by the shifters at La Palma for each data taking night. These runbooks have to be checked for the whole data sample, considering the technical problems occurred during data taking and any other issue affecting acquisition chain. Those runs for which the DAQ was aborted, calibration runs in which the box failed to fire and data with malfunctions of the FADC system due to extreme temperatures of the counting house (as is the case of several runs of 21th and 22th August 2008 of SS 433 observations) have been correspondingly excluded thanks to this check.

- The MAGIC database permits the analyzer to check for runs tagged as test runs, and runs with wrong loaded trigger tables, calibration script or discriminator threshold settings. In addition, the database provides information on the misspointing of the telescope during data taking. The Starguider system provides a measure of this misspointing as well as the number of recognized stars in the FoV. A low number of recognized stars (of the order of a few) would mean that the telescope can not properly compare its pointing position with respect to catalogued positions. Moreover, the telescope Point Spread Function (PSF) can also be found in the database. The PSF defines the telescope optical performance and its imaging resolution, and is calculated from the width in the radial direction of the muon ring images in the camera. The PSF can vary due to adjustments of the optical elements of the telescope (AMC, strong temperature variations), and this must be taken into account in the data reduction process. The analysis performed in this Thesis has been applied to runs with PSF in the range 10.9 mm to 13.5 mm. As will be explained below, information on the PSF is required for the selection of Monte Carlo gamma-ray simulated showers, which are produced for different PSF telescope performances in order to adequate to the data sample conditions.

7.3.3 Image cleaning and parameterization

Image cleaning is the process by which the pixels whose signals are not produced by Cherenkov EAS photons are removed from the analysis chain. Those pixels are kept apart before the parameterization of the shower images, which is usually contained in only a few percent of the total camera pixels (see Fig. 7.7). In the cleaning process, a threshold signal q_{core} ($= 6$ phe in the analysis of the sources presented in Chapter 8) for the number of phe per pixel is adopted to define the core of the shower image. An additional requirement for a pixel to be part of the shower core is that a neighbor pixel has also a signal above q_{core} (rejecting in this way the effects of the PMTs afterpulses). A second level charge q_{boundary} ($= 3$ phe in the analysis performed in this Thesis) is required to define the boundary pixels of the shower image. Depending on the values of both q_{core} and q_{boundary} , a smaller or larger number of pixels per image will be selected to define the shower. A large number of pixels helps in the analysis of low-energy events, since a minimum number of pixels is needed to proceed in the analysis chain. However, a low cleaning level implies the presence of noise pixels in the image and difficults the image parameterization.

The cleaning procedure includes also the timing information of the shower development. The mean arrival time of the core pixels is calculated, and those pixels

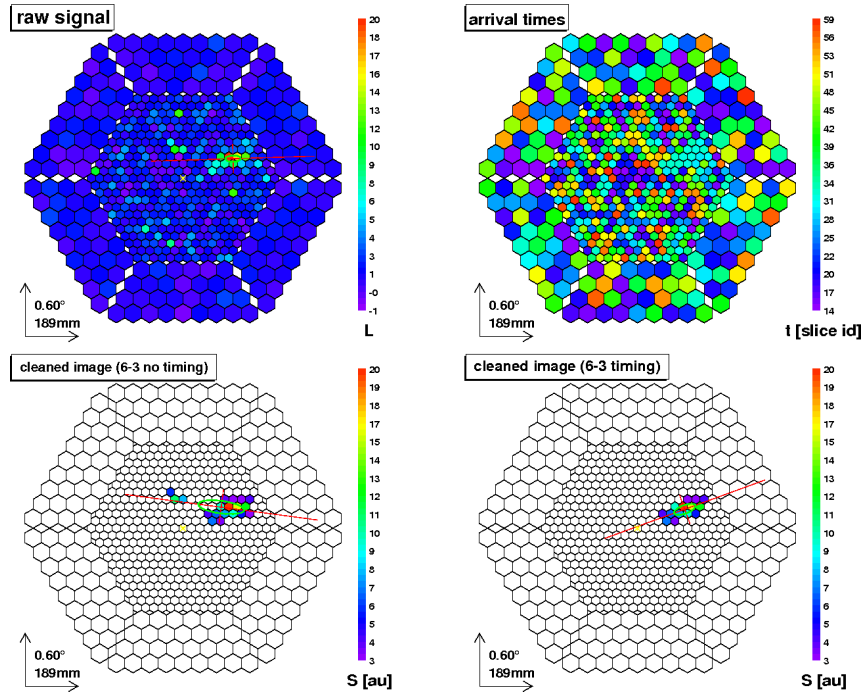


Figure 7.7: Picture of a simulated gamma-ray shower as it is recorded as raw data (upper-left panel) and its arrival times information (upper-right panel); subsequent image cleaning with 6-3 phe minimum charge levels obtained without the time information (bottom-left panel) and with it (bottom-right panel) are also shown. The simulated shower is located at the center of the camera and indicated by a yellow star. (Figure adapted from Aliu et al. 2009).

whose arrival time do not fall inside an interval δt_{core} are excluded from the shower image. Additionally, a time interval lower than a given $\delta t_{\text{boundary}}$ for the difference of a given boundary pixel and its core neighbor is required to keep this boundary pixel in the shower image. A value of $\delta t_{\text{core}} = 4.5$ ns and $\delta t_{\text{boundary}} = 1.5$ ns is typical for the standard MAGIC cleaning procedure (Tescaro et al. 2007), and are also the levels used in this Thesis.

After the image cleaning, the shower image is represented by the surviving pixels distributed in the MAGIC camera plane. Gamma-ray induced showers show an elliptical shape in this plane, the major axis being related to the longitudinal shower development and the minor axis representing its lateral evolution. The so-called Hillas parameters (Hillas 1985) are used to characterize the shower images. This parameters are based on the first, second and third moments of the two-dimensional distribution of the signal along the image, and they are used in the analysis in order to separate the true gamma-ray signals from the background contribution (mostly hadronic showers). The Hillas parameters can be roughly divided in two groups, those depending on the assumed source position in the camera and those independent of it. They are called source-dependent and source-independent parameters,

respectively. They are used for different analysis procedures, and will be separately explained below. Fig. 7.8 shows some of the Hillas parameters defining a shower image.

Source-independent parameters

Since these parameters do not depend on the assumed position of the source in the camera, they can be used to search gamma-ray signals from a slightly extended source or for a emitter location which position is not exactly known in the FoV (as it is the case for the SS 433/W50 eastern interaction regions described in Chapter 8).

- **SIZE**: Charge contained in all the pixels defining the shower image. It provides direct information about the energy of the primary particle.
- **LENGTH**: Half length of the major axis of the shower ellipse. It is related with the longitudinal development of the shower in the Earth atmosphere.
- **WIDTH**: Half width of the minor axis of the shower ellipse, which provides information of the transversal development of the EAS. This is a powerful discriminator parameter, since the lateral spread of a gamma-induced EAS is substantially lower than that corresponding to an hadron-induced one (see Sect. 6.2).
- **CONC(n)**: Fraction of image charge contained in the n brightest pixels with respect to the total charge of the image. It gives information about the compactness of the shower core. A number $n = 2$ is used in the standard analysis, and is the value used in this Thesis.
- **M3LONG**: Third moment of the image along the ellipse major axis. It is used to determine the shower direction, by distinguishing where the shower head and tail are located. When the head of the shower is closer to the camera center, M3LONG is defined positively. This is a powerful discriminator parameter, except for those showers with a low SIZE parameter.
- **LEAKAGE**: Fraction of the total light contained in the pixels of the outermost ring of the camera. High LEAKAGE values indicate that the image is truncated, so information from some parts of the shower is not contained in the camera. Fully contained images have zero or very small values of LEAKAGE. It is a crucial parameter for the reconstruction of the primary particle energy, specially for the highest energies (above ~ 2 TeV).

- **THETA²**: θ is defined as the angular distance between the assumed source position and the estimated source position of the event (see the right panel in Fig. 7.8). The estimated source position is obtained through the DISP method (Domingo Santamaria et al. 2005). This method estimates the source position assuming it has to lie along the major axis of the ellipse. A DISP parameterization is a function of several image parameters, but its solution in determining the source location is not unique in the sense that two different solutions are possible, one for the shower head and the other one for the shower tail. With the help of the M3LONG parameter, however, this degeneracy can be removed. For gamma-rays, the direction of the showers will be close to the direction of the gamma-ray source, whereas for hadrons the directions are isotropically distributed. For convenience, the squared value of θ is used, since its distribution is flat for background events while it peaks at $\theta^2 \rightarrow 0$.
- **TIME RMS**: Defines the root mean square of the arrival times for those pixels that were not rejected in the cleaning process. It provides an estimation of the time spread of the arrival times without any dependence on the precise location in the camera.

Source-dependent parameters

These parameters are calculated with respect to a given position in the camera (for instance the assumed source position). Source-dependent parameters are used for the analysis of point-like sources as the ones presented in Chapter 8, although source-independent parameters have to be also provided in some parts of the analysis chain, for instance for the computation of the sky maps.

- **DIST**: Distance between the image center of gravity and a reference point in the camera plane, normally the camera center. It is related to the shower impact parameter and helps in the estimation of the energy of the EAS.
- **ALPHA**: Angle between the major shower axis and the direction determined by the image center of gravity and a reference point in the camera plane (typically the source position in the camera, most of the cases coinciding with the camera center). ALPHA is the angle by which the main axis of the image misses the reference point. Gamma-induced images point towards the position of the source in the camera, whereas hadron-induced ones are randomly distributed and show a flat ALPHA profile. In this way, ALPHA becomes one of the most powerful parameter for γ /hadron separation.

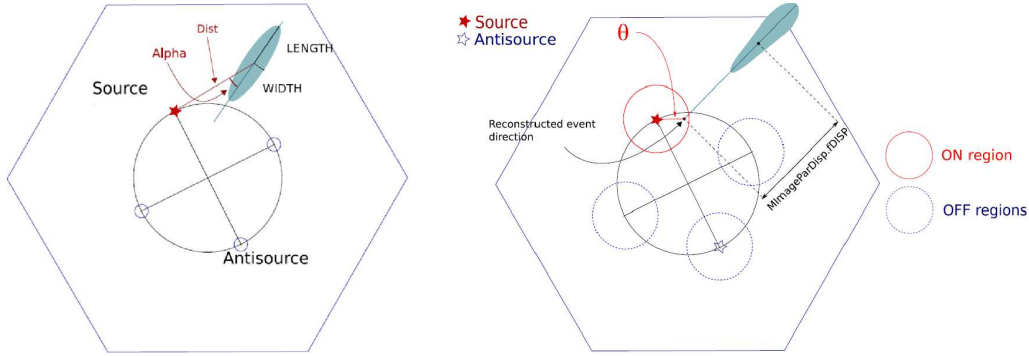


Figure 7.8: Main Hillas parameters defining a shower image as projected in the MAGIC camera plane. The different ON and OFF analysis regions in Wobble mode are displayed (see Sect. 7.4). Figure adapted from Gaug & Moralejo (2008).

- **TIME GRADIENT:** Defines the gradient of the arrival time along the shower major axis. The TIME GRADIENT is defined as positive when the arrival time increases when moving away from the source position in the camera, whereas it is negative otherwise. This definition makes this parameter to be included in the source-dependent group.

Before proceeding with the gamma-ray/background separation, some additional quality checks are performed in order to reject those events that are most likely not generated by a gamma-ray. For instance, camera sparks produced in a photocathode discharge can reflect on the PMT's Winston cones illuminating the PMTs nearby. This produces an intense signal that can be easily removed with a dedicated cut. Furthermore, events with a large impact parameter that are not entirely contained in the camera will provoke a bad Hillas parameter reconstruction. The parameter LEAKAGE is used as a measure of this. In our analysis, LEAKAGE higher than 10% are rejected.

Camera inhomogeneities can arise due to changes in the camera and/or signal transmitters. A check of the images center of gravity and the homogeneity between the calculated Hillas parameters for the ON and OFF data samples is needed (in the case of *Wobble* observations, however, symmetric conditions are directly obtained since the same amount of OFF data is taken from both camera halves). To ensure camera homogeneity, the gain of each PMT can be modified by changing the High-Voltage settings. This process is applied regularly, but does not prevent from having different conditions within the sample to be analyzed. The observations of microquasars presented below were performed in rather compact time intervals (in

Cyg X-1 data were recorded during \sim one month in cycle III, whereas for SS 433 nine consecutive nights during august 2008 have been analyzed), and camera large inhomogeneities are not present in the data set. The Crab data sample used for optimization as well as PSR J0358 data used as OFF data for the interaction regions analysis of SS 433 do not show either strong inhomogeneities for showers with SIZE larger than 80 phe.

7.3.4 γ /hadron separation

The main difficulty in the reconstruction of the physical properties of a gamma-ray shower lies in its identification within the much more numerous hadron-induced showers present in the recorded images (the ratio of gamma-ray to hadronic-induced showers is typically $\sim 10^{-3}$ - 10^{-4}). For this purpose, a multivariate classification method known as the Random Forest Method is used (Albert et al. 2008b). This technique is based on the construction of decision trees built up with some elements of random choices applied to a data sample. This is usually referred as the training procedure, since the resulting matrices that constitute the output of the Random Forest are later applied to the data-sample of interest. In the training process, Monte Carlo gamma-ray simulated showers are used, as well as a sample of background data (although it can also be used a part of a faint source data sample, since as already noted the amount of gamma-induced showers is very low with respect to the hadronic one).

The Random Forest training then establishes the suitability of a given shower image to be gamma-like or hadron-like through the classification parameter HADRONNESS. A given event can be defined as a vector \vec{v} , whose elements are some of the shower image parameters defined above. The Random Forest randomly chooses one of the parameters of the image, and examines if its value is lower or higher than a given cut value. Then it proceeds with another parameter (or by chance the same again) and repeats the operation for the proper parameter cut value. In this way, the vector \vec{v} representing the event follows a track through the tree that is determined by the numerical values of its components and the tree nodes cut values, until it ends up in a terminal node. This terminal node assigns a class label l to \vec{v} , which is denoted by $l_i(\vec{v})$, being i the tree number. The vector \vec{v} will be classified by all trees and, as a final result, the HADRONNESS is calculated through

$$\text{HADRONNESS}(\vec{v}) = \frac{\sum_{i=1}^{n_{\text{trees}}} l_i(\vec{v})}{n_{\text{trees}}}. \quad (7.1)$$

The parameters that have a high power to discriminate and are the input for the Random Forest training are the WIDTH, LENGTH, CONC, DIST, M3LONG, TIME RMS and TIME GRADIENT. In addition, the SIZE and zenith angle under which the source has been observed must be taken into account. The background rejection cuts scale dynamically with SIZE, whereas the same gamma-ray arriving at different zenith angles will show up differently in the image parameter space. To use them for scaling purposes they are not included in the Random Forest training, but the analyzer must check that the corresponding distributions in the Monte Carlo sample and background samples are roughly equal.

The HADRONNESS parameter is the main rejection parameter used for the γ /hadron separation in the analysis chain. The value of HADRONNESS for each event lies in the range [0,1]. The event will be gamma-like for HADRONNESS close to 0, and hadron-like for HADRONNESS near to 1. It is shown that gammas and hadrons are well distinguishable for images with SIZE \gtrsim 300 phe. Below this value the separation of the HADRONNESS distributions is less clear.

7.4 Signal evaluation

In order to evaluate the statistical reliability of a positive result in the search for gamma-rays from a given astrophysical source, one has to determine the probability that the excess count rate is not originated in a spurious background fluctuation. This is done by using a reference source with a well known behavior at gamma-rays, such as the Crab Nebula. The optimization of the cuts in HADRONNESS and ALPHA (or THETA² if we perform a source-independent analysis, see Sect. 7.3.3) on a Crab Nebula sample is performed and the best cut values (those that report the highest analysis sensitivity, see below) are applied to the source data. A cut in SIZE is performed before the HADRONNES and ALPHA cuts. As mentioned above, the γ /hadron separation works well for SIZE \gtrsim 300 phe, whereas the use of the TIME GRADIENT parameter in the Random Forest allows to go down up to SIZE \approx 150 phe. A lower SIZE cut of 150 phe is applied in the analysis presented in this Thesis. When no positive result is found, an upper limit to the gamma-ray flux of the studied source can be placed.

7.4.1 Optimization of HADRONNESS and ALPHA/THETA cuts

The search for a gamma-ray signal proceeds with a cut in the HADRONNESS parameter defined in previous section. However, many of the gamma-ray candidates that survived the background rejection cuts are still hadronic events. The γ /hadron separation can be further optimized through the search for signal in a certain parameter space called the signal region in which gamma-ray events are expected to accumulate. The signal region is defined by the ALPHA parameter, or THETA if the precise location of the source is only known to be within a given angular distance from a certain point in the camera. Below we will refer to the parameter ALPHA, and will comment on particular issues of the THETA analysis when required.

The number of events in the signal region that passed the γ /hadron separation process is called N_{ON} . Similarly, N_{OFF} is defined as the number of events in the OFF region, that is, events coming from a sky region in which no gamma-rays are expected to be present. The cut in ALPHA defines the region in which the number of excess events N_{ex} is evaluated from the subtraction of the OFF ALPHA histogram to the ON ALPHA histogram:

$$N_{ex} = N_{\text{ON}} - \alpha \cdot N_{\text{OFF}}. \quad (7.2)$$

The parameter α (that is independent of ALPHA angular parameter defined above) indicates the ratio of integrated number of events in the ON and OFF regions. It can also be understood as the time devoted to the source observation over that for the background. For *Wobble* mode observations, the analysis can use two additional OFF regions corresponding to the source position rotated by $\pm 90^\circ$ with respect to the camera center (see Fig. 7.8). In such a case the value of $\alpha = 1/3$ is taken.

A scan in the ALPHA and HADRONNESS cuts is performed in a reference data sample, in our case the Crab Nebula observations. The combination of HADRONNESS cut and ALPHA cut that provides the best significance of the Crab Nebula excess signal. It is important to note that both the source and the Crab Nebula samples have to be taken for similar telescope performance conditions. This is accomplished by selecting observation dates as nearby as possible. Furthermore, the zenith angle range has also to be similar.

7.4.2 Significance calculation

There exist various procedures adopted by different experiments to estimate the statistical reliability of a given gamma-ray signal. One option is to directly estimate the standard deviation of the observed number of excess events, N_{ex} . Given that the counts on the ON and OFF regions are results of two independent measurements, the variance of the excess signal can be calculated by

$$\begin{aligned}\sigma^2(N_{ex}) &= \sigma^2(N_{\text{ON}}) + \sigma^2(\alpha N_{\text{OFF}}) \\ &= \sigma^2(N_{\text{ON}}) + \alpha^2 \cdot \sigma^2(N_{\text{OFF}})\end{aligned}\quad (7.3)$$

Assuming a Poisson distribution for both ON and OFF events, $\sigma(N_{\text{ON(OFF)}}) = \sqrt{N_{\text{ON(OFF)}}$, the standard deviation of the excess signal can be expressed as

$$\sigma(N_{ex}) = \sqrt{N_{\text{ON}} + \alpha^2 \cdot N_{\text{OFF}}}\quad (7.4)$$

Now, the significance S is defined as the ratio of the excess counts above background to its standard deviation, and will be given by

$$S = \frac{N_{ex}}{\sigma(N_{ex})} = \frac{N_{\text{ON}} - \alpha N_{\text{OFF}}}{\sqrt{N_{\text{ON}} + \alpha^2 N_{\text{OFF}}}}\quad (7.5)$$

Although the above expressions for S are a useful estimation of the significance of a given excess signal, Li & Ma (1983) demonstrated that it could often produce an overestimation of S of a positive signal. These authors concluded that to correctly evaluate the statistical significance a more accurate expression should be used:

$$S = \sqrt{2} \left\{ N_{\text{ON}} \ln \left[\frac{1 + \alpha}{\alpha} \left(\frac{N_{\text{ON}}}{N_{\text{ON}} + N_{\text{OFF}}} \right) \right] + N_{\text{OFF}} \ln \left[(1 + \alpha) \left(\frac{N_{\text{OFF}}}{N_{\text{ON}} + N_{\text{OFF}}} \right) \right] \right\}^{1/2}\quad (7.6)$$

This last expression is the one used in the analysis presented in this Thesis.

7.4.3 Flux sensitivity

In addition to the significance of the signal computed above, the analysis of a given source can be quantified in terms of the telescope sensitivity. The sensitivity of an IACT is strictly defined as the gamma-ray flux that a source should emit within a given range of energies (or above a given energy for an integral flux sensitivity) to be detectable in 50 hours of observation, this is, to achieve a 5 sigma detection ($S = 5$) in 50 hours. In order to compare the capabilities of different IACTs, it is usually expressed as a percentage of the flux from a well known source, like the Crab Nebula.

Strictly speaking, one should use Eqn. 7.6 for Crab Nebula observations for a given observation time t_{obs} . The number of ON and OFF events can be expressed as $R_{ON}^{Crab} \times t_{obs}$ and $R_{OFF}^{Crab} \times t_{obs}$, respectively, where $R_{ON(OFF)}^{Crab}$ is the ON (OFF) Crab Nebula event rate. Assuming that both R_{ON}^{Crab} and R_{OFF}^{Crab} are kept constant, the number of standard deviations of the signal can be computed for $t_{obs} = 50$ h. Alternatively, by fixing a 5 σ value in Eqn. 7.6 and the same $t_{obs} = 50$ h, a certain rate R_{ON}^{min} is found. The ratio $R_{ON}^{min}/R_{ON}^{Crab}$ ($\times 100$) will provide the minimum percentage of the Crab Nebula flux achievable by the telescope.

Instead of using Eqn. 7.6 to compute the signal significance, it is common to express the flux sensitivity as the minimum gamma-ray flux detectable in 50 h to obtain a gamma-ray excess with signal to noise ratio $N_{ex}/\sqrt{N_{OFF}} = 5$ (see, e. g., Aliu et al. 2009). The number of standard deviations obtained is expressed as a function of time as:

$$S(t) = \frac{N_{ex}}{\sqrt{N_{OFF}}} \sqrt{\frac{t}{T}} \quad (7.7)$$

where T is the observation time in which N_{ex} and N_{OFF} were obtained. This expression, however, does not take into account the uncertainty in the determination of the background and slightly over-predicts the sensitivity of the instrument (Mazin 2007). MAGIC can achieve an integral flux sensitivity of about 1.6 % the Crab Nebula flux at energies $E \geq 200$ GeV for a single telescope by using timing parameters (Tescaro et al. 2007), whereas stereoscopic observations are expected to reduce this value by a factor of 2-3.

7.4.4 Upper limit calculation

When no signal is observed in the observation of a given source, as it is the case of the microquasar analysis done in this Thesis, an upper limit to the differential flux at a certain energy range, or to the integral flux above a certain energy threshold E_{th} can be established. The number of ON and OFF events in the signal region is computed, together with their associated errors. The upper limits on the number of excess events, $N_{ex}^{u.l.}$ is derived with a certain confidence level (CL) as described in Rolke et al. (2005). For a 2σ upper limit it corresponds to a CL of 95.45 %, whereas for a 3σ upper limit, the CL is of 99.9%. The integral flux upper limit $\phi^{u.l.}$ (photons $\text{cm}^{-2} \text{s}^{-1}$) is related to $N_{ex}^{u.l.}$ (for $E \geq E_{th}$) through:

$$\phi^{u.l.} = \frac{N_{ex}^{u.l.}}{A_{eff} t_{obs}} \quad (7.8)$$

where A_{eff} is the effective area of the telescope calculated using Monte Carlo simulated gamma-ray showers. These upper limits assume a source spectral index of -2.6, the one used for the generation of the Monte Carlo simulations. The estimated upper limits at a given energy threshold are expressed in this Thesis in Crab Nebula units. The differential Crab spectrum obtained in Albert et al. (2008c) has been used:

$$\frac{dN}{dE} = 6.0 \times 10^{-10} \left(\frac{E}{300\text{GeV}} \right)^{-2.31-0.26 \log_{10}\left(\frac{E}{300\text{GeV}}\right)} \text{TeV}^{-1} \text{cm}^{-2} \text{s}^{-1} \quad (7.9)$$

7.4.5 MAGIC Analysis and Reconstruction Software (MARS)

MARS is a collection of programs for the analysis of the MAGIC data (Moralejo et al. 2009). It is written in C++ in the framework of the ROOT data analysis software maintained at CERN². It has been developed in order to cover all the data reduction steps, from the reading of the raw FADC data to the calculation of spectra, lightcurves and sky maps of the observed gamma-ray source.

²ROOT is publicly available at <http://root.cern.ch>

MARS divides the analysis chain into several steps, which are performed by an independent program that takes as input the output of one or more of the previous stages. During MARS execution, data are organized in ROOT trees. Each tree includes a set of parameter containers for every data entry. MARS programs typically perform a loop over the entries and executes a defined task for every event in the input file stored in the different parameter containers.

In a first step, the raw data files recorded during the acquisition chain are used as input for the MARS program `calisto`. This program is intended to calibrate the raw data. It subtracts the pedestal offsets and extracts the integrated signal of each pixel, as well as the arrival time of the pulse. `calisto` equalizes the response of the different camera pixels and corrects for relative offsets in the arrival times by using dedicated pedestal and calibration runs (see Sect. 7.3.1). An absolute calibration is also performed by `calisto` through the F-Factor method.

In a second step, a cleaning is performed in order to remove those image pixel that are suspected to contain no light from the shower. Both the signal amplitude and the time information for each pixel is used to accept a certain pixel as part of the image. After cleaning, the next step is the parameterization of each shower image. Both image cleaning and parameterization are realized in MARS through the `star` program.

The image parameters delivered by `star` are intended for the signal/background separation process. MARS makes use of the Random Forest method, and the program in charge of the training phase of the Random Forest is called `osteria`. Its input is Monte Carlo simulated gamma-ray showers and real MAGIC data of a sky region with no strong gamma-ray sources. Its output are a set of matrices that are later used for the γ /hadron separation. Furthermore, also an estimate of the energy of the primary gamma-ray is performed by `osteria` - using an independent set of Monte Carlo files.

The program `melibea` applies the matrices trained in `osteria` to a third Monte Carlo sample, to the data set to be analyzed and to the background data. The HADRONNESS parameter is calculated, being the main rejection parameter used in the analysis chain.

Finally, the application of the cuts on the background events, the calculation of the effective time of observations and the determination of the excess events and the effective areas are used to extract the energy spectrum and the light curve of the analyzed source. These tasks are performed by the MARS program `flux1c`. Projection of the arrival photon directions into celestial coordinates provides a skymap

of the region containing the gamma-ray source. The program `cellestina` performs this task, which in turn can help on the recognition of significant excesses in the FoV.

Bibliography

- Aharonian, F., Akhperjanian, A., Barrio, J. A., et al 2002, APh, 17, 459
- Albert, J., Aliu, E., Anderhub, H., et al. 2008a, NIMPA, 594, 407
- Albert, J., Aliu, E., Anderhub, H., et al. 2008b, NIMPA, 588, 424
- Albert, J., Aliu, E., Anderhub, H. et al. 2008c, ApJ, 674, 1037
- Aliu, E., Anderhub, H., Antonelli, L. A., et al. 2008, Science, 322, 1221
- Aliu, E., Anderhub, H., Antonelli, L. A., et al. 2009, APh, 30, 293
- Barrio J. A. et al. 1998, in *The MAGIC telescope - Design study of a 17 m Cherenkov telescope for Gamma-Astronomy above 10 GeV*, MPI-PhE/98-5
- Daum, A., Hermann, G., Hess, M., et al. 1997, APh, 8, 1
- Domingo-Santamaria, E., Flix, J., Scalzotto, V., et al. 2005, proceedings of the 30st International Cosmic Ray Conference, 363
- Dorner, D. 2008, PhD thesis, Bayerischen Julius-Maximilians-Universität of Würzburg
- Colin, P., Borla, D., Carmona, E., et al. 2009, proceedings of the 31st International Cosmic Ray Conference
- Garczarczyk, M. 2007, PhD thesis, Technical University, Munich
- Gaug, M. 2006, PhD thesis, Universitat Autònoma de Barcelona
- Gaug, M., Moralejo, A. 2008, in *A handbook of the standard MAGIC analysis chain*, in preparation
- Goebel, F., Bartko, H., Carmona, E., et al. 2008, Proceedings of the 30th International Cosmic Ray Conference, 3, 1481
- Heck, D., Knapp, J., Capdevielle, J.N. et al. 1998, Report FZKA 6019, Forschungszentrum Karlsruhe
- Hillas, A. M. 1985, proceedings of the 19th International Cosmic Ray Conference, 3,

445

Li T.-P. & Ma Y.-Q. 1983, ApJ 272, 317

Mazin, D. 2007, Ph.D Thesis, Technische Universität, München

Majumdar, P., Moralejo, A., Bigongiari, C., et al. 2005, proceedings of the 29th International Cosmic Ray Conference, 5, 203

Mirzoyan, R., Kankanian, R., Krennrich, F., et al. 1994, NIMPA, 351, 513

Mirzoyan, R. 1997, proceedings of the 25th International Cosmic Ray Conference, 7, 265

Moralejo, A., Gaug, M., Carmona, E., et al 2009, proceedings of the 31st International Cosmic Ray Conference

Rolke W. A., López, A. M., & Conrad, J., 2005, NIMPA, 551, 493

Tescaro, D., Bartko, H., Galante, N., et al. 2007, proceedings of the 30st International Cosmic Ray Conference, 3, 1393

Weekes, T. C., Cawley, M. F., Fegan, D. J., et al. 1989, ApJ, 342, 379

Chapter 8

Observations of microquasars

8.1 Microquasars as Binary TeV sources

Observations with the first generation of Cherenkov telescopes yielded tentative hints of signal from Cyg X-3 and GRS 1915+105 (see, e.g. Danaher et al. 1981 and Aharonian et al. 1998, respectively). These results were however not conclusive and additional observations did not give a high significance level. Improvements in the spatial resolution and sensitivity of the present gamma-ray facilities were partially motivated to obtain a proper detection or compelling upper limits on the emission from these systems. Besides that, an intense theoretical effort has been accomplished during last years in estimating the expected fluxes from microquasars under a wide variety of scenarios and in the whole electromagnetic spectrum, in particular in the gamma-ray domain (see, e.g., Atoyan & Aharonian 1999; Heinz & Sunyaev 2002; Romero et al. 2005; Bosch-Ramon et al. 2006; Gupta et al. 2006, Dermer & Böttcher 2006; Orellana et al. 2007; Khangulyan et al. 2008; Reynoso et al. 2008, Romero & Vila 2008).

On September 24th 2006, a TeV gamma-ray flare evidence at 4.9σ significance level (4.1σ after trial correction) has been found from the well established microquasar Cyg X-1 (Albert et al. 2007). A microquasar scenario has indeed been assumed for other two binary TeV sources (BTV), namely LS 5039 (Paredes et al. 2000; Aharonian et al. 2005a) and LS I +61 303 (Massi et al. 2004; Albert et al. 2006). Alternatively, these two sources could contain a young non-accreting neutron star where the VHE emission is powered by rotation (Martocchia et al. 2005; Dubus 2006; Dhawan et al. 2006), as it is the case of PSR B1259 -63 (Aharonian et al. 2005b), and not by accretion (see however Romero et al. 2007; Bosc-Ramon &

Khangulyan 2009, and references therein).

In these models the orbital modulation have a strong effect on the injection of particles accreted from the companion. It also affects the target ions with which the stellar wind can fill the binary system region and the photon/magnetic fields capable of producing/preventing electromagnetic cascades. The appearance of outbursts at radio/IR wavelengths or peaks of emission at X-rays can be related to an increase of the activity also at VHE (Jogler et al. 2009), although the time-delay between them could range from hours to days (Atoyan & Aharonian 1999). Moreover, the multifrequency correlation could be present only at some stages of the flare (Albert et al. 2007), rendering the triggering of TeV observations a quite difficult task.

The MAGIC telescope observed the four microquasars GRS 1915+105, Cyg-X3, Cyg-X1 and the system SS 433/W50, for more than 150 h in total from 2005 to 2008. Observations were triggered by radio flaring alerts from the RATAN telescope as well as by ensuring the LH state of the source through *RXTE* and *Swift* monitoring data in the first three objects. In the case of SS 433, a prediction of the minimum absorption super-orbital phase (Reynoso et al. 2008a) was used to trigger the observations.

Below we report on the upper limits of the steady and variable emission from Cyg X-1 in MAGIC cycle III and SS 433 cycle IV observations - during 2007 and 2008, respectively. The results for GRS 1915+105 and Cyg X-3 in observation cycles II (in 2006) and III have been recently published, and a detailed study on the physical implications is in preparation. The reader is referred to the work by Zanin (2009) and Saito et al. (2009) for precise reports. In the next Sections we will describe the observation and analysis details of Cyg X-1 and SS 433. We discuss on the steady state upper limits for both sources and apply the theoretical models presented in Chapters 4 and 5. Concluding remarks are given in last Section.

8.2 Observations of Cyg X-1

8.2.1 Source description and previous observations

Cyg X-1 is an XRB system composed by a $20 \pm 5 M_{\odot}$ black-hole powered by accretion of matter from a $40 \pm 10 M_{\odot}$ O9.7 Iab companion star (Ziółkowski 2005). Located at a distance of about 2.1 kpc, it is one of the brightest source of X-rays in our Galaxy, reaching luminosities of $L_{(1-100) \text{ keV}} \sim \text{few} \times 10^{37} \text{ erg s}^{-1}$. The system displays a period of 5.6 d for an almost circular orbit, and its inclination with respect to the line of sight is about $33^{\circ} \pm 0.5$. (Gies & Bolton 1986). Cygnus X-1 is found most of the time in the LH state (Wilms 2006) when is though that steady compact jets are produced in microquasars (see Chapter 2.4). The X-ray spectrum is dominated by a hard tail in this state, thought to be produced by IC scattering by thermal electrons off soft disk photons in the corona or at the base of a mildly relativistic ($v \sim 0.6c$) jet. At radio energies, a stable emission is found at a level of $\sim 15 \text{ mJy}$ during the low/hard state, displaying a flat spectrum (Stirling 2001). In the high/soft state, the soft thermal component produced by the accretion disk dominates the X-ray spectrum, while in the radio band the emission is quenched or remains below detectable flux levels (Brocksopp et al. 1999). Additionally, flaring episodes have been observed both in X-rays (Golenetskii et al. 2003; Gies & Bolton 2003), in which the flux can vary by more than an order of magnitude, and at radio wavelengths, where the flux can reach $\sim 0.15 \text{ Jy}$ levels (Fender 2006).

Cygnus X-1 is the only confirmed black-hole accretion-powered XRB from which evidence of TeV emission has been found (Albert et al. 2007). The system was observed with the MAGIC telescope between June and November 2006 for 26 nights for a total of 40 h in dark-sky conditions. A search for steady emission did not yield any significant excess. A day-by-day analysis was performed, since the source can exhibit flare activity in time-scales of a few hours. The results were compatible with background fluctuations at 99% CL for all nights except for that in September 24th 2006. Data for that night was further divided in two halves, obtaining a 0.5σ and a 4.9σ signal for the first and second halves, respectively. The post-trial probability is conservatively estimated by assuming 52 trials (2 per observation night) and corresponds to a significance of 4.1σ . The observed excess is consistent with a point-like source located at the position of the Cyg X-1, at RA = $19^{\text{h}}58^{\text{m}}17^{\text{s}}$, DEC = $35^{\circ}12'8''$. The shell region is excluded as the emitter location.

Coincident with the MAGIC detection, an enhancement of the X-ray flux lasting for ~ 3 days was seen by *RXTE* All Sky Monitor (ASM) at 1.5-12 keV, while a

peak in the *Swift* light-curve at energies 5-50 keV was also present in September 24th 2006. Moreover, *INTEGRAL* reported hard X-ray emission in coincidence with the MAGIC measurement, reporting an exceptionally long-lived hard-X-ray flare that lasted for several days (Malzac et al. 2008). The TeV excess was observed about 1.5 h before the hard X-ray maximum. Nevertheless, *Swift* detected a further (and stronger) X-ray peak on September 25th 2006, when MAGIC observations did not find any evidence of gamma-rays. In addition, by the time of the detection the source was at the X-ray maximum of its ~ 326 d super-orbital modulation period (Rico 2008).

At lower gamma-ray energies, significant evidence of steady non-thermal HE emission from Cyg X-1 extending up to few MeV has been observed by the COMPTEL experiment onboard the CGRO (McConnell et al. 2000). This emission is detected in both LH and HS states, although in the later state it has a flux level about 4 times higher than in the former (McConnell et al. 2002). Emission at soft gamma-rays is also reported by *INTEGRAL*, who extensively observed Cyg X-1 during the period 2002–2004 (Cadolle-Bel et al. 2006). At GeV energies, EGRET did not detect the source and unfortunately the upper limit does not provide any further constraint on the spectrum extrapolated from the COMPTEL observations (Hartman et al. 1999; see also McConnell et al. 2001).

Finally, the powerful jets of Cyg X-1 have created a bubble with a radius $\sim 10^{19}$ cm around the binary system. Shock-heated ISM material is observed through thermal Bremsstrahlung radiation from radio to optical wavelengths (Martí et al. 1996, Gallo et al. 2005; Russell et al. 2007). The jet/medium interaction shock (the bow shock) is however not adiabatic, and an important amount of the bow shock kinetic energy is dissipated through radiative mechanisms. Nonetheless, the study of such interactions has revealed a much higher jet power than that inferred from direct observations of the (one-sided) inner jet. Interestingly, a possible solution to account for this difference would come from the presence of thermal protons in the jets (Heinz 2006).

8.2.2 Trigger conditions and data sample

VHE gamma-ray emission in microquasars is generally expected when the jet is present, i.e., in the LH state. The strategy followed in MAGIC cycle III observations of Cyg X-1 focused on the presence of the source in this spectral state. Soft X-ray data (1-20 keV) from the ASM on board the *RXTE* as well as hard X-ray observations (15-150 keV) taken by the Burst Alert Telescope (BAT) on board *Swift*

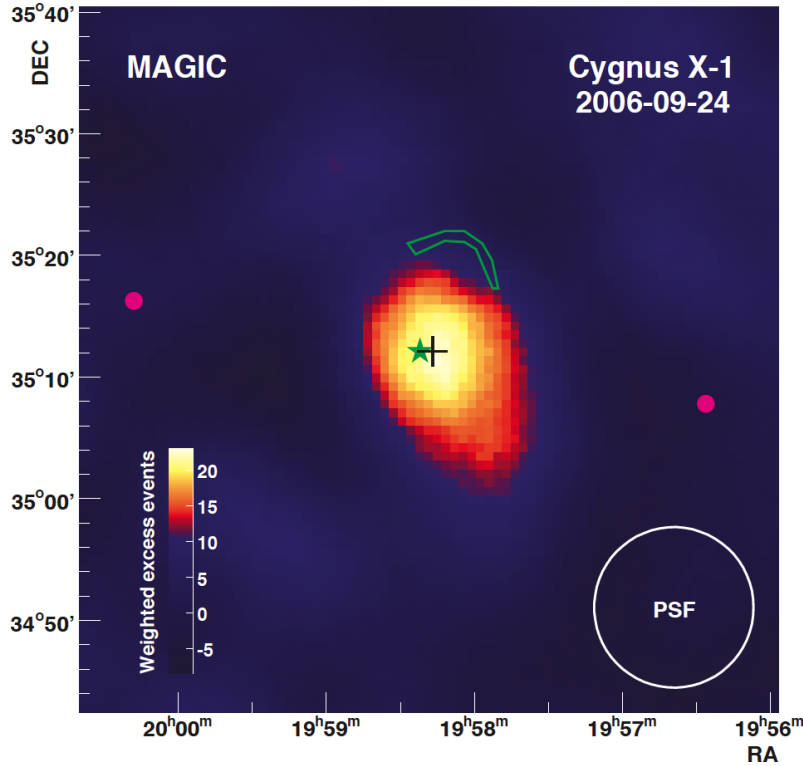


Figure 8.1: Skymap of the gamma-ray excess events from Cyg X-1 after background subtraction above 150 GeV corresponding to 78.9 minutes of effective observation time in MJD 54002.928 to 54002.987. The cross shows the best-fit position of the gamma-ray source, the green star shows the X-ray source position and the green contour is the radio emitting shell location (Martí et al. 1996; Gallo et al. 2005). Figure adapted from Albert et al. (2007).

were used to define the spectral state of Cyg X-1. A selected sample of sources showing high activity is continuously monitored by both instruments. The data are publicly available from their respective web pages soon after satellite downloads them. X-ray fluxes are provided in counts per second. In order to translate these fluxes to physical units, the Crab Nebula flux is used, which represents ~ 75 counts/s in the ASM and ~ 0.22 counts/s in the BAT instrument (see Malzac et al. 2008 and references therein).

The trigger conditions were defined in two ways: first of all a flux level larger than 0.2 counts/sec in the orbitally-averaged light curve obtained by BAT is required. Secondly, the ratio between *RXTE* ASM and *Swift* BAT fluxes has to be below a value of 200. The first constraint is intended to ensure that the source is effectively emitting relatively high fluxes of hard X-rays, while the second prevents the observation during the HS state. It is important to mention that *Swift* encountered technical problems at the end of July 2007, which prevented observations of the source for nearly one month.

The trigger criteria was accomplished for selected nights in July 2007, as well as in October and November 2007. The malfunction of the *Swift* satellite made impossible the monitoring of the sources during August and part of September. In addition, strong calima was present during July at La Palma. The corresponding data is hence affected by a noticeable lower flux (about 30% lower, in average), and is not used in the data analysis. Data from October/November, have a relatively constant trigger rate, and only some runs have been omitted from the analysis due to bad weather conditions or spurious contamination from car flashes. A total of 7 nights have been finally used for the analysis.

The Cyg X-1 processed data show zenith angles in the range $[6^\circ\text{-}28^\circ]$ as observed from the MAGIC site. Data was taken using the false-source tracking *wobble* mode (see Sect. 7.3) where the source is 0.4° from the camera center. In this observation mode, a background estimation is simultaneously obtained and used later in the analysis chain to normalize the source counts in a given *ALPHA* range. Moreover, the *wobble* mode allowed us to avoid the effects of the bright star (3.9 magnitude) η -Cyg, located at $26'$ from Cyg X-1. The total observation time amounts to ~ 13.0 h.

Crab Nebula observations have been used for the optimization process during the analysis chain. About 2.5 h of good quality *wobble* data corresponding to the night of October 9th 2007 are used. Both Cyg X-1 and the Crab Nebula data sets are shown in Table 8.1. Finally, Monte Carlo simulations are also needed for the data analysis process. High and low energy *wobble* Monte Carlo files have been employed for the training and flux estimation process, selected to account for similar PSF and zenith angle characteristics with respect to the Cyg X-1 data.

8.2.3 Data analysis and results

After rejection of those runs showing a rate level below $\sim 30\%$ of the average one for each observation night, the standard analysis chain has been performed on the whole dataset. The Hillas parametrization as well as the Random Forest method events have been used for the training process (see Sect. 7.3). The Crab Nebula sample provided the optimal cuts on the parameters *HADRONNESS* and *ALPHA*, selected as those values that reported the highest sensitivity on the October 9th 2007 data. The optimal values have been $HADRONNESS \leq 0.07$ and $ALPHA \leq 8^\circ$, yielding an analysis sensitivity of 2.19 % of the Crab Nebula flux for a *SIZE* cut of 200 phe.

Our analysis did not yield a significant excess beyond 150 GeV towards the position of Cyg X-1 with respect to the background level (see the *ALPHA* distribution

Table 8.1: Cyg X-1 data sample analysed and Crab Nebula observations used for the optimization of the analysis.

Source	Obs. date	Obs. time (h)	Rate (Hz)	Zenith angle ($^{\circ}$)	PSF (mm)	Obs. mode
Cyg X-1	October 5 th 2007	1.92	183.8	6-26	13.0	<i>wobble</i>
	October 6 th 2007	1.92	255.5	6-26	12.5	<i>wobble</i>
	October 8 th 2007	1.93	226.6	18-28	12.7	<i>wobble</i>
	October 9 th 2007	1.96	194.0	10-28	12.6	<i>wobble</i>
	October 10 th 2007	2.23	194.4	7-26	12.9	<i>wobble</i>
	October 11 th 2007	1.82	176.2	11-27	12.9	<i>wobble</i>
	November 6 th 2007	0.95	194.0	20-28	12.4	<i>wobble</i>
Crab Nebula	October 9 th 2007	2.36	198.3	7-26	12.8	<i>wobble</i>

Table 8.2: *Upper limits to the Cyg X-1 gamma-ray emission at energy thresholds $E_\gamma \geq 150, 300, 500$ and 800 GeV for the whole data sample. In the second column the excess events is shown, $N_{\text{ex}} = N_{\text{ON}} - N_{\text{OFF}}$. Third column displays the significance σ_{LiMa} as calculated in Li & Ma (1983). The computed integral upper limits are displayed in the fourth and fifth columns, in units of $\text{ph cm}^{-2} \text{s}^{-1}$ and percentage of the integrated Crab Nebula flux (calculated from Albert et al. 2008), respectively.*

E_{th}	N_{ex}	σ_{LiMa}	$\phi_{\text{u.l}}$	Crab units
$E_\gamma \geq 150 \text{ GeV}$	-7.7 ± 37.7	-0.26	8.06×10^{-12}	2.15 %
$E_\gamma \geq 300 \text{ GeV}$	-6.7 ± 22.0	0.32	4.24×10^{-12}	3.45 %
$E_\gamma \geq 500 \text{ GeV}$	6.5 ± 13.2	0.51	2.4×10^{-12}	4.17 %
$E_\gamma \geq 800 \text{ GeV}$	11.7 ± 8.1	1.41	2.0×10^{-12}	8.24 %

Table 8.3: *Integral upper limits have also been computed in a day-by-day basis. The results for an energy threshold of $E \geq 200 \text{ GeV}$ are shown. Observations of Cyg X-1 in 2006 have shown that the source has rapid variability (Albert et al. 2007). Hence it is worthy to search for rapid variations of the VHE flux. The meaning of each column head is the same as in Table 8.2.*

Date	N_{ex}	σ_{LiMa}	$\phi_{\text{u.l}}$	Crab units
October 5 th 2007	10.0 ± 7.2	0.94	1.5×10^{-11}	6.32 %
October 6 th 2007	-11.7 ± 8.3	-0.64	9.5×10^{-12}	4.01 %
October 8 th 2007	-35.3 ± 16.8	-1.17	5.1×10^{-12}	2.18 %
October 9 th 2007	4.7 ± 26.2	0.77	1.1×10^{-11}	4.81 %
October 10 th 2007	-16.9 ± 17.3	-0.64	7.1×10^{-12}	2.99 %
November 6 th 2007	9.6 ± 20.6	0.49	2.4×10^{-11}	10.07 %

in Fig. 8.2). Analysis at higher energy thresholds have also been computed, without positive results. Furthermore, since a hint of gamma-ray flare was apparent in cycle II observations of Cyg X-1 only for one night, a day-by-day analysis of the data has been performed. The same optimization cuts obtained by comparison with the Crab sample have been applied. No signal is found beyond a statistical significance of 1.5σ . The integral upper limits at 95% C. L. for the whole sample at different energy thresholds and those for each observation night for $E \geq 200 \text{ GeV}$ are shown in Table 8.2 and Table 8.3, respectively. The Rolke method (Rolke et al. 2005) with a systematic error of 30 % has been employed for their calculation, while an assumed spectral index of $\Gamma = 2.6$ characterizes the Monte Carlo simulated showers

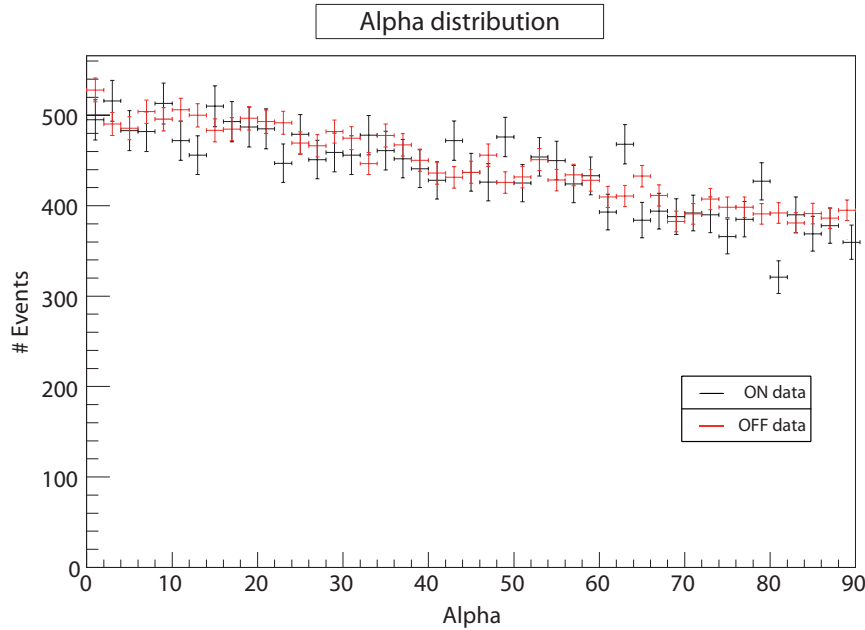


Figure 8.2: *ALPHA* plot of the ON and OFF events for the whole data sample for energies $E \geq 150$ GeV. The *ALPHA* distribution provides one of the most effective background rejection method. It relies on the isotropic distribution of the hadronic showers, while an enhancement of the excess events should appear at low *ALPHA* values where the shower major axis is pointing to the assumed source position. No such excess events at low *ALPHA* ($\leq 8^\circ$) values above the background counts is found.

used in the effective area calculation.

A phase-folded analysis has also been performed covering most of the orbital phases of the binary system. We have used an orbital period of $P_{orb} = 5.599836$ d and a reference date for phase $\Psi = 0$ on MJD 41163.631 (Gies & Bolton 1982, Brocksopp et al. 1999) for the superior conjunction of the black hole, that is, when the companion star is between the compact object and the observer. We provide in Fig. 8.3 the differential upper limits to the gamma-ray emission from Cyg X-1, both for the whole data sample and in a phase by phase basis. Their values range between 5%-12% the Crab Nebula differential flux, and will be used below to constrain the spectral energy distribution at VHE and compare it with the theoretical expectations.

8.3 Discussion

We intend to explore the gamma-ray emission that can be produced in the micro-quasar Cyg X-1 by applying the framework presented in Chapter 4. The calculations presented there were performed for a binary system with similar characteristics as

those of Cyg X-1. Moreover, the short orbital period of the system, ~ 5.6 d, allows the present MAGIC observations to cover a significant orbital phase range. The gamma-ray emission in a hadronic scenario estimated in Chapter 4 considered the attenuation factor of the inner regions of Cyg X-1 as a function of the orbital phase. Hence, a proper comparison of the VHE luminosities under different absorption conditions can be performed. Fig. 8.3 shows the differential upper limits in three different phase ranges, $\psi \in [0.9-0.1]$, $[0.4-0.6]$, and $[0.7-0.8]$, obtained above $E = 150$ GeV. The results for the whole data set are also displayed.

In order to compare the upper limits with the luminosity estimations obtained in Chapter 4 (see Fig.4.2), we assume a distance to Cyg X-1 of $d = 2.1$ kpc (Ziółkowski 2005); the differential flux is expressed in units of TeV^{-1} , so we multiply each point in the different phase-range figures by a factor $(E/\text{TeV})^2$ to obtain the upper limit source luminosity, which we then convert conveniently to units of erg s^{-1} . The most constraining upper limit of $L_\gamma(E) = (4\pi d^2) \times E^2 \times dN(E)/dE$ for the studied ranges comes from phases $\Psi \in [04 - 06]$. The attenuation due to cascading in the photon field of the companion star is the lowest in this range, and the gamma-ray SED presented in Fig. 4.2 suffers only a small absorption at energies $\gtrsim 0.6$ TeV. The maximum luminosity allowed by the MAGIC upper limits from Fig. 8.3 in $\phi \in [0.4-0.6]$ is about $L_\gamma = E \times L_\gamma(E) \sim \text{few} \times 10^{33} \text{ erg s}^{-1}$. In particular, the luminosity $L_\gamma = 1.7 \times 10^{33} \text{ erg s}^{-1}$ found at $E = 0.6$ TeV is the most stringent constraint on the source luminosity in the analysis performed here. This value restricts the total power injected in the jet as relativistic protons L_p (the rest of parameter values are those for the scenario presented in Chapter 4, where a TeV emitter close to the black hole is assumed), to be $\lesssim 5.48 \times 10^{35} \text{ erg s}^{-1}$, corresponding to a fraction of the Eddington luminosity going to relativistic protons $q_{rel} = 4.56 \times 10^{-4}$. Under the assumed conditions, a higher fraction of the jet power to accelerated particles would violate the MAGIC constraints in our hadronic model.

We use the above limiting value for q_{rel} to estimate the non-thermal radiation produced by secondary leptons. The emission of Cyg X-1 at radio frequencies show a flux of about 12-15 mJy at cm wavelengths during the LH state (Pooley et al. 1999; see also Fender et al. 2000, Stirling et al. 2001). Small variations of $\sim \pm 2$ mJy are observed, which could be due to a periodic super-orbital modulation of the accretion rate. The fluxes obtained in our model are at the level $\leq 1 \times 10^{-3} \text{ erg cm}^2 \text{ s}^{-1} \text{ Hz}^{-1} = 1 \text{ mJy}$ at cm wavelength, taking $d = 2.1$ kpc. This value is well below the averaged radio fluxes of Cyg X-1 in the hard state at these frequencies. It is then necessary to conclude that a primary component must be present. Otherwise, our model accounts for local electron/positron injection from π^\pm -decay within the jet, which radially decay as $\propto z_{jet}^{-2}$ and it is nearly suppressed at $\sim 10^{12}$ cm. Cooling due to

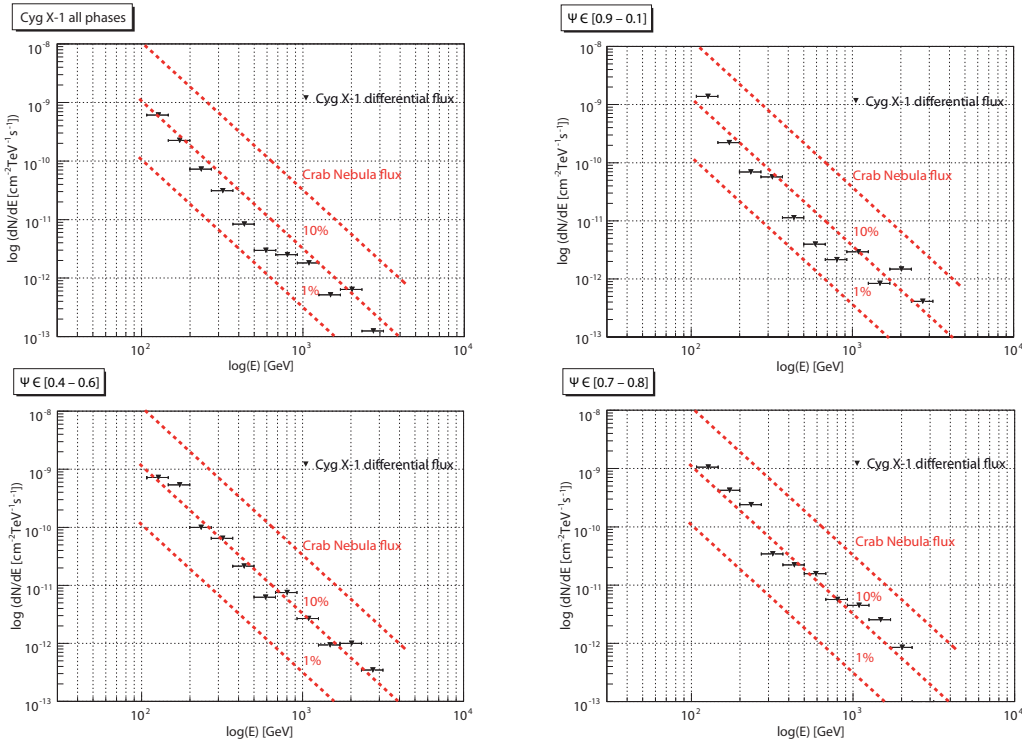


Figure 8.3: Differential upper limits to the gamma-ray flux from Cyg X-1 at energies $E \geq 150$ GeV during orbital phases in the ranges $[0.9 - 0.1]$, $[0.4 - 0.6]$ and $[0.7 - 0.8]$ (note that the predicted absorption in this last phase range is equal to that in the range $[0.2 - 0.3]$, (see Chapter 4)). The differential flux for the whole data is also displayed.

radiative and adiabatic losses affect the steady non-thermal leptonic distributions. Re-acceleration along the jet could bring the radio fluxes at the level of the observed values. Particles accelerated up to distances $\geq 10^{12}$ cm have been suggested to explain the TeV hint detected by the MAGIC telescope in September 24th 2006 (see below).

At hard X-rays Cyg X-1 shows a luminosity of about 5×10^{36} erg s^{-1} at (10–150) keV in the low-hard state (Gierliński et al. 1999; Malzac et al. 2008), although it is not clear if this emission has a thermal or non-thermal origin (see, e.g. Markof et al. 2005). Flaring activity can rise this flux by an order of magnitude, but we will restrict to the steady state emission of the source in the LH state. The X-ray luminosity in the range (10–150) keV from secondary leptons obtained for the conditions derived above is found at a level of $\sim 10^{32}$ erg s^{-1} . This low value cannot account for the whole X-ray emission. A primary leptonic component, thermal or non-thermal, is then required.

The TeV flare observed in September 24th 2006 took place during phases 0.90 to 0.91. The luminosity in the energy interval (0.1–1) TeV was about 2.2×10^{34}

erg s⁻¹ (Albert et al. 2007). We remark that gamma-rays produced in the inner regions of the system are strongly attenuated in this orbital phase. In particular, such a luminosity is higher than that predicted in our hadronic model at phases $\psi \sim 0$ for a relativistic proton power of $L_p = 6 \times 10^{36}$ erg s⁻¹ and would point to a very efficient accelerator and/or a very dense target field provided by the wind of the companion star. Alternatively, gamma-rays could be generated far away, at distances beyond the binary system length-scale ($\gtrsim 10^{12}$ cm). This scenario has been proposed in Bosch-Ramon et al. (2008), who conclude that the only possibility for the emitter to be well into the binary system requires a companion star with a very low magnetic field (allowing for the generation of cascading processes). Moreover, Zdziarski et al. (2009) investigate the gamma-ray IC emission from primary leptons scattering off the accretion disk and the companion photon fields. These authors use Monte Carlo simulations of the cascade processes occurring through photon-photon absorption, pair creation and IC scattering (see also Bednarek & Giovanelli 2007). Their spectra predict too much emission at energies above 1 TeV, and too little at energies below 0.2 TeV. Although some improvement is accomplished when a steep power-law injection is considered, this would require a great increase of the flare kinetic energy. Therefore both an hadronic and a leptonic cascade scenario need a very high jet power to fit the MAGIC observations at least qualitatively.

Finally, the expansion of the Cyg X-1/ISM interaction structures is braked down since radiation processes are efficient enough to dissipate most of the kinetic energy transported in the jets. In this scenario, the interaction model presented in Chapter 5 would provide only a rough estimate of the geometrical and physical properties of the interaction regions. Furthermore, the capabilities of the shocks to accelerate particles in a radiative shock could be severely reduced. First order Fermi acceleration depends in the shock velocity roughly as $\propto v_{\text{shock}}^2$. In addition, the medium properties in a radiative shock scenario could also make the particle maximum energies to be lower (see, e.g., Drury et al. 1996).

A very low shock acceleration efficiency χ would suppress the production of non-thermal emission from the interaction structures, which in fact has not been detected so far. Gallo et al. (2005) report the observation of thermal bremsstrahlung emission from the shell region, from which a bow shock velocity of about 5×10^6 cm s⁻¹ is derived. Our interaction model predicts a bow shock velocity a factor 3 to 10 times higher (we remark that we considered an adiabatic shock). At radio wavelengths, the scaling down of the acceleration efficiency imply luminosities of about $(0.01\text{--}0.1) \times 10^{32}$ erg s⁻¹ for the cocoon and shell regions adopting the most powerful set of parameters. Even in this case, flux densities at the level of ~ 0.1 mJy/arcmin at cm wavelengths would be obtained. For less extreme parameters for the power,

age and ISM particle densities ($L_{\text{jet}} \leq 3 \times 10^{36}$ erg s $^{-1}$, $t_{\text{MQ}} \leq 3 \times 10^4$ yr and $n_{\text{ISM}} \leq 0.3$ cm $^{-3}$), radio fluxes would be clearly undetectable. At higher energies, both soft-to-hard X-ray and gamma-ray flux production will be also rather low in these circumstances, and the luminosities obtained are clearly below the current instrument sensitivities .

8.4 Observations of the SS 433/W50 system

8.4.1 Source description and previous observations

SS 433 was the first stellar compact object in which relativistic jets were discovered (Spencer 1979). It was identified 30 years ago as a star emitting H α lines located in the Galactic plane (Stephenson & Sanduleak 1977), as a variable non-thermal radio source (Feldman et al. 1978) and as an X-ray source (Marshall et al. 1978), and since then it has been object of intensive studies as a binary system with unique properties. The system is located at a distance of 5.5 ± 0.2 kpc (Blundell & Bowler 2004) and contains a $9 M_{\odot}$ black hole orbiting every 13.1 days a $30 M_{\odot}$ A3–7 supergiant star in a circular orbit with radius $\sim 79 R_{\odot}$ (Fabrika 2004; Cherepashchuk et al. 2005). SS 433 displays relativistic jets at a velocity of $0.26c$ (Margon & Anderson 1989) precessing with a period of 162.4 days in cones of half opening angle $\theta \approx 21^{\circ}$ with respect to the normal to the orbital plane, which in turn subtends an angle of $i \approx 78^{\circ}$ with the line of sight (Eikenberry et al. 2001). These collimated jets (with opening angle of $\approx 1^{\circ}.2$) can be distinguished in the X-ray, optical and radio bands. The emission at the X-ray band is radiated by hot gas ($T \sim 10^8$ K) that cools due to expansion and radiative losses as it propagates outwards. However, gas at $T \sim 10^7$ K is still observed at large distances in the jet, indicating that a continuous source of heating is required (Migliari et al. 2002). At radio wavelengths, the observed synchrotron flux density is about 1 Jy at 1 GHz, with luminosities reaching $\sim 4 \times 10^{32}$ erg s $^{-1}$. The radio jets are clearly visible on VLBI scales down to resolutions of ~ 2 mas (see Fig. 8.4; Paragi et al. 2000).

SS 433 is the only X-ray binary system in which the presence of hadrons in its jets has been found (Fabian & Rees 1979; Kotani et al. 1998; Marshall et al. 2002). Clouds of plasma with baryonic content propagate along ballistic trajectories to large distances without appreciable deceleration. In addition, the donor star provides a powerful flow of gas through Roche lobe overflow, leading to the formation of a supereddington accretion disk. Such high accretion regime would be responsible for the large kinetic power carried by the jets, $L_k \sim 10^{39}$ erg s $^{-1}$ (Dubner et al. 1998).

SS 433 is surrounded by the radio shell of W50, a large $2^{\circ} \times 1^{\circ}$ nebula catalogued as SNR G39.7–2.0 (Green 2006). Its present morphology is the result of the interaction between the jets of SS 433 and the nebula. SS 433 is at the center of W50, and the elongation of the nebula in the east-west direction follows the axis of precession of the jets (forming the so called “ears” of W50; see Safi-Harb & Ögelman 1997). Radio, IR, optical and X-ray emitting regions are also aligned with the jet

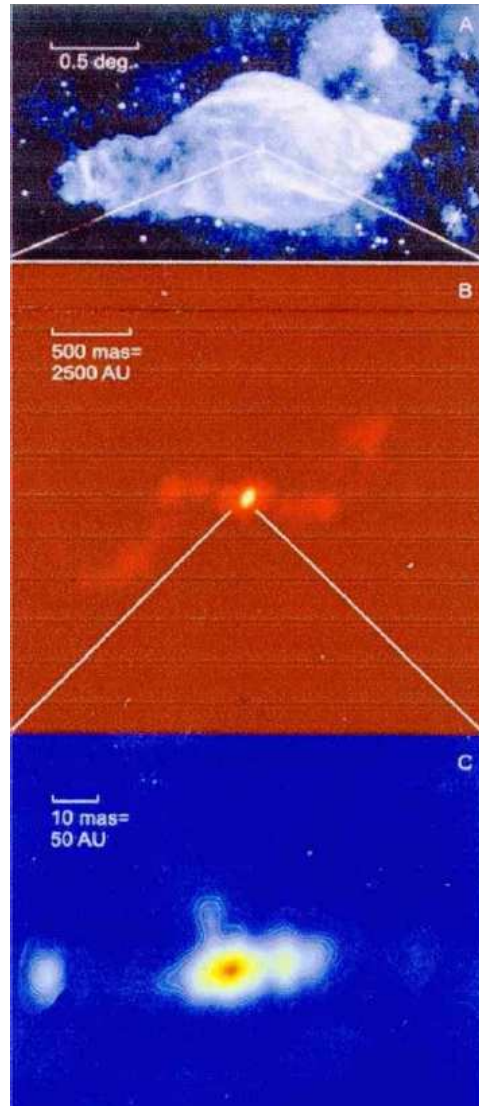


Figure 8.4: Radio images of SS 433 at various angular scales (from Paragi et al. 2000). **Top:** The binary system is surrounded by the W50 nebula, which shows an elongated shape due to the jets pressure. **Middle:** The jets are visible at arcsec scales, where precession is found with period ~ 162 d. **Bottom:** The inner regions mapped with VLBA, where the radio shining zone about 50 mas along the jet is observed.

precession axis. At a distance of $\sim 10^{20}$ cm, the jets are decelerated and, together with an enhanced intensity of the emission at radio wavelengths, large-scale X-ray lobes are observed. The extended X-ray emission is likely of non-thermal origin and much softer than the emission from the central source.

SS 433/W50 has been previously observed in the gamma-ray energy band by the HEGRA collaboration (Aharonian et al. 2005). Observations took place under a variety of observation modes, including *wobble*, ON/OFF and also selected runs

taken from the HEGRA galactic plane scan (Aharonian et al. 2002). Data were taken over 4 years and a total of 391 runs were analysed, reaching an exposure in excess of 100 h for the central binary system and the western interaction regions. About 72 h were obtained for each of the “e1” and “e2” regions in the eastern interaction lobe. The reported upper limits to the integral flux are at a level of 3.2 % of that of the Crab Nebula for $E \geq 0.8$ TeV (see Aharonian et al. 2005). However, it is now known that severe absorption effects produced by the accretion disk wind could be at work for about 80% of the ~ 162 d precessing period of the system (see below). The reported HEGRA gamma-ray flux upper limits from the inner regions of the system do not take this into account.

The Cangaroo-II telescope, on the other hand, pointed to the west interaction regions of the SS 433/W50 system for a total observation time of 85 h (Hayashi et al. 2003). After rejection of low-quality data runs, about 60 % of the total time was kept for the analysis. These observations did not yield any significant excess. Unfortunately, no precise flux upper limits have been reported.

Gamma-ray production and absorption processes in SS 433

In a leptonic framework, gamma-rays could be produced through IC scattering off ambient photon fields. In addition, self-synchrotron Compton (SSC) emission as well as interaction of accelerated electrons with jet ions through relativistic Bremsstrahlung processes could also generate VHE emission. In a hadronic scenario, interactions of relativistic protons in the jet can also produce gamma-rays through π^0 -decay. The target ions could be provided both by the companion and disk winds, or by the pool of thermal protons outflowing within the jet itself.

Gamma-ray fluxes generated in the inner regions of SS 433 can be however strongly attenuated. Both the donor star and the compact object are embedded in a thick extended envelope (Zwitter et al. 1991) that can provide a large amount of low energy UV and mid-IR photons, causing a strong opacity to the propagation of VHE γ -rays. Furthermore, a mass loss rate of $\sim 10^{-4} M_{\odot} \text{ yr}^{-1}$ is thought to be expelled within the $\sim 30^{\circ}$ half opening angle subtended by the envelope. Absorption of VHE γ -rays can occur due to γ -nucleon interactions processes as well. In addition, nucleons from the donor star can absorb gamma-rays and photo-produce pions, while the companion’s photon field can also effectively reduce the gamma-ray flux through pair creation (Reynoso et al. 2008a). The most pronounced attenuation of the gamma-rays produced in the very inner regions of the system comes from the periodic (13.1 days) eclipse caused by the companion star when it crosses the line

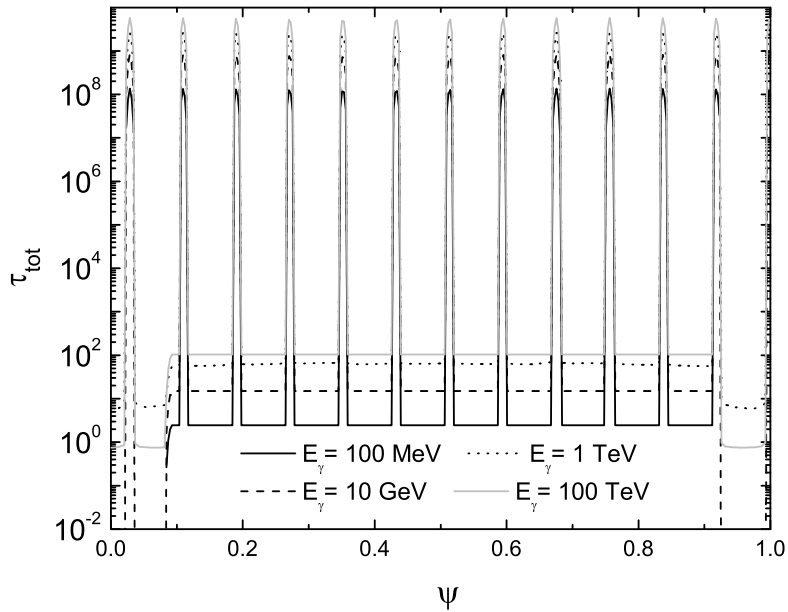


Figure 8.5: Absorption of the inner regions of SS 433 for different energies of the gamma-ray photons, as a function of the precessional phase. The effects of the companion star crossing the line of sight are observed in the periodic (~ 13 d) enhancement of the optical depth. (Figure from Reynoso et al. 2008b)

of sight (see Fig 8.5). Moreover, depending on the precessional phase Ψ , absorption from the equatorial envelope can also be important; at $\Psi \sim 0.5$, the envelope blocks the inner jet emitting region and the putative gamma-ray fluxes generated at this phase would be difficult to observe.

8.4.2 Trigger conditions and data sample

The trigger criteria driving the observations of SS 433 was based on the best opportunity to detect gamma-rays from the inner regions of the system. The minimum absorption precessional phases are in the range $\Psi \in (0.91-0.09)$ (Reynoso et al. 2008b). According to the ephemeris of Gies et al. (2002), precessional phase $\Psi = 0$ took place on 2008 August 20th. The MAGIC telescope pointed to the SS 433/W50 system for 9 nights, for a total amount of time of 14.8 h. Observations began on August 21th, and finalized on August 29th. The observation trigger considered also the periodic eclipse produced by the companion star covering the inner jet regions each 13.1 d for a time range of ~ 2 d. Hence the nights of August 27th and August 28th

were not used to analyse the central binary system (but were used for the interaction regions). In addition, the observations were granted with dark sky conditions. Full moon took place during August 18th, so neither August 18th nor August 19th were considered in spite of the low precessional attenuation of the system in those dates.

At the MAGIC site, SS 433/W50 was observed at zenith angles in the range [24°–30°] using the false-source tracking *wobble* mode (see Sect. 7.3) in which the telescope points at 0.4° offset from the true source position. This allowed to image not only the central binary system, but also the eastern interaction regions “e1” and “e2”. The *wobble* mode provided in addition the simultaneous background sky regions necessary for the data reduction process of the inner regions. The analysis of the “e1” and “e2” regions has been performed for about half of the total observation time, as a consequence of the *wobble* mode pointing positions. Furthermore, the eastern region falls nearly at the center of the camera. The analysis procedure has been more complex than that for the inner system. First of all a search for OFF data at similar zenith angles and telescope conditions was performed. The source PSR J0358 was the best candidate, since a thorough analysis of the ~ 6 h data (after the rejection of low quality events) was recently performed (O. Blanch, private communication) without yielding any gamma-ray signal evidence. These data were taken in *wobble* mode. The next step was the translation of the source location in camera coordinates from the *wobble* pointing position to the camera center at the Osteria level (see Sect. 7.3). This source repositioning was done both for the ON data (the SS 433 *wobble* data) and for the OFF data (the PSR J0358 *wobble* data).

Crab Nebula observations were used to optimize the analysis cuts both for the inner system and the interaction region analysis. In the first case, a Crab *wobble* data sample corresponding to October 25th and 26th 2008, for a total amount of ~ 3 h was used. In the interaction analysis, instead, the only Crab observations in ON mode available, with similar telescope performance and zenith angle conditions in cycle IV, were those taken using the Sumtrigger configuration. After conveniently remove the Sumtrigger flag, a total amount of ~ 2 h of Crab data have been used. Table 8.4 shows the SS 433 inner system and the “e1” and “e2” data sample date, observation rate, zenith angle range, telescope PSF and observation mode. PSR J0358 and Crab Nebula samples are also displayed.

Finally, Monte Carlo data of simulated gamma-ray showers were downloaded from the Port d’Informació Científica (PIC). These simulations were chosen to fit the zenith angle conditions, PSF characterization and observation mode (*wobble* vs ON/OFF) to be latter applied to both the inner region and interaction analysis.

Both high energy and low energy Monte Carlo simulations have been used for the training and the flux estimation processes.

8.4.3 Data analysis and results

Quality cuts based on the event rate have been applied to the entire dataset. A total amount of 11.5 hours has finally been processed through the standard MAGIC analysis chain. The Hillas image parametrization and the Random Forest method are used for the background rejection (see Sect. 7.3), whereas the Crab Nebula sample provided the analysis cut optimization on the parameters *HADRONNESS*, *ALPHA* and *THETA*. An *ALPHA* analysis is applied to the central binary system, which is assumed to be a point-like source, while *THETA* is used to search for extended emission from the interaction regions.

The best cuts found have been $HADRONNESS \leq 0.04$ and ≤ 0.07 for the central system and interaction region analysis, respectively. For *ALPHA* and *THETA*, the optimization with the Crab Nebula sample has yielded the most suitable values of $ALPHA \leq 9^\circ$ for the central system analysis, while a value $THETA \leq 0.16^\circ$ was used to account for the extension of the eastern non-thermal X-ray emitting regions where the VHE production is studied (Safi-Harb & Petre 1999).

Our analysis do not show any significant excess beyond 150 GeV above the background level (see Fig. 8.6) neither for the central binary system nor for the east interaction regions. We have also searched for a signal hint at different energy thresholds, at 300 GeV, 500 GeV and 800 GeV with no positive results. The 2σ upper limits on the number of excess events have been calculated using the Rolke method, with a systematic error of 30 % (Rolke et al. 2005). The derived upper limits assume a source spectral index of $\Gamma = 2.6$, the same as the Monte Carlo files used for the calculation of the effective areas (see Sect. 7.3).

Table 8.5 summarizes the obtained integral upper limits to the emission from the central binary system and the “e1” and “e2” interaction regions at different energies. To further investigate the presence of a significant VHE gamma-ray signal, a sky map of the arrival directions of gamma-like showers was produced. This is shown in Fig. 8.6 for an energy threshold of 150 GeV. The W50 nebula radio contours are also included for better localization of the inner binary system and the interaction regions. The differential upper limits have also been calculated, and are displayed in Fig. 8.7 and Fig. 8.8, together with the Crab Nebula flux for comparison.

Table 8.4: SS 433 data sample and observation conditions, together with Crab Nebula and PSR 0358 data sets used for the optimization and OFF sample, respectively.

Source	Obs. date	Obs. time (min)	Rate (Hz)	Zenith angle ($^{\circ}$)	PSF (mm)	Obs. mode
SS 433	August 21 th 2008	46.40	66.6	25-30	12.7	<i>wobble</i>
	August 22 th 2008	115.03	149.4	24-28	12.1	<i>wobble</i>
	August 23 th 2008	177.38	111.2.5	24-29	11.8	<i>wobble</i>
	August 24 th 2008	145.40	114.2	24-32	12.3	<i>wobble</i>
	August 25 th 2008	15.77	170.2	26-27	12.2	<i>wobble</i>
	August 26 th 2008	111.93	170.6	24-30	12.4	<i>wobble</i>
	August 29 th 2008	157.50	191.2	24-31	13.4	<i>wobble</i>
e1 + e2	August 21 th 2008	23.03	66.6	25-30	12.7	ON
	August 22 th 2008	58.25	149.4	24-28	12.1	ON
	August 23 th 2008	89.67	111.5	24-29	11.8	ON
	August 24 th 2008	72.81	114.2	24-32	12.3	ON
	August 25 th 2008	15.77	170.2	26-27	12.2	ON
	August 26 th 2008	52.56	170.6	24-30	12.4	ON
	August 27 th 2008	54.27	162.2	24-30	12.4	ON
	August 28 th 2008	58.37	174.1	24-30	12.4	ON
	August 29 th 2008	19.22	191.2	24-31	13.4	ON
Crab Nebula	October 25 th 2008	104.84	199.5	7-20	13.7	<i>wobble</i>
	October 26 th 2008	101.90	198.5	6-20	14.5	<i>wobble</i>
Crab Nebula	November 30 th 2008	204.37	145.9	7-30	13.5	ON (Sumtrigger)
	December 1 st 2008	53.73	124.1	7-18	13.6	ON (Sumtrigger)
PSR J0358	January 18 th 2009	58.81	233.0	26-30	14.7	OFF
	January 20 th 2009	73.82	215.0	26-29	15.2	OFF
	January 22 th 2009	65.60	215.4	26-28	14.7	OFF
	January 24 th 2009	55.88	211.6	26-28	14.8	OFF
	January 27 th 2009	46.23	187.6	26-27	26-27	OFF

Table 8.5: Upper limits to the emission from the central binary system and east interaction regions “e1” and “e2” at energies $E_\gamma \geq 150, 300, 500$ and 800 GeV. $N_{\text{ex}} = N_{\text{ON}} - N_{\text{OFF}}$ is the difference between ON and OFF events. The significance σ_{LiMa} is calculated following Li & Ma (1983). The integral upper limits are expressed in units of $\text{ph cm}^{-2} \text{s}^{-1}$. We have integrated the differential Crab Nebula flux reported in Albert et al. (2008) in last column (see also Sect. 7.4).

Source	N_{ex}	σ_{LiMa}	$\phi_{\text{u.l}}$	Crab units
$E_\gamma \geq 150$ GeV				
SS 433	-38.0 ± 32.0	-1.17	3.61×10^{-12}	0.95 %
e1 + e2	-4.6 ± 32.7	-0.16	2.14×10^{-11}	5.67 %
$E_\gamma \geq 300$ GeV				
SS 433	-11.7 ± 19.7	-0.59	1.89×10^{-12}	1.54 %
e1 + e2	-3.3 ± 18.4	-0.21	7.43×10^{-12}	6.04 %
$E_\gamma \geq 500$ GeV				
SS 433	6.3 ± 12.3	0.51	1.87×10^{-12}	3.47 %
e1 + e2	-13.6 ± 15.4	-1.14	3.31×10^{-12}	6.16 %
$E_\gamma \geq 800$ GeV				
SS 433	4.7 ± 7.36	0.64	1.06×10^{-12}	4.25 %
e1 + e2	-10.9 ± 11.5	-1.29	2.12×10^{-12}	8.46 %

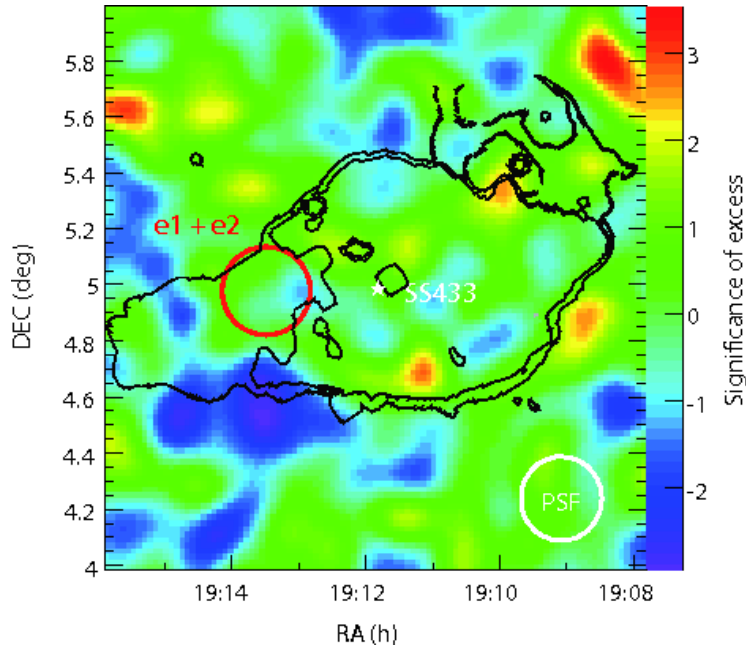


Figure 8.6: Skymap of the SS 433/W50 system as observed at $E \geq 150$ GeV. The colour scale represents the excess events significance. The small star at the center marks the central binary system position, while the east interaction regions “e1” and “e2” are marked with a red circle. The W50 nebula radio contours are also displayed (Dubner et al. 1998).

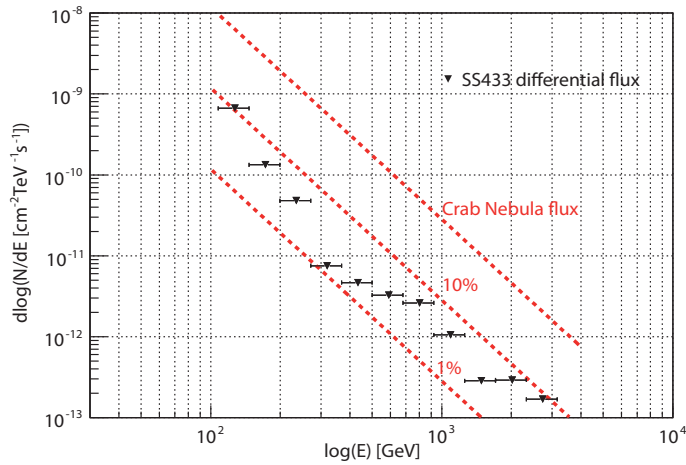


Figure 8.7: Differential upper limits to the gamma-ray fluxes generated at the inner regions of SS 433. The three red-dotted lines indicate, from top to bottom, the Crab Nebula flux, its 10% and its 1% fractions. The Rolque method (Rolque et al. 2005) with a systematic uncertainty of 30% has been applied.

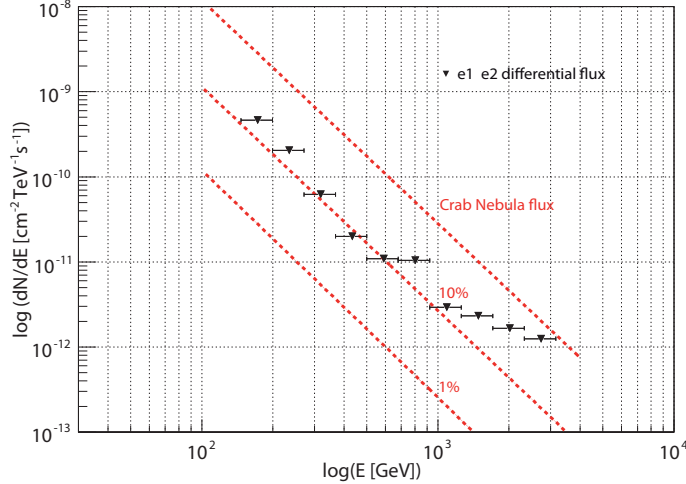


Figure 8.8: Differential upper limits for the “e1” and “e2” eastern interaction regions.

8.5 Discussion

The reported upper limits to the γ -ray fluxes from SS 433/W50 can help to constrain some physical mechanisms operating in this system. VHE emission could be produced both in the inner regions and within the interaction zones in which the jet impacts the surrounding nebula. Below, we discuss separately both scenarios. The main parameters of the system used in our computations are listed in table 8.6.

8.5.1 Steady emission from SS 433

Gamma-ray production requires particle acceleration and the presence of dense photon or matter fields. The power transferred to the accelerated non-thermal particle populations will depend on the acceleration efficiency $q_{\text{accel}} = q_e + q_p$ defined as the ratio of the non-thermal power of relativistic particles over the jet bulk kinetic power, $q_{\text{accel}} = L_{\text{rel}}/L_{\text{kin}}$. Here q_e and q_p will determine which fraction is used for the acceleration of electrons and protons, respectively. In addition, acceleration can take place over an unknown distance $\Delta z_{\text{jet}}^{\text{accel}} \equiv z_{\text{jet},f} - z_{\text{jet},i}$ at different heights along the jet.

In a leptonic scenario, the spectral index of the non-thermal particle distribution and the maximum energies that leptons can reach will also depend on the nature of

Table 8.6: *List of the parameters that remain with a constant value in the analytic model.*

<i>Parameter</i>	<i>Symbol</i>	<i>Value</i>
Jet kinetic power (erg s ⁻¹)	Q_{jet}	10^{39}
ISM density (cm ⁻³)	n_{ISM}	1
Source age (yr)	t_{MQ}	5×10^4
Jet Lorentz factor	Γ_{jet}	1.04
Jet opening angle (°)	Ψ	5
Luminosity companion star (erg s ⁻¹)	L_{\star}	10^{39}
Self-Similar parameter	R	3
Magnetic equipartition fraction	η	0.1
Non-thermal luminosity fraction	χ	0.01

the acceleration mechanism. It is hard to derive precise values for these parameters, and we assume in the following that a given fraction of the total jet power is delivered to a leptonic accelerated plasma that follows a power-law distribution, $N_e \propto \gamma_e^{-p}$, with a spectral index $p = 2$. We consider acceleration and emission taking place along a given slice $\Delta z_{\text{jet}}^{\text{accel}}$ within the jet, and we do not account for radiative nor expansion losses that would affect the particle spectral distribution. We remark that a strong absorption of gamma-rays is present in the inner regions, at $z_{\text{jet}} \leq 10^{13}$ cm (see Reynoso et al. 2008a). We therefore consider only acceleration regions beginning further away than that point. We note that the contribution of accelerated particles from the highly absorbed region prior to $\sim 10^{13}$ cm is negligible at the energies of interest, since their radiative life-times are much shorter than the jet propagation time-scale. Fig. 8.9 shows a sketch of the scenario considered.

To estimate the gamma-ray fluxes produced through IC process, we approximate both the companion star and the disk envelope as point-like sources of isotropic black-body radiation at temperatures $T=8500$ K and 21.000 K, respectively (Gies et al. 2002; Fuchs et al. 2006). We use the IC cross section including both Thompson and Klein-Nishina regimes for this process, since $\gamma_e \gtrsim \gamma_{\text{KN}} \equiv (4\epsilon_0)^{-1}$, where $\epsilon_0 \times m_e c^2 \sim 2.7 K_{\text{B}}T$ is the peak energy of each corresponding photon field. The orbital separation is taken to be $a_{\text{orb}} = 79 R_{\odot}$, the jet kinetic power is $L_{\text{kin}} = 10^{39}$ erg s⁻¹, and a distance to the system $d = 5.5$ kpc is used.

It is worth noting that synchrotron losses could be severe enough to dominate

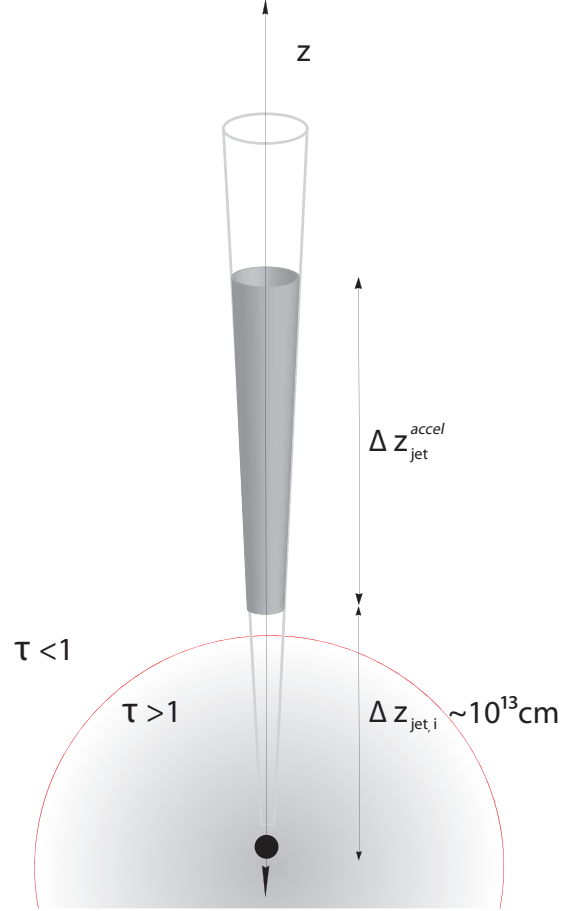


Figure 8.9: We consider acceleration along a given slice $\Delta z_{\text{jet}}^{\text{accel}}$ beginning at a height $z_{\text{jet},i}$, beyond which the attenuation is lower, $\tau \lesssim 1$.

the energy losses of the high energy radiating particles. A magnetic to radiation field energy density fraction $\eta \equiv u_{\text{mag}}/u_{\text{rad}}$ high enough would make this channel to dominate and the gamma-ray fluxes would be partially suppressed (here $u_{\text{mag}} = B^2(z_{\text{jet}})/8\pi$ and $u_{\text{rad}} = L_{\star}/4\pi(z_{\text{jet}}^2 + a_{\text{orb}}^2) c$, where $B(z_{\text{jet}})$ is the magnetic field present at a certain jet height z_{jet} and L_{\star} is the companion star luminosity). We restrict our study to the case $\eta \leq 1$, constraining the magnetic field to be $B \leq 250 \left(\frac{10^{13} \text{ cm}}{z_{\text{jet}}}\right) \text{ G}$ for the adopted value of the star luminosity, $L_{\star} = 10^{36} \text{ erg s}^{-1}$. This value of the magnetic field is also used to compute the acceleration time-scale and compare it to adiabatic and radiative losses (we use the expressions provided in Chapter. 3). A maximum particle Lorentz factor $\gamma_e^m = 10^6$ is used in our computations.

Integral luminosities for energies $E_{\gamma} \geq 150 \text{ GeV}$ of $L_{\gamma} \sim 10^{34} \text{ erg s}^{-1}$ ($L_{\gamma} \sim 10^{33} \text{ erg s}^{-1}$) are obtained if gamma-rays are generated and emitted at distances $z_{\text{jet},i} \sim 10^{13} \text{ cm}$ (10^{14} cm) up to $z_{\text{jet},f} \sim 10^{17} \text{ cm}$. We note that taking $z_{\text{jet},f}$ much

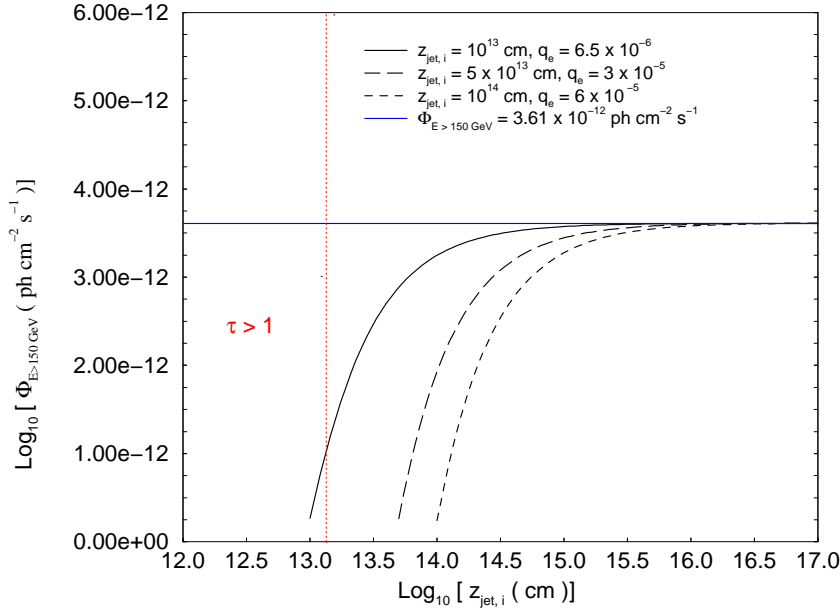


Figure 8.10: Integral flux upper limit obtained for $E_\gamma \geq 150$ GeV (horizontal blue line), together with the total flux obtained through IC process for three different values of the acceleration efficiency q_e and acceleration injection height $z_{\text{jet},i}$ (we recall that leptons are accelerated along $\Delta z_{\text{jet}}^{\text{accel}} = z_{\text{jet},f} - z_{\text{jet},i}$, and we have used $z_{\text{jet},f} = 10^{17}$ cm in all cases; see text for details). The region at the left side of the red-dotted line has optical depth values ≥ 1 (see Reynoso et al. 2008a).

higher than 10^{17} cm does not significantly change our results, since at these distances the photon field energy density is negligible (we do not consider the contribution from the CMB in our calculations). Besides that, the IC time-scale at distances larger than $\sim 10^{17}$ cm for the most energetic particles becomes longer than the jet propagation time-scale, and the emitter would become larger than the accelerator. We also compute the expected integral fluxes produced along the accelerator-emitter region $\Delta z_{\text{jet}}^{\text{accel}}$ as a function of the injection point and the acceleration efficiency. This is shown in Fig. 8.10, where the upper limit $\phi_{\text{u.l}} \leq 3.61 \times 10^{-12}$ ph cm $^{-2}$ s $^{-1}$ for $E_\gamma \geq 150$ GeV for the central regions of SS 433 is also displayed.

The values stated above depend linearly on q_e and the acceleration region within the jet, which are nonetheless poorly constrained under a theoretical point of view. A value of q_e far larger than $\sim 10^{-5}$ for $\Delta z_{\text{jet}}^{\text{accel}}$ starting at $z_{\text{jet},i} \sim 10^{13}$ cm is ruled out within our flux estimations and the reported upper limits, while $q_e \geq 10^{-4}$ is not allowed provided the acceleration region $\Delta z_{\text{jet}}^{\text{accel}}$ starts at $z_{\text{jet},i} \geq 10^{14}$ cm. Acceleration processes could be much less efficient than expected, though it seems unlikely since acceleration is actually required to explain the non-thermal emission at lower energies.

In addition to the IC process, relativistic Bremsstrahlung and SSC can also play a role in the generation of VHE emission. These mechanisms are however expected to be important only at the very inner regions near the jet base, where magnetic fields and ion densities are the highest. The opacity in these zones (up to $z_{\text{jet}} \sim 10^{13}$ cm) should make the gamma-ray luminosity to decrease by a factor of $2 \times 10^{-2} - 6 \times 10^{-3}$ (Reynoso et al. 2008b), so their contribution at VHE would be difficult to observe.

Regarding the VHE photons that could be produced in a hadronic scenario, Reynoso et al. (2008b) have recently addressed the possibility of detecting VHE γ -ray emission from proton-proton interactions in the inner jets of SS 433. This emission depends nevertheless on the densities adopted, which are a strong function of the distance to the compact object. The authors predict an integral gamma-ray flux for $E_\gamma \geq 800$ GeV of $\phi_{E \geq 800 \text{ GeV}} \sim 2 \times 10^{-12}$ ph cm $^{-2}$ s $^{-1}$ for $q_p = 10^{-4}$ with absorption effects at precessional phases $\Psi \in [0.9 - 0.1]$ already taken into account. By using the HEGRA upper limit on the VHE γ -ray flux from SS 433, q_p is constrained to be $\lesssim 3 \times 10^{-4}$. These values assume however that HEGRA observations took place during unknown precessional phases. In order to account for the absorption of the gamma-ray photons, they consider a Ψ -averaged flux to derive the upper limit on q_p . The actual MAGIC observations were performed during the lowest absorption phases. By comparing the proton-proton expected gamma-ray fluxes with the MAGIC reported upper limits at $E_\gamma \geq 800$ GeV a more stringent constrain of $q_p \leq 7.4 \times 10^{-5}$ can be derived.

8.5.2 Interaction regions of SS 433/W50

Non-thermal emission from relativistic electrons has been proposed to account for the radio to X-ray extended emission both in the west and east SS 433/W50 interaction regions (Moldowan et al. 2005; Safi-Harb & Ögelman 1997; Safi-Harb & Petre 1999). The spectra of X-rays coming from the extended lobes are well represented by a power-law model, and a radio spectra calculated using a synchrotron model for the radio emission fits consistently with the observed low-energy emission (Safi-Harb et al. 1997). This would imply the existence of TeV electrons in those regions, produced by acceleration processes in strong shocks, both in the jet material or propagating into the surrounding medium. High and VHE emission can also be produced in this context.

In the following, we will apply the model presented in Chapter 5 to compare the obtained upper limits with the theoretical expectations. A value of $L_{\text{kin}} \sim 10^{37}$ erg s $^{-1}$ was used there, so a necessary scaling up to $L_{\text{kin}} = 10^{39}$ erg s $^{-1}$ is required for the

application of the model to the powerful jets of SS 433. This higher power does not modify the assumptions regarding the self-similar growing of the structures, since the characteristic length-scale l_0 (see Sect. 3.6) is $\sim 5 \times 10^{15}$ cm for SS 433, which is still much shorter than the distances up to which the jets are detected, $\geq 10^{20}$ cm.

We take a source age of about 5×10^4 yr (Watson et al. 1983 and references therein), and fix the medium density at a conservative value of $n_{\text{ISM}} = 1 \text{ cm}^{-3}$. The W50 nebula is the product of a SN explosion that swept up the surrounding medium, with initial particle densities $\sim 0.1 - 1 \text{ cm}^{-3}$. Far behind the SN shock front, the shocked medium material has steadily expanded, and the SN blast wave strong shock condition $n_{\text{ISM}}^{\text{shocked}} \approx 4 \times n_{\text{ISM}}$ will be relaxed to some extent.

The system parameters for the computation of the non-thermal emission, as well as the physical conditions obtained for the shocked regions, are listed in table 8.6 and 8.7, respectively. The bow shock is found at $\sim 10^{20}$ cm, and the jets tips are located at about $\sim 6 \times 10^{20}$ cm, where the reverse shock is produced; the cocoon has a width of $\sim 10^{18}$ cm, according to the chosen self-similar ratio $R = 3$. These geometrical derivations are in good agreement with the SS 433/W50 observed properties (see for instance Dubner et al. 1998; Safi-Harb & Ögelman 1998). Varying their value by small factors would just slightly change our results, and they serve as a consistent check to establish the shock velocities, magnetic fields and emitter locations where the non-thermal emission is computed.

In Fig. 8.11 we show the SED computed for the shell, the cocoon and the re-confinement interaction regions. Relativistic Bremsstrahlung is the most efficient gamma-ray production mechanism in the shell zone, reaching luminosities at the level of $3 \times 10^{33} \text{ erg s}^{-1}$. IC is the main radiation channel of high and VHE energy output in the cocoon and re-confinement regions, with luminosities at the level of a few $\times 10^{31} \text{ erg s}^{-1}$. The integrated gamma-ray flux for energies $E \geq 150 \text{ GeV}$ is found to be $1.6 \times 10^{-13} \text{ ph cm}^{-2} \text{ s}^{-1}$, roughly 3 times lower than the upper limits listed in table 8.5.

It is interesting to compare the radio to X-ray emission levels predicted in our model with those obtained in previous works. Watson et al. (1983) report the observation of soft X-ray extended emission at distances $\sim 1.7 \times 10^{20}$ cm from the central system (assuming a distance $d = 5.5 \text{ kpc}$). This emission can be associated to the interaction of SS 433 jets with the surrounding nebula. They find a spectral softening of the X-ray spectrum both in the radial (along the jet) and azimuthal (transverse to the jet) directions, which is expected if efficient acceleration is mainly produced at the tip of the jet. At larger distances the most energetic particles will have cooled somewhat and since no fresh particles are further injected, a softening

Table 8.7: *Physical properties of the three interaction zones obtained with the parameter values listed in table ???. The values at t_{MQ} are displayed, but we remark that they have a time dependence (see Chapter 5).*

<i>Physical properties</i>	<i>Inferred values</i>
<i>SHELL</i>	
Magnetic field B (G)	6×10^{-5}
Shock velocity v_b (cm s $^{-1}$)	4.4×10^7
Emitter size r (cm)	2.3×10^{20}
Rad. energy dens. u_* (erg cm $^{-3}$)	5.0×10^{-14}
Maximum energy E_{max} (TeV)	54.2
Target density n_t (cm $^{-3}$)	4.0
<i>COCOON</i>	
Magnetic field B (G)	3.8×10^{-5}
Shock velocity v_s (cm s $^{-1}$)	1.6×10^{10}
Emitter size r (cm)	5.5×10^{19}
Rad. energy dens. u_* (erg cm $^{-3}$)	6.4×10^{-14}
Maximum energy E_{max} (TeV)	280.5
<i>RECONFINEMENT</i>	
Magnetic field B (G)	5.2×10^{-5}
Shock velocity v_{conf} (cm s $^{-1}$)	1.9×10^9
Emitter size r (cm)	1.9×10^{20}
Rad. energy dens. u_* (erg cm $^{-3}$)	2.5×10^{-10}
Maximum energy E_{max} (TeV)	5.2

of the overall spectrum should be observed. Watson et al. (1983) find a peak luminosity $\sim 10^{34}$ erg s $^{-1}$ in the range (0.4-4.5) keV. Our model predicts a similar soft X-ray luminosity, at the level of a few $\times 10^{33}$ erg s $^{-1}$. The small difference can be accounted for the smaller magnetic fields found in the cocoon region, $B = 6 \times 10^{-5}$ G, as compared to $B \sim 10^{-4}$ G assumed in Watson et al. (1983). Observations by Yamauchi et al. (1994) at 1-10 keV with *ASCA*, on the other hand, reveal that the X-ray lobes are most probably of non-thermal origin. Similar conclusions are derived in the work of Safi-Harb & Petre (1999) using *RXTE*, *ROSAT* and *ASCA* data. For the non-thermal interpretation, Safi-Harb & Petre (1999) find that a synchrotron

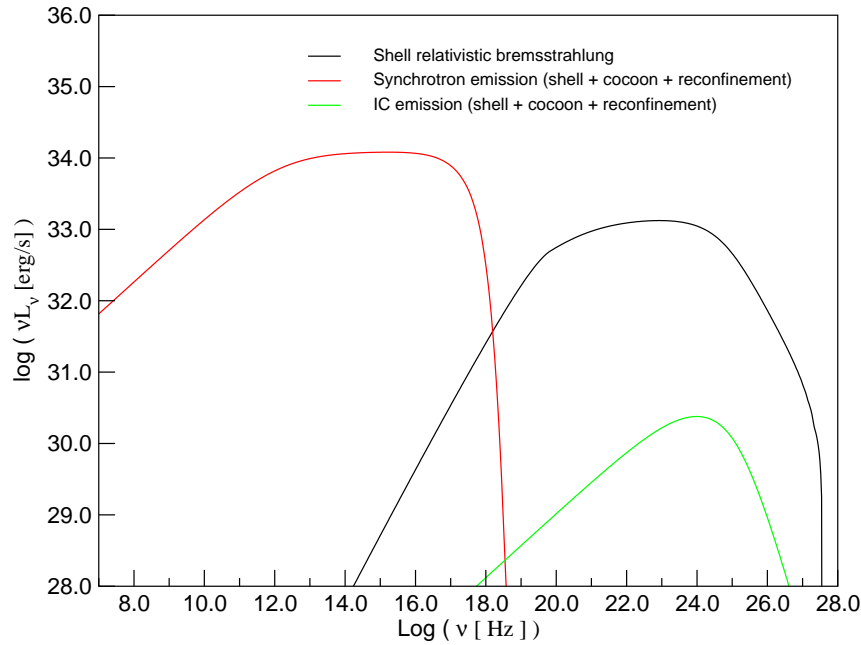


Figure 8.11: *SED of the interaction regions obtained for the parameters listed in table 8.6 and the physical properties shown in 8.7. The sum of the contributions from the shell region, the cocoon and the reconfinement region is displayed. Relativistic bremsstrahlung is important only in the shell region, due to the low particle densities in the jet and cocoon.*

framework fits well their observations. They derive an X-ray luminosity of about $(3-5) \times 10^{-11} \text{ erg cm}^{-2} \text{ s}^{-1}$ in the (0.5–100 keV) range, again in agreement with our estimations. Finally, observations in the radio band at 1465 MHz at the level of $\sim 70 \text{ Jy}$ have been reported (Downes et al. 1981; Dubner et al. 1998). The corresponding flux produced in the eastern wing of the W50 nebula accounts for about 21% of the total flux, providing $\sim 15 \text{ Jy}$. At a distance of 5.5 kpc, this represents $\sim 10^{33} \text{ erg s}^{-1}$, similar to the $7 \times 10^{32} \text{ erg s}^{-1}$ we find.

The huge kinetic luminosity and baryonic content delivered by the jets of SS 433, plus the high surrounding matter densities, render proton-proton interactions a good TeV emission mechanism as well, as shown for even more modest energy budgets (see, e.g., Bosch-Ramon et al. 2005). In addition, distinct spectral features have been predicted resulting from the acceleration of protons at the shock interfaces (see Heinz et al. 2002). We did not explore their role in our interaction model. Nevertheless, the formation of the self-similar structures in a hadronic and leptonic framework could be roughly similar (see Scheck et al. 2002). The computation of the gamma-ray fluxes in a hadronic interaction scenario is left for further work.

Bibliography

- Aharonian, F. A., Akhperjanian, A. G., Beilicke, M., et al. 2002, *A&A*, 395, 803
- Aharonian, F. A., Akhperjanian, A. G., Aye, K.-M., et al. 2005a, *Science*, 309, 746
- Aharonian, F. A., Akhperjanian, A. G., Aye, K.-M., et al. 2005b, *A&A*, 442, 1
- Aharonian, F. A., Akhperjanian, A. G., Beilicke, M., et al. 2005c, *A&A*, 439, 635
- Aharonian, F. A. & Heinzlmann, G. 1998, *Nuclear Physics B Proceedings Supplements*, 60, 193
- Albert, J., Aliu, E., Anderhub, H., et al. 2006, *Science*, 312, 1771
- Albert, J., Aliu, E., Anderhub, H., et al. 2007, *ApJ*, 665, L51
- Albert, J., Aliu, E., Anderhub, H. et al. 2008, *ApJ*, 674, 1037.
- Atoyan, A. M., & Aharonian, F. A 1999, *MNRAS*, 302, 253.
- Bednarek W., & Giovanelli, F. 2007, *A&A*, 464, 437
- Blundell, K. M., & Bowler, M. G. 2004, *ApJ*, 616, L159
- Bonnet-Bidaud J.M., & Chardin G., 1988, *Phys. Reports*, 170, 325
- Brocksopp, C., Fender, R. P., Larionov, et al. 1999, *MNRAS*, 309, 1063
- Brocksopp, C., Tarasov, A. E., Lyuty, V. M., & Roche, P. 1999, *A&A*, 343, 861
- Bosch-Ramon, V., Romero, G. E., & Paredes, J. M. 2006, *A&A*, 447, 263
- Bosch-Ramon, V., Khangulyan, D., & Aharonian, F. A. 2008, *A&A*, 489, L21.
- Bosch-Ramon, V. & Khangulyan, D. 2009, 18, 347
- Bosch-Ramon, V., Aharonian, F. A., & Paredes, J. M. 2005, *A&A*, 432, 609.
- Cadolle Bel, M., Sizun, P., Goldwurm, A., Rodriguez, J. et al. 2006, *A&A*, 446, 591
- Cherepashchuk, A. M., Sunyaev, R. A., Fabrika, S. N., et al. 2005, *A&A*, 437, 561
- Danaher, S., Fegan, D. J., Porter, N. A., Weekes, T. C., et al. 1981, *Nature*, 289,

568

- Dermer, C. D., & Böttcher, M. 2006, ApJ, 643, 1081.
- Dhawan, V., Mioduszewski, A., & Rupen, M. 2006, PoS, Proceedings of the VI Microquasar Workshop: Microquasars and Beyond, ed. T. Belloni, p. 52.1
- Downes, A. J. B., Pauls, T., & Salter, C. J. 1981, A&A, 103, 277.
- Drury, L. O'C, Duffy, P., & Kirk, J. G. 1996, A&A, 309, 1002
- Dubner, G. M., Holdaway, M., Goss, W. M., & Mirabel, I. F. 1998, AJ, 116, 1842
- Dubus, G. 2006, A&A, 456, 801
- Eikenberry, S. S., Cameron, P. B., Fierce, et al. 2001, ApJ, 561, 1027
- Fabian, A. C., & Rees, M. J. 1979, MNRAS, 187, 13
- Fabrika, S. 2004, ASPRv, 12, 1
- Feldman, P. A., Purton, C. R., Stiff, T., & Kwok, S. 1978, IAU Circ. N3258, 1
- Fender, R. P., Pooley, G. G., & Durouchoux, P. 2000, MNRAS, 312, 853.
- Fender, R. 2006, MNRAS, 369, 603
- Fuchs, Y., Miramond, L. K., & Abraham, P. 2006, A&A, 445, 1041
- Gierliński, M., Zdziarski, A. A., Poutanen, J., et al. 1999, MNRAS, 309, 496
- Gies D. R., & Bolton C. T., 1982, ApJ 260, 240
- Gies, D. R., & Bolton, C. T. 1986, ApJ, 304, 371
- Gies, D. R., Huang, W., & McSwain, M. V. 2002, ApJ, 578, L67
- Green, D. A. 2006, A Catalog of Galactic Supernova Remnants, Astrophysics Group, Cavendish Laboratory, Cambridge, United Kingdom (<http://www.mrao.cam.ac.uk/surveys/snrs/>)
- Golenetskii, S., Aptekar, R., Frederiks, D., et al. 2003, ApJ, 596, 1113
- Gupta, S., Böttcher, M., & Dermer, C. D. 2006, ApJ, 644, 409.
- Hartman, R.C., Bertsch, D. L., Bloom, S. D., et al. 1999, ApJS, 123, 79.
- Hayashi, S. et al. 2003, Proceedings of the 28th ICRC, 2533
- Heinz, S. 2002, A&A, 388, L40
- Heinz, S. & Sunyaev, R. 2002, A&A, 390, 751
- Jogler, T., Puchades, N., Blanch Bigas, O., et al. 2009, Proceedings of the the 31st ICRC

- Khangulyan, D., Aharonian, F., & Bosch-Ramon, V. 2008, MNRAS, 383, 467.
- McConnell, M. L., Ryan, J. M., Collmar, W. et al. 2000, ApJ, 543, 928.
- McConnell, M. L., Zdziarski, A. A., Bennett, K. et al. 2002, ApJ, 572, 984
- McConnell, M. L., Bennett, K., Bloemen, H. et al. 2001, AIP Conference Proceedings, 587, 96
- Malzac, J., Lubiński, P., Zdziarski, A. A., et al. 2008, A&A, 492, 527
- Markoff, S., Nowak, M. A., & Wilms, J. 2005, ApJ, 635, 1203
- Marshall, F. E., Mushotzky, R.F., Boldt, E.A., Holt, S.S., & Serlemitsos, P.J. 1978, IAU Circ. N3314, 2
- Marshall, H. L., Canizares, C. R., & Schulz, N. S. 2002, ApJ, 564, 941
- Massi, M., Ribó, M., Paredes, J. M., Garrington, S. T., Peracaula, & M., Martí, J. 2004, A&A, 414, L1
- Margon, B., & Anderson, S. F. 1989, ApJ, 347, 448
- Martocchia, A., Motch, C., & Negueruela, I. 2005, A&A, 430, 245
- Murata, K. & Shibazaki, N. 1996, PASJ, 48, 819
- Paragi, Z., Fejes, I., Vermeulen, et al. 2000, in *Galaxies and their Constituents at the Highest Angular Resolution*. IAU Symp. N205, 266, R.T. Schilizzi, Manchester, United Kingdom.
- Paredes, J.M., Martí, J., Ribó, M., & Massi, M. 2000 Science 288, 2340
- Pooley, G. G., fender, R. P., & Brocksopp, C. 1999, MNRAS, 302, L1
- Reynoso, M. M., Christiansen H. R., & Romero G. E. 2008, APh, 28, 565
- Reynoso, M. M., Romero, G. E., & Christiansen, H. R. 2008, MNRAS, 387, 4, 1745
- Rolke W. A., López, A. M., & Conrad, J., 2005, NIMPA, 551, 493
- Romero, G. E., Christiansen, H. R., & Orellana, M. 2005, ApJ, 632, 1093
- Romero, G. E., Okazaki, A. T., Orellana, M., & Owocki, S. P. 2007, A&A, 474, 15
- Romero, G. E., & Vila, G. S. 2008, A&A, 485, 623
- Rico, J. 2008, ApJ, 683, L55
- Russell, D. M., Fender, R. P., Gallo, E., & Kaiser, C. R. 2007, MNRAS, 376, 1341
- Safi-Harb, S., & Ögelman, H. 1997, ApJ, 483, 868
- Safi-Harb, S., & Petre, R. 1999, ApJ, 512, 784
- Saito, T. Y., Zanin, R., Bordas, P. et al. 2009, Proceedings of the 31st ICRC

- Scheck, L., Aloy, M.A., Martí, J.M., Gómez, J.L., & Müller, E. 2002, MNRAS, 331, 615
- Schilling et al. 2001, Proceedings of the 27th ICRC, 6, 2521
- Spencer, R. E. 1979, Nature, 282, 483
- Stephenson, C. B., & Sanduleak, N. 1977, ApJS, 33, 459
- Stirling, A. M. 2001, MNRAS, 327, 1273
- Vladimirsky, B. M., Stepanian, A. A., Fomin, V. P., et al. 1973 Proceedings of the 13th, 1, 456
- Watson, M. G., Willingale, R., Grindlay, J. E., & Seward, F. D. 1983, ApJ, 273, 688
- Wilms, J. 2006, A&A, 447, 245
- Zanin, R., 2009, Master thesis, Institut de Fisica d'Altes Energies, Barcelona
- Zdziarski, A. A., Malzac, J., Bednarek, W. 2009, MNRAS, 394, L41
- Zealey, W. J., Dopita, M. A., & Malin, D. F. 1980, MNRAS, 192, 731
- Ziólkowski, J. 2005, MNRAS, 358, 851
- Zwitter, T., Calvani, M., & D'Odorico, S. 1991, A&A, 251, 92

Chapter 9

Concluding remarks

The work presented along this thesis has been divided in two parts. In Part I we follow a rather definite theoretical approach and we explore some of the physical processes occurring in the jets of microquasars and in their surrounding medium. Part II is devoted to the search for gamma-ray emission from microquasars, and we adopted instead a predominantly observational approach. Nevertheless, some modeling is also present in this second part, and the theoretical predictions are tested against the MAGIC analysis results.

The composition of the jets observed in a wide variety of astrophysical sources stands as an intriguing question since their discovery. In a microquasar scenario, the presence of relativistic electrons seems to be required in its jets to explain the observed radio to X-ray synchrotron emission. However, relativistic leptons do not necessarily account for the whole jet power, which could come from the contribution of several components. Furthermore, if only hot e^\pm pairs were the main energy carriers, IC off disc photons at the base of the jet would be severe, and a significant fraction of the jet power would be radiated in gamma-rays in a time-scale much shorter than the dynamical time-scale. Such effect is not observed. For a jet composed by hot protons, on the other hand, a huge magnetic field would be needed to confine them. The most economic assumption is then to consider a cold matter dominated jet, composed by protons, electrons and positrons, and magnetic fields. Only a tiny fraction of the matter content would be in the form of accelerated particles.

In the case of SS 33, the presence of hadrons has been directly observed in its jets. Recently, a hadronic gamma-ray emission model has been proposed, which takes into account the periodic eclipse of the inner regions of the binary system by

the accretion disk envelope. The MAGIC upper limits have been obtained during the lowest absorption phase, and are used to constrain the proton acceleration efficiency in this scenario. Furthermore, the analysis results have also been used to constrain the gamma-ray emission in a leptonic framework. Some important simplifications have been made, however, and a more realistic treatment should include adiabatic losses and a proper evolution of the particle energy distribution. Nevertheless, it can be used to provide rough constraints on the electron acceleration efficiency and the gamma-ray emitter location.

In the case of Cyg X-1, the non-detection of steady gamma-ray emission has also been used to constrain the acceleration of protons that may take place in its jets. In addition, the secondary leptonic emission under the constrained parameter values should produce a flux level of non-thermal radiation lower than that observed at the radio and X-ray bands. A primary leptonic population seems therefore to be required, although the possibility of reacceleration of the secondary particles along the jet cannot be ruled out. On the other hand, emission of gamma-rays through direct π^0 -decay is found to depend strongly on the magnetic field value at the surface of the companion star. For high magnetic field values the cascading processes within the binary system would be suppressed. On the contrary, for magnetic fields low enough, the model predicts orbital signatures of the photon-photon absorption due to the phase-dependent paths that gamma-rays have to cover.

The MAGIC collaboration reported a signal evidence of gamma-ray emission at a significance level of 4.1σ from Cyg X-1. This hint corresponded however to orbital phases in which the absorption is at its maximum level. The emitter should then be located at distances larger than the binary system length-scale, $\geq 10^{12}$ - 10^{13} cm. On the other hand, the gamma-ray hint was found for just a half of an observation night, pointing to a flare origin of the signal. The non-detection of steady emission would also imply the necessity of an enhanced jet activity during flaring events, since the persistent gamma-ray emission could be intrinsically too faint to be observed.

Four promising microquasars have been observed with the MAGIC telescope. The analysis details of Cyg X-1 and SS 433 for cycles III and IV observations, respectively, have been presented in this thesis, whereas a detailed report for GRS 1915+105 and Cyg X-3 is in preparation. Different trigger strategies intended to maximize the possibilities to detect their gamma-ray emission have been used. In particular, radio alerts were used to observe GRS 1915+105 and Cyg X-3 during flaring states. Unfortunately, this approach did not lead to a clear signal above the background level. It could be the case that emission at radio energies is not well correlated with TeV emission. The emitter location as well as the particle popula-

tions responsible for the emission in each band could be different. In this regard, monitoring at energies closer to the MAGIC range could enhance the possibility of detecting a given flare. The recently launched spaced-borne missions AGILE and *Fermi* are well suited for this task. Even better would be a continuous monitoring through Cherenkov telescopes. This will be possible in the near future, when new facilities like CTA could be used for this purpose.

Finally, the non-thermal emission predictions of the interaction model presented in Chapter 5 have been applied to the observations of the SS 433/W50 system. A large jet kinetic power of $\sim 10^{39}$ erg s $^{-1}$ has been adopted, producing an enhancement of the expected emission level at gamma-ray energies as compared to the parameter values used in Sect 5.2. An integral gamma-ray flux $\sim 10^{-13}$ erg cm $^{-2}$ s $^{-1}$ is predicted, which is close to the actual sensitivity limits of the MAGIC telescope. Therefore, the expected improvement through the implementation of a second MAGIC telescope could bring for the first time the detection of the microquasar jet/medium interactions at VHE.